

Voltage-driven Reactivity of Liquid Ga and CuGa Nanoparticles for Electrocatalytic CO₂ Reduction and Synthesis

Présentée le 14 décembre 2023

Faculté des sciences de base
Laboratoire de nanochimie pour l'énergie
Programme doctoral en chimie et génie chimique

pour l'obtention du grade de Docteur ès Sciences

par

Valery OKATENKO

Acceptée sur proposition du jury

Prof. W. L. Queen, présidente du jury
Prof. R. Buonsanti, directrice de thèse
Prof. M. Dickey, rapporteur
Prof. L. Protesescu, rapporteuse
Prof. K. Sivula, rapporteur

Acknowledgements

Getting at this point of this journey would not be possible without those who contributed to who I am, what I believe in and what I know, and I cannot imagine acknowledging every person in a commensurate way. PhD part of it, these last 4 years were so full of challenges at all levels that it would not be possible to accomplish without the support I was fortunate to have.

I express my genuine gratitude to Professor Raffaella Buonsanti. I could not be luckier to have a thesis advisor who cares. And as long people care, nothing is impossible. The support and time you dedicated to me as a student gave me the opportunity to grow so much professionally. I could truly enjoy the balance between freedom in taking research decisions, even directions at times, and not feeling alone with the struggles which come with it, which I find invaluable. Over this journey, I had all I needed to make it work, which would not be possible without your full support, especially during harder times. Thank you for providing me the opportunity to be a part of the group, and I am very much looking forward to continuing and applying all what I have learned here with the best memories of it.

I would like to thank the members of the jury: Prof. Wendy Lee Queen, Prof. Kevin Sivula, Prof. Loredana Protesescu and Prof. Michael Dickey for dedicating time to read and evaluate my thesis and providing the valuable comments during the discussion.

I thank all the LNCE members, past and present, for the time as part of one team. Dr. Anna Loiudice, your importance for the group cannot be overestimated. I can barely imagine how things would work without the person who keeps the good traditions in the laboratory, who you can ask and always hear back, especially when this kindness doesn't end with the lab doors. Dr. Dragos Stoian, ever since I came the LNCE and later as a scientist at ESRF, you were always there to advise me or just chat, and every single time I would learn or just get some understanding of the struggles I faced, which is sometimes all you need to feel better. Dr. Min Wang, I cannot count how much time we spent in discussions, at synchrotron, working as neighbors in the lab and how many issues we solved on this way. It has been great time. Dr. James Pankhurst, you are one of the most efficient, in the best sense of this word, people I met. I learned much from you that helped me a lot till now and will do so in future. Dr. Gian Luca De Gregorio, with you as the person to take care of my first training in LNCE, I could develop the practical skills that helped me a lot over this journey, and I appreciate this very much. Dr. Alexander Chen, you are a very kind, professional and organized person, it was always easy, comfortable, and enjoyable to work together. Dr. Mark Newton, I truly enjoyed

some conversations we had over last year, science-related and not, and to be able to ask and learn from you was just great. Dr. Philippe Green, my ice hockey fellow, you are just such a kind and knowledgeable person, and your spirit makes every day better for the people around you. Dr. Kevin Rossi, Dr. Jari Leemans, Dr. Krishna Kumar – we did not have that much time working together, but each one of you is a great personality, extremely helpful, open, and professional, that the group would be incomplete without every one of you. I could not imagine having nicer postdocs around over these years, and I can only thank you all once again.

I thank all the fellow PhD students, those who are already LNCE Dr.'s, will become one, or chose a different path to follow. Dr. Laia Castilla i Amoròs, you have been more than a desk neighbor and collaborator. I feel of you as a co-founder of our liquid metals team, and I find the synergy we had working together just amazing. I am proud of what we could do together, and of the spirit we kept on this way. Dr. Pranit Iyengar, you are such a brilliant, kind-hearted, and open-minded person. I feel we share similar vision on many aspects of life, and I value every conversation we have had over all hours in the electrochemistry lab and beyond. Dr. Chethana Gadiyar, every chat we had was warm and pleasant. You may not even realize how much you contributed to my life, bringing us to our dear cat, Elrond. It changed our life, and I fail to express how grateful I am. Dr. Seryio Saris, the time we had was a great pleasure for me, either as to learn from you as a more experienced fellow, or to chat about living in large cities and what comes with it. Dr. Valeria Mantella, you are a person of rare mindfulness and thoughtfulness. The attention you put to everything is inspiring and having you as my first desk neighbor as a starting PhD student was a great joy to have. Dr. Yannick Guntern, with you being great both at science and in music, I keep hope that I will find my way to restart playing in the band in near future. Thank you for this inspiration, from all my heart! Dr. Seyedehbehnaz Varandili, your energy makes everyone around feel that one can do so much if one truly wants it, thank you for bringing this attitude to the lab. Dr. Jan Vavra, you are a great colleague and knowledgeable person, the projects we worked on together were my big pleasure.

Ona Segura Lecina, with you, a next-to-be Dr. in LNCE, we had the largest overlap in our stay here. The extent to which you contribute to LNCE being a team is amazing. You are a great professional and person in its best possible combination. Petru Albertini, you make our lab special in many ways. You are kind to help every single time one asks you for this, thank you very much for that. Ludovic Zaza, you have been a perfect Master student to have. Now you are and, I am sure, will be a great PhD student in the upcoming years, and it just feels great when your students do so well. Coline Boulanger, even with the short overlap we have had in

our PhD studies, it has been my great pleasure to have you as my collaborator over this last year. I am happy that liquid metals team lives on and is in safe hands. Seongeun Moon, it has been great to have such kind and humble person starting as part of LNCE. Anastasia Blokhina, Kimoon Lee, although limited in time, it was great to work with someone so kind and hard-working, I wish you to find your perfect ways forward.

LNCE would not operate smoothly without the support it has. Laure Dayer, you are just the best administrator I can imagine. With you nothing was ever an issue. Emad Oveisi, Pascal Schouwink, Natalia Gasilova – as scientists in LNCE Valais, you always have us as students backed up, and I thank you for that wholeheartedly. Robin Cyril Deleze, Stephane Voeffray, Cedric Passerini, Jean Perruchoud, Laurent Seydoux, Annabelle Coquoz – each one of you is vital for us to operate. Thank you all for your time and work.

PhD journey takes much even to start it, not to mention to accomplish, especially with the challenges these particular 4 years brought. And it is beyond what one can express with words how much grateful I am to my fiancée, Irina Sinenko. You are the one most important person in my life, and having you by my side is the biggest blessing I could have. Your constant support helps me to be the best version of myself, and I cherish every single moment we spent and will spend together. I am immensely proud of our path till now, of how much we grew together, and of how we manage to cope with challenges while keeping what we could build between us. I could not wait more for our forthcoming marriage and life as family, and we both know the great things and new adventures that wait for us ahead. And although he will not read it, in the end he is a cat, I thank our dear Elrond, the concentrated happiness who greatly changed our life and made our home a true family home, even fuller of love and joy.

I thank my parents, Dmitry and Tatiana. Without your dedication and bravery in caring for me, giving me everything you could, I just would not make it to this point of life, and I will never forget what you did for me to be here. You are and have always been there for me, and I value you being not only my family but also senior friends. This extends to my grandparents, Valery I. and Lyudmila Okatenko, Andrey and Anastasia Bilous, my uncle, Alexey Okatenko, my aunt and godmother, Olga Logvinenko, and the new part of my family, Leonid and Irina A. Sinenko – each one of you, the closest family I have, which I am proud to be a part of. It has been a long journey for all of us until today, and who knows what lies ahead. I am endlessly thankful to all of you for being my guiding lights since I was a child, being real life examples of dedication, love, and kindness, and for the inspiration to become who I am.

Abstract

The rising atmospheric level of carbon dioxide, CO₂, contributes to climate change and poses urgent need to find scalable solutions both to decrease its emissions and to be able to recycle it, if the goals of Paris Agreement to limit the temperature rise are to be met. The electrochemical CO₂ reduction (CO₂RR) offers a solution towards this goal, as it converts CO₂ into valued-added products, which are extensively used in industry and enable storage of renewable energy.

However, there are still some major scientific challenges on the way to the practical use of CO₂RR. Cu-based materials are the only catalysts enabling hydrocarbon production with reasonable performance. With huge progress made to improve the catalysts' selectivity, activity and provide mechanistic insights on CO₂RR on Cu, the catalyst stability aspect remained largely out of focus. At the same time, this point must be addressed to make tangible impact.

This thesis proposes two routes to tackle the stability of CO₂RR electrocatalysts. The first one relies on the current knowledge on the Cu catalyst reconstruction and on alloying as a strategy to prevent its degradation. The second one proposes a paradigm shift towards the use of liquid metals (LMs) as continuously dynamically changing electrocatalysts to drive CO₂RR.

After providing fundamental background in Chapter 1 and experimental details in Chapter 2, Chapter 3 focuses on how alloying Cu with Ga improves the stability of CuGa nanocatalysts. CuGa NPs with 17 at. % of Ga preserve most of their CO₂RR activity for 20 hours while Cu NPs of the same size degrade in 2 hours. Ga reduces the propensity of Cu to oxidize at open circuit potential and CO₂RR and enhances the bond strength in the NPs, thus addressing two key issues behind the degradation of Cu NPs during CO₂RR.

Chapter 4 proves that LM NPs can be implemented as electrocatalysts. The use of NPs as electrocatalysts maximizes surface-to-volume ratio of the material, but LM NPs are expected to rapidly coalesce, similarly to liquid drops, under CO₂RR conditions when a cathodic potential is applied. Yet, we demonstrate that liquid Ga NPs drive CO₂RR and remain well-separated. Experimental proofs indicated that the native oxide skin of the Ga NPs remains present during CO₂RR and provides a barrier to coalescence.

Chapter 5 explores the chemical reactivity of LM Ga and Cu as a function of applied voltage, which is crucial to implement multi-metallic LM NPs electrocatalysts. Voltage and spatial proximity of the two metals dictate the reaction outcome as the voltage controls the reduction

of Ga native oxide skin. This voltage-driven process allows to obtain CuGa₂ alloys or solid@liquid CuGa₂@Ga core@shell NPs, which have unique composition and morphology, respectively, by tuning the reaction stoichiometry. With rationale behind such reaction mechanism, the criteria to predict the outcome for various liquid Ga-based NPs are defined.

The thesis is concluded with a summary and an outlook towards addressing the challenges which the CO₂RR community faces by looking into different and underexplored classes of materials, such as LMs.

Keywords: CO₂RR, electrocatalysis, liquid metals, nanoparticles, alloying, copper, gallium.

Résumé

L'augmentation du taux de CO₂ dans l'atmosphère contribue au changement climatique. Par conséquent, trouver des solutions pour réduire ces émissions et recycler le CO₂ est essentiel pour respecter les objectifs de l'Accord de Paris visant à limiter le réchauffement global. La réduction électrochimique du CO₂ (CO₂RR) pourrait constituer une solution pour atteindre cet objectif, en convertissant le CO₂ en produits à valeur ajoutée pour l'industrie tout en offrant une opportunité de stockage de l'énergie renouvelable.

Cependant, il reste des défis scientifiques majeurs à relever pour parvenir à une utilisation pratique de la CO₂RR. Actuellement, seuls les catalyseurs à base de Cu permettent une production d'hydrocarbures avec des performances raisonnables. Bien que d'énormes progrès aient été réalisés pour améliorer la sélectivité et l'activité des catalyseurs et pour fournir des informations mécanistiques sur la CO₂RR sur Cu, la stabilité des catalyseurs reste largement inexplorée. Il est impératif de résoudre ce problème pour avoir un impact significatif.

Cette thèse propose deux approches pour améliorer la stabilité des électrocatalyseurs CO₂RR. La première repose sur les connaissances actuelles concernant la reconstruction du catalyseur Cu et l'utilisation d'alliage comme stratégie pour prévenir sa dégradation. La seconde propose un changement de paradigme en optant pour l'utilisation de métaux liquides (LM) comme électrocatalyseurs, offrant une évolution dynamique continue pour générer de la CO₂RR.

Après avoir fourni des informations fondamentales dans le chapitre 1 et des détails expérimentaux dans le chapitre 2, le chapitre 3 se concentre sur la façon dont l'alliage de Cu avec Ga améliore la stabilité des nanocatalyseurs CuGa. Les nanoparticules (NPs) de CuGa avec 17 at. % de Ga conservent leur activité CO₂RR pendant 20 heures tandis que les NPs de Cu de même dimension se dégradent en 2 heures. Ga réduit la propension du Cu à s'oxyder au potentiel de circuit ouvert tout comme durant la CO₂RR et améliore la force de liaison dans les NPs, résolvant ainsi deux problèmes clés à l'origine de la dégradation des NPs de Cu au cours de la CO₂RR.

Le chapitre 4 prouve que les LM NPs peuvent être utilisées comme électrocatalyseurs. L'utilisation de NPs comme électrocatalyseurs maximise le rapport surface/volume du matériau. Cependant, dans des conditions de CO₂RR où un potentiel cathodique est appliqué, il est attendu que les LM NPs fusionnent rapidement, de la même manière que des gouttes liquides. Contre toute attente, nous démontrons que les NPs liquides de Ga permettent la

CO₂RR toute en restant bien séparées. Des preuves expérimentales ont indiqué que l'oxyde des NPs de Ga reste présent pendant la CO₂RR et constitue une barrière à la coalescence.

Le chapitre 5 explore la réactivité chimique des NPs de Ga et Cu en fonction de la tension appliquée, ce qui est crucial pour l'utilisation de LMs multimétalliques comme électrocatalyseurs. La tension et la proximité spatiale des deux métaux dictent le résultat de la réaction, car la tension contrôle la réduction de l'oxyde natif de Ga. Ce processus gouverné par la tension permet d'obtenir des alliages CuGa₂ ou des NPs solides@liquides CuGa₂@Ga coeur@enveloppe, qui ont respectivement une composition et une morphologie uniques, en ajustant la stœchiométrie de la réaction. Avec l'étude du mécanisme de réaction, les critères permettant de prédire le résultat pour divers NPs liquides à base de Ga sont établis.

La thèse se termine par un résumé et des perspectives pour relever les défis auxquels la communauté CO₂RR est confrontée en examinant différentes classes de matériaux sous-explorés, telles que les LMs.

Mots clés : CO₂RR, électrocatalyse, métaux liquides, nanoparticules, alliages, cuivre, gallium.

List of abbreviations

CO ₂ RR	Electrochemical CO ₂ reduction reaction
DFT	Density functional theory
DOA	Di- <i>n</i> -octylamine
DWF	Debye-Waller factor
ECSA	Electrochemically active surface area
EDXS	Energy-dispersive X-ray spectroscopy
EGaIn	Eutectic Ga-In (75 wt. % Ga)
EIS	Electrochemical impedance spectroscopy
EXAFS	Extended X-ray absorption fine structure
FE	Faradaic efficiency
FT	Fourier-transform
FTIR	Fourier-transform infrared
Galinstan	Ga-In-Sn (69 wt. % Ga, 21 wt. % In, 10 wt. % Sn)
GaO _x	Native Ga oxide skin
GC	Gas chromatography
GIXRD	Grazing incidence X-Ray diffraction
GRR	Galvanic replacement reaction
HAADF-STEM	High-angle annular dark-field scanning transmission electron microscopy
HER	Hydrogen evolution reaction
HPLC	High-performance liquid chromatography
HRTEM	High-resolution transmission electron microscopy
ICP-MS	Inductively coupled plasma mass spectrometry
ICP-OES	Inductively coupled plasma optical emission spectrometry
LCA	Linear combination analysis
LM(s)	Liquid metal(s)
MP(s)	Microparticle(s)
ND(s)	Nanodimer(s)
NP(s)	Nanoparticle(s)
ocp	Open-circuit potential
ODE	1-octadecene
OLAC	Oleic acid

OLAM	Oleylamine
PVD	Physical vapor deposition
RHE	Reversible hydrogen electrode
SAED	Selected area electron diffraction
SCALMS	Supported catalytically active liquid metal solutions
SEM	Scanning electron microscopy
SHE	Standard hydrogen electrode
SLICE	Shearing liquids into complex particles
STEM	Scanning transmission electron microscopy
SWV	Square-wave voltammetry
TOA	Tri- <i>n</i> -octylamine
TDPA	Tetradecylphosphonic acid
TEM	Transmission electron microscopy
TOPO	Tri- <i>n</i> -octylphosphine oxide
XANES	X-ray absorption near edge structure
XAS	X-Ray absorption spectroscopy
XPS	X-Ray photoelectron spectroscopy
XRD	X-Ray diffraction

Table of Contents

Acknowledgements	i
Abstract	iv
Résumé	vi
List of abbreviations	viii
Introduction	1
1.1 Motivation.....	1
1.2 Electrochemical CO ₂ RR and the stability challenge of Cu catalysts	2
1.2.1 General CO ₂ RR overview	2
1.2.2 Structural reconstruction of Cu electrocatalysts during CO ₂ RR.....	4
1.2.3 Strategies towards stable CO ₂ RR catalysts	5
1.3 Liquid metals and the unique place of Ga among them	6
1.3.1 General overview of liquid metals, Ga and Ga-based materials.....	6
1.3.2 Ga surface oxide and oxide-related properties.....	9
1.3.3 Electrochemistry of pure Ga.	12
1.4 Synthetic routes to obtain Ga and Ga-based multimetallic NPs	15
1.4.1 Top-down approaches	15
1.4.2 Bottom-up approaches	17
Experimental section	20
2.1 Chemicals	20
2.2 Synthetic procedures	20
2.3 <i>Ex situ</i> materials characterization	24
2.4 Electrochemical characterization and electrocatalytic testing.....	26
2.5 <i>Operando</i> X-Ray absorption spectroscopy.....	31
2.6 Theoretical models.....	33
Alloying as a Strategy to Boost the Stability of Copper Nanocatalysts during the Electrochemical CO₂ Reduction Reaction	38
3.1 Introduction	39

3.2 Catalyst synthesis and characterization.....	41
3.3 CO ₂ RR performance.....	43
3.4 Compositional and structural characterization of the catalysts before and after CO ₂ RR ...	46
3.5 <i>Operando</i> X-Ray absorption characterization.....	52
3.6 Mechanism of stability enhancement in CuGa NPs.....	57
3.7 Conclusions.....	60
The Native Oxide Skin of Liquid Metal Ga Nanoparticles Prevents Their Rapid Coalescence during Electrocatalysis	62
4.1 Introduction.....	63
4.2 Materials synthesis and characterization.....	64
4.3 Electrochemical CO ₂ reduction.....	65
4.4 Investigation of the morphology and surface of the Ga NPs post-electrolysis.....	66
4.5 Transmission electron microscopy characterization.....	69
4.6 Voltammetric characterization.....	70
4.7 <i>Operando</i> XAS study of Ga particles during CO ₂ RR.....	72
4.8 Mechanistic discussion.....	75
4.9 Conclusions.....	81
Voltage-driven Chemical Reactions Enable the Synthesis of Tunable Liquid Ga – Metal Nanoparticles.....	82
5.1 Introduction.....	83
5.2 Voltage-driven synthesis of Ga – Cu NPs.....	84
5.3 Influence of synthesis parameters on the reaction outcome.....	89
5.4 Mechanism of the voltage-driven reaction between Ga and Cu.....	94
5.5 Generality of the voltage-driven liquid Ga reactivity at the nanoscale.....	96
5.6 Conclusions.....	99
Conclusions and outlook	101
References.....	103
Curriculum vitae.....	132

Chapter 1

Introduction

1.1 Motivation

In the second half of XIX century, John Tyndall and Svante Arrhenius set the foundation for the knowledge on greenhouse effect of atmospheric CO₂ on Earth.^{1,2} Over the last century, this discovery turned from an optimistic hypothesis to a factor placing the biosphere at risk of irreversible changes.³ The Paris Agreement on climate change puts a target of limiting the global warming to 1.5°C compared to pre-industrial level, which requires meaningful and coordinated efforts on levels spanning from global policy to research bench needed to secure economic, energy and climate security to various countries with very different challenges, resources and cultures.⁴

Intergovernmental Panel on Climate Change have reported that not only the decrease in CO₂ emissions, but also valorization of CO₂ will be required to limit global warming to 1.5°C.⁵ The electrochemical CO₂ reduction (CO₂RR) is a highly promising approach towards CO₂ valorization, as it allows to upgrade CO₂ removal from being a waste disposal to a strategy which adds value to chemical industry, is performed at mild conditions (ambient temperature and pressure, aqueous electrolytes) and can be fueled by renewable electricity.⁶⁻⁹

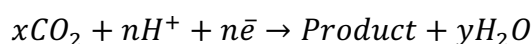
Currently, the main setback for the practical implementation of CO₂RR is the lack of the appropriate catalyst, which is required to convert CO₂ into product of interest and must be selective, active, and stable simultaneously.^{10,11} The selectivity issue is intrinsic to CO₂RR as CO₂ can be reduced into a variety of different chemicals such as CO, HCOOH, CH₄, C₂H₄, C₂H₅OH and others.^{6,12} Cu-based catalysts are the most promising materials to obtain products other than CO and HCOOH, and huge progress was made over the last decade to improve the selectivity and activity of CO₂RR electrocatalysts.^{6,13-23} The use of Cu nanoparticles (NPs) has emerged as beneficial both to maximize mass activity, because of higher surface to volume ratio, and selectivity, via morphology control, for example with Cu nanocubes which favor C₂H₄ or nanooctahedra which favor CH₄ as main reaction products.¹³

However, the stability aspect of electrocatalysts for CO₂RR has been less investigated so far.^{7,24} Generally, very few solutions have been proposed so far to the reconstruction of copper occurring during CO₂RR which often results in performance loss. This gap provides the motivation behind this thesis which covers two main approaches. The first one is based on alloying of copper NPs with a different metal. The second one proposes the utilization of liquid metal (LM) NPs as a different and largely unexplored class of CO₂RR electrocatalysts.

1.2 Electrochemical CO₂RR and the stability challenge of Cu catalysts

1.2.1 General CO₂RR overview

One of the bottlenecks towards a wide implementation of CO₂RR is the need of a catalyst which is active, selective and stable during operations. The primary reason for the need to use a catalyst is to decrease the energy needed to convert the thermodynamically stable CO₂ molecule and provide its high conversion rate.⁶ The reaction itself is a multi-electron process which can be written as follows:



As a result, CO₂RR may lead to a large variety of products depending on the number of electrons involved. These electrons are provided via the application of an external voltage, in principle supplied via excess renewable energy. The formation of various products is both a benefit and a challenge, as producing just one product at a time is not straightforward in most cases. In addition to that, CO₂RR requires protons, which inherently leads to the rise of competing H₂ evolution reaction (HER). Historically, Hori et al. were the first to systematically investigate different metals as electrocatalysts to drive CO₂RR.^{25,26} Interestingly, Cu was the only metal generating products beyond CO and HCOOH, including CH₄, C₂H₄, EtOH and PrOH in reasonable quantities. These products are sought after because of their higher energy content and economic value compared to CO and HCOOH.⁶ The rest of the metals can be classified in several groups, namely those producing CO (e.g. Ag, Zn, Au), those producing HCOOH (e.g. Cd, Hg, Pb) and H₂-producing (not active towards electrochemical CO₂RR; e.g. Pd, Ni, Pt). This behavior was later explained with a correlation between the intrinsic properties of the metals and their binding energy to crucial reaction intermediates, which include OH* and OCHO* (**Figure 1.1**). Furthermore, the development of experimental analytical techniques revealed that 16 different products are generated from polycrystalline copper.¹² Altogether these studies made Cu-based materials the most utilized electrocatalysts for CO₂RR for the past

decade. Most of these studies focused on enhancing its activity and, especially, its selectivity. Different strategies have been implemented to steer the selectivity of Cu-based electrocatalysts. These strategies include the use of single atom catalysts, multimetallic catalysts, hybrid materials such as metal/metal oxide, metal/polymers, metal/frameworks, oxide-/nitride-/sulphide-derived catalysts, as well as electrode and device engineering.^{27–35}

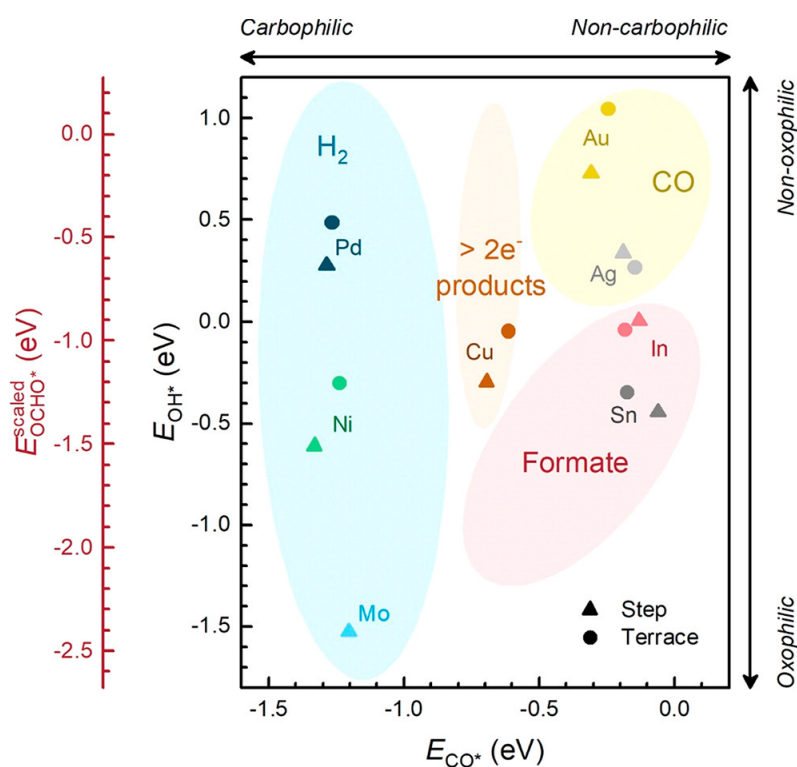


Figure 1.1. Scaling relationships between binding energies of CO₂RR intermediates and primary products for selected metals. The CO* binding energy (E_{CO^*}) and OH* binding energy (E_{OH^*}) well describe the binding energies of key intermediates of COOH*/CHO* and OCHO*, respectively. The scaled binding energy of OCHO*, E_{OCHO^*} , is also shown as an additional y-axis. The metals are therefore categorized into three groups based on the relative binding strengths of CO* and OH* to those of Cu: (I) non-oxophilic and non-carbophilic metals (Ag and Au), which primarily produce CO; (II) oxophilic and non-carbophilic metals (In and Sn), which primarily produce formate; (III) carbophilic metals (Pd, Ni, and Mo), which primarily produce H₂.³⁶

In electrocatalysis, the use of NPs offers a combination of advantages.^{37,38} First, NP electrocatalysts maximize surface-to-volume ratio and minimize the use of material, which is crucial especially when using the metals which are not abundant on Earth. Second, the recent

developments in atomically precise nanoscience allow the synthesis of NPs with well defined, tunable and homogeneous size and exposed facets. These NPs provide an ideal material platform to gain knowledge on structure/properties relationships and to exploit properties well beyond simply lowered material consumption. For example, the original study from Hori et al. on Cu single crystals suggested that the Cu (100) facet favors C₂H₄ production over other products.³⁹ Single crystals have very low surface-to-volume ratio, which limits their application to fundamental studies in device configurations far from those industrially relevant. Herein, studies with facet-engineered cubic Cu NPs, which expose mostly (100) surface, allowed to verify that the selectivity holds also in industrially relevant conditions, which are defined as devices which operate at high current densities (≥ 100 mA/cm²).^{13,40} In addition, a very interesting size-dependent trend emerged, which revealed that the selectivity for ethylene is maximized for 44 nm Cu nanocubes compared to smaller or bigger sizes.⁴¹ This information coupled with theory indicated that an optimal balance between edge and facet sites exist to generate C-C coupling and ethylene formation on copper.⁴² Cu NPs with other shapes were also utilized to reveal the structure-dependence selectivity towards other products, including methane and ethanol.^{6,43,44}

1.2.2 Structural reconstruction of Cu electrocatalysts during CO₂RR

While copper exhibits an ideal behaviour in terms of selectivity, various studies report that copper electrodes reconstructs under CO₂RR conditions, which often implies degradation and loss of their electrocatalytic performance (i.e. activity and selectivity) over time.^{7,45–50} To address this issue is of fundamental importance for the technological implementation of CO₂RR.⁴⁰ Yet, the stability aspect has been rarely considered explicitly until recent, and it still remains underexplored.^{7,24}

For Cu NPs catalysts, recent work using *in situ* electron transmission microscopy has evidenced that their restructuring occurs via dissolution/precipitation mechanism, specifically voltage-driven Ostwald ripening (**Figure 1.2A,B**).⁴⁸ Surface oxidation at open circuit potential (ocp) accounts for the initial dissolution which continues during operation mediated by soluble Cu intermediate species. Evidences build up in the literature that these intermediate species are complexes formed between Cu surface atoms and reaction intermediates, generally CO (**Figure 1.2C**).^{45,48,51–57} Indications that similar driving forces are involved in the reconstruction of bulk copper electrodes exist in the literature.⁴⁹

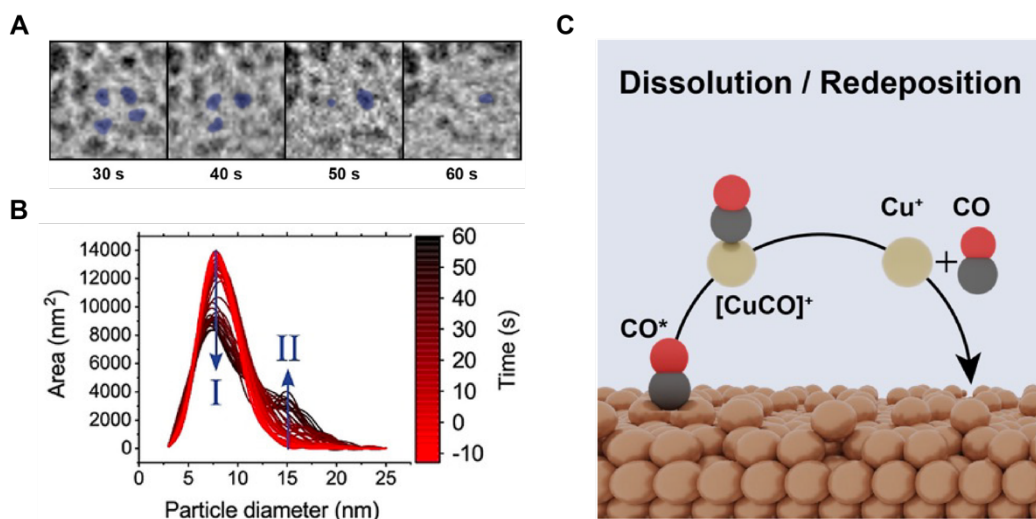


Figure 1.2. Cu degradation and reconstruction patterns during CO₂RR. (A) Snapshots of TEM grid selected area during 30 – 60 s of operation illustrating that the disappearance of the original Cu NPs is accompanied by the growth of other NPs.⁴⁸ (B) Evolution of total Cu NPs projected areas (obtained by TEM) during startup phase of CO₂RR.⁴⁸ (C) Schematic illustration of the copper reconstruction mechanism under CO₂RR conditions, where adsorbed CO* intermediates drive the transient dissolution followed by redeposition.⁵¹

1.2.3 Strategies towards stable CO₂RR catalysts

It should be noted upfront that a rational framework on how to confer stability to copper based on the above mentioned mechanistic understanding of its reconstruction during CO₂RR has yet to be developed. Yet, a few studies do report on possible strategies to generate stable CO₂RR electrocatalysts based on Cu NPs.

These strategies include the utilization of Cu-containing materials, such as Cu-based ternary oxides (e.g. SrCuO₂), or interfacing Cu with different domains (e.g. CeO_x, Cu₃N).^{58–62} The main driving force behind the increased durability of the catalyst is a stabilization of Cu in a desired valence or in a specific crystallographic site by another element or the phase in proximity. For example, ternary SrCuO₂ oxide is able to retain oxidized Cu species after exposure to CO₂RR conditions for longer than CuO-derived Cu catalyst, which allows higher FE towards C₂₊ products for longer time.⁵⁸ Furthermore, incorporation of Sr in the lattice allows to retain the Cu sites with lower coordination number in the ternary oxide, which has higher catalytic activity than the sites with higher coordination number. However, the non-metallic nature of such materials complicates their processing and application.

Carbon and carbon-based shells have been also proposed to stabilize Cu NPs during CO₂RR.^{63–66} They provide a physical barrier against dissolution, which can prevent fragmentation and sintering of the NPs during operation. However, the NPs which must be stable under the often harsh conditions used for the synthesis of these coatings (*e.g.*, high temperature required for the carbonization of organic layers). It also implies the trade-off between the activity, which is defined by access of CO₂ to catalytically active surface, and stability of Cu with respect to dissolution, which benefits from thicker and denser coating.

More recently, the increased stability of Cu nanocubes in tandem system with Fe porphyrin molecular catalyst was reported.⁶⁷ The authors attribute the increased durability of the catalyst to the CO being produced on the site other than Cu, but no further elaboration was provided. Lastly, alloying of Cu with Bi was reported to stabilize the Cu-based NP catalyst, but no stabilization mechanism was proposed.⁶⁸

Overall, the need of defining a more rational framework to stabilize Cu from reconstructing or perhaps proposing new paradigms to generate stable catalysts exists in the field of CO₂RR.

1.3 Liquid metals and the unique place of Ga among them

1.3.1 General overview of liquid metals, Ga and Ga-based materials

Non-radioactive metals which possess melting points close to the room temperature include Cs (28.5 °C), Rb (39.3 °C), Hg (−38.8 °C) and Ga at 29.8 °C.^{69–74} Alkali metals are too reactive to be used in their metallic state. Ga was discovered relatively late, in 1875, and does not form ores of its own, which strongly limited its use until second half of XX century.⁷⁵ So, for a long time, the use of LMs was mostly limited to mercury, Hg, which is known to humanity in its metallic state since antiquity and beyond. Hg has number of unique advantages which made it indispensable for various applications over these centuries. To name few recent areas where was used, LM nature of Hg made it ideal for polarographic studies, which in many ways was a cornerstone for modern electrochemistry research, and for which Jaroslav Heyrovsky was awarded Nobel Prize in 1959.⁷⁶ On industrial scale, Hg electrodes were used in the electrochemical chloro-alkali process, thus supplying chlorine, hydrogen and sodium hydroxide to the entire chemistry and chemical engineering industry.⁷⁷ However, as a result of the growing concerns about Hg toxicity, its use steadily decreased over the following decades.

Recently, the field of LMs has undergone a true renaissance, which has partly been driven by the increasing interest in wearable devices.^{69–74} Most research has centered on Ga and its

alloys due to their low toxicity and melting point, with the most common compounds being metallic Ga, eutectic GaIn (EGaIn, 75 wt. % Ga) and GaInSn (Galinstan, 69 wt. % Ga, 21 wt. % In, 10 wt. % Sn) alloys. These compounds possess many peculiar properties beyond those of just metals and just liquids, which resulted in an explosive growth of their prospective applications (**Figure 1.4**).⁷⁸

In terms of applications, LMs hold a lot of promise for soft wearable electronics, where metallic Ga, EGaIn and Galinstan alloys are implemented as self-healing electric circuits.^{79–82} Malleability and electric conductivity also make LMs appealing for the fabrication of conductive LM-polymer composites, self-healing flexible battery electrodes, as well as for other energy harvesting and conversion approaches, or even soft robots.^{79,83–89} Lastly, Ga is not toxic, to the extent it can be used for intravenous injections, which makes it a promising candidate for drug delivery.^{90–92} Together with the ability to form stable microfluidic channels, this makes Ga-based LMs perfect for bioimaging.^{82,93,94}

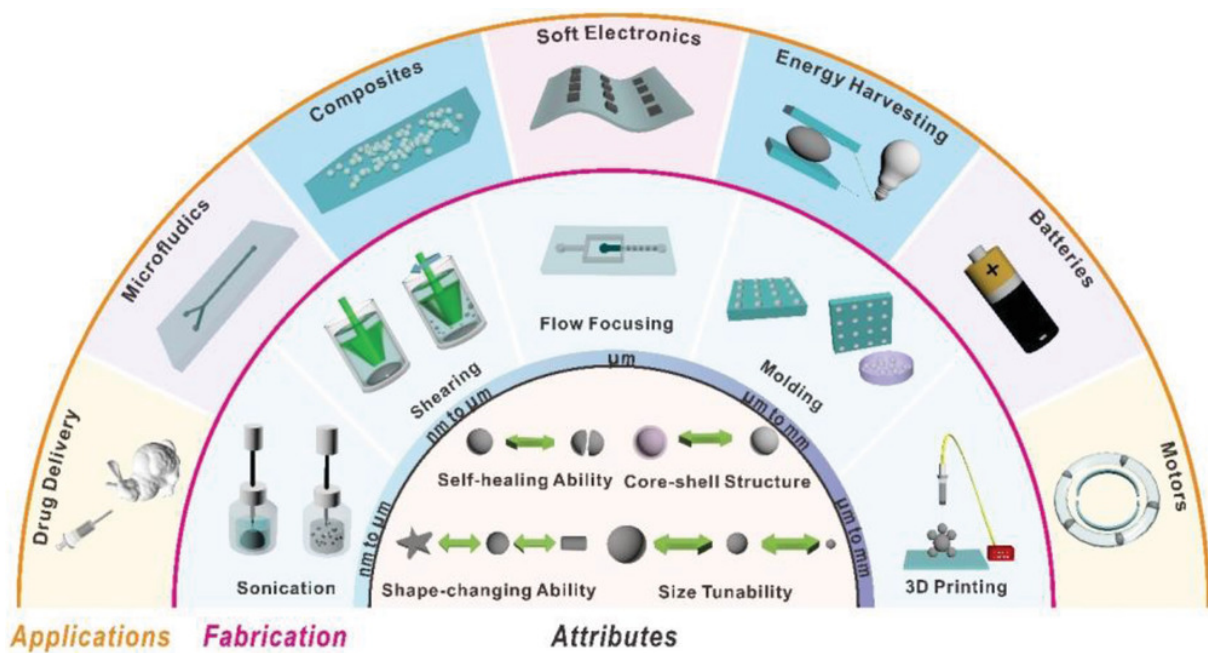


Figure 1.4. Attributes, fabrication, and applications of liquid metal particles. The inner semi-circle illustrates the attributes of liquid metal particles; the middle ring describes methods to fabricate liquid metal particles with different sizes; the outer ring presents several application areas of liquid metal particles.⁷⁸

LMs have also emerged as a new class of catalysts wherein the highly dynamic liquid surface offers greater flexibility compared to solid catalysts.^{74,95–108} Most of the studies so far have focused on thermal catalysis, including dry reforming of methane and alkane dehydrogenation, where so-called SCALMS (supported catalytically active liquid metal solutions) catalyst concept was introduced.^{95,101–103} For example, Pd atoms popping up on the surface of liquid Ga in PdGa alloys were shown to be extremely selective for the dehydrogenation of alkane while being resistant to coke poisoning (**Figure 1.5A,B**).⁹⁵ In this case, noble metal is actually dissolved in Ga which acts as its vessel, as later shown for Pt where it was fully coordinated by Ga atoms in similar SCALMS architecture.⁹⁷ Applications of LMs are emerging also in electrocatalysis.^{87,96,98,99,104–108} In one example, metallic Ce nanoparticles (NPs) were stabilized within Ga droplets to promote the electrochemical conversion of CO₂ to solid carbonaceous species without undergoing deactivation by the buildup of reaction products (**Figure 1.5C,D**).¹⁰⁴ In a second example, a selectivity change from hydrogen evolution to selective electrochemical CO₂ reduction was observed to follow the solid-liquid conversion of a Ga-Sn-In catalyst.¹⁰⁵ Lately, Bi-Ga LM electrocatalysts have been shown to possess self-healing abilities which allow to fully recover the catalyst activity after its degradation.⁹⁶

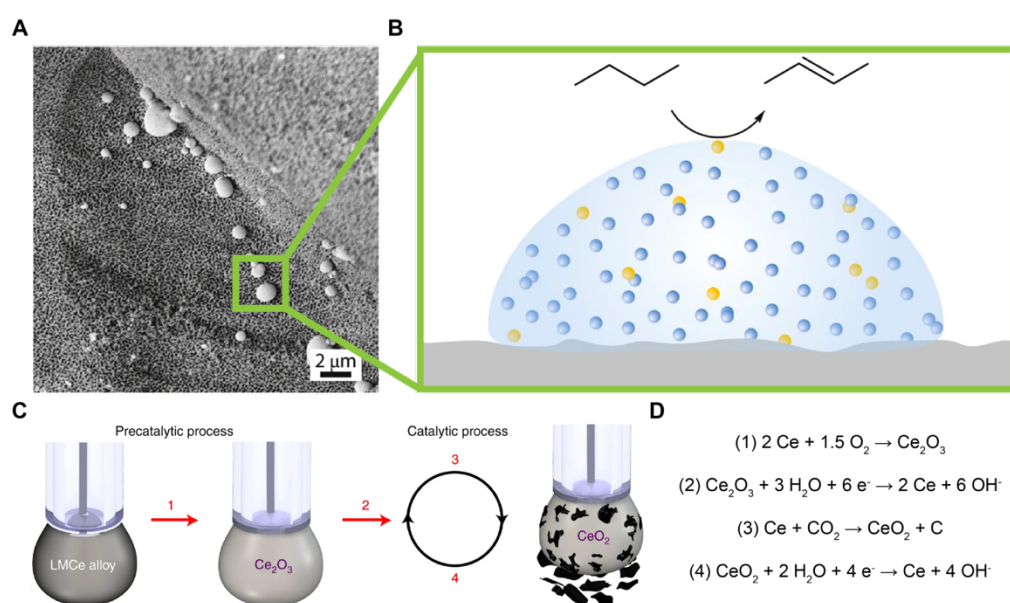


Figure 1.5. Catalytic applications of LMs. (A) SCALMS Pd-Ga catalyst for ethane dehydrogenation and (B) the reaction schematic.^{95,109} (C) Schematic of hanging-drop Ce-doped Ga electrode implemented as electrocatalyst for CO₂-to-carbon conversion, with illustration of solid carbon delamination process and (D) its CO₂RR catalytic cycle.¹⁰⁴

Despite these exciting opportunities in catalysis, the aforementioned studies are mostly based on bulk LMs.^{74,95,101–107} NPs are highly beneficial in heterogeneous catalysis as their high surface area maximizes the number of active sites per mass of material, and nanoscale effects, which improve activity or selectivity, can also emerge.^{37,38} At the same time, NPs catalysts tend to sinter, which requires the development of protection schemes, such as oxide coatings.^{110,111} Because of their fluidity, LM NPs are expected to coalesce even more rapidly compared to solid NPs, which poses doubts regarding their utilization as catalysts.

Ga itself has not been tested much in electrocatalytic applications. It belongs to the CO-producing metals family, with the best selectivity being ~77% for gallium oxide-derived nanocatalysts.¹¹² For conventional bulk Ga electrocatalyst, Hori et al. reported *ca.* 20 % selectivity for CO, with the rest being competing HER reaction.¹¹³

Overall, existing studies indicate the potential of LMs in catalysis, however such potential has not been fully exploited yet, especially in the form of NPs.

1.3.2 Ga surface oxide and oxide-related properties

One unique feature of Ga-based LMs is the presence of a native oxide skin surrounding their liquid metal core (**Figure 1.6A**).^{69–74,114} This oxide forms even at low partial pressures of O₂ (*ca.* 10⁻⁷ mbar),¹¹⁵ and regulates the surface properties of the LMs, thus it is important for many of their applications.^{69–74,114} This skin is viscoelastic, which reveals unique rheological behavior, being malleable and varying from elastic to liquid-like depending on mechanical stress applied.^{82,93,116,117} Extensive changes in surface tension of the LM droplet can be observed depending on the presence of this oxide skin, its thickness and degree of oxidation. As one example, Khan et al. could track these changes with camera, showing the shape recombination abilities of EGaIn (**Figure 1.6B**).¹¹⁸ Oxide-covered surface has near-zero interfacial tension, resulting in tremendous wetting ability (**Figure 1.6C**). When the oxide shell is removed, the droplet tends to form ideal spherical shape, with *ca.* 700 mJ/m² surface tension.¹¹⁹ The presence of this surface oxide can be controlled either chemically (e.g., by chemical dissolution in acidic or basic electrolytes) or electrochemically (by applying oxidative or reductive potential) (**Figure 1.6B,C**).^{118,120}

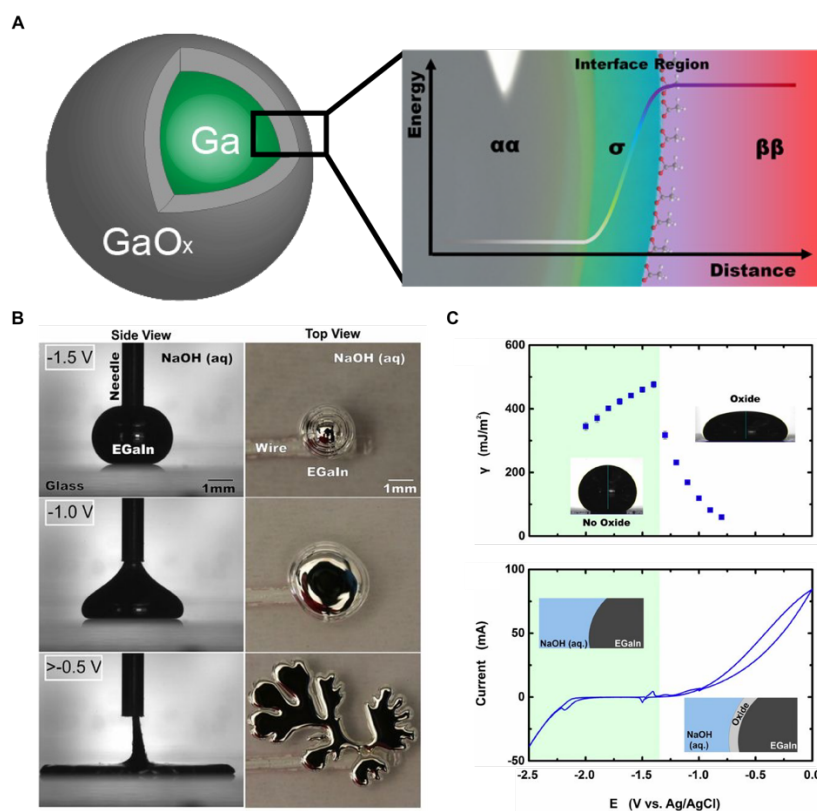


Figure 1.6. Key attributes and properties of Ga native oxide skin. (A) Schematic of Ga NPs with its native oxide skin (denoted as GaO_x) and energy diagram representing its continuous change over oxide thickness.¹¹⁴ (B) Oxidative spreading of a bead of liquid EGaIn in 1 M NaOH solution, with a needle and a wire serving as electrical contacts to the droplet. The drop keeps a spherical shape initially due to the large surface tension of non-oxidized EGaIn surface, with complete flattening taking place oxidative potential is applied and oxide skin is formed.¹¹⁸ (C) The change of surface tension (top) and current as a function of applied voltage with and without Ga oxide skin.¹¹⁸

This surface oxide is amorphous and often consists of a non-stoichiometric matrix of Ga atoms bound with oxygen atoms, H₂O molecules, OH⁻ groups or other anions, depending on the chemical environment.^{121–126} Furthermore, a continuous gradient in its properties exists across its thickness (**Figure 1.6A**), contrary to sharp change in properties of different layers common for conventional solid layered structures such as core@shell NPs or self-assembled monolayers on coinage metals, where clear boundaries exist between the layers.¹¹⁴ In addition to that, the growth of this oxide is self-limiting, as it follows the Cabrera-Mott mechanism.^{114,127–129} This mechanism starts with initial adsorption of oxygen atoms on LM Ga surface, which creates an initial oxide layer. As long as the oxide remains thin, electrons can

tunnel through it and generate a potential gradient (Mott potential) and electric field between the outer and inner boundaries of the oxide. The creation of a potential jump on the inner metal/oxide interface causes metal ions to ionize and migrate to the surface. The oxide skin continues to grow until the oxide gets too thick, which reduces the electric field gradient and ability of electrons to tunnel through the oxide. As a result, the oxide skin of liquid Ga typically stops to grow at an oxide thickness of 2 – 3 nm, with 0.5 – 5 nm range accessible depending on the oxide growth conditions.¹²⁹

In the case of NPs, the presence of surface oxide induces additional peculiarities. First, the Cabrera-Mott model implies even faster oxidation of the NPs surface compared to bulk case, although the oxide thickness still remains limited to few nanometers.¹²⁸ Second, the presence of an oxide leads to pronounced supercooling (also called undercooling) effect in Ga NPs.¹¹⁴ This supercooling effect is a decrease in the freezing point of material below the thermodynamically favored liquid/solid phase transition temperature. In Ga NPs, this effect is due to the spatial confinement provided by the shell: solidification of liquid Ga into its bulk-stable α -Ga phase comes with volume expansion due to lower density of α -Ga compared to liquid Ga (5.904 vs. 6.095 g/cm³).¹³⁰ As the oxide skin defines a finite volume of the NPs, the oxide completely suppresses the formation of α -Ga in Ga NPs. Ga has other polymorphs, which are metastable and have higher densities than liquid Ga: β -Ga (6.23 g/cm³), γ -Ga (6.20 g/cm³) and δ -Ga (6.22 g/cm³).¹³⁰ So, as the size of the NPs decreases, the stable solid phase changes as α -Ga (particle size > 800 nm) \rightarrow β -Ga (600 – 800 nm) \rightarrow γ -Ga (300 – 600 nm) \rightarrow δ -Ga (< 300 nm), with bulk melting points of 29.8, -16.2, -35.6 and -19.4 °C, respectively.¹³¹ Moreover, the oxide shell thickness itself can also affect the freezing point of particles with different size.¹³² The impact of the shell on the stability of different phases makes the phase transitions in liquid Ga droplets particularly complex and, together with conventional melting point depression which occurs in NPs, the supercooling effect in Ga NPs brings their phase transition point down to -100 °C and beyond, with large hysteresis (tens °C) between the freezing and melting.^{133,134} This supercooling effect is particularly helpful for the applications where the LM needs to stay liquid at temperatures below its freezing point, such as in room-temperature printed electronics, preparation of lead-free solders and biomimetic lithography (printing on biological surfaces, including non-adhering surfaces like brain).^{135,136}

Another unique role that the oxide skin plays is to keep the Ga NPs separated while in contact with each other. In fact, liquid droplets will merge easily due inherent mobility of atoms in liquid. Indeed, Cheek et al. reported the merging of Ga nanodroplets upon the removal of

native oxide skin with *in situ* TEM.¹³⁷ Removal of oxide is a clear trigger for the merging to start, which takes only few seconds to reach completion. At the same time, with the surface oxide present, suspensions of LM NPs are stable for months and years without any sign of coalescence.^{114,135}

If stable under reaction conditions, the native oxide will also play a crucial role in catalysis, especially when moving from bulk to NPs.^{69–74,138,139} For example, in the context of photocatalysis, studies show that it contributes to charge separation as a semiconducting material.^{138,139} More generally, it may possess catalytic activity on its own or regulate the access of reactants to the liquid core while preventing the NPs coalescence. However, very little attention has been given to the NPs native oxide skin in the context of catalysis, or even Ga electrochemistry in broader sense.^{69–74}

1.3.3 Electrochemistry of pure Ga.

The knowledge about the electrochemical properties of Ga remains very limited.¹⁴⁰ According to the Pourbaix diagram (**Figure 1.7**), Ga is present as oxide at steady conditions in neutral and moderately basic solutions with no potential applied. Above pH=11.4, Ga₂O₃ dissolves as $\text{Ga}_2\text{O}_3 + 6\text{OH}^- = 2\text{GaO}_3^{3-} + 3\text{H}_2\text{O}$. At the same time, corrosion of Ga in basic solutions is not prominent until very basic pH values (~14).¹⁴¹

Stoichiometric Ga₂O₃ is reduced to metallic Ga at potential below -0.48 V_{RHE} at any given pH where no corrosion takes place. Depending on the oxide composition and state of Ga (liquid or solid), this potential varies between -0.6 – -0.4 V_{RHE}, with higher affinity of the oxide to solid Ga (that is, lower reduction potential).^{105,121,142,143}

The complete chemical conversion pathway of the electrochemical reduction of Ga oxide and its formation is not established yet. Here, the key takeaways are provided based on existing evidence in the literature, although the LMs community would highly benefit if this mechanism was experimentally elaborated.

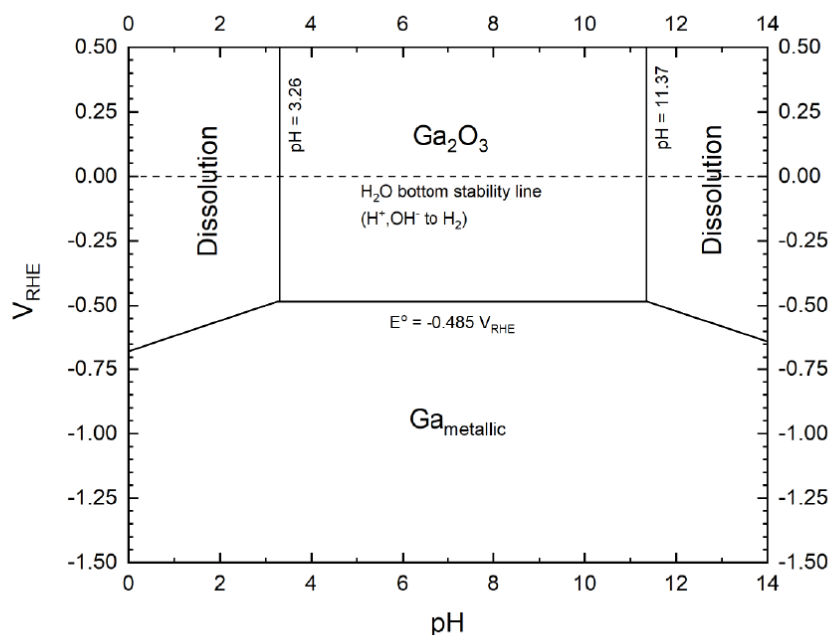


Figure 1.7. Pourbaix diagram of Ga in aqueous solutions. The diagram is simplified to represent the equilibrium phases and is recalculated into reversible hydrogen electrode (RHE) scale from the original standard hydrogen electrode (SHE) scale (adapted from ref.¹⁴²).

A reduction of the oxidized Ga surface is normally associated with the reduction of the oxide/hydroxide passivating film (peaks C1, C2 on **Figure 1.8A**). However, this reduction is not a one-step process and has peculiarities, such as dependence of the oxide reduction potential on the voltage where the cathodic wave starts.^{121,122} The chronopotentiometric curves obtained by Popova et al. point at two main events, with reduction event occurring at more positive potential attributed to the overstoichiometric oxygen reduction, and the more cathodic event to the reduction of the main Ga oxide phase.^{121,122} More recent papers on anodic passivation of Ga propose that oxide layer in aqueous electrolyte is composed of few layers of oxohydroxide films (colloid-like and barrier layer) (**Figure 1.8B**),^{124–126} in line with reports from Popova et al. assuming that colloid-like and barrier layers have different oxygen stoichiometry.

Interestingly, Popova et al. claim that even though Ga surface becomes shiny and active after cathodic activation, some oxide should still be present, as the hydrogen reduction reaction and the gallate reduction on activated Ga happens at higher overvoltage than for the oxide-free Ga.¹²² Extra anions in the electrolyte, which can bind chemically to Ga or its oxide, may shift the reduction potential both to the negative (e.g. F⁻ for liquid Ga) and positive (e.g. F⁻ for solid Ga) voltages, depending on the affinity of the oxide/hydroxide layer to the metallic

surface.^{123,125} As a consequence of that, the reduction of oxide is easier on liquid Ga than on solid Ga (that is, oxide layer has larger stability window on solid Ga because of its higher affinity to rigid, solid surface).^{121,122}

The anodic part has at least three different regions, with the exact interpretation of them largely unknown (marked as A1, A2, A3 on **Figure 1.8A**).^{118,124–126,144,145} Existing reports suggest that Ga oxidation starts with formation of few oxide/hydroxide monolayers (insoluble GaOOH or soluble $[\text{Ga}(\text{OH})_4]^-$, depending on the electrolyte pH),^{121,122,124} possibly of mixed composition if other anions are present (*e.g.*, $\text{Ga}(\text{OH})_2\text{CO}_3^-$ is proposed to exist in carbonate buffer solutions).¹²⁵ There are two pathways which can enable this. The electrochemical pathway would be enabled by direct oxidation of Ga^0 to Ga^{3+} , which then dissolves (as Ga^{3+} in acidic or $[\text{Ga}(\text{OH})_4]^-$ in basic electrolytes) or reacts with H_2O to form insoluble GaOOH/ $\text{Ga}(\text{OH})_3$ hydroxide. The alternative electrochemical/chemical pathway would first imply oxidation of Ga^0 to Ga^+ , which then reduces hydrogen in H_2O molecule as follows:



The studies by Selekova et al. and Corbett et al. justify that the second mechanism (that is, electrochemical oxidation of Ga^0 to Ga^+ and chemical reduction of H_2O to H_2 with Ga^+) is more probable, and that the existence of Ga^{2+} species is highly unlikely.^{144,146–150} Selekova et al. further show that as the potential becomes more positive, the direct electrochemical oxidation of Ga^0 to Ga^{3+} takes over.

Further oxidation is enabled by specific adsorption of H_2O molecules, which takes place at *ca.* $-0.45 \text{ V}_{\text{RHE}}$, and passivates the surface with the formation of barrier GaOOH layer.^{124,144} At more positive voltages, growing electric field allows ejection of Ga through this barrier layer,¹²⁴ in a way similar to how Mott potential drives oxidation of Ga surface. These Ga^{3+} species hydrolyze and form colloid-like loose oxide/hydroxide layer, probably with further chemical dissolution if pH is basic enough (**Figure 1.8B**).¹²⁴ In case of liquid Ga, this latter stage of surface oxide/hydroxide development is associated with linear decrease in the surface tension, until the breakup of the drop into fractal-like patches which lose electric contact with the current supply, and the anodic process stops;¹¹⁸ on solid Ga, insulating Ga_2O_3 oxide eventually forms above $0.5 \text{ V}_{\text{RHE}}$, as evidenced by electron diffraction.¹⁵¹

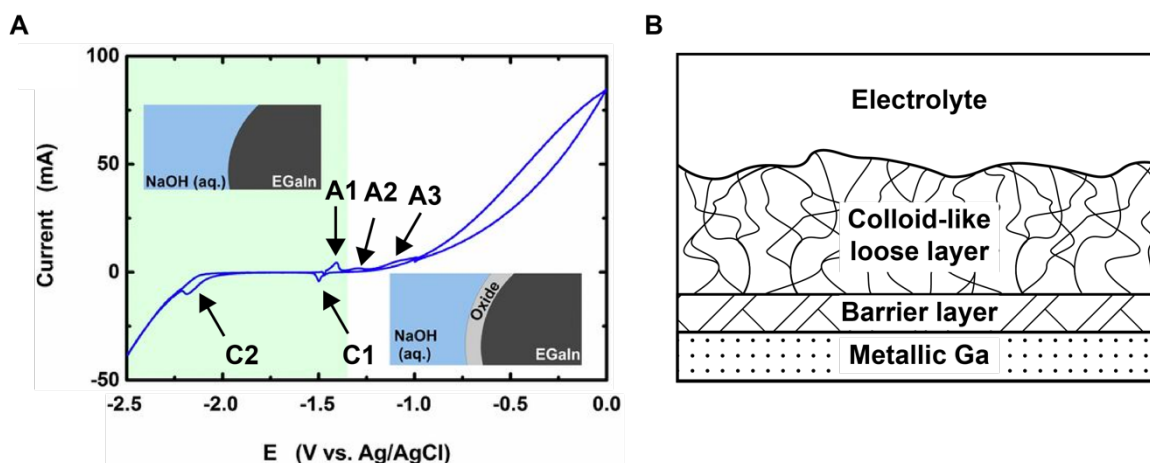


Figure 1.8. Electrochemistry of Ga and Ga oxide in aqueous solutions. (A) Current as a function of applied voltage highlighting cathodic (C1, C2) and anodic (A1, A2, A3) processes.¹¹⁸ (B) Composition of Ga oxide/hydroxide skin according to the model proposed by Korshunov et al. (adapted from ref.¹²⁴).

1.4 Synthetic routes to obtain Ga and Ga-based multimetallic NPs

1.4.1 Top-down approaches

By definition, NPs are the particles which are less than 100 nm in diameter.¹⁵² The approaches to synthesize LM NPs can be grouped into top-down and bottom-up approaches, each with their benefits and drawbacks.

Top-down synthesis starts from a bulk material which is then fragmented into smaller particles. Such approaches are particularly common for the LM NPs, as they can be implemented in a very simple way.⁷⁸ One example of top-down synthesis is sonication.⁷⁸ Here, bulk Ga, EGaIn or Galinstan are placed in the liquid medium (water, toluene etc.), heated up, if needed to melt, and placed in the sonication bath. Within few tens of minutes or few hours, the energy supplied by sonication breaks up the bulk LM into NPs. Probe sonication decreases the reaction time to the range of few minutes only.⁷⁸ The downside of top-down approaches is the low monodispersity of obtained particles. The size of the obtained particles ranges from *ca.* 30 nm to few μm , following lognormal distribution often peaking at few hundred nanometers. Although certain strategies, such as use of coordinating ligands, temperature control or size-selective precipitation and filtering, allow to narrow the size distribution of the obtained particles, the size distribution still remains rather broad (**Figure 1.9A-G**).^{153–156}

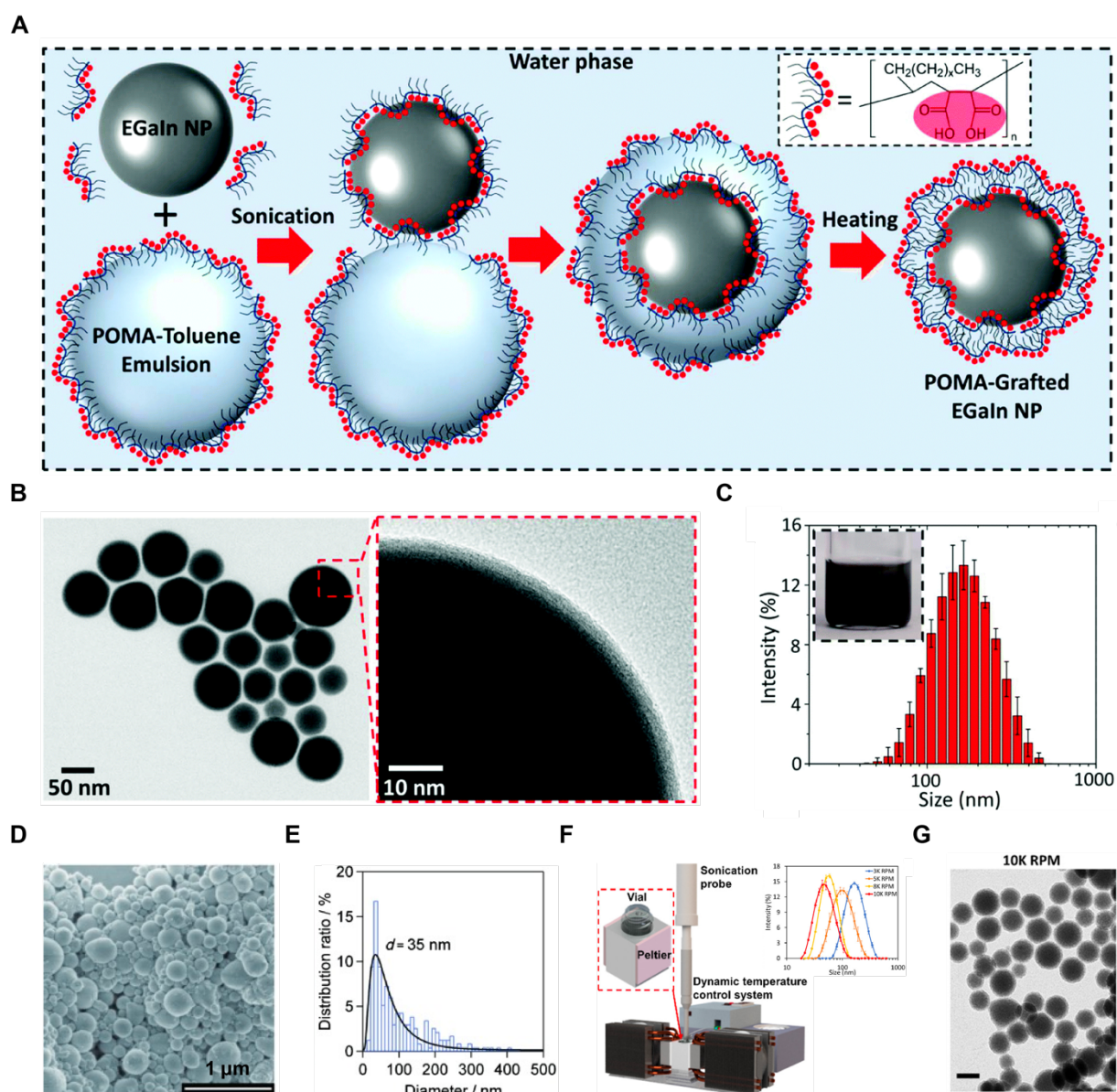


Figure 1.9. Ga NPs obtained by bottom-up sonication-based synthesis. (A) Reaction scheme, (B) low-resolution TEM image with high-resolution inset highlighting the presence of Ga native oxide skin and (C) size distribution of Ga NPs/microparticles (MPs) obtained by sonication with poly(1-octadecene-alt-maleic anhydride) (POMA) stabilization.¹⁵³ (D) SEM image and (E) size distribution of Ga NPs/MPs obtained by sonication with dodecanethiol stabilization.¹⁵⁴ (F) Dynamic temperature control-assisted sonication setup with size distribution of Ga NPs/MPs and (G) low-resolution TEM of Ga NPs obtained by Lu et al, where rpm stands for the centrifugation rate used to separate NPs/MPs of different sizes.¹⁵⁵

Another top-down approach to obtain LM particles is the shearing method (shearing liquids into complex particles, SLICE).¹⁵⁷ This method relies on mechanical energy supplied by speed rotary machine to break bulk LM into particles. Similar observations apply to SLICE method as to sonication approach: the synthesis yields NPs and MPs with broad lognormal size distributions ranging from few nanometers to few microns, which can be improved by implementing ligands and changing shearing parameters.

Overall, top-down approaches are very versatile and simple to use but suffer from broad size distribution as their main drawback. Thus, these approaches are suitable for the applications where size distribution of the particles is not so important, such as fabrication of conductive soft composites or SCALMS thermal catalysis. However, bottom-up approaches are not ideal when a narrow size distribution is crucial to gain reliable knowledge or to be able to use the LM NPs at all, such as plasmonic and certain catalytic studies.

1.4.2 Bottom-up approaches

Bottom-up approaches exploit building-up of NPs from molecular precursors. One bottom-up approach to synthesize LM NPs is a physical vapor deposition.¹⁵⁸ This method allows to obtain the LM NPs in 10 – 100 nm range with narrower size distribution than sonication or SLICE methods. Physical vapor deposition produces NPs attached to the substrate, which limits the versatility of the method for the applications which benefit from solution processing, such as inkjet printing, which is inherently possible for other synthesis methods of LM NPs.

Among bottom-up approaches, colloidal synthesis emerges as ideal method to obtain well defined tunable NPs with homogeneous size and shape with narrow size distribution.^{37,38,159,160}

As one example, Yarema et al. have reported the use of thermal decomposition to obtain monodispersed Ga NPs.¹⁶¹ Here, a Ga molecular precursor, $\text{Ga}_2(\text{NMe}_2)_6$, is dissolved in 1-octadecene (ODE) and, with the addition of di-*n*-octylamine (DOA), is injected into ODE solution in N_2 -atmosphere at 280 °C, with the Ga NPs starting to form *ca.* 40 s after injection (**Figure 1.10A**). Each Ga NPs is covered with oxide skin (**Figure 1.10B**), and the standard deviation of the NPs size is *ca.* 8 % (**Figure 1.9C**). ODE acts as a non-coordinating solvent, while DOA acts as surfactant and as agent which controls the kinetics of Ga precursor decomposition rate.

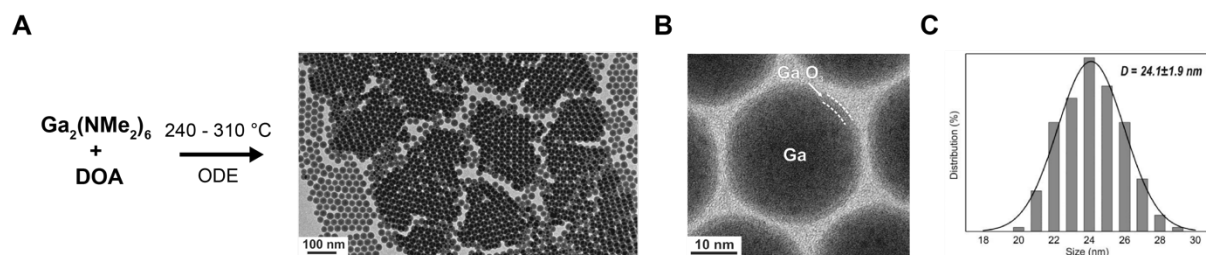


Figure 1.9. Monodisperse Ga NPs obtained via colloidal synthesis. (A) Reaction scheme and low-resolution TEM image, (B) TEM image of one NPs highlighting Ga core and Ga oxide shell and (C) size distribution of Ga NPs obtained by Yarema et al.¹⁶¹

Moving towards Ga-based multimetallic NPs, Castilla-Amorós et al. have reported the synthesis of well-controlled CuGa, AgGa dimeric and AgCuGa trimeric NPs with the use of galvanic replacement reaction (GRR) (**Figure 1.10A,B**).¹⁶² GRR relies on the difference in reduction potentials of the two metals, which provides driving force for the reaction. As Cu ($E_{Cu^{2+}/Cu^0} = 0.34 V$) has higher reduction potential than Ga ($E_{Ga^{3+}/Ga^0} = -0.56 V$), the GRR between Ga^0 and Cu^{2+} is expected to occur.¹⁴³ Indeed, the authors reacted pre-synthesized Ga NPs with Cu (II) acetate in ODE to form phase segregated Ga/Cu nanodimers (ND) wherein Ga remains liquid and the Cu domain is instead crystalline. It is noted that the morphology of NDs is unusual for GRR, which generally leads to formation of alloyed NPs. The different behavior of the Ga NPs was attributed to the presence of Ga oxide skin. Size control of the Cu domain in the NDs was achieved by tuning the reaction time or the amount of Cu precursor added in the reaction.

In another example, Clarysse et al. have reported the synthesis of solid alloyed Ga-based NPs, including Cu, Pd, Au, Ni, Ag (**Figure 1.10C,D**).¹⁶³ This synthesis relies on amalgamation-driven seeded-growth, where the Ga molecular precursor is added to pre-synthesized Cu NPs at high temperature in presence of mildly reducing agent (i.e. oleylamine, OLAM). The driving force for this reaction is liquid nature of Ga, which, in absence of oxide shell, readily amalgamates with most metals.¹⁶⁴ Controllable Ga content was achieved by varying the amount of Ga precursor injected to the reaction mixture.

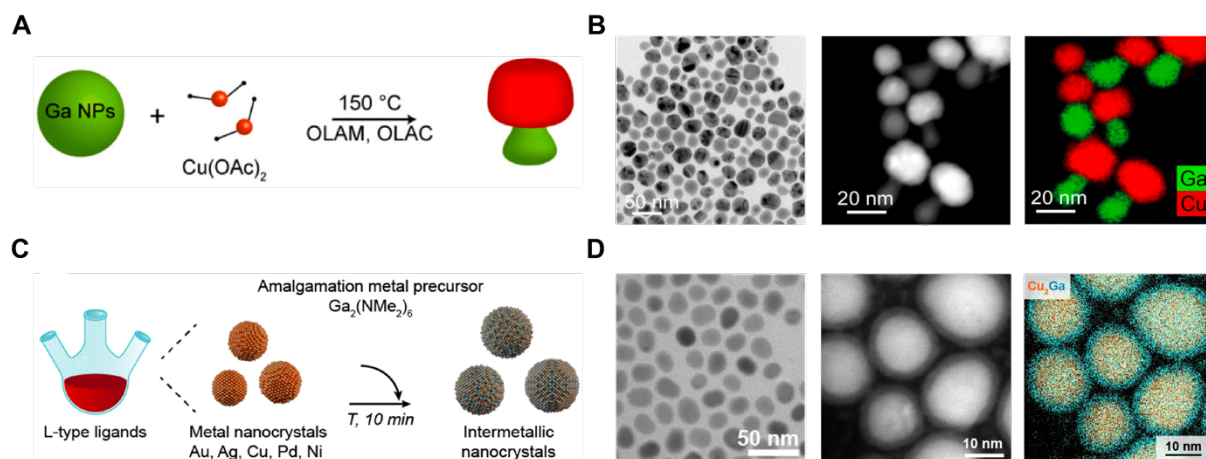


Figure 1.10. Monodisperse CuGa NPs of different morphologies obtained via colloidal synthesis. (A) Reaction scheme and (B) low-resolution TEM, HAADF-STEM images and Cu and Ga elemental map of the phase-separated Ga/Cu NDs.¹⁶² (C) Reaction scheme and (D) low-resolution TEM, HAADF-STEM images and Cu and Ga elemental map of the as-synthesized CuGa alloy NPs.¹⁶³

Overall, the existing examples of colloiddally synthesized Ga and Ga-based multimetallic NPs indicate that colloidal chemistry is the best approach when well-defined and tunable NPs in size, shape and composition are desired. Furthermore, colloidal NPs come as inks which are easily processible, thus ideal for many of the applications involving LM NPs.

Chapter 2

Experimental section

2.1 Chemicals

Gallium (III) chloride (GaCl_3 , 99.999 %), tris(dimethylamino)gallium (III) dimer ($\text{Ga}_2(\text{NMe}_2)_6$, 99.9 %) and di-*n*-octylamine ($\text{C}_{16}\text{H}_{35}\text{N}$ or DOA, 98 %) are purchased from ABCR. Copper (I) bromide (99 %), copper (II) acetate ($\text{Cu}(\text{OAc})_2$, 99.999%), copper (I) acetate (CuOAc , 98%), tungsten (IV) chloride (WCl_4), tri-*n*-octylamine (TOA, technical grade, 98%), tetradecylphosphonic acid (TDPA, 97%), tri-*n*-octylphosphine oxide ($\text{C}_{24}\text{H}_{51}\text{PO}$ or TOPO, 99 %), *n*-Butyllithium solution 2.7 M in heptane (*n*-BuLi), oleylamine ($\text{C}_{18}\text{H}_{35}\text{NH}_2$ or OLAM, 70 %), oleic acid ($\text{C}_{17}\text{H}_{33}\text{CO}_2\text{H}$ or OLAC, 90 %), 1-octadecene ($\text{C}_{18}\text{H}_{36}$ or ODE, 90 %), toluene (anhydrous, 99.8 %) and ethanol (anhydrous, 99.5 %) were purchased from Sigma-Aldrich. Potassium carbonate (K_2CO_3 , 99+ %, ACS reagent) was obtained from Acros organics. DOA, TOA, ODE, OLAM and OLAC were degassed and dried under a vacuum at 110 °C for 4 h, cooled to room temperature, and then transferred airless to the glove box. All syntheses were carried out under an inert atmosphere using anhydrous solvents and standard glovebox and Schlenk-line techniques. Post-synthetic purification (“washing”), ligand exchange, handling, and storage of the as-synthesized materials were also carried out under inert atmosphere.

2.2 Synthetic procedures

7 nm Cu NPs

7 nm Cu NPs were synthesized following a protocol adapted from Kim et al.¹⁶⁵ In a typical synthesis, TOA (20 mL) was introduced in a 50 mL three-necked round bottom flask and then degassed under dynamic vacuum at 130°C for 1 hour while stirring. The flask was then refilled with N_2 gas and cooled to 50°C. TDPA (270 mg, 1 mmol) and CuOAc (245 mg, 2 mmol) were added to the flask as a powder, forming a green, cloudy mixture. The mixture was heated to 180°C and held for 30 minutes, during which the mixture turned light brown. After 30 minutes, the mixture was rapidly heated to 270°C, quickly forming a dark red mixture. After 30 minutes

at 270°C, the dark red colloidal suspension was allowed to cool down to room temperature by removing the heating mantle. Then, the reaction mixture was transferred into 40 mL glass vials with a septum filled with N₂ via a 20 mL plastic syringe. To each 5 mL portion of the crude reaction mixture, hexane (5 mL) and ethanol (15 mL) were added. The particles were isolated by centrifugation at 13500 rpm for 8 minutes, and the supernatant was discarded. The particles were then washed using hexane (5 mL) and ethanol (15 mL) and again isolated after centrifugation. Finally, the particles were redispersed and combined into a single suspension using toluene and were stored in an N₂-filled glovebox.

40 nm Cu NPs

40 nm Cu spherical NPs were synthesised by modifying the procedure reported by Loiudice et al.⁴¹ 0.7 g of TOPO was added to 11.5 ml of OLAM in a three-necked round bottom flask and degassed for at least 30 minutes under strong magnetic stirring, during which time the TOPO dissolves in the OLAM and the solution turns colorless. The Cu precursor solution was prepared by dissolving 50 mg of CuBr in the 5 ml of degassed TOPO and OLAM. This solution was heated for 15 min at 80°C in the glovebox to dissolve TOPO and CuBr. Then, the Cu precursor solution was transferred to the three-necked flask with a syringe to avoid oxidation. After that, the reaction mixture was brought to the temperature of 260°C under N₂-flow and left at this temperature for 60 min. As a result, reddish-brown solution is formed. The heating was then removed and the flask was allowed to cool to 90°C. The solution was transferred to the glovebox and washed once with anhydrous hexane (1 : 1 hexane to reaction mixture ratio) by centrifuging at 6000 rpm for 10 minutes. The supernatant was disposed of, and the precipitate recovered in degassed OLAM for further use as seeds, or in anhydrous toluene for the further use as electrocatalyst (with the final concentration of *ca.* 5 mg/mL).

CuGa alloy NPs

CuGa alloy NPs were synthesized according to a modified procedure based on Clarysse et al.¹⁶³ 15 mg of Cu NPs in OLAM were added to the three-necked round bottom flask with 11.5 ml of degassed OLAM. The solution was heated to 280°C under flowing N₂. This step was followed by the hot-injection of a Ga-precursor, prepared by dissolving 17, 35 or 70 mg of Ga₂(NMe₂)₆ in 3 ml of degassed ODE to obtain CuGa₄, CuGa₁₇ and CuGa₃₇ samples, respectively. After the hot injection, the reaction solution was kept at a temperature of 280°C for 1 hour, and allowed to cool to room temperature. The solution was transferred to the glovebox and washed once with anhydrous hexane (1 : 1 hexane to reaction mixture ratio) by centrifuging at 6000 rpm for 10 minutes. After that, the supernatant was disposed of, and the precipitate recovered in hexane. Ethanol was then added in 1 : 1 ratio, followed by

centrifugation for 5 min at 6000 rpm. Finally, the supernatant was disposed of, and the CuGa nanoparticles were dispersed in 5 ml of toluene (with the final concentration of *ca.* 1 mg/mL).

18 nm Ga NPs

18 nm Ga NPs were synthesized by modifying a previously reported procedure.¹⁶⁶ 12 mL of ODE and 1.1 mL of DOA were loaded into a 50 mL three-necked flask equipped with a reflux condenser and dried under vacuum at 120 °C for 1 h. Next, the reaction flask was filled with N₂ and heated to 250 °C, followed by a rapid injection of 1.3 mL of *n*-BuLi 2.7 M in a 10 mL syringe. After 30 s, the mixture color changed from colorless to yellow, and 22 mg of GaCl₃ dissolved in 0.5 mL of anhydrous toluene were quickly injected with a 2 mL syringe. After that, the heating mantle was removed immediately, and the reaction was quenched with an ice bath after a few seconds after the color changed to dark grey. At 150 °C, 12 mL of anhydrous toluene were injected into the solution, and 0.05 mL of dried OLAC were injected at 50 °C. The solution was then left stirring for a few minutes. To purify Ga NPs and separate them from by-products and unreacted precursors, 15 mL of anhydrous ethanol were added, followed by centrifugation at 5000 rpm for 20 min. After supernatant disposal, the Ga NPs were redispersed in anhydrous toluene, and the purification/precipitation step was repeated once more with addition of 0.1 mL of OLAC. The Ga NPs were stored in anhydrous toluene.

26 nm Ga NPs

26 nm Ga NPs were synthesized by following a previously reported procedure.^{161,162} 7 mL of ODE were loaded into a 25 mL three-necked flask equipped with a reflux condenser and dried under vacuum at 110 °C for one hour. Then, the reaction flask was filled with N₂ and heated to 290 °C, followed by a rapid injection of a pre-prepared solution containing 50 mg of Ga₂(NMe₂)₆ and 2.3 mL of DOA in 3.8 mL of dried ODE with a 10 mL syringe. Right after the injection, the temperature dropped to 235 – 240 °C, and the solution color changed from yellow to dark grey after 30 s, which indicated the NPs formation. The reaction flask was then quenched using an ice bath and cooled down to room temperature. At 50 °C, 0.04 mL of dried OLAC were injected, and the solution was left stirring for a few minutes. To purify Ga NPs and separate them from by-products and unreacted precursors, 15 mL of anhydrous ethanol were added, followed by centrifugation at 5000 rpm for 20 min. After supernatant disposal, the Ga NPs were redispersed in anhydrous toluene, and the purification/precipitation step was repeated once more with addition of 0.1 mL of OLAC. The Ga NPs were stored in anhydrous toluene (with the final concentration of *ca.* 0.3 mg/mL).

39 nm Ga NPs

39 nm Ga NPs were synthesized by following the same synthetic protocol used for the **26 nm Ga NPs**, except that the precursor solution injected at 290 °C consisted of 40 mg of Ga₂(NMe₂)₆ and 3.4 mL of DOA in 2.6 mL of dried ODE.

Ga MPs

Ga MPs were synthesized according to Falchevskaya *et al.*¹⁶⁷ In a typical synthesis, 50 mg bulk Ga was placed in a 20 mL glass vial with 10 mL of toluene and heated at 50 °C until the drop melted. The vial was subject to ultrasound treatment in the ultrasonic bath (Bandelin Sonorex) at 50 °C until the full dispersion of the metal, which took *ca.* 30 min. Upon completion, the Ga MPs were left to cool down and stored in the same vial.

Liquid Ga/Cu NDs

Liquid Ga/Cu NDs were synthesized according to a previously reported procedure.¹⁶² 2 mL of a solution of pre-synthesized **26 nm Ga NPs** in ODE (4 mM), 2 mL of a solution of Cu(OAc)₂ in ODE (4 mM), 1 mL of OLAC and 1 mL of OLAM were added to a 5 mL vial and then stirred at 600 rpm on a hot plate at 150 °C inside a glovebox for 6 h (GaCu_{0.1}) or 12 h (GaCu_{0.7}). Ga/Cu NDs were separated from by-products and from unreacted precursors by adding ethanol (6 mL), followed by centrifugation at 13000 rpm for 10 min. The product was redispersed in toluene, and the purification/precipitation step was repeated once more before finally being stored in anhydrous toluene (with the final concentration of *ca.* 0.1 mg/mL).

Liquid Ga/Ag NDs

The Ga/Ag NDs were synthesized according to a previously described procedure.¹⁶² 1 mL of Ga NPs solution in toluene (4 mM) and 1 mL of a solution of AgNO₃ in toluene (4 mM) were added to a 5 mL vial and then stirred at room temperature for 4 h. The reaction product was separated from the by-products and from unreacted precursors by adding ethanol (2 mL), followed by centrifugation at 13000 rpm for 10 min. Ga/Ag NDs were redispersed in toluene, and the purification/precipitation step was repeated once before finally being stored in toluene.

Liquid Ga/Sn NDs

1 mL of Ga NPs solution in ODE (4 mM), 50 µL of SnCl₄ (4.2 mmol) and 3.95 mL of ODE were added to a 5 mL vial and then stirred at room temperature for 4 h. The reaction product was separated from the by-products and unreacted precursors by adding ethanol (4 mL), followed by centrifugation at 13000 rpm for 10 min. Liquid Ga/Sn NDs were redispersed in toluene, and the purification/precipitation step was repeated before being stored in toluene.

Co NPs

TOA (10 mL), TDPA (137 mg) and CoCO_3 (118 mg) were placed into the three-necked flask and degassed for 30 min. After that, the temperature was increased to 130 °C under vacuum remove any residual water. Then, the reaction mixture was heated to 180 °C and held for 30 min. Finally, the temperature was increased to 260 °C and kept for another 30 min. The reaction mixture was cooled down to room temperature, and the NPs were washed in the way similar to Cu NPs.

Liquid Ga/Co ND

7 mL of ODE was placed into a 25 mL three-necked flask equipped with the reflux condenser and a stir bar, and dried under vacuum at 110°C for 1 h. After that, the flask was put under nitrogen atmosphere and heated up to 290°C. At the same time, 50 mg of $\text{Ga}_2(\text{NMe}_2)_6$ in 2 mL of dried ODE and 0.035 mmol of Co NPs in 2.26 mL ODE were prepared in two different vials and left stirring. Then, Ga precursor and Co NPs were brought together in one vial, and hot injected into the reaction flask. The flask was heated at 260°C for 1 h after the hot injection and cooled down to room temperature afterwards. Following that, the product was washed by collecting the reaction solution, adding 15 mL of ethanol and centrifuging at 5000 rpm for 10 min. The precipitate was redispersed in toluene, sonicated and washed once more by addition of 1 mL of ethanol followed by centrifugation at 5000 rpm for 10 min. The NPs were stored in toluene inside the glovebox.

WO₃ NPs

WO₃ NPs were synthesized following a previously reported procedure.^{168,169} 5.3 mL of OLAC were added to a three-neck flask together with 1.8 mL of OLAM and 100 mg of WCl_4 . The mixture was heated under the nitrogen flow to 300°C under stirring, and the temperature was kept for 2 h, after which the reaction mixture was cooled to room temperature. The NPs were washed in acetone three times by centrifugation/redispersion steps (15 minutes each, 3800 rpm). The NPs were finally stored in toluene.

2.3 *Ex situ* materials characterization

Bright-field transmission electron microscopy (TEM) images of NPs were acquired on a Thermo-Fisher Tecnai-Spirit at 120 kV. 5 – 20 μL of as-synthesized Ga NPs were drop-casted on a carbon coated copper TEM grid (Ted Pella, Inc.) to prepare the sample for imaging. Particle size distribution was evaluated with the use of ImageJ software from datasets of at

least 200 particles each. To analyze the samples after CO₂RR, golden TEM grid (Ted Pella, Inc.) was placed on the electrode inside the glovebox, 10 – 20 µl of ethanol were placed on the area coated with the catalyst, and the catalyst film was gently scratched with the grid.

Selected area electron diffraction (SAED) patterns of NPs were acquired on a Thermo-Fisher Tecnai-Spirit at 120 kV. To analyze the samples after CO₂RR, the samples were prepared in the way same to described for bright-field TEM imaging.

High-angle annular dark field scanning transmission electron microscopy (HAADF-STEM) coupled with energy-dispersive X-ray spectroscopy (EDXS) was performed using a FEI Tecnai Osiris TEM in STEM mode with an accelerating voltage of 200 kV. The TEM was equipped with a high brightness XFEG gun and four windowless Super-X silicon drift detectors for EDXS. Bruker Esprit was used for data analysis. To analyze the samples after CO₂RR, the grid was prepared in the way similar to described earlier for bright-field TEM imaging.

Cryo-TEM heating experiments were performed on Thermo-Fisher Talos F200s at 200 kV with Gatan Sci. temperature control holder cooled with liquid N₂. The specimen was heated by resistive elements to the preset temperature.

Scanning electron microscopy (SEM) images were acquired with Thermo-Fisher Teneo using an in-lens (Trinity) detector at beam energy of 5 keV and current of 25 pA – 0.1 nA. Samples were imaged on conductive glassy carbon substrates used as electrodes for CO₂RR measurements.

Powder X-Ray diffraction (XRD) patterns were acquired on a Bruker D8 Advance diffractometer with a Cu K α source equipped with a Lynxeye one-dimensional detector. The diffractometer operated at 40 kV and 40 mA with a Cu K α source with wavelength of 1.54 Å.

Grazing incidence X-Ray diffraction (GIXRD) data were collected on a Bruker D8 Discover Plus equipped with a rotating anode (Cu) and a Dectris Eiger2 detector. A focusing 60 mm Göbel mirror was used and the background was optimized with an anti-scatter nozzle and anti-scatter screen. A primary 2.5° axial Soller slit and a secondary 1.0° equatorial Soller slit were placed in the beam path. The incidence angle was optimized on each sample and chosen between 0.1 and 0.25° depending on the sample, the beam was selected using 0.2 or 0.1 mm divergence slits. 2 θ scans were collected at stepsizes of 0.5 – 0.6 °2 θ and 5 – 10 s per step.

X-Ray photoelectron spectroscopy (XPS) was performed by using an Axis Supra (Kratos Analytical) instrument using the monochromated K α X-ray line of an Al anode. The pass energy was set to 40 eV with a step size of 0.15 eV. The samples were electrically insulated from the sample holder, and charges were compensated. Ga NPs samples were prepared by drop-casting

films onto clean glassy carbon substrates. The same substrates were used in electrochemical experiments. XPS fitting was performed in CasaXPS software. All data were referenced to the principal C 1s peak at 284.8 eV after fitting. In the Ga 2p region, only the Ga 2p_{3/2} peaks were used for fitting and quantification. In the Ga 3d region, both Ga-metal and Ga-oxide peaks were fitted with contributions from spin-orbit coupling; the Ga 3d_{3/2} and Ga 3d_{5/2} peak separations were fixed at 0.46 eV, and the relative intensities were fixed at 0.633. In the Cu 2p region the area under the peak at around 932.5 eV was used for the quantification. In general, all peaks from a particular region were first fitted with equal line widths, and then this constraint was relaxed to refine the fit.

The NPs solution concentration was determined by Inductively Coupled Plasma Optical Emission Spectrometry (ICP-OES) performed on an Agilent 5100 device with a VistaChip II CCD detector. Each sample aliquot (20 µl) was first dried, then digested overnight in 142.5 µL of 70 % HNO₃ ICP grade solution and finally diluted with Milli-Q water to obtain the 2 wt. % acid content needed for the analysis. ICP grade standard solutions (1000 ppm in 2 wt. % HNO₃) were diluted with 2 wt. % HNO₃ to get fresh standards before each analysis used to create the calibration plot employed to determine the concentration of the sample solutions.

The content of Ga and Cu ions in the electrolyte after CO₂RR reaction was analyzed by Inductively Coupled Plasma Mass Spectrometry (ICP-MS) using kinetic energy discrimination (KED) mode with He as a collision gas on NexIon 350 D ICP-MS instrument (PerkinElmer). The samples were diluted 300 times with 2 % HNO₃ solution prior to the analysis. Y (yttrium) was added as an internal standard at concentration of 2 ppb to all the solutions. Absolute quantitation was performed using external calibration curve with standards in 0.05 – 50 ppb range. All measurements were performed in triplicates.

2.4 Electrochemical characterization and electrocatalytic testing

Electrode preparation

Glassy carbon plates (2.5 cm × 2.5 cm × 0.3 cm, Sigradur G, HTW) coated with electrocatalyst were used as the working electrode. Before coating, the glassy carbon plates were cleaned by consecutive sonication (Bandelin Sonorex RK 106, 35 kHz) in acetone, isopropanol and water for 10 min each to remove adsorbed contaminants of different nature. After this, the glassy carbon plates were polished using an alumina paste (50 nm alumina,

BAS Inc.) on a polishing pad. Then, the substrates were sonicated in Milli-Q water for another 10 min, polished again on the pad free of alumina to make sure that alumina was removed and, finally, the glassy carbon plate was blown dry with N₂.

The working electrodes (cathodes) were prepared by drop-casting the NPs in 14 μ L of toluene onto a circular area of 1.33 cm² on the glassy carbon plates. To redispersed desired amount of NPs in 14 μ L of toluene, the NPs stock solution aliquot was centrifuged for 10 min at 13300 rpm, then the supernatant was disposed and, finally, the NPs precipitate was re-dispersed in 14 μ L of anhydrous toluene (the material was kept under protective N₂ atmosphere during all manipulations). No binder (e.g. Nafion) or carbon were added to the catalyst, as NPs electrode films prepared as described do not detach from the electrode surface during the measurement and are sufficiently conductive on their own. After drop-casting, the electrodes were allowed to dry for 10 min, rinsed with ethanol to remove ligands, and with water to remove excess of ethanol. The electrodes were blown dry and tested as prepared.

Electrodes for square-wave voltammetry (SWV) were prepared in the same way except that higher loading was used to obtain better signal and a different substrate was used. That is, a rod-shape 3.0 mm diameter (0.28 cm²) glassy carbon electrode (MF-2012, Bioanalytical Systems, Inc.) was covered with 25 μ g of Ga NPs in 2 μ L of toluene. For the tests of bulk Ga, a Ga pellet was placed in the custom J-shape electrode with bowl-like volume to prevent the loss of electric connection between liquid Ga and current collector because of Ga detachment. Electric current was supplied through a wire which was embedded into the plastic electrode body and kept isolated from the electrolyte.

The working electrodes were prepared by spray-coating the a NPs solution in hexane onto the microporous layer of a Sigracet 39BC gas-diffusion layer with a circular catalyst geometric surface area of 1.33 cm², following the procedure reported earlier by our group.¹³ The suspension for spraying was prepared by dilution of a stock solution in hexane to 1.2 mL, to obtain a catalyst loading on the electrode of 50 μ g cm⁻².

Electrochemical measurements

All the electrochemical measurements were controlled with Biologic SP-300 potentiostat.

Ambient pressure CO₂ electrolysis was carried out in a home-built, custom-made, gas-tight, electrochemical H-cell made of polycarbonate and fitted with Buna-N O-rings. In this electrochemical cell configuration, the working electrode and counter electrode are configured parallel to each other to ensure a uniform potential distribution across the surface. Both working

and counter electrodes exposed geometric surface areas of 1.33 cm² limited by the O-rings. Catholyte and anolyte compartments were each filled with 2 mL electrolyte to concentrate liquid products and permit their detection. A Selemion AMV anion exchange membrane was used to separate the anodic and cathodic compartments and minimize reoxidation of CO₂RR products on the anode. Pt foil was used as the counter electrode, and Ag/AgCl electrode (leak free series) (Innovative Instruments, Inc.) was used as the reference electrode.

0.1 M KHCO₃ solution was used as electrolyte. To prepare such solution, 0.276 g of K₂CO₃ were diluted in 40 mL of Milli-Q water to obtain 0.05 M K₂CO₃ solution, which was bubbled for 30 min with CO₂ (99.999 %, Carbagas) prior to the start of measurements. During electrolysis, CO₂ was pre-humidified by flowing through a water bubbler, and constantly supplied to both cell compartments via custom-made ceramic frits at a flow rate of 5 sccm each. With this, the gas was bubbled through the electrolyte to prevent CO₂ depletion, as well as to allow continuous analysis of gaseous products via a gas chromatograph. A mass flow controller (Bronkhorst) was used to control the flow rate of CO₂. For the experiments under N₂ atmosphere, the only difference was the gas source (N₂, 99.999 %, Carbagas); all the other details remained the same. The electrolysis experiments were performed in chronoamperometry mode.

The CO₂RR measurements in flow cell configuration were performed in a conventional Teflon flow cell electrolyzer, which is described in detail in a previous publication.¹³ Ni mesh (McMaster–Carr, 100×100 mesh size) was used as the counter electrode. The reference electrode and the anionic exchange membrane were the same as the ones used in the H-cell (that is, Ag/AgCl leak-free electrode from Innovative Instruments and Selemion AMVN). Anolyte and catholyte solutions were CO₂-saturated 1.0 M KHCO₃ (40 mL each), which were circulated through both compartments by a dual-channel peristaltic pump (Behr PLP380) at a constant flow rate of 1.25 mL min⁻¹ per channel. High purity CO₂ gas (Carbagas) was fed into the back chamber of catholyte compartment at a constant flow of 10 sccm, which was controlled by a digital mass-flow controller (Bronkhorst). The output from the cathode compartment fed directly to an in-line gas chromatography instrument for gas-product analysis, where gas sampling was performed at regular intervals of 10 minutes. At the end of the reaction, liquid aliquots were recovered from both catholyte and anolyte chambers for liquid-product analysis by HPLC. The measurements were performed in chronopotentiometry regime.

SWV was performed using the same potentiostat in the three-electrode glass cell under CO₂ atmosphere. Pt wire was used as counter electrode, and Ag/AgCl electrode (MF-2056,

Bioanalytical Systems, Inc.) was used as a reference electrode. The same 0.1 M KHCO₃ solution was used as electrolyte.

In all electrochemical tests, electrochemical impedance spectroscopy (EIS) was implemented prior to the main measurement to determine the electrochemical cell resistance (R_{cell}) and compensate for the ohmic losses. Four spectra were measured at the ocp, using 41 points between 1 MHz and 100 Hz, using a sinus amplitude of 20 mV and a pause time of 0.6 s between each frequency. Software utility in-built into the potentiostat software (EC-lab) was used to apply the ohmic loss correction to further measurement.

Products analysis

Gas chromatograph (GC, SRI instruments) equipped with a HayeSep D porous polymer column, thermal conductivity detector and flame ionization detector was used for the analysis of gaseous products. The GC was calibrated for H₂, CO, CH₄, C₂H₄ and C₂H₆. Five standard gas mixtures (Carbagas, 50 – 1000 ppm for CO, CH₄, C₂H₄ and C₂H₆, 100 – 5000 ppm for H₂) were used to obtain the calibration plots for gaseous products concentrations determination. Ultra-high purity N₂ (99.999 %) was used as a carrier gas.

The Faradaic efficiency for the gaseous products is calculated with the following equation:

$$FE = \frac{n_e \times F \times C \times f \times P}{R \times T \times I}$$

where n_e is the number of electrons transferred to product; F is the Faraday constant (96485 C mol⁻¹); C is the product concentration measured by GC (in ppm); f is the CO₂ flow rate (mL s⁻¹); P is the pressure (1.01×10⁵ Pa); I is the applied current (in A); R is the universal gas constant (8.314 J mol⁻¹ K⁻¹); T is the temperature (K). Values obtained after 10 min of CO₂RR are not included in the FE calculation, as the GC gas flow is not stabilized at that point.

The FE of liquid products was determined in a similar manner. 0.25 mL of both the catholyte and the anolyte were collected and analyzed with high-performance liquid chromatography (HPLC) on UltiMate 3000 instrument from Thermo Scientific, which is equipped with Refractive Index Detector for products quantification and Aminex HPX-87H (BioRad) column for products separation (1 mM H₂SO₄ was used as eluent). The necessity to collect electrolyte from both compartments is reasoned by the possible products crossover from the catholyte to the anolyte (i.e., formic acid and acetic acid which exist in their anionic forms formate and acetate in the neutral solution and can migrate through the anion exchange membrane which separates the two compartments).

The resulting formula used for calculations of liquid products' FE is:

$$FE = \frac{n_e \times F \times C}{V \times I \times t}$$

where n_e is the number of electrons transferred to product formation; F is the Faraday constant; C is the measured concentration of the product by HPLC (mol mL^{-1}); V is the cell volume (4 mL); I is the measured current (A); t is the duration of electrolysis.

The electrode potential is recalculated with respect to RHE reference using iR compensation according to the equation:

$$E_{RHE} = E_{Ref} + 0.206 + 0.0591 \times pH - (R_{cell} \times I)$$

where E_{Ref} is the recorded potential against the Ag/AgCl reference electrode (V); +0.206 V is the Ag/AgCl reference electrode correction; R_{cell} is the ohmic resistance between the working and the reference electrode, which was defined using electrochemical impedance spectroscopy analysis prior to the measurement (Ohm); I is the imposed current (A).

For all values, error bars, representing standard deviations obtained with triplicate measurements, are given.

Voltage-driven synthesis from Ga/Cu NDs.

Liquid Ga/Cu NDs precursors were deposited on the same glassy carbon plate used for electrocatalytic measurements. 5 μg of the NPs in 14 μL of toluene were drop-casted onto a circular area of 1.33 cm^2 . After drop-casting, the plates were allowed to dry for 10-15 min, then rinsed with ethanol and with water.

A Biologic SP-300 was used as a potentiostat. Same electrochemical H-cell as in electrocatalytic studies was used as the reactor. The carbon plates with the deposited NPs were implemented as the working electrode in 0.1 M KHCO_3 solution. EIS was implemented to determine the electrochemical cell resistance and compensate for the ohmic losses.

Electrochemical studies with bulk liquid Ga – Cu.

The electrochemical studies were performed with Biologic SP-300 potentiostat in open glass cell in two-electrode geometry with the use of Ohmic drop compensation built in the software. The cathode wire was connected to the back of the working electrode, and Pt wire was used as anode. 0.1 M KHCO_3 solution was used as electrolyte. The cell was heated to *ca.* 35 $^\circ\text{C}$ with the heating plate from the bottom of the cell.

2.5 *Operando* X-Ray absorption spectroscopy

Operando X-Ray absorption spectroscopy (XAS) measurements, at both Cu K- and Ga K-edges, were made in fluorescence mode at BM31 of the Swiss-Norwegian beamlines at the ESRF, Grenoble, France.¹⁷⁰ A Si(111) double crystal monochromator, and a Vortex[®] single-element Si drift fluorescence detector with XIA-Mercury digital electronics were used. The X-ray beam was applied in an unfocused state and shaped to *ca.* 3 mm (horizontal) and 0.5 mm (vertical) via the uses of slits.

The samples were drop-casted onto polished glassy carbon electrodes equivalent to the ones used in the lab based studies, except the smaller thickness in the case of the XAS studies (0.05 cm). The loading was increased to 60 – 80 μg to improve the signal-to-noise ratio. The prepared catalyst film on the electrode was then mounted in a custom-made electrochemical system the details of which may be found elsewhere.^{171,172} The cell reproduces the same H-cell used in the lab experiments, but with a Kapton window in the back of working electrode to allow the X-rays to pass through to the sample and fluorescence X-rays detected. This way, the experiment environment was as close to the in-house electrochemical testing as possible to allow *operando* material characterization. To obtain the Cu reference spectra, Cu foil was used, along with Cu₂O and CuO powders diluted in boron nitride and shaped into the form of pellet. A metallic Ga film, obtained by exfoliation of warm Ga pellet with Kapton tape, and Ga₂O₃ powder diluted in boron nitride and shaped into the form of pellet, were used as references for the Ga K-edge. Other testing parameters were identical to those used in the lab-based tests.

The *operando* measurements were carried out in fluorescence mode at an incident angle of *ca.* 45 degrees. The cell was aligned with a multi-use beamline fixation support, which permitted the cell alignment with respect to the incoming beam *via* an XYZ high-precision translation stage. A Si(111) double crystal monochromator was used to condition the beam from the corresponding bending magnet.

Fluorescence X-Ray absorption near edge structure (XANES) and extended X-Ray absorption fine structure (EXAFS) spectra were acquired using a Vortex[®] one-element silicon drift detector with XIA-Mercury digital electronics. Normally, *ca.* 8 min scans were collected to obtain EXAFS spectrum, and certain number of scans were averaged to improve the signal-to-noise ratio. To get kinetic information about the material state during CO₂RR, shorter and more rapid (*ca.* 2 mins per spectrum) XANES data was collected. In all cases, the experimental conditions (CO₂ flow rate, electrolyte etc.) were kept identical to the lab-based tests.

Data extraction, normalization, and averaging to obtain the heat maps of XAS spectra during operation were performed using the Demeter package (Athena and Artemis).¹⁷³ In addition, the XAS data were reduced and normalized using the Prestoprnto package that was also subsequently used to perform linear combination analyses.¹⁷⁴

Analysis of the extracted EXAFS data was performed using EXCURV (v. 9.3).¹⁷⁵ In terms of reporting the analysis, we have confined ourselves by and large to only analyses of the first coordination M – M shell (N1), its associated bond distance (d, Å) and disorder parameter (the Debye-Waller factor (DWF), Å²).

E_F refers to the edge position relative to Vacuum zero (Fermi energy, eV), and the AFAC parameter (0.9 in all cases), determined through fitting of a copper foil standard relates to the proportion of electrons undergoing scattering post absorption that contribute to the EXAFS. In assessing the quality of the fits obtained, the R-factor (R%) is defined as follows as follows:

$$R = \sum_i^N \frac{1}{\sigma_i} (\chi_i^e(k) - \chi_i^t(k))^2 \cdot 100\%$$

where $\chi_i^e(k)$ and $\chi_i^t(k)$ are the experimental and theoretical EXAFS, respectively, and k is the photo-electron wave-vector (Å⁻¹). σ_i is the uncertainty in the data, with

$$\frac{1}{\sigma_i} = \frac{k_i^n}{\sum_j^N k_i^n (\chi_i^e(k_j))^2}$$

The fitting range used in R space (δR) was 1 – 3, whilst the range of k space used for the fitting of the EXAFS was between 2.5 – 3 and 12.5 – 13 (Å⁻¹).

Linear combination analysis

Linear combination analysis (LCA) of the Cu K-edge was carried out using the Prestoprnto package.¹⁷⁴ For the Cu K-edge the references employed were a Cu foil and pressed samples of Cu₂O and CuO measured in transmission. Ordinarily, the use of transmission-based standards to model fluorescence yield data would be ill advised as a result of the latter suffering from the phenomenon of “self-absorption”. However, empirically it has been found that the electrode samples under study are so thin that the bulk references made in transmission are more appropriate as standards to assess the speciation than those collected in fluorescence mode.

Using these three standards, different models were applied, for instance, Cu foil, Cu foil + CuO, Cu foil + Cu₂O, and Cu foil + Cu₂O +CuO, to fit the data and a comparison made of the how the statistical measured of goodness of fit (Chi²) changed between each model with time. From this comparison it was then determined whether the addition or replacement of a given

reference had a significant effect (positive or negative) on the ability of the model to fit the XANES data.

Surface oxide thickness calculation from linear combination analysis

The thickness of the surface oxide on the NPs surface was calculated assuming spherical shape of the NPs. With this, and with the assumption that the mass and atomic fractions of the oxide are similar (x , %), the surface oxide thickness, r_{ox} (nm), is calculated as:

$$V_{total} = \frac{4\pi r_{total}^3}{3}$$

$$V_{core} = \frac{4\pi r_{core}^3}{3} = (1 - x)V_{total} = (1 - x)\frac{4\pi r_{total}^3}{3}$$

$$r_{core} = \sqrt[3]{(1 - x)r_{total}^3}$$

$$r_{ox} = r_{total} - r_{core} = \left(1 - \sqrt[3]{(1 - x)}\right)r_{total}$$

2.6 Theoretical models

Ga NPs surface area calculation

We found that the electrochemical double-layer capacitance or underpotential deposition are not readily accessible to determine the electrochemically surface area (ECSA) for Ga. The use of these methods generates unreliable and irreproducible results. The presence of a native oxide layer in all the voltage ranges where no Faradaic processes occur might explain these issues, which are similar to those encountered for oxide electrocatalysts.¹⁷⁶ Impedance measurements with the implementation of equivalent electric circuit have been used for oxide electrocatalysts.^{177–179} However, this circuit has to be reliably established first for the given system, which is beyond the scope of this study.

Similarly to Reske et al.,¹⁸⁰ we have defined the total surface area, S (cm²) as follows:

$$S = S_p N_p = \pi d_p^2 \cdot \frac{m_{total}}{m_p} = \frac{\pi d_p^2 m_{total}}{\rho_{Ga} V_p} = \frac{\pi d_p^2 m_{total}}{\rho_{Ga} \cdot \frac{1}{6} \pi d_p^3} = \frac{6m_{total}}{\rho_{Ga} d_p},$$

where S_p (m²) is a surface area of a particle, N_p is a number of particles, d_p (m) is the average particle diameter (obtained from the particles size analysis), m_{total} (kg) is the catalyst

loading, m_p (kg) is a particle mass, $\rho_{Ga} = 6095 \text{ kg m}^{-3}$ is the density of liquid Ga,¹³⁰ V_p (m^3) is a particle volume.

To transfer to more convenient units with respect to the scale (cm^2 , nm, μg , g, cm^3), correction coefficient is needed, and the final formula yields

$$S = \frac{60m_{total}}{\rho_{Ga}d_p},$$

where the units are S_p (cm^2), m_{total} (μg) is the catalyst loading, ρ_{Ga} (g cm^{-3}), d_p (nm).

Gallium oxide shell thickness calculated by XPS measurements

The Ga-oxide shell thickness (d , nm) for the Ga NPs was calculated by using XPS following a previously reported procedure.¹⁸¹ Specifically, d is calculated by using the well separated Ga-metal and Ga-oxide peaks in the Ga $2p$ region of the XPS spectrum. The following equation describes the relation between d and fraction of Ga oxide (x , %) measured by XPS:

$$d = -\lambda * \ln\left(\frac{x - \lambda}{-\lambda}\right)$$

where λ is the inelastic mean free path (\AA). The λ value was calculated for the Ga $2p$ photoelectrons to be 11.3 \AA , as described by Castilla-Amorós et al.¹⁸¹ Note that the %Ga₂O₃ values are the area percentages of the oxides obtained from the Ga $2p$ high resolution XPS spectra multiplied by the calculated %Ga₂O₃ to give an area that is compatible with the model as previously reported.¹⁸¹ This approach provides approximations to the Ga-oxide shell thickness within *ca.* 10%. In particular, the Ga-oxide shell thickness measured after 1 h electrocatalysis carried out at different applied potentials is reported in **Table 4.1**. No particular trend of the shell thickness versus applied potential is evident. We note that the shell thickness of the as-prepared Ga NPs matches the one measured by TEM and *operando* XAS measurements. Instead, larger shell thickness values compared to the one obtained from *operando* measurements can be explained by the fact that the Ga NPs are exposed to the electrolyte and air before the XPS measurement is carried out.

Ga oxide content calculation based on *operando* XAS measurements

Operando XAS is a bulk technique. As the linear fitting of oxide and metallic Ga components yields bulk ratio of these two components, we can use the data to obtain the thickness of Ga oxide layer (assuming all oxide is at the particle surface).

The total particle volume (V_p , nm³) is obtained as the sum of metallic core (V_{met} , nm³) and oxide shell (V_{ox} , nm³):

$$V_p = V_{met} + V_{ox}$$

On the other hand, V_p and V_{met} can be calculated according to common equations for the volume of the sphere:

$$V_p = \frac{1}{6}\pi d_p^3 \quad V_{met} = \frac{1}{6}\pi d_{met}^3,$$

where d_p (nm) is the initial size diameter, d_{met} (nm) is the diameter of the metallic core.

From the linear fitting of the *operando* XAS measurements, we can obtain ω_{met} , which is the mass fraction of metallic Ga in the particle:

$$V_{met} = \omega_{met} V_p$$

This allows to obtain d_{met} :

$$d_{met} = \sqrt[3]{\frac{6}{\pi} V_{met}} = \sqrt[3]{\frac{6}{\pi} \omega_{met} V_p} = \sqrt[3]{\frac{6}{\pi} \omega_{met} \frac{1}{6} \pi d_p^3} = d_p \sqrt[3]{\omega_{met}}$$

Finally, if we define r_{ox} (nm) as oxide thickness, and considering that $d_p = d_{met} + 2r_{ox}$, we obtain the oxide thickness according to the following resulting equation:

$$r_{ox} = \frac{d_p - d_{met}}{2} = \frac{d_p - d_p \sqrt[3]{\omega_{met}}}{2} = \frac{d_p}{2} (1 - \sqrt[3]{\omega_{met}}), \text{ or}$$

$$r_{ox} = r_p (1 - \sqrt[3]{\omega_{met}}),$$

where r_p (nm) is the particle radius.

Density functional theory calculations

Density Functional Theory (DFT) calculations, adopting the Perdew Burke Ernzerhof functionals, were performed through the CP2K suite.¹⁸² The DZVP-MOLOPT basis set was adopted in the calculations, where core electrons are represented as per the dual-space Goedecker–Teter–Hutter pseudopotential framework.^{183,184} The planewave cut-off was set to 500 Ry (relative cut-off of 50 Ry). The DFT self-consistent loops to estimate the system total energy were considered as converged when a difference lesser than 10⁻⁸ Ry was found between two successive iterations. A Fermi-Dirac smearing with an electronic temperature of 300K was adopted in the calculations.

An *fcc* structure was considered for Cu and Cu-rich phases, in agreement with experimental measurements. For the Cu-rich phases, 3 and 12 Cu atoms are respectively substituted in the Cu slab with Ga atoms. Lattice distances are then modified according to Vegard's law. The (111) facet was chosen to inspect properties of the Cu-rich system, as the latter is the most energetically favorable one in Cu. A (4 × 4) slab with 4 layers, with periodicity along the slab plane was considered. The Cu₉Ga₄ phase was used to model the properties of the CuGa₃₇ sample. 4 layer slabs were also considered for this system. Input and outputs are also available from the Materials Cloud (<https://doi.org/10.24435/materialscloud:ft-s8>).

To assess changes in the electronic structure of the system as a function of the Ga content, we evaluated the Bader charge density of the candidate adsorption site in relaxed slabs, or neighboring Ga atom, utilizing the algorithm and code developed by Henkelman and coworkers.¹⁸⁵ The slab lowermost and next lowermost layers were kept fixed during each structural relaxation. These calculations were considered converged when all the atomic forces resulted less than 0.5 meV Å⁻¹.

To evaluate changes in the catalyst selectivity towards C₁ or C₂ products induced by an increase in the catalyst Ga content, we used $\Delta E_{*CHO} - \Delta E_{*OCCOH}$ as a descriptor of the propensity for *CO protonation vs. C–C coupling.^{186,187}

We calculated the formation energy of OCCOH via C-C coupling of two adsorbed CO, ΔE_{OCCOH} :¹⁸⁸

$$\Delta E_{OCCOH} = E_{*OCCOH} - E_{*CO,*CO} - E_{H_2}/2,$$

and the formation energy for *CHO and *CO by following the protonation of one of two adsorbed CO molecules:

$$\Delta E_{*CHO,*CO} = E_{*CHO,*CO} - E_{*CO,*CO} - E_{H_2}/2$$

In these equations, E_{*OCCOH} is the potential energy of a system comprising a Cu slab and an adsorbed OCCOH, $E_{*CHO,*CO}$ is the potential energy of a system comprising a Cu slab, an adsorbed CHO and an adsorbed CO molecule, and $\Delta E_{*CO,*CO}$ labels the energy of a system consisting of a Cu slab and 2 adsorbed CO molecules.

To evaluate ΔE_{*CO} , we screened non-equivalent sites and considered the most favourable one. Successively, we look at different protonation directions and HOCCO orientation and report formation energies referring to the most favourable configurations.

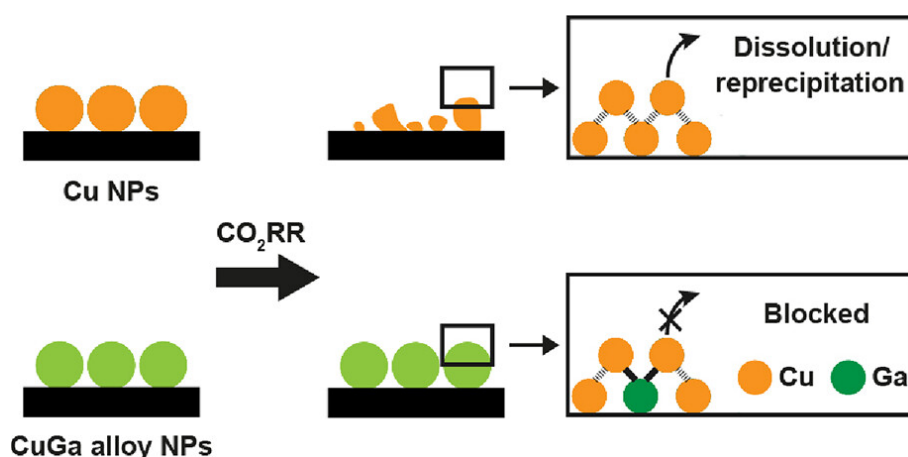
To probe, in a qualitative (if not quantitative) fashion, the tendency of Cu, CuGa₄, CuGa₁₇, and Cu₉Ga₄ systems to undergo structural rearrangements, we assessed their finite temperature stability by means of *ab initio* Molecular Dynamics. Newton's equation of motions are integrated with a 2 fs time step while a Canonical Sampling through Velocity Rescaling (CSVR) thermostat with time constant of 30 fs is used to regulate the temperature of the system. The slab lowermost layer was kept fixed during dynamics. Inputs were gathered and stored in the Materials Cloud repository.

To contain the computational cost of the simulation while retaining robust statistics, we sampled the system evolution over 10 independent trajectories of 0.75 ps at 407 K and 678 K, respectively one third and one half of the Cu melting temperature. We observed no structural rearrangements for Cu-rich slabs. These systems appear stable also when extending the sampling up to 1 ps. Viceversa, we witnessed significant restructuring in the Cu₉Ga₄ structure, at both 407 K (1 simulation), and 678 K (3 simulations), notwithstanding the short simulation timescale. An example of the observed structural rearrangement is highlighted in **Figure 3.13D**. These results are well-aligned with the thermal stability of the bulk phases, with Cu-rich phases being largely more robust to melting than the Cu₉Ga₄ phase.

Chapter 3

Alloying as a Strategy to Boost the Stability of Copper Nanocatalysts during the Electrochemical CO₂ Reduction Reaction

The content of this Chapter is based on published work with permission from the journal: *J. Am. Chem. Soc.* 2023, 9, 5370: <https://pubs.acs.org/doi/full/10.1021/jacs.2c13437>. Copyright 2023 American Chemical Society.



Abstract: Copper nanocatalysts are among the most promising candidates to drive the electrochemical CO₂ reduction reaction (CO₂RR). However, the stability of such catalysts during operation is sub-optimal, and improving this aspect of catalyst behavior remains a challenge. Here, we synthesize well-defined and tunable CuGa nanoparticles (NPs) and demonstrate that alloying Cu with Ga considerably improves the stability of the nanocatalysts. In particular, we discover that CuGa NPs containing 17 at. % of Ga preserve most of their CO₂RR activity for at least 20 hours while Cu NPs of the same size reconstruct and lose their CO₂RR activity within 2 hours. Various characterization techniques, including X-Ray photoelectron spectroscopy and *operando* X-Ray absorption spectroscopy, suggest that the addition of Ga suppresses Cu oxidation at open circuit potential (ocp), and induces significant

electronic interactions between Ga and Cu. Thus, we explain the observed stabilization of the Cu by Ga as a result of the higher oxophilicity and lower electronegativity of Ga, which reduce the propensity of Cu to oxidize at ocp and enhance the bond strength in the alloyed nanocatalysts. In addition to addressing one of the major challenges in CO₂RR, this study proposes a strategy to generate NPs which are stable under a reducing reaction environment.

Authors: Valery Okatenko, Anna Loiudice, Mark A. Newton, Dragos Constantin Stoian, Anastasia Blokhina, Alexander N. Chen, Kevin Rossi, Raffaella Buonsanti.

Contribution: Performed all electrochemical studies, XRD, bright-field TEM and SEM imaging, image statistical analyses and supplementary calculations, STEM-EDXS data processing and interpretation, SAED analysis, *operando* XAS measurements, and wrote the manuscript with contributions from all authors.

3.1 Introduction

In Chapter 1, we have pointed that the lack of stable catalysts for CO₂RR is currently one of the main bottlenecks for their practical implementation.^{7,45–48} As the reconstruction of Cu NPs is associated with Cu dissolution and reprecipitation which results in the NPs fragmentation,^{48,49,51,53,54} modifying Cu NPs in a way which could prevent this while maintaining desired selectivity profile is highly desirable.

One promising route to realize the catalyst stabilization approach while keeping the NPs in its metallic state is alloying. Studies in oxygen electrocatalysis have proved that the alloying of Pt, Pd and Ir NPs with guest elements dramatically improves the stability of these NPs against dissolution during catalysis by virtue of effects which span from the increase in the metal oxidation potential to the sacrificial dissolution of the less noble metals.^{189–195} For example, Zhang et al. report that Au clusters deposited on the surface of Pt NPs enhance the stability of Pt as an oxygen reduction reaction catalyst because the *d*-band interactions between Au and Pt increase the oxidation potential of Pt.¹⁸⁹ In another study, a Pd overlayer on the surface of Au NPs was demonstrated to be more resilient to dissolution than pure Pd NPs because of the Au – Pd bond being stronger compared to the Pd – Pd bond.¹⁹⁰ Another prospect which alloying may potentially provide is a shift towards thermodynamically stable metallic

nanoparticles, in comparison to often kinetic stabilization in the case of NPs shelling: for example, the study by Chookajorn et al. proposes that certain guest-host combinations in metallic NPs may offer them greater stability than their bulk counterparts.¹⁹⁶

With respect to Cu, Cu-based alloyed NPs are currently investigated as CO₂RR catalysts; however, these studies mostly focus on tuning the selectivity rather than aim at developing guidelines towards increasing the performance stability of the Cu NPs.^{43,197–201} Based on the current knowledge regarding the reconstruction of Cu in CO₂RR, and inspired by the studies on oxygen electrocatalysis, we hypothesize that the combination of Cu with an element M which possesses a higher oxophilicity and lower electronegativity than Cu should reduce the tendency of Cu to oxidize at ocp and form heteroatomic Cu – M bonds with higher dissociation energies than Cu – Cu, which should further hamper Cu dissolution and thus improve the performance stability of Cu NPs during CO₂RR.

Among various guest elements, Ga is an interesting candidate to explore. First, it does match the criteria listed above, namely that Ga is more oxophilic than Cu, and the Cu – Ga bond energy is greater than either Cu – Cu, Ga – Ga, or Cu – CO, with CO recently proposed to be the key reaction intermediate driving Cu reconstruction.^{49,51,53,54,202,203} In addition, Cu – Ga have similar atomic and metallic radii, as they are close to each other in the Periodic Table, which makes alloying between them more probable. This is confirmed by Cu – Ga bulk phase diagram, which suggests large chemical versatility to form new compounds, including alloys with different configuration, between the two elements (**Figure 3.1**).²⁰⁴ Specifically, up to *ca.* 20 at. % of Ga can be alloyed into Cu while conserving original *fcc* lattice, which is perfect for systematic evaluation of alloying impact on the catalyst stability. In addition, there are other alloy structures (such as γ -family of distorted cubic solid solution brasses with varied level of oxygen vacancies which are crystallized in $Pm\bar{3}m$ space group, or CuGa₂ intermetallic crystallized in tetragonal $P4/mmm$ space group).²⁰⁵ Furthermore, DFT and machine learning-based calculations propose that addition of Ga to Cu would enhance the CO₂RR activity of the catalyst.^{21,206}

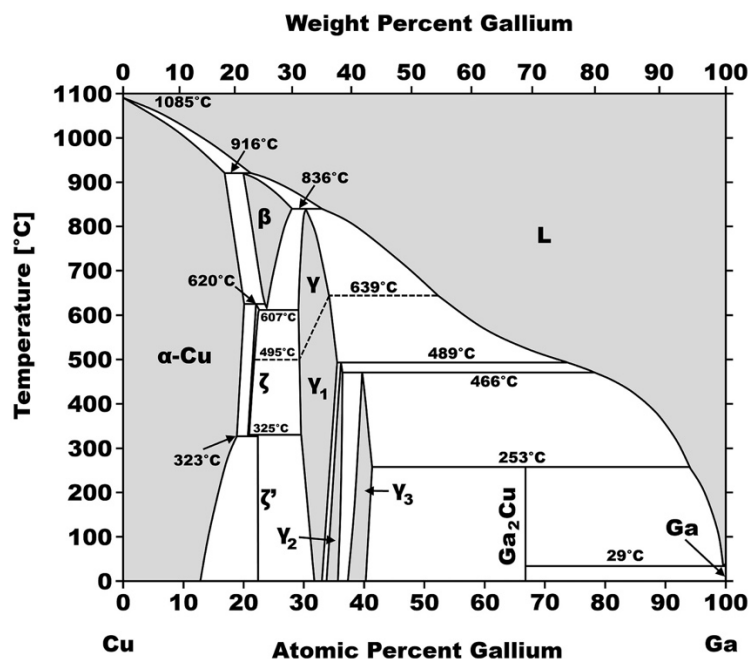


Figure 3.1. Cu – Ga bulk phase diagram. Reproduced from Priputen et al.²⁰⁴

This Chapter focuses on the study of CuGa alloy NPs with tunable composition as CO₂RR catalysts. After presenting synthesis and initial characterization of the CuGa NPs, which feature narrow size distribution and three different compositions (4 at. %, 17 at. % and 37 at. % of Ga content) (section 3.2), we evaluated their CO₂RR performance from selectivity and stability perspectives (section 3.3). Following that, in-depth *ex situ* characterization of the catalyst at different stages of CO₂RR with STEM, STEM-EDXS and XPS is presented (section 3.4). Then, *operando* XAS results, which allowed to follow the state of the catalyst during CO₂RR, are discussed (section 3.5). Together, these observations provide necessary information to elucidate the mechanism of stability enhancement in CuGa alloy NPs (section 3.6).

3.2 Catalyst synthesis and characterization

CuGa NPs were synthesized by following a previously reported seeded-growth method, where a Ga molecular precursor is injected into a flask containing pre-synthesized Cu NPs (i.e. the seeds) at 280 °C (**Figure 3.2A**).¹⁶³ CuGa NPs containing 4, 17 and 37 at % of Ga (further denoted as CuGa4, CuGa17 and CuGa37, respectively), as determined by the ICP-OES, were obtained by tuning the amount of Ga precursor during the synthesis (see section 2.2 for details). TEM images of the Cu NPs used as seeds and of the as-synthesized CuGa NPs are reported in

Figure 3.2B-E. These images show that all the NPs have same morphology and similar size between 40 nm and 50 nm with 10 % standard deviation within each sample (**Figure 3.2F**). The XRD characterization in **Figure 3.2G** reveals that CuGa4 and CuGa17 are crystallized with the same Cu-based *fcc* lattice as the only crystalline phase. The shift of the (111) and (200) peaks to lower 2θ values is consistent with the incorporation of increasing Ga content in the Cu lattice, according to the Vegard's law. Ga has a greater atomic radius than Cu and thus increases the interplane distances and unit cell parameter as it is included in the lattice. By contrast, the CuGa37 consists mostly of the Cu₉Ga₄-type primitive cubic lattice, with a minor contribution from an *fcc* Ga-rich phase, in agreement with other reports.^{207,208}

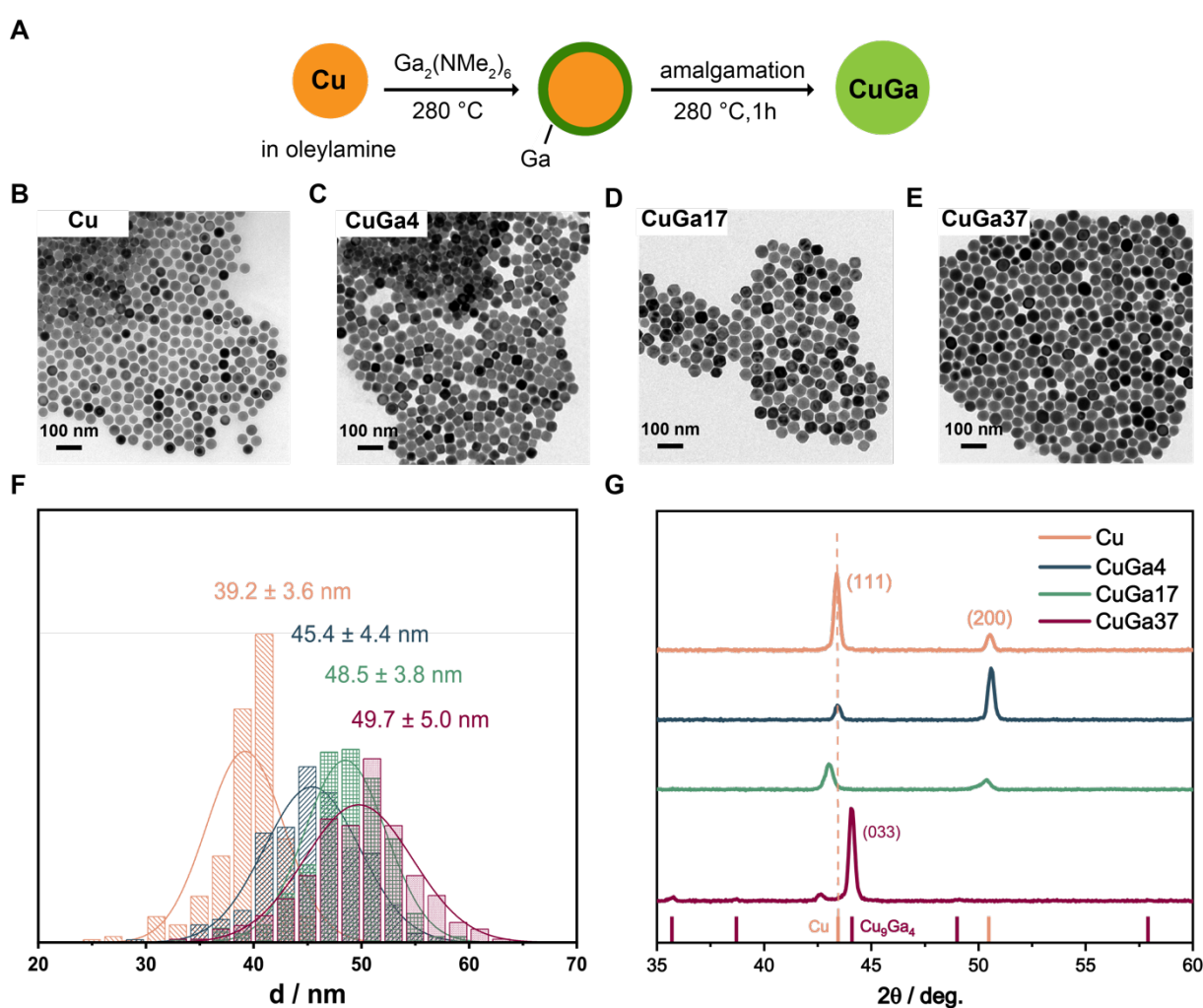


Figure 3.2. Synthesis and characterization of CuGa NPs. (A) Simplified synthetic scheme; (B-E) Bright field TEM of (B) Cu, (C) CuGa4, (D) CuGa17 and (E) CuGa37 NPs, their (F) size analysis and (G) XRD patterns. These data indicate that CuGa NPs with the same morphology, very similar size and different Ga content were synthesized.

3.3 CO₂RR performance

Having synthesized well-defined CuGa NPs with tunable composition, we proceeded to test their behavior as CO₂RR electrocatalysts (**Figures 3.3, 3.4**). We selected the Cu NPs, used as seeds for the synthesis of the CuGa NPs, as the reference catalyst. We do not include the Ga NPs as they are liquid under the conditions required for testing, and therefore distinctly different from the solid alloy NPs; in terms of the selectivity, Ga NPs produce only H₂ and CO.¹⁷¹

Figure 3.3A reports the Faradaic efficiency (FE, left axis) of all samples averaged over 45 minutes of chronoamperometry at different voltages, together with the corresponding total geometric current density (*j*, right axis). The addition of Ga to Cu suppresses the production of ethylene and promotes methane across the entire potential range, which becomes more evident when looking at the FE_{CH₄}/FE_{C₂H₄} reported in **Figure 3.3B**. CuGa17 reaches the highest FE_{CH₄} of 52 % at -1.2 V_{RHE}, which, in absolute numbers, accounts for CH₄ constituting 90 mol.% of all CO₂RR gaseous products (namely, CO, CH₄ and C₂H₄). CO₂RR measurements performed in a gas-fed flow cell generated a FE_{CH₄} of 51 % and *j*_{CH₄} of 76 mA cm⁻² (**Figure 3.3C**), which is close to the state of the art for electromethanation performed in neutral KHCO₃ electrolyte reported in the literature.

We note that potentials more positive than -1.0 V_{RHE} generate mostly hydrogen from the competing hydrogen evolution reaction (HER). Detection of small amounts of CO₂RR products at low overpotentials was also reported.²⁰⁹ From a mechanistic perspective, one way to rationalize the methane promotion by addition of Ga to Cu is to consider the higher oxophilicity of Ga which favours the CO protonation and stabilizes the intermediate derived by this step.^{68,172,210} Indeed, density-functional theory (DFT) calculation show a volcano-type dependance from Cu to CuGa37 peaking at CuGa17 for $\Delta E_{\text{-CHO}} - \Delta E_{\text{*OCCOH}}$, which is used as a descriptor of the propensity for *CO protonation vs. C–C coupling (**Figures 3.3D**).^{186,187} Along with CH₄, HER is promoted as the Ga amount increases, which is reasonable considering that Ga alone generates CO and H₂.^{113,171}

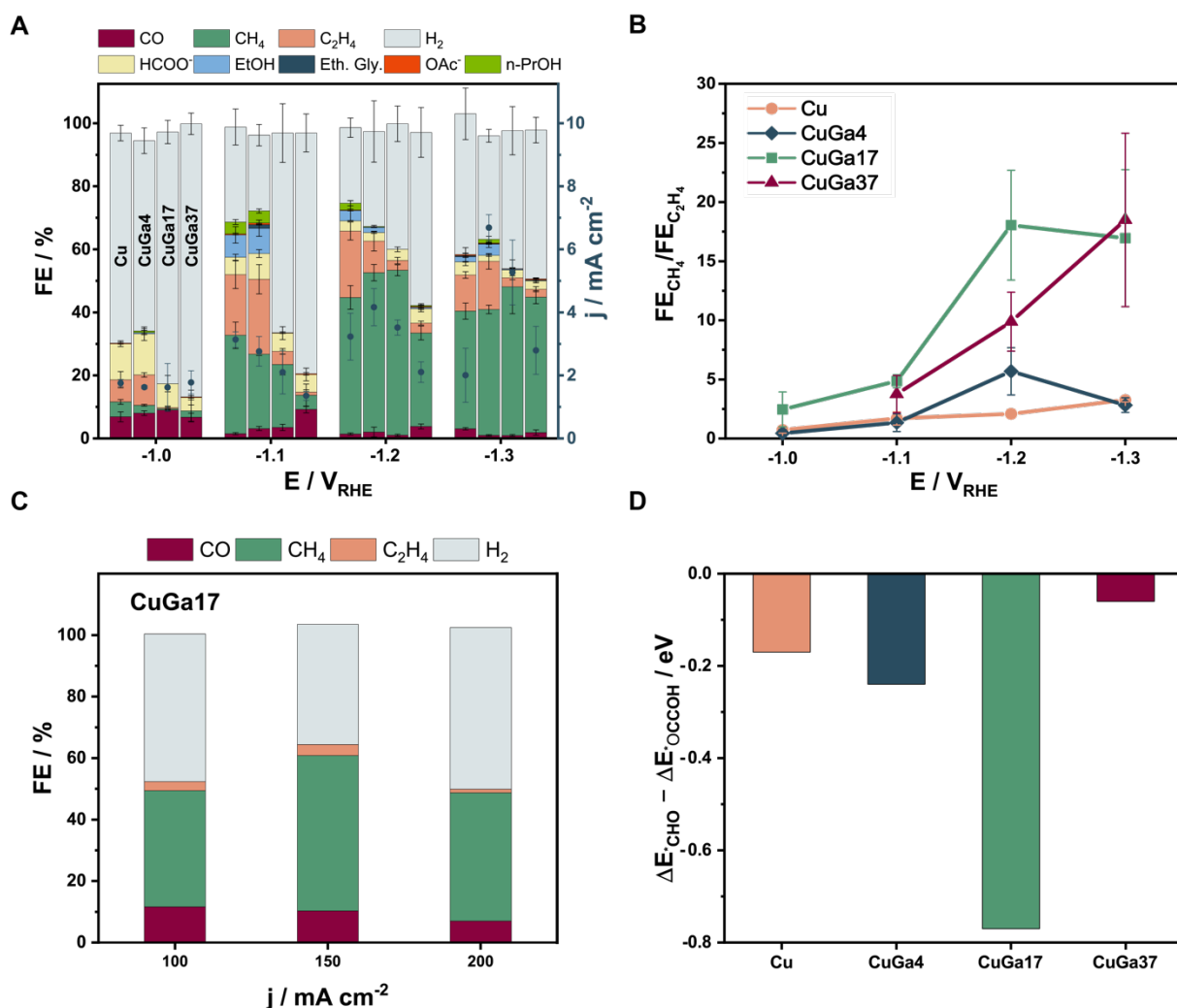


Figure 3.3. Selectivity of the CuGa NPs as CO₂RR electrocatalysts. (A) Average FE (left axis) and geometric current density (right axis) for Cu, CuGa4, CuGa17 and CuGa37 NPs during 45 min CO₂RR in CO₂-saturated 0.1 M KHCO₃ at different applied potentials (the NPs loading was kept constant at 15 μg on glassy carbon with geometric area of 1.33 cm²). (B) Ratio of the FE for CH₄ and C₂H₄ and (C) molar fraction of CH₄ among gaseous CO₂RR over the same potential range, which indicates the CH₄ promotion in the CuGa NPs. (D) Average FE for CuGa17 NPs during 1 h of CO₂RR in CO₂-saturated 1 M KHCO₃ in a gas-fed flow cell at different applied current densities, which indicate that promoted CH₄ selectivity is retained at industrially relevant current densities.

Having assessed the potential-dependent product distribution of the newly synthesized catalysts, we selected -1.2 V_{RHE} as the most representative voltage for stability tests with 4 hours as the initial monitoring time. **Figure 3.4** reports an overview of the obtained results.

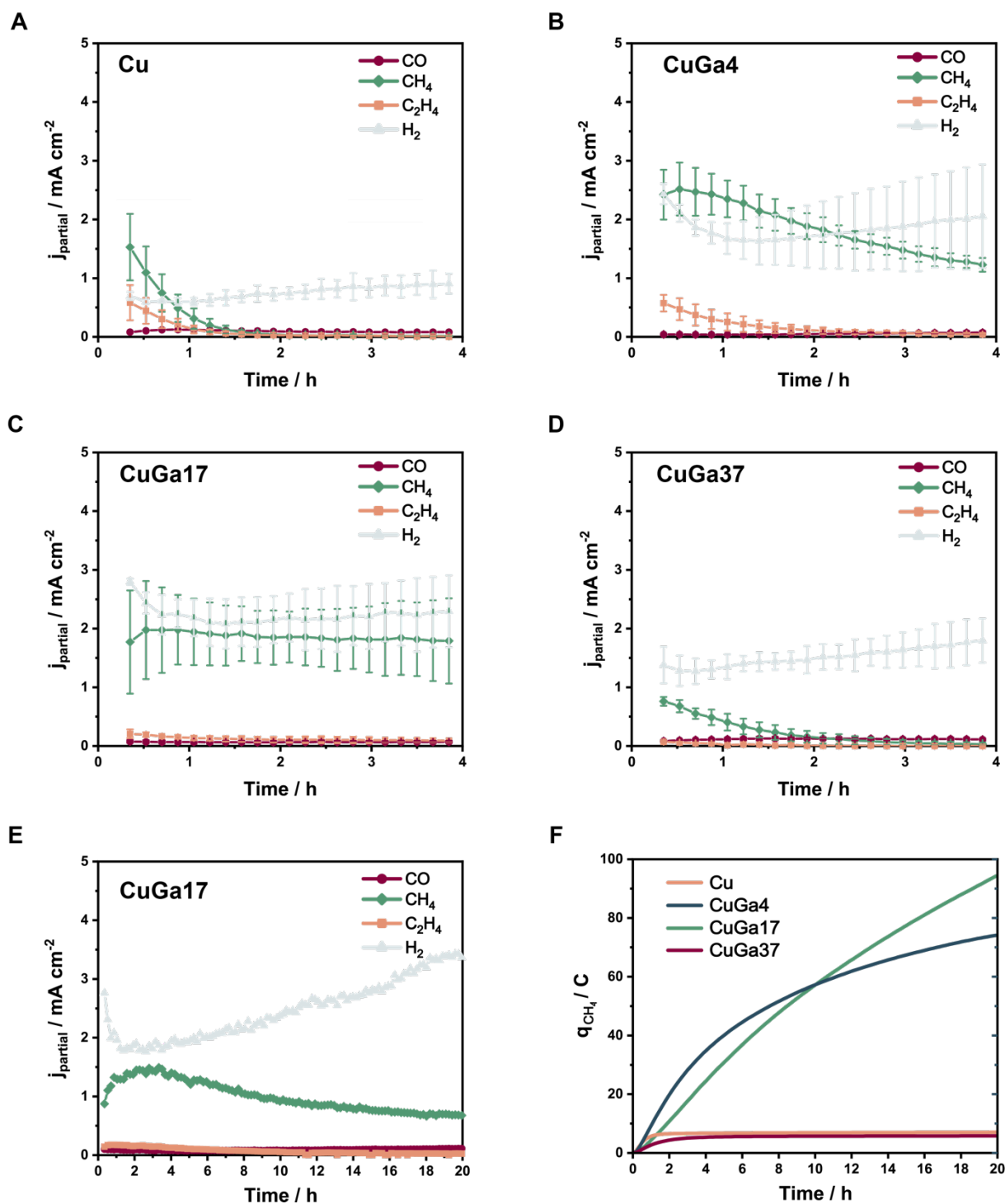


Figure 3.4. CO₂RR performance over time. (A – D) Partial current densities of the main gas products (i.e. H₂, CO, CH₄, C₂H₄) monitored over time for (A) Cu, (B) CuGa4, (C) CuGa17 and (D) CuGa37 NPs during 4 h of CO₂RR at -1.2 V_{RHE} in CO₂-saturated 0.1 M KHCO₃. (E) Partial current densities of H₂, CO, CH₄, C₂H₄ over 20 h CO₂RR at -1.2 V_{RHE} for CuGa17. (F) Accumulated charge consumed towards CH₄ formation for Cu, CuGa4, CuGa17 and CuGa37 NPs during 20 h CO₂RR at -1.2 V_{RHE}.

The performance of the Cu NPs deteriorates within the first 2 hours of electrolysis, during which the partial current densities corresponding to the CO₂RR products drops to zero (**Figure 3.4A**). The addition of Ga clearly improves the CO₂RR current stability. Specifically, CuGa4 significantly stabilizes the CH₄ partial current density with around 50% of initial value being retained after 4 h test (**Figure 3.4B**), which is remarkable considering the small % Ga in the sample. With further Ga addition (CuGa17), the catalyst performance becomes even more stable, with more than 90% of initial CH₄ partial current density retained after 4 h test (**Figure 3.4C**). Strikingly, CuGa37 is less stable than CuGa4 and CuGa17 (**Figure 3.4D**). Longer testing, over 20 h, shows that the CuGa17 still retains half of its initial j_{CH_4} (**Figure 3.4E**), and that its overall CH₄ production over this extended timescale surpasses that of Cu by *ca.* 12 times thanks to the improved stability (**Figure 3.4F**).

3.4 Compositional and structural characterization of the catalysts before and after CO₂RR

To gain more insight into the observed changes in stability, we performed different characterization techniques, including STEM and STEM-EDXS, selected area electron diffraction (SAED) and XPS before and after CO₂RR.

Figure 3.5 and **Figure 3.6** summarize the results obtained from STEM and STEM-EDXS. We characterized the catalysts after 1 h, which is the time when Cu loses most of its activity while all the CuGa samples still maintain theirs to varying degrees, and after 4 hours, which is the time when CuGa4 and CuGa37 undergo significant decrease of current density while CuGa17 still preserves its electrocatalytic performance. In bimetallic catalysts, both morphology and composition play a key role in governing the stability of catalytic performance.^{200,211,212} Thus, the following paragraphs discuss changes in both factors, while keeping in mind that deconvoluting the two is not trivial.

After 1 h of CO₂RR, the morphology of Cu clearly changes, resulting in the formation of NPs with undefined shape (**Figure 3.5**). Inductively coupled plasma – mass spectroscopy (ICP-MS) of electrolyte indicates that there is no significant dissolution of Cu into electrolyte (the Cu signal corresponds to < 1 % of total loading in all samples), which is consistent with previous data correlating the morphological changes to dissolution and redeposition of copper.⁸

On the contrary, all the CuGa NPs maintain their morphology after 1 h of CO₂RR (**Figure 3.5**). Notable differences between the CuGa samples emerge after 4 hours of CO₂RR.

Indeed, the CuGa4 evolves into hollow NPs which resemble the reference Cu NPs after 1 h of operation, the CuGa17 does not show any change in its morphology, while significant surface roughening becomes evident for CuGa37.

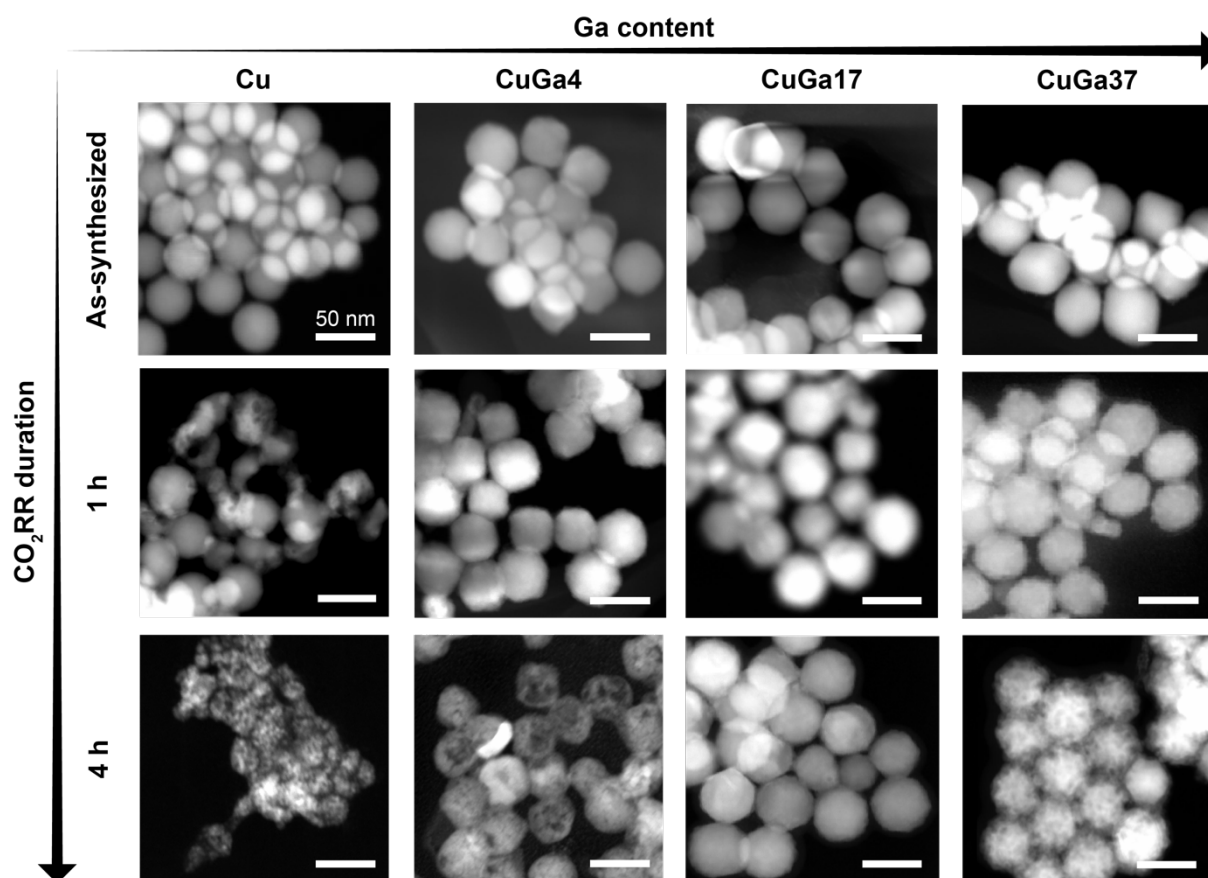


Figure 3.5. Morphological characterization of the NPs after CO₂RR. STEM images of Cu, CuGa4, CuGa17 and CuGa37 NPs in as-synthesized state and after 1 h and 4 h of CO₂RR at -1.2 V_{RHE}. The scale bars are 50 nm. These data highlight a morphological stability of the NPs during CO₂RR according to the following trend CuGa17 > CuGa4 ≥ CuGa37 >> Cu.

We used STEM-EDXS and line scans on single NPs to gain information on eventual changes in composition of the CuGaNP (**Figure 3.6**). The data of the as-synthesized CuGa NPs indicate a homogeneous spatial distribution of the Ga and Cu signal within the NPs core, which is consistent with the XRD data showing alloying of the two metals. Furthermore, the elemental content obtained from EDXS quantification of the entire imaged area, which is indicated on the top of the each image, is consistent with the values from ICP-OES. At the same time, Ga-

rich shells are visible in all samples, most pronounced for the CuGa4 and CuGa17. The oxygen signal suggests an oxidized state of these shells, which can either form during the synthesis or subsequent exposure to air of the samples.

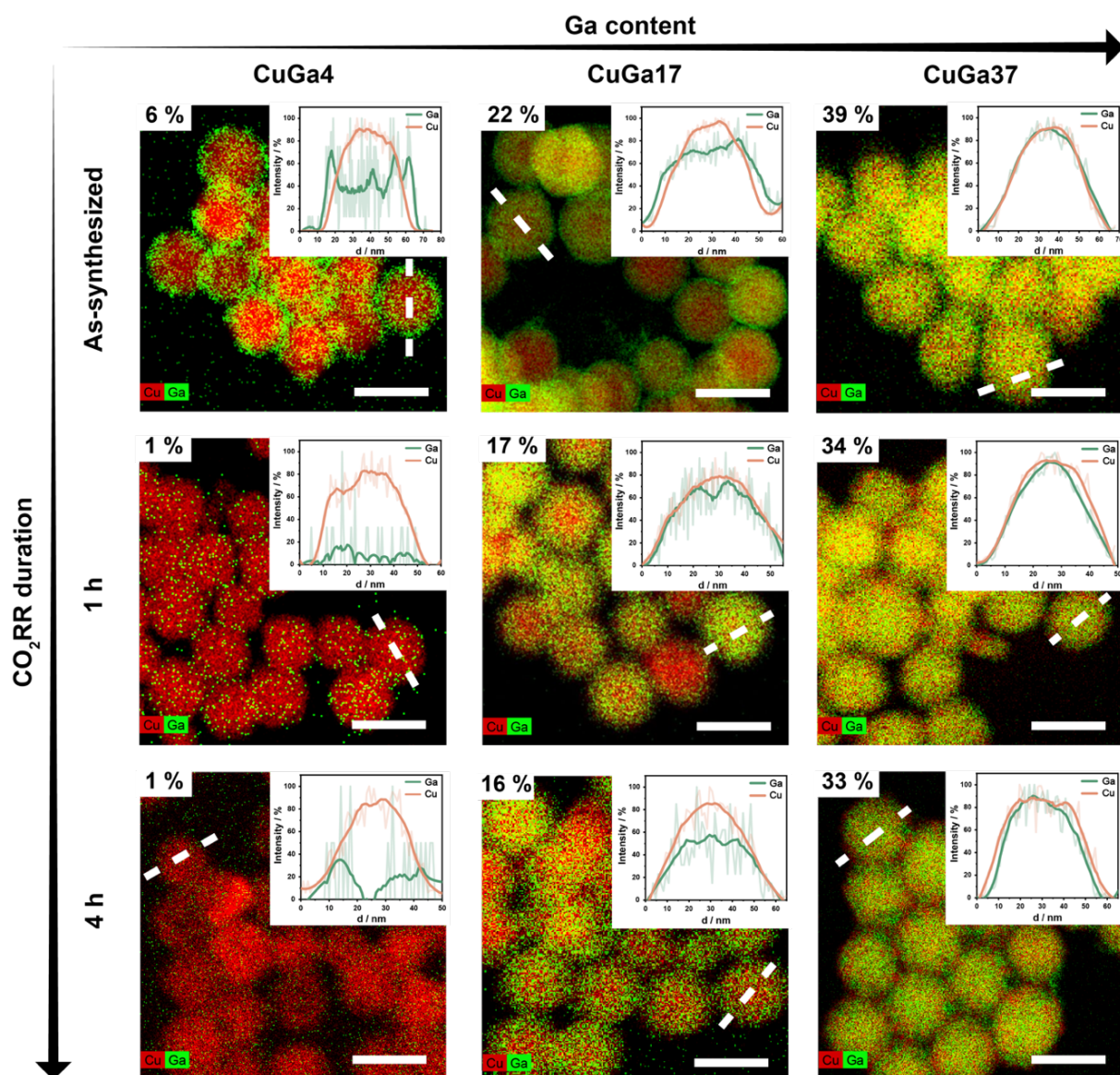


Figure 3.6. Composition and elemental distribution of the NPs after CO₂RR. STEM-EDXS elemental mapping (Cu – red, Ga – green) along with the line profile scan of one representative particle of CuGa4, CuGa17 and CuGa37 NPs in as-synthesized state, after 1 h and 4 h of CO₂RR at -1.2 V_{RHE}. The scale bars are 50 nm. Quantified Ga content is reported on the top-left corner of the images (in at. %).

After 1 h of CO₂RR, the Ga content decreases for all the samples. The most dramatic change in terms of relative at.% occurs for the CuGa4, although the EDX spectrum does confirm that Ga is still present in the sample. However, the absolute loss of Ga, which is around 5 at. % is similar for all the samples. Meanwhile, the STEM-EDXS mapping shows that the Ga-rich shells disappear for CuGa4 and CuGa17 while a slightly Cu-rich surface forms for CuGa37. After 4 hours of CO₂RR, no change in composition occurs. In terms of elemental distribution, additional Cu surface enrichment is observed in the line scans for CuGa37, which correlates well with the features accounting for the surface roughness in the STEM image.

The SAED patterns confirm that the phase of the NPs core, after the 4 h of CO₂RR, remains the same as the as-synthesized samples, namely *fcc* for Cu, CuGa4 and CuGa17 and Cu₉Ga₄-type primitive cubic lattice for CuGa37 (**Figure 3.7A**). CuGa17 NPs preserve their *fcc* alloy structure and their morphology after 20 h of operation as well (**Figure 3.7B**).

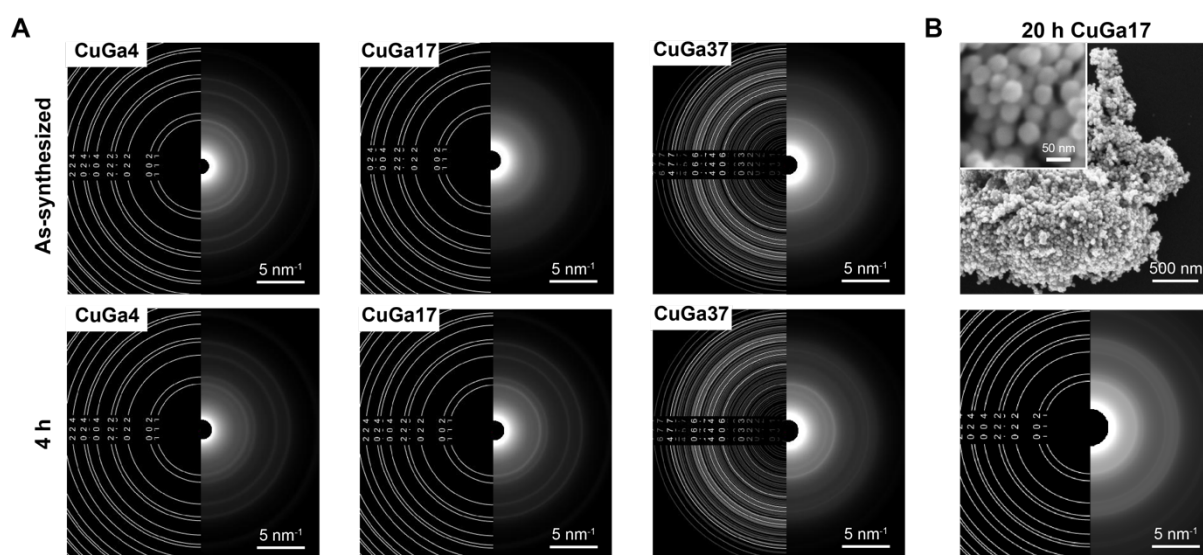


Figure 3.7. Crystallographic and SEM characterization of the NPs after CO₂RR. (A) SAED patterns of CuGa4, CuGa17 and CuGa37 NPs in as-synthesized state and after 4 h electrolysis at -1.2 V_{RHE} in CO₂-saturated 0.1 M KHCO₃. (B) SEM image of as-synthesized CuGa17 NPs, along with SAED patterns and SEM images of CuGa17 NPs after 20 h electrolysis at -1.2 V_{RHE}. The SAED confirms the preservation of the *fcc* alloy structure and the SEM evidence no change in their size and morphology.

XPS was used as complementary characterization technique to gain insight into the surface composition of the as-synthesized CuGa NPs and of those after 4 h of CO₂RR (**Figure 3.8**).

Figure 3.8A reports the XPS data for the as-synthesized CuGa with different Ga content. The first panel shows the Ga 3*d* region, which was fitted with two components according to the literature.^{129,171,181,213} These two components are Ga₂O₃ and metallic Ga at higher and lower binding energy, respectively. While the contribution of the oxide to the signal remains constant across the samples, the contribution of the metallic Ga increases with the Ga content. This observation is consistent with the higher Ga content in the NPs core, which is presumably metallic, considering that the thickness of the Ga oxide shell is roughly 2 nm and the X-Ray penetration depth is up to 6 nm for the Ga 3*d* region. Furthermore, the Ga peaks shift to the higher binding energy as the Ga content increases.

Interestingly, a similar shift is observed for the Cu 2*p* spectra shown in the second panel of **Figure 3.8A**. XPS shifts for Cu 2*p* core level towards higher binding energies compared to the bulk metal have been reported for systems in which Cu particles are in contact with metal oxide supports and explained by the formation of an interfacial charge transfer and/or the formation of new chemical bond between the metal alloys.²¹⁴⁻²¹⁶ Similarly, a convoluted effect arising both from the formation of an oxide/metal interface and from the formation of Cu-Ga alloy can account for these shifts to higher BE, which become more pronounced as the Ga content increases, in the Cu-Ga NPs.

Finally, the Cu LMM Auger region in the third panel of **Figure 3.8A** provides information on the Cu oxidation state. The higher the Ga content is, the more metallic the Cu is, which suggests that the Ga-rich shell in CuGa₄ and CuGa₁₇ acts as protecting layer rendering the CuGa core less prone to oxidation at ambient conditions.

In addition, XPS quantification of the Ga content revealed an almost double amount of Ga content in all samples compared to the values obtained by EDXS quantification (**Figure 3.8A**). Considering that the XPS is a surface technique, these data confirm that the as-synthesized CuGa NPs consist of an alloyed CuGa core with a Ga-rich shell, which forms during the synthesis and oxidizes upon exposure to air and/or the electrolyte, in agreement with the STEM-EDXS data (**Figures 3.6**).

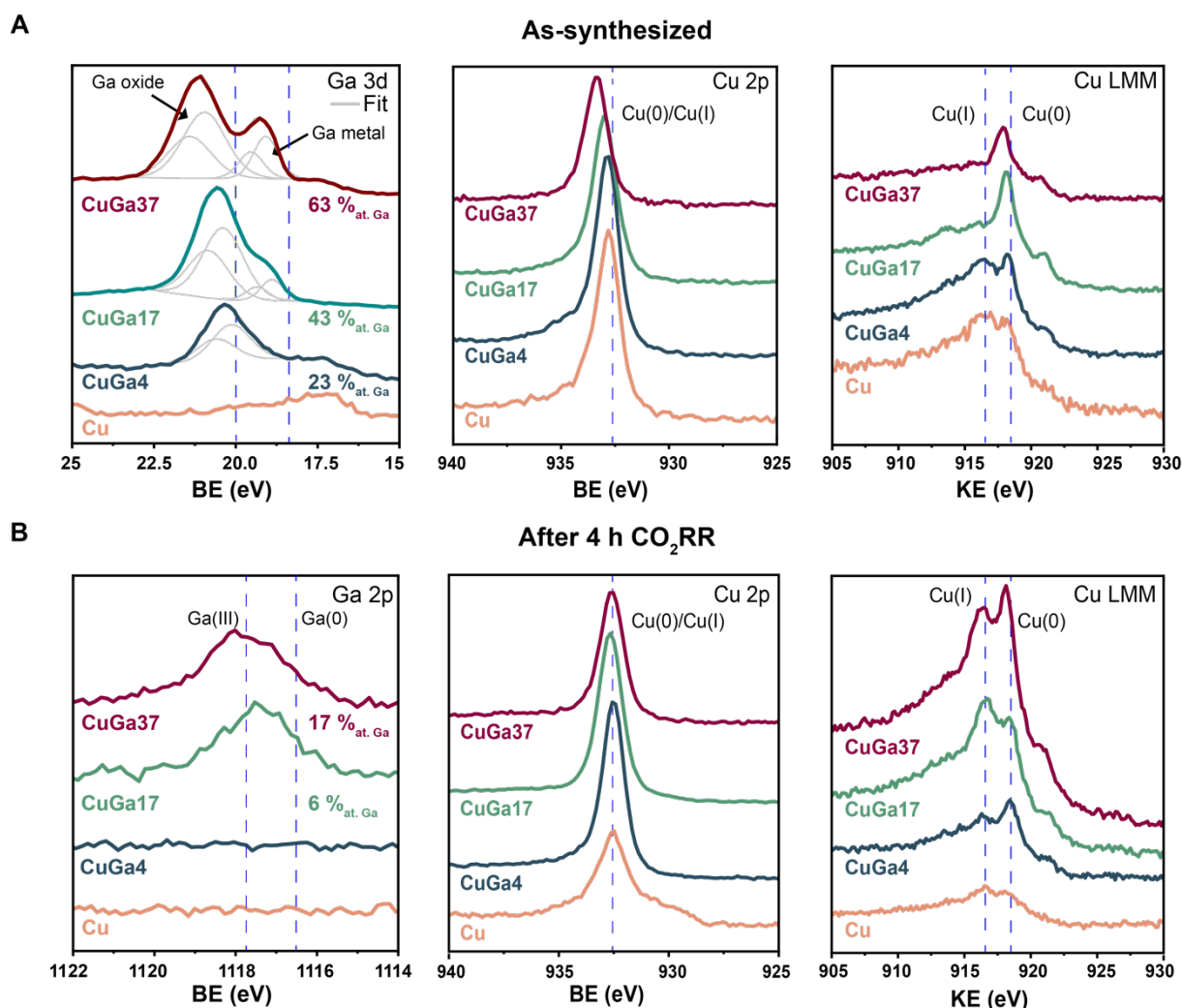


Figure 3.8. Surface analysis of the CuGa NPs before and after CO₂RR. (A) Ga 3d, Cu 2p XPS profiles and Cu LMM Auger spectra for the as-synthesized Cu, CuGa₄, CuGa₁₇ and CuGa₃₇ NPs. (B) Ga 2p, Cu 2p XPS profiles and Cu LMM Auger spectra for the Cu, CuGa₄, CuGa₁₇ and CuGa₃₇ NPs after 4 h of CO₂RR at -1.2 V_{RHE} in CO₂-saturated 0.1 M KHCO₃. Dashed lines indicate the reference Ga 3d_{5/2}, Ga 2p_{3/2}, Cu 2p_{3/2} and Cu LMM peaks.^{217,218}

We also carried out the same XPS analysis on the electrodes after 4 h of CO₂RR, which is reported in **Figure 3.8B**. Please note that Ga 3d could not be used for this purpose, as potassium in the electrolyte deposits on the electrode during CO₂RR and the XPS signal of K 3p overlaps with the one of Ga 3d (washing the samples reduced the K 3p signal but did not remove it). Therefore, Ga 2p was used for the analysis. Because of the reduced penetration depth of the X-Ray in this energy range, only Ga oxide is detected in CuGa₁₇ and CuGa₃₇; the amount of Ga in CuGa₄ is probably below the detection limit. The chemical shift is still present both in the

Ga 2*p* and in the Cu 2*p* post-CO₂RR in the samples with higher amount of Ga, which are CuGa17 and CuGa37. However, the magnitude of the shift to higher binding energy is much smaller compared to that observed in the as-synthesized samples, which can be attributed to the fact that interfacial charge transfer effects due to the Ga oxide shell are no longer present, and only the shift contribution due to Cu-Ga alloying remains. Furthermore, the Cu LMM Auger peaks indicate that the oxidized Cu(I) is now present on the surface of all samples. The surface content of Ga is twice lower than determined by STEM-EDXS (**Figures 3.6**). Altogether, the post-CO₂RR XPS supports the hypothesis that the Ga-rich shells are removed during CO₂RR, Cu gets exposed at the surface, and the remaining Ga is bound to Cu in the bimetallic core.

3.5 *Operando* X-Ray absorption characterization

To gather complementary insight to those provided by the *ex situ* characterization, we performed *operando* XAS and monitored the catalyst state during CO₂RR at -1.2 V_{RHE}. **Figures 3.9 – 3.11** and **Table 3.1** report the results for the Cu and CuGa NPs during CO₂RR .

We note that the Ga K-edge signal for CuGa4 was too weak and noisy to yield any viable information. However, the data were sufficient to confirm that Ga is present on the electrode, supporting STEM-EDXS and XPS observations that Ga persists in this sample under operation although at very low content (*ca.* 1 at. %). The Ga K-edge spectra of both CuGa17 and CuGa37 are characterized by a rising edge at *ca.* 10368 eV both at ocp and during CO₂RR at -1.2 V_{RHE} (**Figures 3.9A,B**), which indicate the presence of mostly metallic Ga. The application of the cathodic voltage slightly reduces the intensity of the Ga signal, in agreement with the observed loss of Ga in the STEM-EDXS and XPS data. The Ga signal remains then stable during the next 3 h of CO₂RR at -1.2 V_{RHE} (**Figure 3.10**). Because Ga is crystallized in the *fcc* (CuGa17) and Cu₉Ga₄-type (CuGa37) lattices for which there are no Ga and Ga₂O₃ standards, linear combination analysis (LCA) for the quantification of the metallic and oxidized components in the Ga K-edge was not applicable. However, the Ga K-edge XANES shape profiles qualitatively indicate that a minor fraction of Ga might still be oxidized under operation because of the features at *ca.* 10377 eV, most evident for CuGa17, which persist at -1.2 V_{RHE}.

The position and the shape profile of the Cu K-edge indicate that the Cu is mostly metallic at ocp and under cathodic potential (**Figure 3.9C,D**). LCA of the Cu XANES profiles provides the fraction of Cu₂O and Cu at ocp and at -1.2V_{RHE} during CO₂RR in the different samples (**Figures 3.9E**). The LCA at ocp indicates that the fraction of oxidic copper is significant for pure Cu NPs (~25 %) and for CuGa4 NPs (~35 %), while it drops substantially for CuGa17.

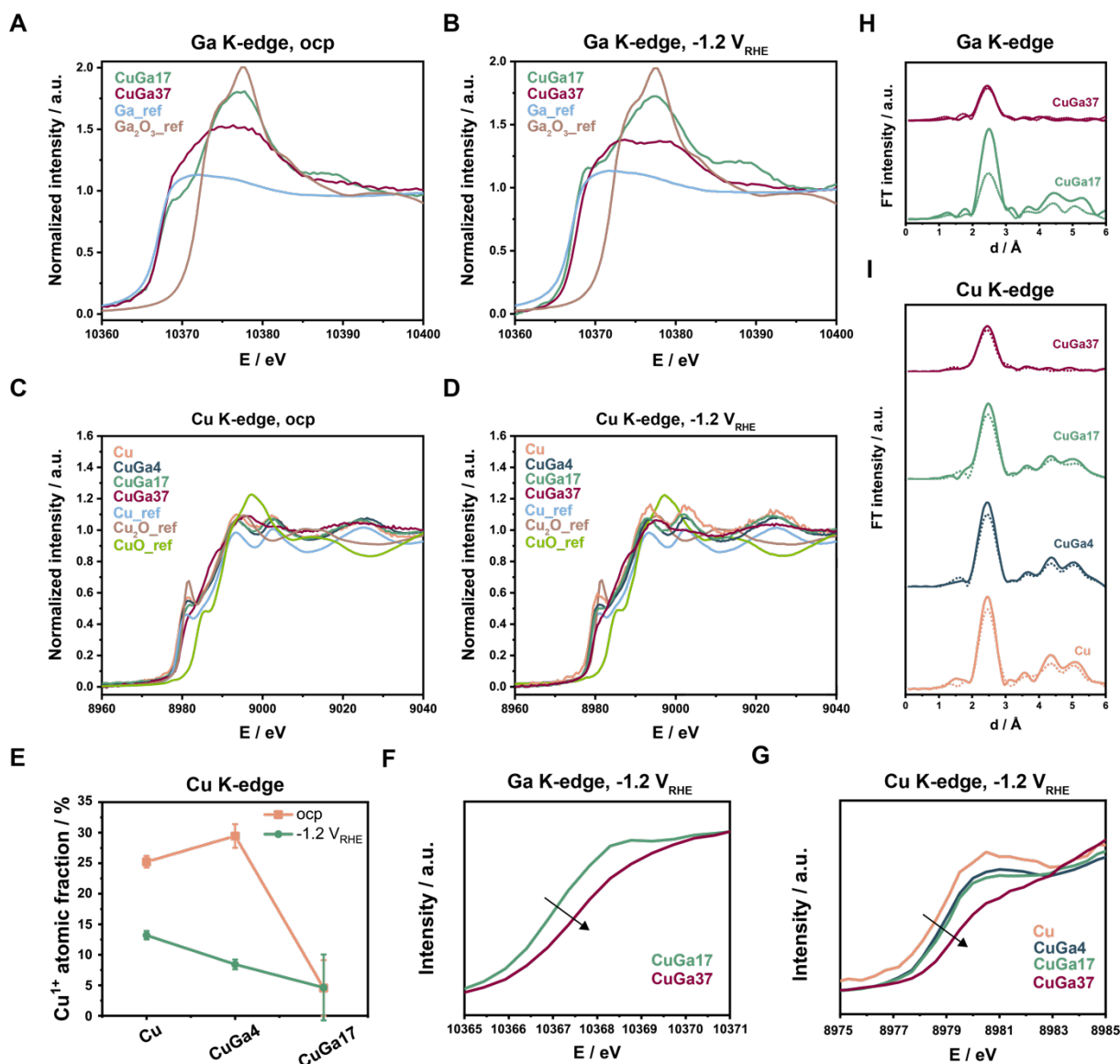


Figure 3.9. Operando X-Ray absorption spectroscopy at ocp and during CO₂RR. (A, B) XANES of Ga K-edge for CuGa17, CuGa37 NPs and the standard samples (A) at ocp and (B) *operando* at -1.2 V_{RHE}. (C, D) XANES of Cu K-edge for Cu, CuGa4, CuGa17 and CuGa37 NPs and the standard samples (C) at ocp and (D) *operando* at -1.2 V_{RHE}. (E) Atomic fraction of Cu¹⁺ obtained from LCA for Cu, CuGa4 and CuGa17 NPs at ocp and *operando* at -1.2 V_{RHE}. (F) Zoomed-in XANES of Ga K-edge for CuGa17 and CuGa37 NPs *operando* at -1.2 V_{RHE}. (G) Zoomed-in XANES of Cu K-edge for Cu, CuGa4, CuGa17 and CuGa37 NPs *operando* at -1.2 V_{RHE}. (H) EXAFS of the Ga shell for CuGa17 and CuGa37 NP at ocp (dot line) and *operando* at -1.2 V_{RHE} (solid line). (I) EXAFS of the Cu shell for Cu, CuGa4, CuGa17 and CuGa37 NP at ocp (dot line) and *operando* at -1.2 V_{RHE} (solid line). The bulk standard samples were measured *ex situ*. All *operando* measurements were run for 3 h of CO₂RR.

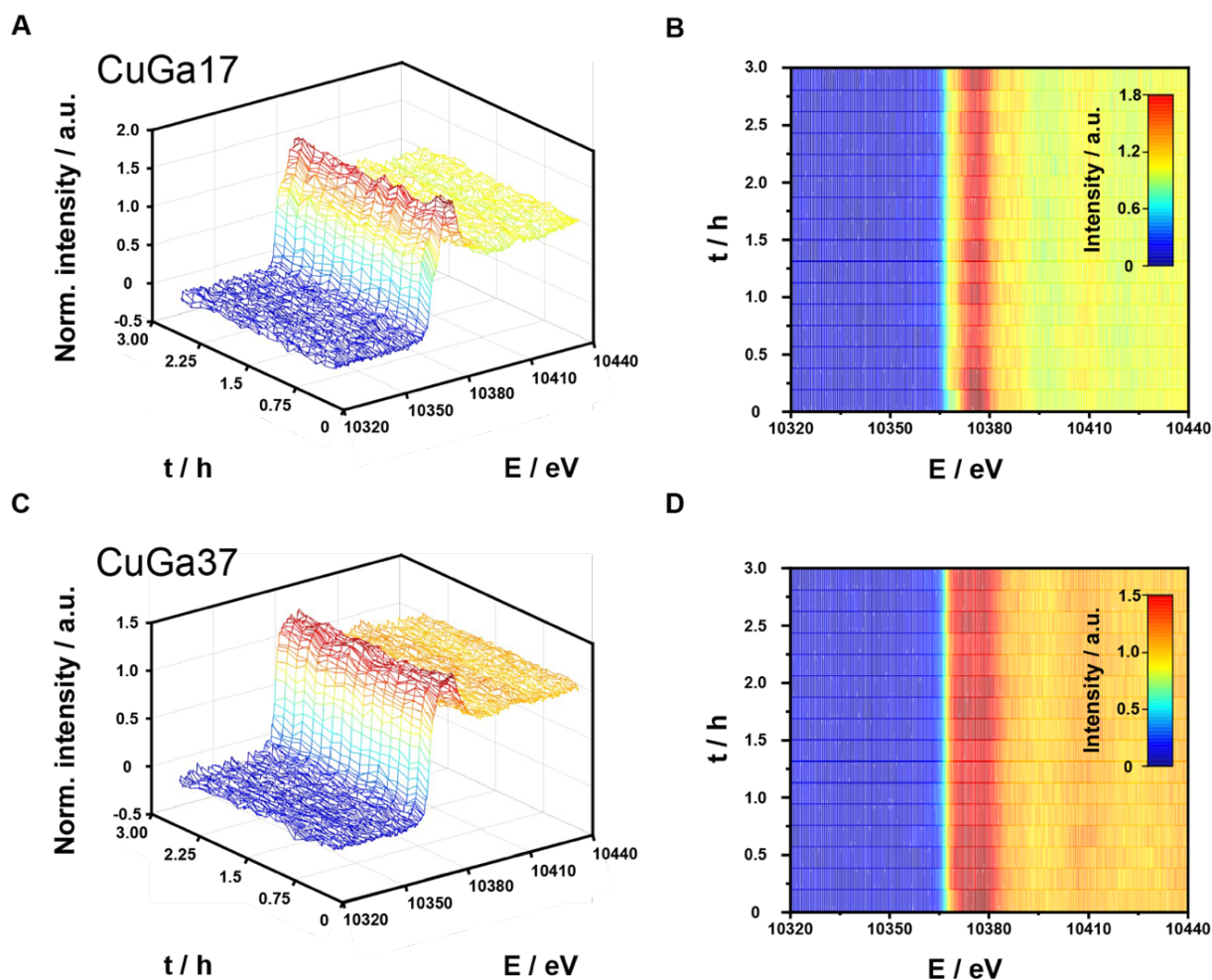


Figure 3.10. Operando XANES evolution of Ga K-edge during CO₂RR. (A – D) Ga K-edge *operando* XANES spectra during 3 h CO₂RR at -1.2 V_{RHE} in CO₂-saturated 0.1 M KHCO₃ for (A, B) CuGa17 and (C, D) CuGa37 NPs: (A, C) 3D maps in time – energy – normalized intensity coordinates and (B, D) corresponding 2D maps in time – energy coordinates. Averaging was performed over every five consecutive scans.

As the Cu₂O content obtained by LCA fitting for CuGa17 is not statistically different from zero, the LCA analysis suggests that surface oxidation is suppressed at ocp for this sample. LCA is not applicable for Cu in CuGa37, as there are no appropriate Cu and Cu₂O standards for the Cu₉Ga₄-type structure. Yet, the K-edge position qualitatively suggests that Cu is purely metallic. Altogether, the LCA analysis at ocp suggests that the Ga-rich samples protect copper from oxidizing, consistent with conclusions made from Auger spectroscopy carried out on the as-synthesized sample (**Figure 3.8A**). The reduction of the oxidized Cu₂O surface formed at ocp is very rapid upon the application of the cathodic voltage, consistently with the previous reports.^{48,219} No further change is observed during 3 h of CO₂RR at -1.2 V_{RHE} (**Figure 3.11**).

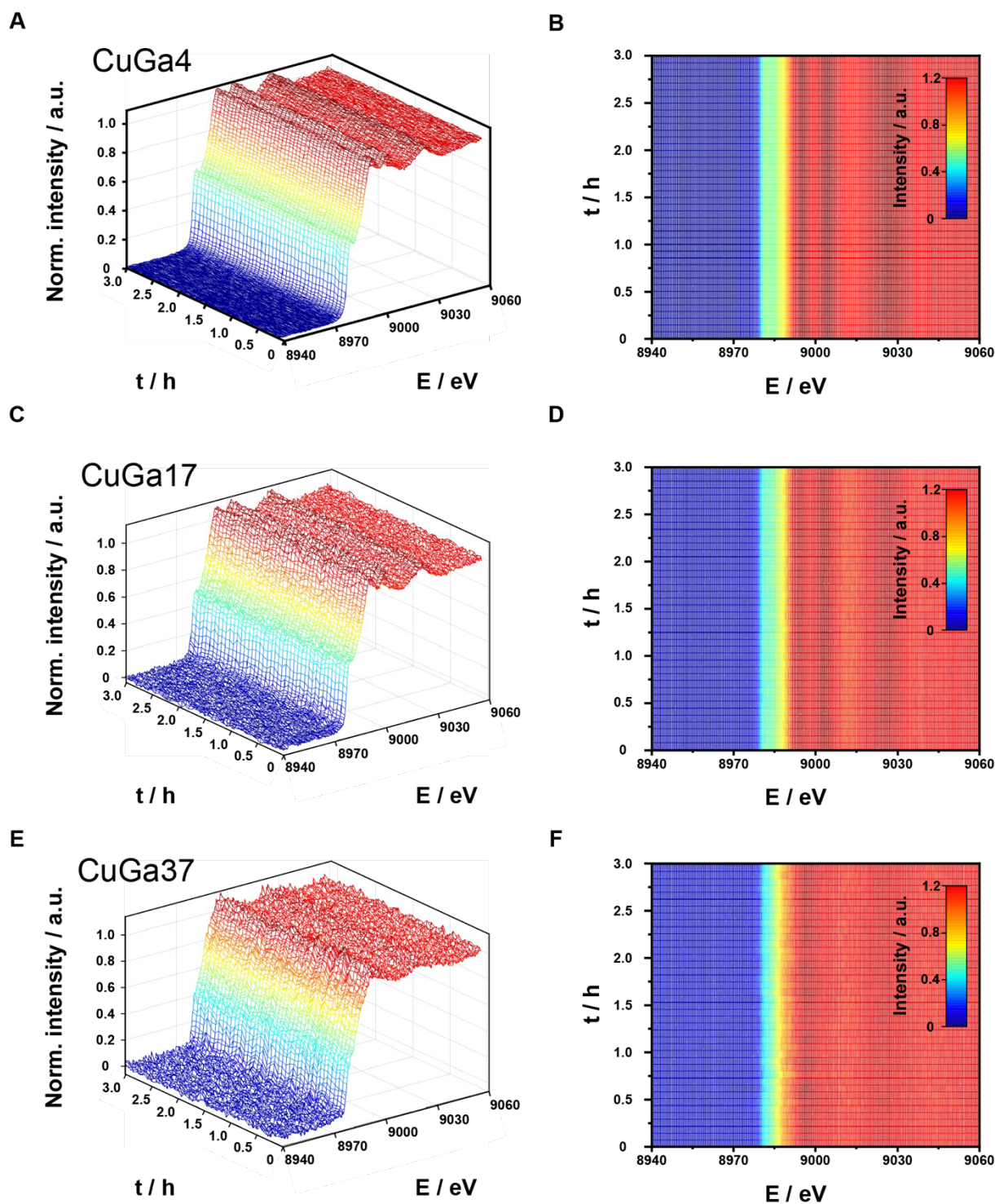


Figure 3.11. *Operando* XANES evolution of Ga K-edge during CO₂RR. Cu K-edge *operando* XANES spectra during 3 h CO₂RR at -1.2 V_{RHE} in CO₂-saturated 0.1 M KHCO₃ for (A, B) CuGa₄, (C, D) CuGa₁₇ and (E, F) CuGa₃₇ NPs: (A, C, E) 3D maps in time – energy – normalized intensity coordinates and (B, D, F) corresponding 2D maps in time – energy coordinates. Averaging was performed over every two consecutive scans.

Finally, one interesting observation in the XANES data is that the Cu and Ga K-edge positions follow a composition-dependent trend: as the Ga content in the CuGa NPs increases, the Cu and Ga K-edge absorption edges shift to higher energies (**Figures 3.9F,G**). As this shift is not accompanied by the rise of Cu pre-edge feature at *ca.* 8981 eV, which is characteristic of Cu(I) presence, this increase cannot be attributed to the Cu oxidation upon increase in Ga content in the alloy. Instead, it may indicate an increasing binding energy of both metals in the lattice, which agrees with the observation made in the XPS data.

We gained further structural insight from the EXAFS spectra for Cu and Ga (**Figures 3.9H,I, Table 3.1**). The degree of structural order, which is one of the factors contributing to the intensity of the signal, follows a composition-dependent trend for both metals and decreases as the Ga content increases. When the cathodic voltage of -1.2 V_{RHE} is applied, the intensity of the Fourier transform (FT) signal increases in all samples, which indicates that some form of structural change accompanies the CO₂RR in all cases. The extent of absolute change in EXAFS intensity is highest (when viewed from the Cu K-edge) for Cu NPs and follows the trend CuGa17 \geq CuGa4 > CuGa37 for the CuGa NPs when looking at both the Cu and the Ga K-edge EXAFS data. As the coordination numbers and disorder are highly correlated, the source of these changes is best captured by the correlation maps, that relate the Debye-Waller Factor (DWF, Å²) with either the first shell *fcc* interatomic distance (*d*, Å) or the first shell *fcc* coordination number (N1). **Table 3.1** reports the most probable range of values for Cu and Ga extracted from the correlation maps, derived from explicit analysis using EXCURV.³⁷ The most pronounced changes are observed in the pure Cu NPs, from the perspective of the Cu K-edge, and in the CuGa17 NPs, with regards to the Ga K-edge. In the case of Cu NPs, such changes might be linked to the dramatic reconstruction of the NPs (**Figure 3.5**) and to the reduction of any copper surface oxide initially present leading to a higher net order in the reduced copper phase that remains post CO₂RR. However, as no major change in size and/or morphology occurs for the CuGa NPs (**Figure 3.5**), we attribute the change in the values of DWF, *d* and N1 exclusively to an increase in the overall (static and dynamic) order of the bulk of the crystallites and, in the case of CuGa17, the formation of an alloy with more uniform Ga distribution within the NPs under the operation conditions.

Interestingly, the *d* values calculated for Cu and Ga converge towards each other in CuGa17 but not in CuGa37 during CO₂RR. This observation may serve as an indication that Ga tends to rearrange and occupy the crystal sites allowing more uniform distribution of the elements within one NPs in CuGa17 NPs; instead, Cu and Ga are less uniformly distributed in CuGa37 during CO₂RR, in agreement with the surface spatial segregation observed in the STEM-EDXS

images (**Figure 3.5**). This unique behavior of the CuGa37 might be related to its crystal structure, which is distorted and distinctly different from the Cu *fcc*. We hypothesize that such structure might reconstruct more easily than the *fcc* lattice, which is confirmed by molecular dynamics simulations (**Figure 3.13C,D**).

Table 3.1. Structural data extracted from analysis of Cu K-edge and Ga K-edge EXAFS at ocp and *operando* at -1.2 V_{RHE}.

Sample	N _{1Cu}	N _{1Ga}	d _{Cu} , Å	d _{Ga} , Å	DWF _{Cu} (2σ ²), Å ²	DWF _{Ga} (2σ ²), Å ²
Cu ocp	8.5-11		2.537		0.012-0.017	
Cu -1.2 V _{RHE}	10-12		2.519		0.010-0.015	
CuGa4 ocp	8-12		2.533		0.015-0.020	
CuGa4 -1.2 V _{RHE}	8-12		2.536		0.014-0.018	
CuGa17 ocp	8-12	9.5-12	2.556	2.574	0.016-0.022	0.016-0.022
CuGa17 -1.2 V _{RHE}	8-12	11-12	2.562	2.567	0.014-0.020	0.007-0.012
CuGa37 ocp	6-10	6-8	2.535	2.523	0.018-0.027	0.012-0.020
CuGa37 -1.2 V _{RHE}	6-10	7-10	2.542	2.529	0.017-0.024	0.014-0.022

3.6 Mechanism of stability enhancement in CuGa NPs

With the evidence provided by STEM-EDXS, XPS and *operando* XAS, we rationalize the observations made in this study as it follows and report a summary in **Figure 3.12**.

First, the pristine 40 nm Cu NPs, which are the reference sample, reconstruct into hollow structures and smaller particles are observed on the electrode (**Figure 3.5**), which is consistent with previous studies on particles with comparable size.^{45,46,48} These changes are driven by the dissolution/reprecipitation of Cu surface oxide forming at ocp and continue during CO₂RR following the same mechanism via soluble transient species.^{45,46,48} These morphological changes result into the degradation of the catalytic performance with the CO₂RR current density dropping to zero after *ca.* 2 hours (**Figure 3.4A**).

When it comes to CuGa alloy NPs, STEM-EDXS images evidence that morphological changes are significantly suppressed by the addition of Ga (**Figures 3.5, 3.6, 3.7**).

Concomitantly, the CO₂RR current is much more stable over time following a trend of CuGa17 > CuGa4 > CuGa37 (Figure 3.4B-D). XPS and operando XAS data indicate that Ga suppresses Cu oxidation at ocp (Figures 3.8, 3.9). We further confirm this observation with ICP-MS of the electrolyte after 5 min immersion of the electrodes, which proves that less Cu dissolves at ocp in the case of CuGa17 and CuGa37 compared to the pristine Cu NPs (Table 3.2).

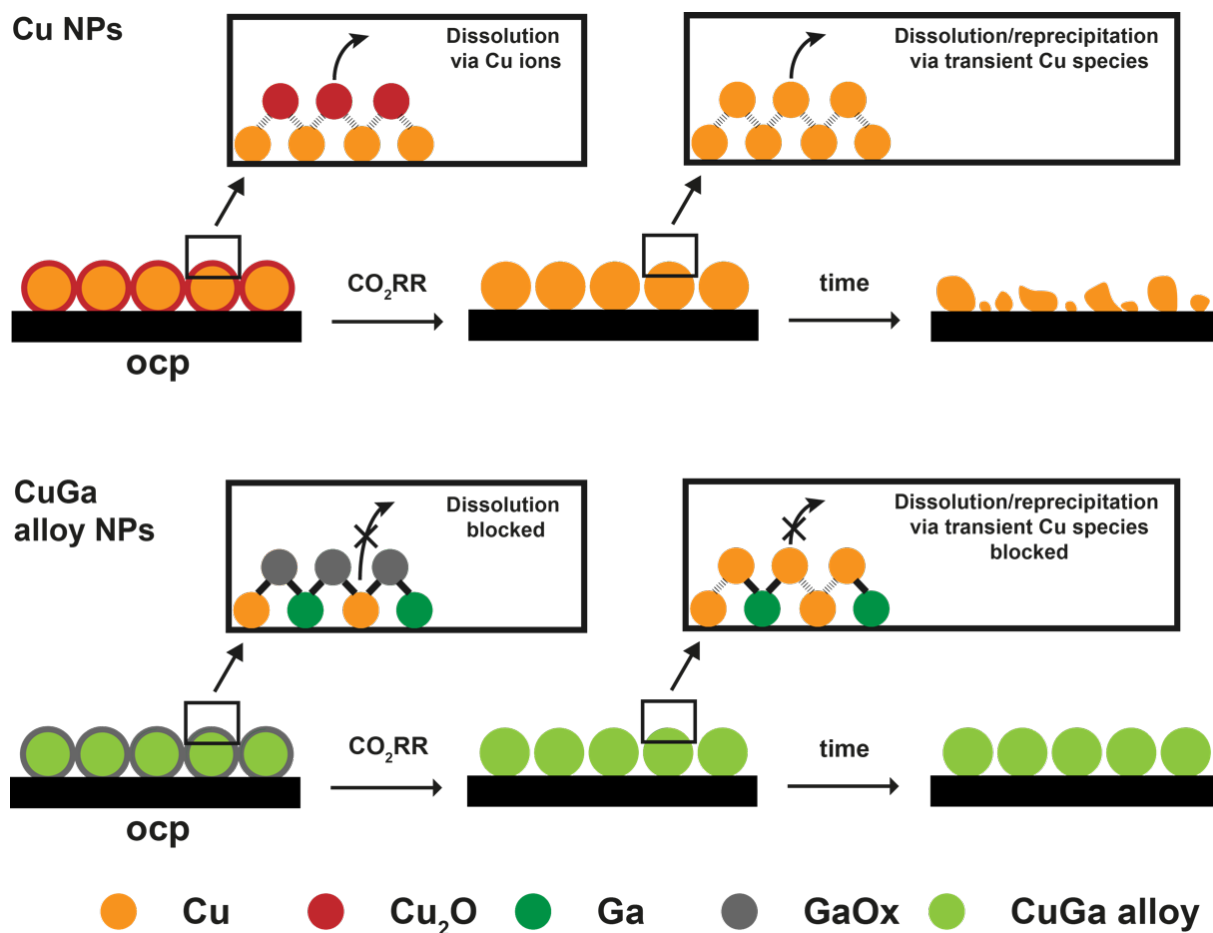


Figure 3.12. CO₂RR stabilization mechanism in CuGa alloy NPs compared to Cu NPs.

Table 3.2. ICP-MS measurements of Cu and CuGa NP electrodes after 5 min immersion in CO₂-saturated 0.1 M KHCO₃ at ocp.

Sample name	Ga, ng/ml	Cu, ng/ml
Cu	-	45
CuGa4	25	47
CuGa17	86	19
CuGa37	163	-

Additionally, XPS and *operando* XAS point to significant electronic interactions between Ga and Cu which increase the electron binding energies of both elements within the CuGa NPs. This observation suggests that the alloying lowers the system energy and makes the bond stronger, which agrees well with the fact that the Cu – Ga bond energy (216 kJ/mol) is significantly greater than Cu – Cu (201 kJ/mol) or Ga – Ga (106 kJ/mol).²⁰²

The lower electronegativity of Ga indicate that electron density might shift from Ga towards Cu atoms.²⁰³ Bader charge calculations for the CuGa alloys propose the same outcome, with higher Ga content resulting in larger charge localized on Cu atoms (**Figure 3.13A,B**). Actually, the presence of an electron rich Cu correlates well with CH₄ evolution, as recent literature has suggested the presence of an electron poor Cu^{δ+} to be critical to the promotion of the C-C coupling.^{220–222} Overall, the more electron rich Cu and stronger bonds within the alloys compared to the pristine Cu NPs hinder Cu oxidation, and thus dissolution, at ocp and the subsequent reconstruction of the NPs during operation via dissolution mediated by transient soluble intermediates. As for the stability trend observed within the CuGa samples, we should consider that CuGa4 has very little Ga amount within the alloy (*ca.* 1 at.% during operation), so the performance loss is slower but eventually takes place. CuGa37 has a structure which is intrinsically more distorted and prone to reconstruction (**Figure 3.13C,D**).^{207,208} Eventually, Cu is re-exposed on the surface (**Figure 3.6**), which might explain the faster performance degradation compared to the CuGa4 and CuGa17. Considering all the factors coming into play, CuGa17 emerges as the most efficient in preserving the CO₂RR performance.

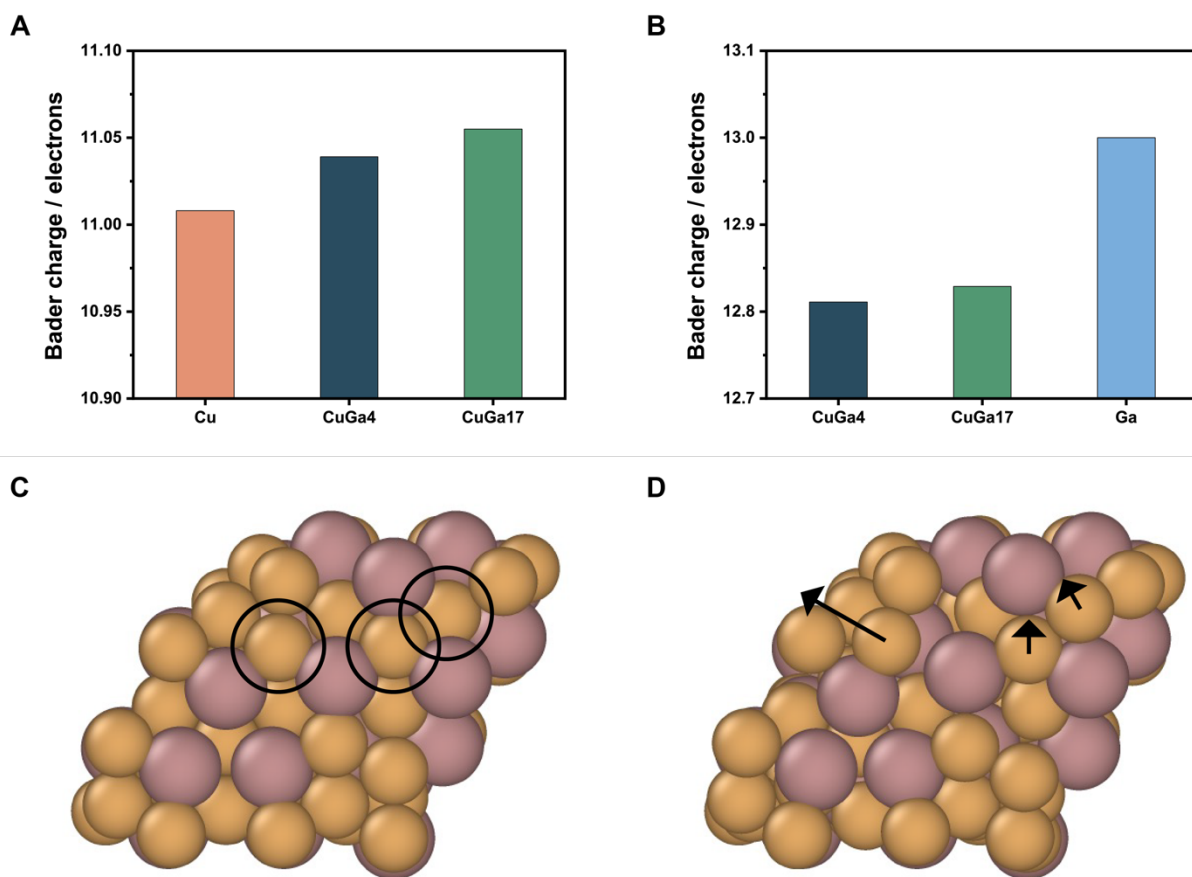


Figure 3.13. Bader charge calculation and molecular dynamics simulation results for Cu and CuGa NPs. (A,B) Bader charge calculation results for (A) Cu atoms and (B) Ga atoms in Cu and CuGa alloys. Expected values for the Bader charge of pure Cu and Ga based on the Periodic Table are 11 and 13 electrons, respectively. To avoid misrepresentation, CuGa37 was not considered to keep only the *fcc* structures, where all crystal lattice positions are equivalent to each other. (C,D) Molecular dynamics simulations representing the atomic arrangement for the CuGa37 surface at (C) steady conditions and (D) after 1 ps of dynamics at 900 K. The Cu atoms which appear on the surface are marked by the circles, and the arrows indicate the displacement direction. Under the same simulations conditions, Cu, CuGa4 and CuGa17 do not undergo changes. Notably, the reconstruction results in Cu atoms popping on the surface, which comes in line with STEM-EDXS line scan after 4 h of CO₂RR (**Figure 3.6**).

3.7 Conclusions

We have demonstrated that alloying Ga into Cu greatly enhance the stability of the NPs under the reducing conditions of CO₂RR. Compared to the parent Cu NPs, which deactivate rapidly (< 2 h), the addition of Ga results in NPs that do not degrade over extended period of

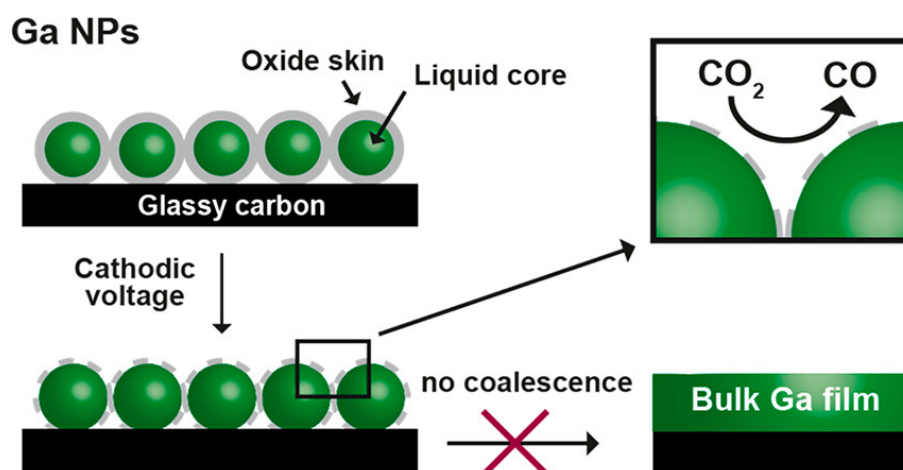
time (up to 20 h). Using a variety of experimental (*ex situ* and *operando*) and theoretical tools we have constructed a framework to rationalize this observation based on the current knowledge on the reconstruction mechanism of Cu NPs during CO₂RR.

We believe that this work can inspire further development of alloyed Cu-based CO₂RR nanocatalysts which are inherently stable during CO₂RR or under other reducing reaction environments. We envision that the metals which have higher oxophilicity and strong M – Cu bonding energies (e.g., early 3*d* metals, e.g. Sc, Ti, and *p*-group metals, e.g. Al, In, Bi) to have similar mechanism of hindering Cu reconstruction while driving CO₂RR towards different products of interest and, in general, generating more stable NPs.

Chapter 4

The Native Oxide Skin of Liquid Metal Ga Nanoparticles Prevents Their Rapid Coalescence during Electrocatalysis

The content of this Chapter is based on published work with permission from the journal: *J. Am. Chem. Soc.* **2022**, *44*, 22, 10053: <https://pubs.acs.org/doi/full/10.1021/jacs.2c03698>. Copyright 2022 American Chemical Society.



Abstract: Liquid metals (LMs) have been used in electrochemistry since the 19th century, but it is only recently that they have emerged as electrocatalysts with unique properties, such as inherent resistance to coke-poisoning, which derives from the dynamic nature of their surface. The use of LM nanoparticles (NPs) as electrocatalysts is highly desirable to enhance any surface-related phenomena. However, LM NPs are expected to rapidly coalesce, similarly to liquid drops, which makes their implementation in electrocatalysis hard to envision. Herein, we demonstrate that liquid Ga NPs (18 nm, 26 nm, 39 nm) drive the electrochemical CO₂ reduction reaction (CO₂RR) while remaining well-separated from each other. CO is generated with a maximum faradaic efficiency of around 30 % at -0.7 V_{RHE}, which is close to that of bulk Ga. The combination of electrochemical, microscopic and spectroscopic techniques, including *operando* X-Ray absorption, indicates that the native oxide skin of the Ga NPs is still present

during CO₂RR and provides a barrier to coalescence during operation. This discovery provides an avenue for future development of Ga-based LM NPs as a new class of electrocatalysts.

Authors: **Valery Okatenko**, Laia Castilla-Amorós, Dragos Constantin Stoian, Jan Vávra, Anna Loiudice, Raffaella Buonsanti.

Contribution: Performed all electrochemical studies, bright-field TEM and SEM imaging, image statistical analyses and supplementary calculations, *operando* XAS measurements, FTIR measurements, Ga microparticles synthesis, and wrote the manuscript with contributions from all authors.

4.1 Introduction

As introduced in Chapter 1, liquid metals (LMs) are unique materials which combine the low viscosity and good fluidity of liquids with the high thermal and electrical conductivity of metals.^{69–74,114} Recently, the field of LMs has undergone a true renaissance, with research largely centered on Ga and its alloys due to their low toxicity and melting point.^{69–72} These materials have also emerged as a new class of (electro)catalysts wherein the highly dynamic liquid surface offers greater flexibility compared to solid catalysts.^{74,87,95,101–108}

Despite these exciting opportunities in catalysis, the aforementioned studies are mostly based on bulk LMs.^{74,95,101–107} NPs are highly beneficial in heterogeneous catalysis as their high surface area maximizes the number of active sites per mass of material, and nanoscale effects, which improve activity or selectivity, can also emerge.^{37,38} At the same time, NPs catalysts tend to sinter, which requires the development of protection schemes, such as oxide coatings.^{110,111} Because of their fluidity, LM NPs are expected to coalesce even more rapidly compared to solid NPs, which poses doubts regarding their utilization as catalysts.

One unique feature of Ga-based LMs is the presence of a native oxide skin surrounding their liquid metal core which regulates the surface properties of the LMs.^{69–74,114} If stable under reaction conditions, the native oxide will also play a crucial role in catalysis, especially when moving from bulk to NPs.^{69–74,138,139} For example, in the context of photocatalysis, studies show that it contributes to charge separation as a semiconducting material.^{138,139} More generally, it may possess catalytic activity on its own or regulate the access of reactants to the liquid core

while preventing the NPs coalescence. However, very little attention has been given to the native oxide skin in the context of catalysis.^{69–74}

In this work, we study Ga NPs as catalysts for the electrochemical CO₂ reduction (CO₂RR). While it does not possess exceptional selectivity compared to other single metals (e.g. Au and Ag), Ga can convert CO₂ to CO.^{112,113} Furthermore, Ga-containing metals have been demonstrated to produce different products.^{104,105,108} We show that the Ga NPs retain their size during CO₂RR. This finding is opposite to the intuitive expectation that liquid particles would coalesce into a larger drop when placed close to each other while applying the highly cathodic potential needed for CO₂RR, which is supposed to remove the native oxide skin. The combination of analytical electrochemistry, electron microscopy and *operando* X-Ray absorption spectroscopy reveals the unique behavior of the oxide skin which accounts for the observed resistance towards coalescence of liquid Ga NPs during CO₂RR.

4.2 Materials synthesis and characterization

Ga NPs were synthesized by means of colloidal chemistry, following a previously reported protocol.^{161,162,181} This wet chemistry approach provides the uniform size distribution which is essential when investigating eventual size and morphology changes of the catalysts during operation. **Figure 4.1A** reports a representative transmission electron microscopy (TEM) image illustrating the uniformity of the Ga NPs which possess a diameter of 26 nm with the particles size distribution less than 10 %. Scanning transmission electron microscopy (STEM) imaging (**Figure 4.1B**) along with energy dispersive X-Ray spectroscopy (EDXS) elemental mapping of O and Ga and the line profile over one Ga NPs (**Figure 4.1C-E**) evidence the presence of a native oxide skin around 2.6 nm thick on the Ga NPs, which is consistent with previous studies.^{161,162,181}

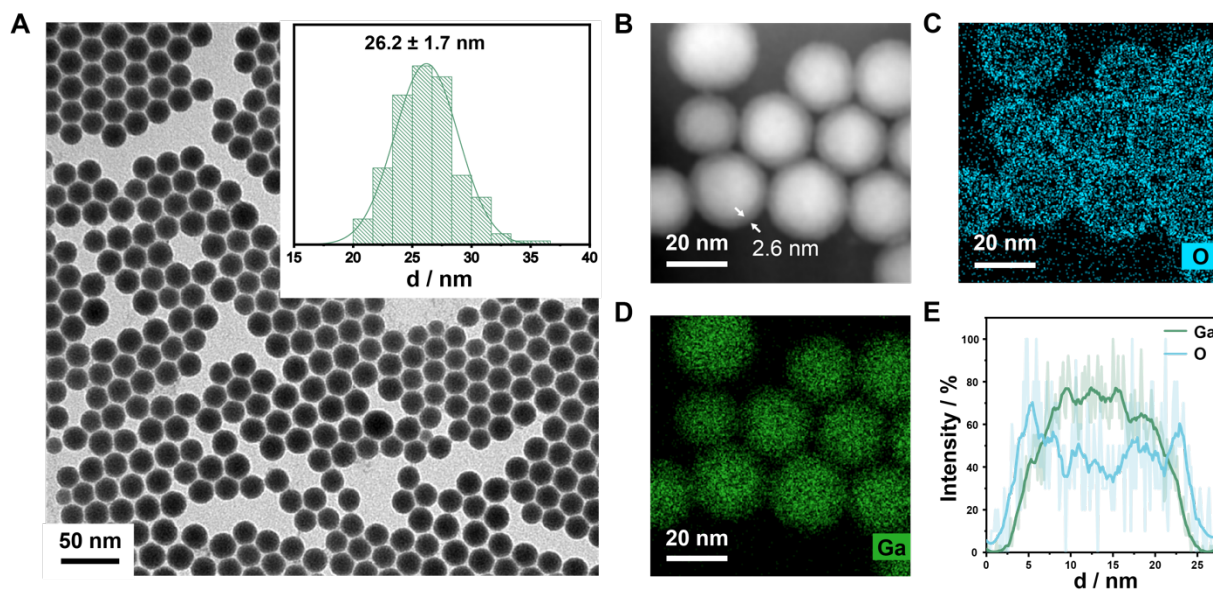


Figure 4.1. Synthesis and characterization of Ga NPs. (A) Bright field TEM image and size distribution of as-synthesized Ga NPs. (B-E) STEM characterization including (B) a typical image, (C, D) STEM-EDXS elemental mapping of Ga and O. (E) the line profile over one Ga NPs, which confirm the presence of native oxide skin on as-synthesized Ga NPs.

4.3 Electrochemical CO₂ reduction

Bulk Ga electrodes were reported to be selective for CO₂RR with faradaic efficiency (FE) for CO of around 20%, the rest being H₂ from the competing hydrogen evolution reaction.¹¹³ We evaluated the catalytic performance of the Ga NPs to assess if they yielded a similar product distributions. **Figure 4.2A** reports the CO FE measured over one hour of chronoamperometry at three different voltages, -0.7, -0.9 and -1.1 V_{RHE} (RHE = reversible hydrogen electrode), with the rest being H₂. At voltages more positive than -0.7 V_{RHE} the current density j is too low. Voltages which are more negative than -1.1 V_{RHE} result only in the increase of H₂ production. The selectivity of the Ga NPs varies with voltage. CO FE of Ga NPs is the highest at -0.7 V_{RHE} with an average value of 29 %. This value is slightly higher compared to that of bulk, which indicate possible size-dependent selectivity. As the voltage becomes more negative, CO FE decreases, and more H₂ is produced. In addition to CO and H₂, a minor amount of formate (<1 %) is detected at -1.1 V_{RHE}. With this products selectivity profile and CO₂ as carrier, the resulting gas mixture could be treated as H₂-rich syngas, which is a precursor for thermocatalytic dimethyl ether and methanol production.^{223,224} **Figure 4.2B** confirms that the current density remains stable for one hour electrolysis without any major declining.

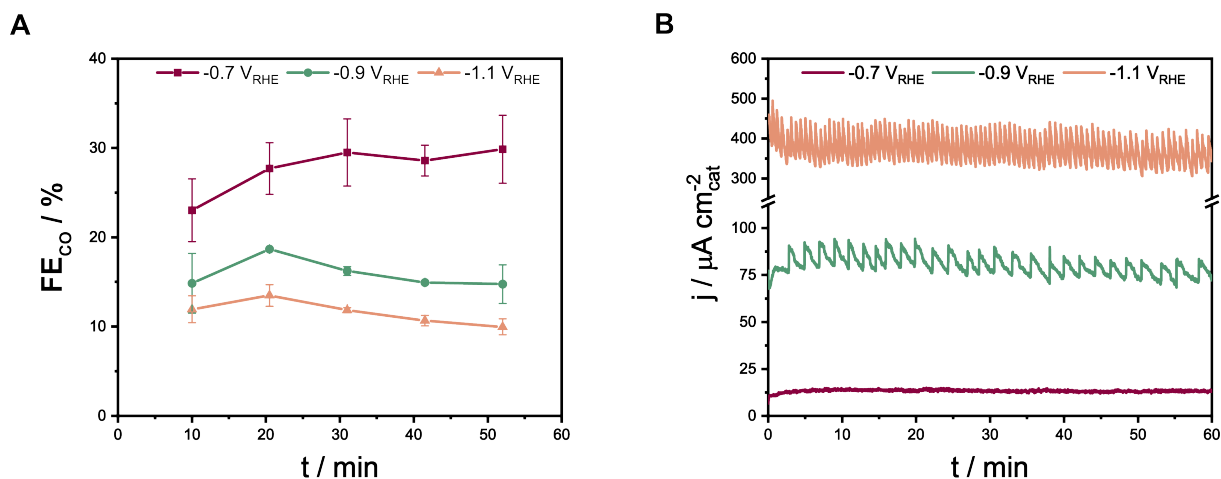


Figure 4.2. Ga NPs as CO₂RR electrocatalysts. (A) CO FE and (B) total current densities normalized by the area of the Ga NPs over one hour of CO₂RR in 0.1 M KHCO₃ at different applied potentials. Oscillations in current density are attributed to the formation of bubbles. The area of Ga NPs was calculated according to the model described in the section 2.6.

4.4 Investigation of the morphology and surface of the Ga NPs post-electrolysis

The Pourbaix diagram of Ga in aqueous solution indicates that the gallium oxide skin reduces to metallic Ga at $-0.485 V_{RHE}$ (**Figure 1.7**). Also, Ga NPs are liquid at room temperature.¹⁶¹ Thus, Ga NPs without the oxide skin should rapidly coalesce into bulk metallic gallium at the cathodic potentials applied during CO₂RR. Yet, no visual changes were observed on the electrodes post-electrolysis along with no change in the catalytic performance.

To assess morphological changes of the Ga NPs during CO₂RR, we analyzed the electrodes before and after electrolysis at different applied potentials (**Figure 4.3A**). The scanning electron microscopy (SEM) images evidence that the Ga NPs do remain well-separated from each other during the course of electrolysis. This observation is remarkable because other metal NPs of similar size and under the same conditions undergo tremendous changes and form aggregated structures, sometimes even during the potential ramp.^{48,66,165,225} We note that the size and size distribution of the Ga NPs do increase after electrolysis at the more cathodic voltages, however no major coalescence is observed (**Figure 4.4**). Even 70 hours of CO₂RR at $-0.7 V_{RHE}$ does not result in noticeable coalescence of Ga NPs (**Figure 4.3B**).

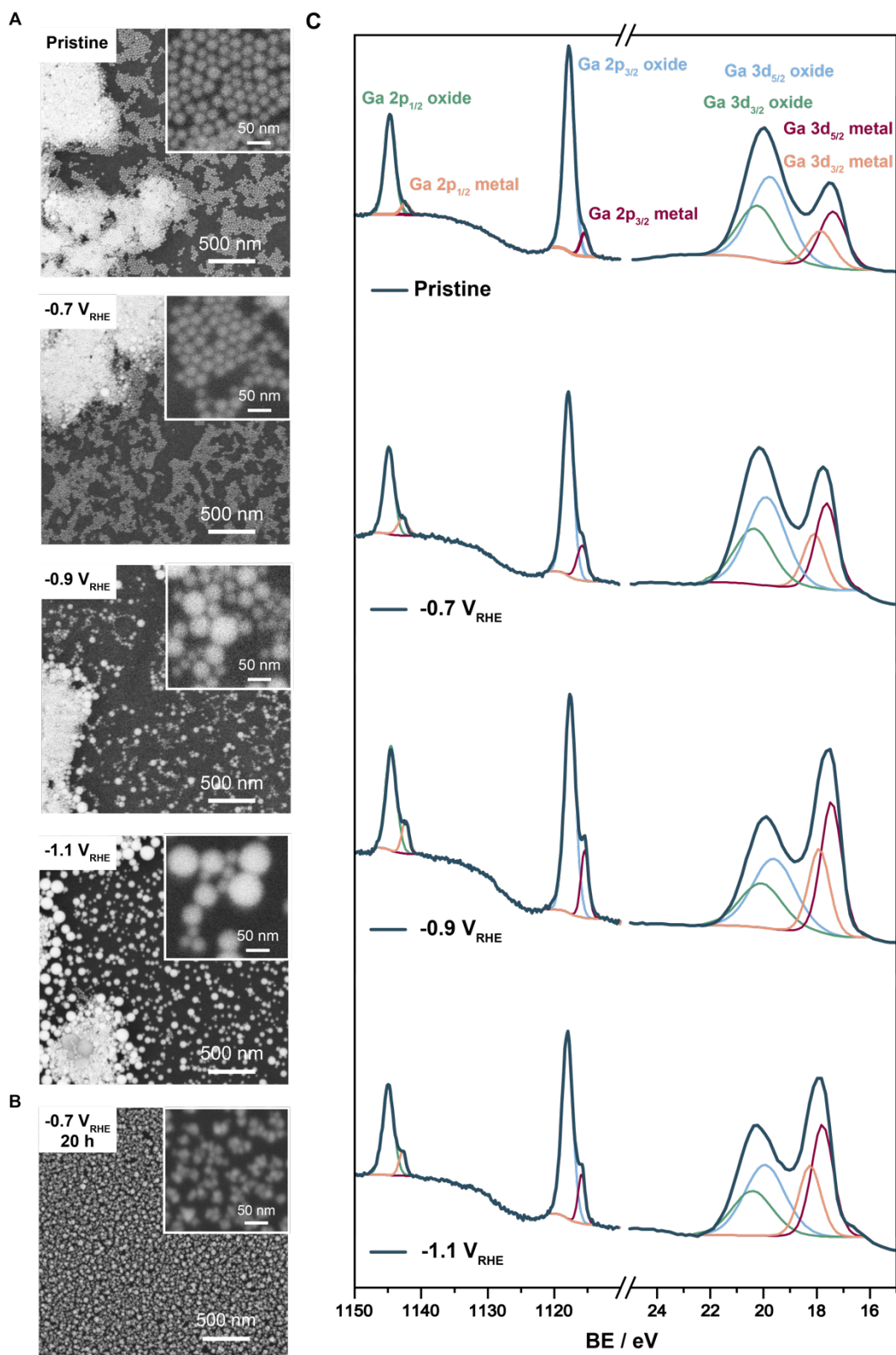


Figure 4.3. Characterization of Ga NPs after CO₂RR. (A) SEM images of pristine Ga NPs electrodes and after 1 h CO₂RR at -0.7 V_{RHE}, -0.9 V_{RHE} and -1.1 V_{RHE}. (B) SEM image of Ga NPs electrodes after 70 h CO₂RR at -0.7 V_{RHE}. (C) XPS analysis confirming the presence of the native oxide skin on pristine Ga NPs and after 1 h CO₂RR at a given potential.

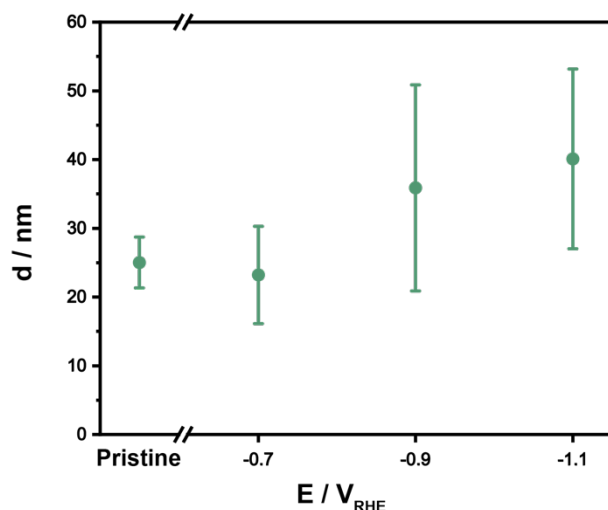


Figure 4.4. Size analysis of Ga NPs before and after CO₂RR. Statistical analysis performed on SEM images of Ga NPs after 1 h CO₂RR at different voltages. The first point refers to the size of Ga NPs on the as-prepared electrode.

To probe the oxide layer, we performed XPS analysis of the Ga NPs electrodes before and after electrolysis at different voltages (**Figure 4.3C**). First, XPS confirms presence of both the metallic and the oxide components in the as-synthesized Ga NPs. The fitting results indicate that the thickness of oxide layer is *ca.* 2.7 nm, which agrees well with the results of STEM-EDXS (**Figure 4.1B-E**). After electrolysis, the oxide contribution decreases, yielding *ca.* 1.6 – 2.3 nm thickness of oxide skin depending on the applied voltage (**Table 4.1**). We note that the XPS experiment was done *ex situ*, so the electrode surface reoxidizes in the time interval between the release of the cathodic potential and the XPS analysis. Nevertheless, the data clearly indicate that a certain fraction of Ga oxide is reduced during CO₂RR.

Table 4.1. Ga₂O₃ thickness after CO₂RR at different applied potentials calculated from XPS.

Applied potential / V _{RHE}	Ga ₂ O ₃ shell thickness / nm
Pristine Ga NPs	2.7
Ga NPs 1 h @ -0.7 V _{RHE}	2.3
Ga NPs 1 h @ -0.9 V _{RHE}	1.6
Ga NPs 1 h @ -1.1 V _{RHE}	2.0

4.5 Transmission electron microscopy characterization

The melting point of bulk Ga is slightly above room temperature at 29.8 °C.⁶⁹ The melting point of Ga NPs is expected to be lower because of size effects.^{131,226–229} At the same time, unexpected behavior can arise at the nanoscale.^{230,231} For example, Ga clusters smaller than 2 nm were predicted to have a higher thermal stability than bigger NPs.²³⁰ One study also reported the thermally stable coexistence of liquid and solid phases in Ga NPs.²³¹ As the presence of a solid domain in the NPs might explain the absence of rapid coalescence in the Ga NPs, we decided to investigate further the structure of the Ga NPs. Therefore, we performed *in situ* HRTEM experiment with heating from cryogenic temperatures back to room temperature.

An interference contrast image along with selected area electron diffraction were recorded at few pre-selected temperatures (**Figure 4.5A**). When cooled to liquid nitrogen temperature (-196 °C), the NPs solidify, which is revealed by visible crystalline planes in the high-resolution images and by the appearance of spots in the SAED. The co-existence of diffuse rings arises from the presence of thin amorphous Ga oxide shell, which is also visible in the HRTEM. The SAED pattern evidences that the solid Ga NPs are crystallized as δ -Ga (**Figure 4.5B**). This result indicates that the α -Ga, which is a stable phase in bulk Ga, is suppressed in Ga NPs, which is in line with previous results in the literature.¹⁶¹ The Ga NPs persist in the same structure at -80 °C, but melt when heated up to -60 °C, which is indicated by the disappearance of the bright spots in the SAED patterns. The cooling of the NPs back to -80 °C does not result in solidification; indeed, only the diffuse rings are visible in the SAED. Supercooling effects and hysteresis between the crystallization and melting points have been previously reported for Ga NPs and explain this observation.^{161,226–228,232}

Altogether, HRTEM and SAED analysis provide no indication of solid domains being present within the liquid Ga NPs at both ambient and low temperatures. Despite different conditions between *cryo*-HRTEM and CO₂RR as well as a different substrate, these findings make the presence of solid domains at operating conditions highly unlikely.

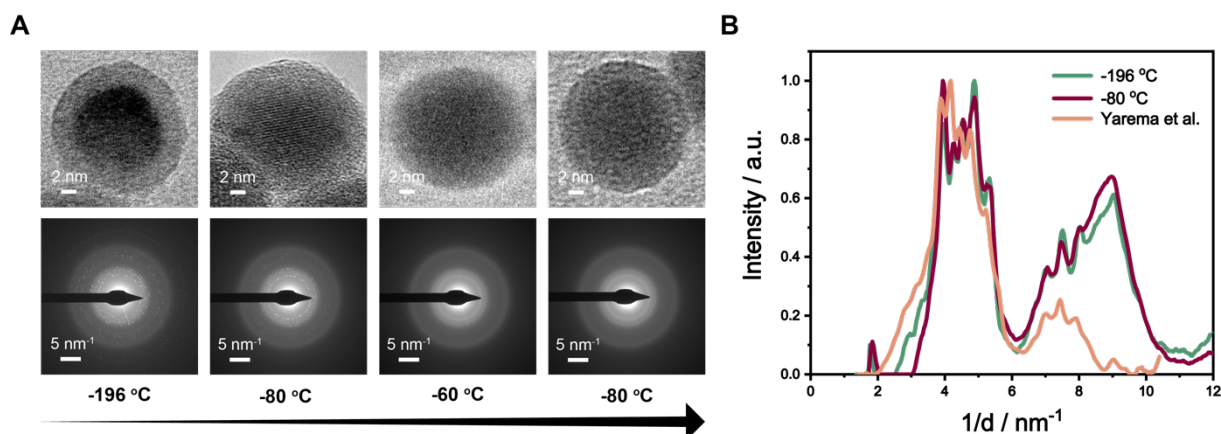


Figure 4.5. *In situ* heating HRTEM and SAED of Ga NPs. (A) *Cryo*-HRTEM (left) and SAED (right) study of Ga NPs at different temperatures: at liquid N₂ temperature (-196 °C), at -80 °C, at -60 °C and again at -80 °C. (B) Circular averaged electron diffraction pattern of Ga NPs at -196 °C and -80 °C, where Ga NPs SAED is characterized with the presence of the diffraction spots; for reference, the circular averaged electron diffraction pattern obtained by Yarema et al.¹⁶¹ is presented.

4.6 Voltammetric characterization

The electrochemical properties can change when size shrinks to the nanoscale, which is attributed to different electronic configuration or strain effects of the surface.^{233,234} Shifts in the redox potentials of the Ga NPs and bulk Ga might explain why Ga NPs do not undergo rapid coalescence.

To assess this possibility, we performed a voltammetric study of Ga NPs in CO₂-saturated 0.1 M KHCO₃, which is the electrolyte used for electrochemical CO₂ reduction tests (**Figure 4.6A**). We utilized squared wave voltammetry (SWV), which exhibits enhanced sensitivity compared to a conventional cyclic voltammetry experiment. We selected the testing range in a region where repetitive cycles yield no changes in SWV response. The acquired SWV of bulk Ga is shown for the reference. We note that bulk Ga is solid at room temperature, instead the Ga NPs are in their liquid state. To evaluate possible differences arising from the material physical state, we measured bulk Ga below and above its melting point (at 24 °C and 35 °C, respectively).

The curves of the Ga NPs and of the bulk liquid Ga are qualitatively similar. This result points at the liquid nature of the particles, which is consistent with the HRTEM in **Figure 4.5**, and to the absence of size-induced differences in their redox properties. Overall, there are two distinctive features in the investigated potential range: a reduction peak at *ca.* $-0.54 V_{RHE}$ and an oxidation peak at *ca.* $-0.51 V_{RHE}$. Both values are close to the standard reduction potential of Ga^{3+}/Ga ($E_{Ga_2O_3/Ga}^\circ = -0.485 V_{RHE}$, $E_{GaOOH/Ga}^\circ = -0.493 V_{RHE}$, $E_{Ga(OH)_3/Ga}^\circ = -0.415 V_{RHE}$).^{142,143} These numbers agree well with earlier reported investigation of bulk Ga in different electrolytes.^{105,124–126,140,235,236} The reduction peak is assigned to the oxide skin, which is followed by steady non-capacitive current increase (assigned to hydrogen evolution reaction and CO₂RR) at more negative voltage. The oxidation peak on the reverse scan is attributed to the formation of oxide skin.

The solid Ga electrode is distinctly different from the other curves. The observed peaks are broader and shifted *ca.* 0.1 V negative compared to the bulk liquid Ga, in accordance with previous studies.^{105,121} The negative shift and peak broadness can be explained by the higher affinity of oxide to solid Ga than to its liquid counterpart.¹²¹ To prove that these differences arise from the difference in the Ga state and are not the direct effect of heating, SWV of Ga NPs was recorded both at ambient and elevated temperature, showing no significant difference between the two curves (**Figure 4.6B**).

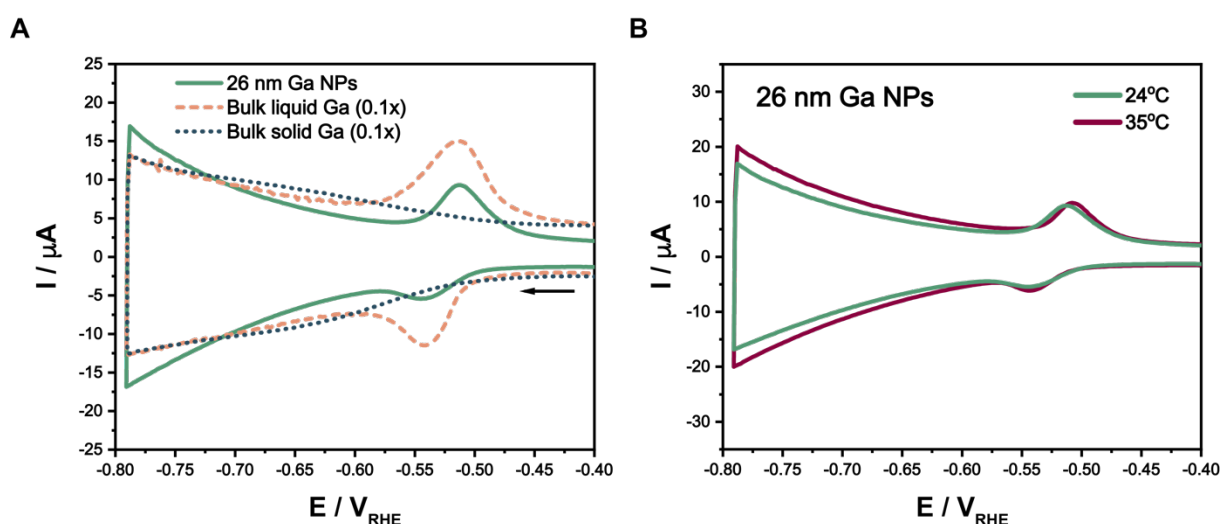


Figure 4.6. Voltammetric study of Ga NPs. (A) SWV curves of Ga NPs and bulk Ga (in the liquid and solid state) in CO₂-saturated 0.1 M KHCO₃. The arrow indicates the scan direction. (B) SWV of Ga NPs in CO₂-saturated 0.1 M KHCO₃ measured at 24 °C (below bulk Ga melting point, green line) and 35 °C (above bulk Ga melting point, red line).

Overall, the voltametric characterization indicates that the oxide skin should be reduced and, thus, the Ga NPs should exist in their liquid metallic state under CO₂RR conditions, which questions the reason for absence of immediate Ga NPs coalescence.

4.7 Operando XAS study of Ga particles during CO₂RR.

As Ga spontaneously reoxidizes upon air exposure and at ocp, the only way to probe the presence of the oxide skin during CO₂RR is via *operando* studies. Thus, we performed *operando* X-ray absorption spectroscopy (XAS) of Ga NPs during CO₂RR (**Figures 4.7, 4.8**).

We did not observe any difference when operating the electrolyzer at different voltages (**Figure 4.7**); -1.1 V_{RHE} was selected as representative voltage for further analysis. The X-ray absorption near edge structure (XANES) map evidenced a shift of the Ga absorption edge position towards lower energy when the cathodic voltage is applied (**Figures 4.7, 4.8A**), which means that the metallic Ga component increases. This observation agrees well with SWV data indicating the reduction of Ga oxide at -0.54 V_{RHE}, which means that majority of Ga oxide should get reduced at operating voltages. XANES characterization performed at -1.1 V_{RHE} with 20 s time resolution indicated that the reduction of the Ga oxide component takes place during the first 2 min of operation (**Figures 4.8B**), and no further changes occur over one hour of electrolysis (**Figure 4.7**). The linear fitting of the XANES curves evidence that the Ga oxide content evolves from 24% to 3% going from ocp to -1.1 V_{RHE}, which correspond to a change in the average oxide thickness from 1.1 nm to ca. 0.1 – 0.2 nm (calculation details are reported in section 2.6; the initial size and size after CO₂RR are 26 and 40 nm as obtained by analyzing mean NPs size from SEM images in **Figure 4.4**). Chronoamperometry at -1.1 V_{RHE} for 5 hours confirmed that oxidation state of the Ga NPs remains stable after the initial reduction step (**Figure 4.8C**).

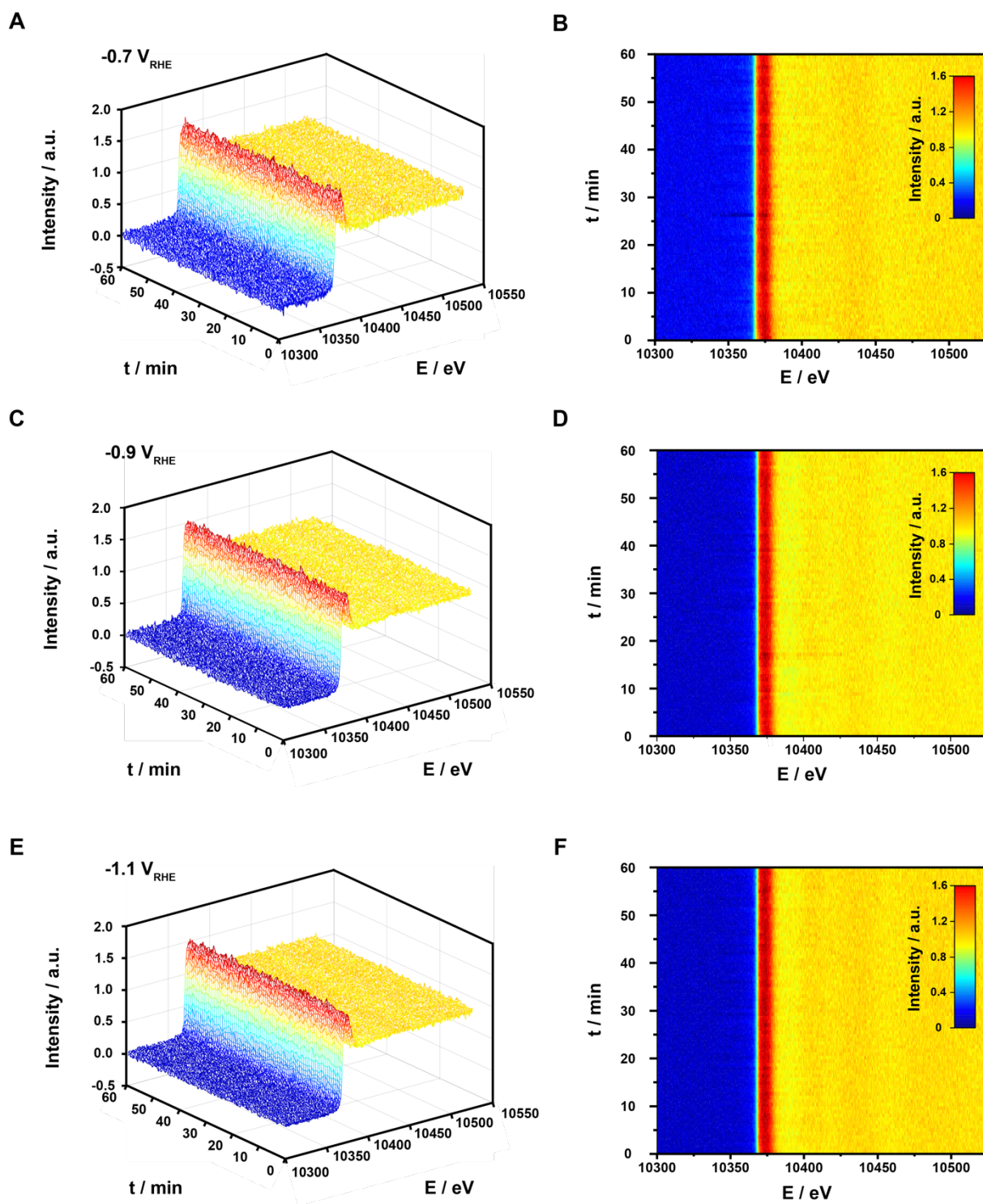


Figure 4.7. Operando X-Ray absorption spectroscopy of Ga NPs during CO₂RR. Operando XANES spectra of Ga NPs during 1 h CO₂RR at (A, B) $-0.7 V_{\text{RHE}}$, (C, D) $-0.9 V_{\text{RHE}}$ and (E, F) $-1.1 V_{\text{RHE}}$: (A, C, E) 3D maps in time – voltage – intensity coordinates and (B, D, F) corresponding 2D maps in time – voltage coordinates.

Extended X-ray absorption fine structure (EXAFS) analysis provided further insight into the Ga local chemical environment. **Figure 4.7D** indicates a pronounced signal from Ga-O at ocp. When the cathodic voltage is applied, the Ga-O contribution to the signal decreases, yet it is clearly still present in the EXAFS pattern. Altogether, the XANES and EXAFS results are consistent with the presence of roughly a monolayer of Ga oxide on Ga NPs during CO₂RR.

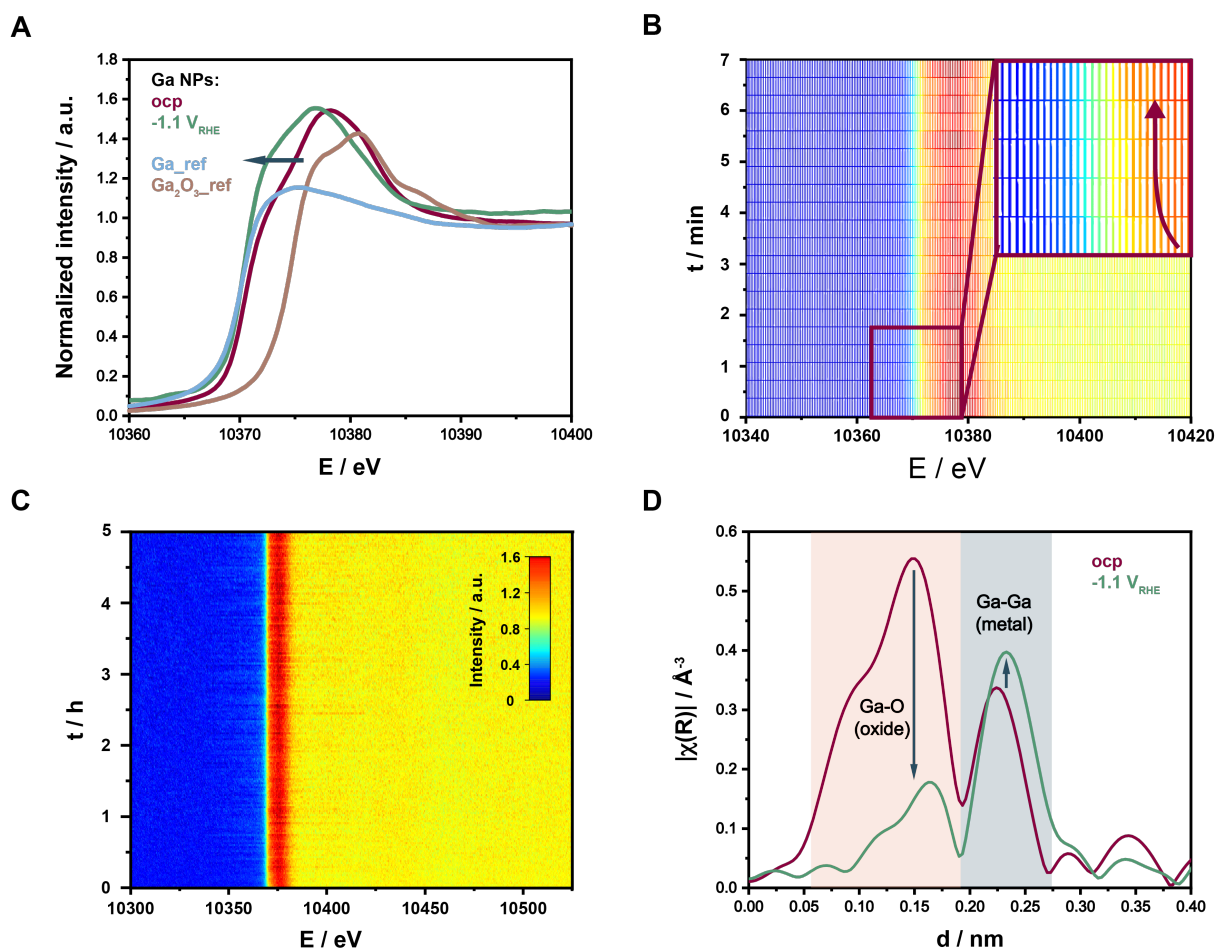


Figure 4.8. (A) Comparison of the XANES scans at ocp and at -1.1 V_{RHE}, (B) 2D map of XANES spectra with 20 s scan duration at -1.1 V_{RHE}, (C) 2D map of XANES spectra during 5 hours of CO₂RR at -1.1 V_{RHE}, (D) interatomic distances derived from *operando* EXAFS measurements of Ga NPs at ocp and at -1.1 V_{RHE}. Interatomic distances were not corrected for the phase shift. The red and gray areas indicate distances corresponding to Ga-O and Ga-Ga bonds, respectively.

4.8 Mechanistic discussion

The discovery that Ga oxide is still present under the highly cathodic potential driving CO₂RR is intriguing. Interestingly, this result resembles the residual gallium oxide found in CuGa catalysts under the highly reducing conditions of the thermal CO₂ hydrogenation reaction as long as a few ppm of oxygen were present.¹¹⁵ Reports by Popova et al. dating back to the 70's claim that even after Ga activation (i.e., at voltages more negative than the reduction peak) a “residual film” of different chemical nature persists on the surface and increases the HER overpotential compared to Ga free of the surface oxide.^{122,123} Having acquired this new knowledge, questions regarding the structure and the role of the oxide layer on the Ga NPs during the electrocatalysis arise.

First of all, it is difficult to say whether the oxide of roughly one monolayer thickness is uniformly covering the surface of the Ga NPs or is present in the form of islands on the surface. Both situations are possible. Second, the oxide layer can be static or dynamic. Whether static or dynamic, the oxide layer would prevent the rapid coalescence of the Ga NPs during CO₂RR. Indeed, even in case of a dynamic oxide, the surface reoxidation, which is a chemical process, would be faster than NPs coalescence, which is a physical phenomenon, thus inhibiting it.^{237,238}

In the case of a static oxide, a fraction of the native oxide skin would always be present on the Ga NPs surface during CO₂RR (**Figure 4.9A**). Herein, CO₂RR could occur on the oxide itself, on the metal surface or at metal/oxide interfacial sites. To gain further insight, we attempted to obtain pure gallium oxide NPs as a reference by electrochemically oxidizing the Ga NPs. However, the current density under the applied potential dramatically decreases with fully oxidized NPs and reliable studies cannot be performed. Furthermore, most of the oxide is reduced back when the cathodic potential is applied, so learning about the CO₂RR reaction of GaO_x NPs is practically impossible.

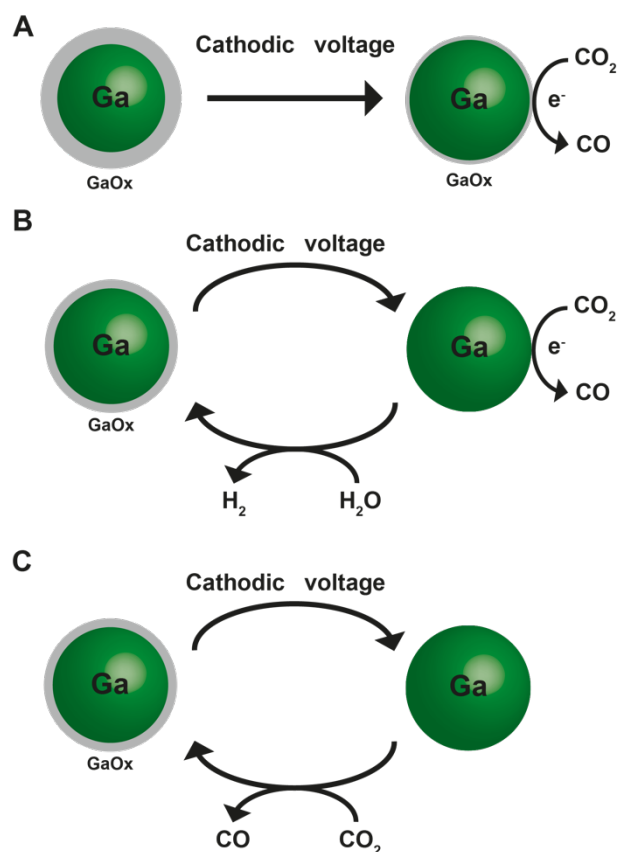


Figure 4.9. Possible mechanisms of oxide-retarded coalescence in Ga NPs electrocatalysts. The possibilities include the presence of (A) a static and (B,C) a dynamic oxide skin. Within a few minutes from the application of the cathodic voltage, the thickness of the native oxide skin ($\sim 1\text{-}2$ nm) is reduced to monolayer (uniform or patchy, $\sim 0.1\text{-}0.2$ nm thick). In (A), this monolayer persists during CO₂RR. In (B,C) the monolayer is dynamic, meaning that it reduces to pure Ga and it reforms during the course of electrolysis via coupling with the chemical water reduction (B) or CO₂RR itself (C). Herein, the monolayer thickness measured by EXAFS would correspond to an average value between two states. The oxide skin is indicated as GaO_x as its specific stoichiometry is unknown. While the bulk stable oxide phase is Ga₂O₃, earlier studies suggest that Ga(III) oxyhydroxides of mixed compositions may form as well as unstable Ga species such as Ga(I) (oxy)hydroxides, and even incorporation of anions into the skin is probable.^{123–125,144}

Alternatively, one can envision the oxide skin to be involved in a dynamic redox cycle where the applied potential reduces it and the coupling with a chemical reaction forms it back (**Figure 4.9B,C**). This chemical reaction can be either the reduction of H₂O to H₂ (**Figure 4.9B**) or the

reduction of CO₂ to CO (**Figure 4.9C**). If the surface oxidation of Ga to GaO_x was coupled with the reduction of H₂O to H₂, the CO₂ reduction to CO would occur on the surface of metallic Ga driven by the applied voltage while H₂ production would result from a chemical step (**Figure 4.9B**). This mechanism is in qualitative agreement with an earlier study of Ga electrode behavior in alkaline electrolyte with concomitant chemical H₂ evolution.¹⁴⁴ Instead, if the surface oxidation of Ga to GaO_x was coupled directly with the reduction of CO₂ to CO, the negative applied voltage would regenerate the metallic Ga surface and restarts the cycle (**Figure 4.9C**). This model has been referred to as incipient hydrous oxide adatom mediator model, and it is similar to the mechanism proposed for Ce catalyst dissolved in Galinstan.^{104,239} More recently, the involvement of a dynamic oxidized Ga layer forming between the LM Ga and a Ni co-catalyst has been proposed to explain the insurgence of triboelectric effects driving the conversion of methane into carbon.¹⁰⁸ These studies, along with our results, provide credibility to the hypothesis that dynamic Ga oxidation may happen during catalytic processes.

While we cannot conclude which exact mechanism takes place, we further validated that the oxide is crucial to prevent coalescence of the Ga NPs. For instance, strong metal/support interactions can contribute to anchor nanocatalysts in place and prevent their sintering.^{37,38} While the formation of Ga-C bonds is highly unlikely,²⁴⁰ one can still imagine an interplay between the glassy carbon and the metallic Ga NPs which anchors them during CO₂RR. To test this hypothesis, we chemically removed the oxide skin by dipping the Ga NPs electrodes in hydrochloric acid (**Figure 4.10**). This treatment was chosen because the most commonly used for the etching of the native Ga oxide skin.²⁴¹ As a result, big Ga agglomerate formed (**Figure 4.10C**), which eliminates the sole role of the substrate in the prevention of coalescence.

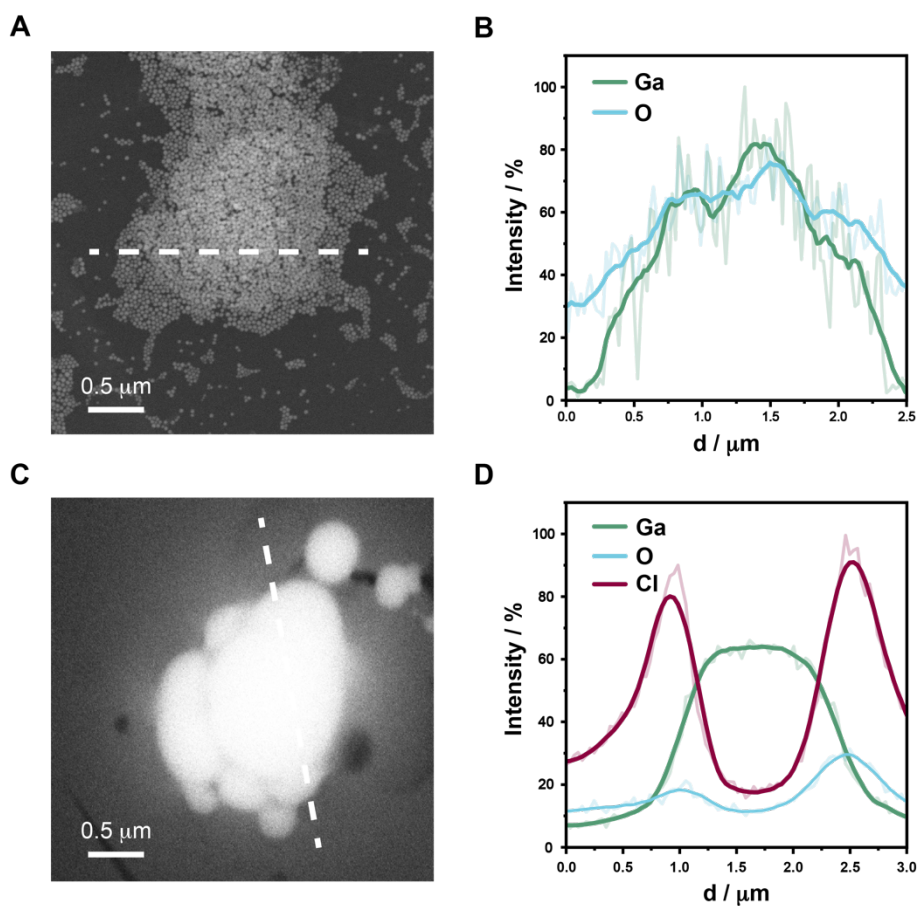


Figure 4.10. Influence of acid on Ga NPs. (A,C) SEM images with (B,D) corresponding SEM-EDXS line profile of a Ga NP electrode before (A,B) and (C,D) after 10 min immersion in 1 M HCl. Well dispersed Ga NPs are observed as-deposited, and the EDXS line scan indicates correlated intensity of Ga and O signal which is consistent with each NP being covered with the native oxide skin. After the acid treatment, big Ga aggregates are observed, and the corresponding EDXS line scan indicates a Ga-rich core with a shell rich in Cl and O. The oxygen signal is consistent with surface oxidation after coalescence upon exposure to air.

We also found out that CO₂ supply and bicarbonate are not essential to prevent coalescence (**Figure 4.11**), thus the phenomenon appear to be general as far as water is present in the environment. Oxygen dissolved in the electrolyte could contribute to the GaO_x skin retention if the pH is not acidic or alkaline enough to dissolve the shell chemically.

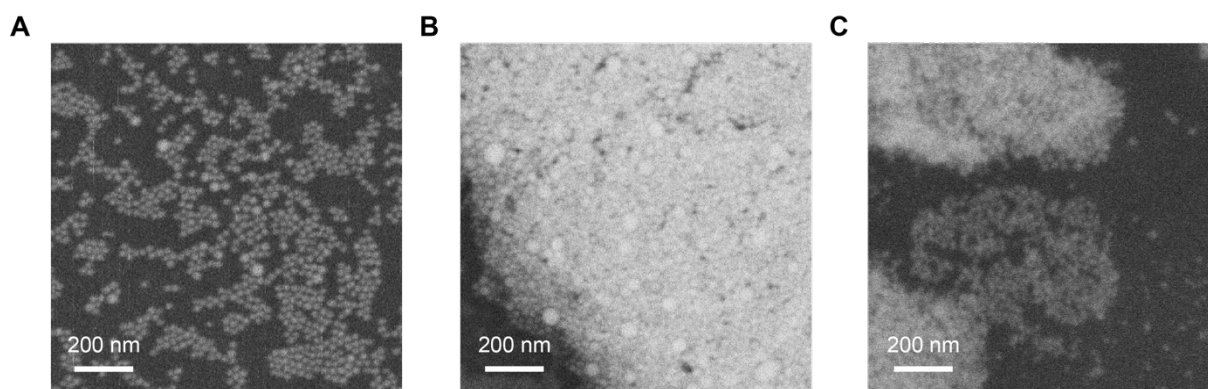


Figure 4.11. Effect of electrolyte choice on Ga NPs. SEM images of Ga NPs electrodes after electrolysis at $-0.7 V_{\text{RHE}}$ in (A) 0.1 M phosphate buffer (pH = 6.8) under CO₂ flow, (B) 0.1 M KHCO₃ under N₂ flow and (C) 0.1 M phosphate buffer (pH = 6.8) under N₂ flow.

Finally, we demonstrated that the behavior observed for the 26 nm Ga NPs is retained for other sizes (**Figures 4.12**). Smaller (18 nm) and bigger (39 nm) NPs possessed comparable CO₂RR performance and resistance to coalescence. Interestingly, a more pronounced size change with increasing cathodic potential occurs for the bigger NPs. This behavior is counterintuitive as generally coalescence occurs more easily for smaller and more active NPs.¹¹⁰ Yet, it suggests that the lower surface to volume ratio of the bigger NPs makes the oxide skin protection less effective. To provide further insight on the size dependent behavior, we attempted to study micron-size Ga particles, however their broad size distribution prevented us to draw reliable conclusions.

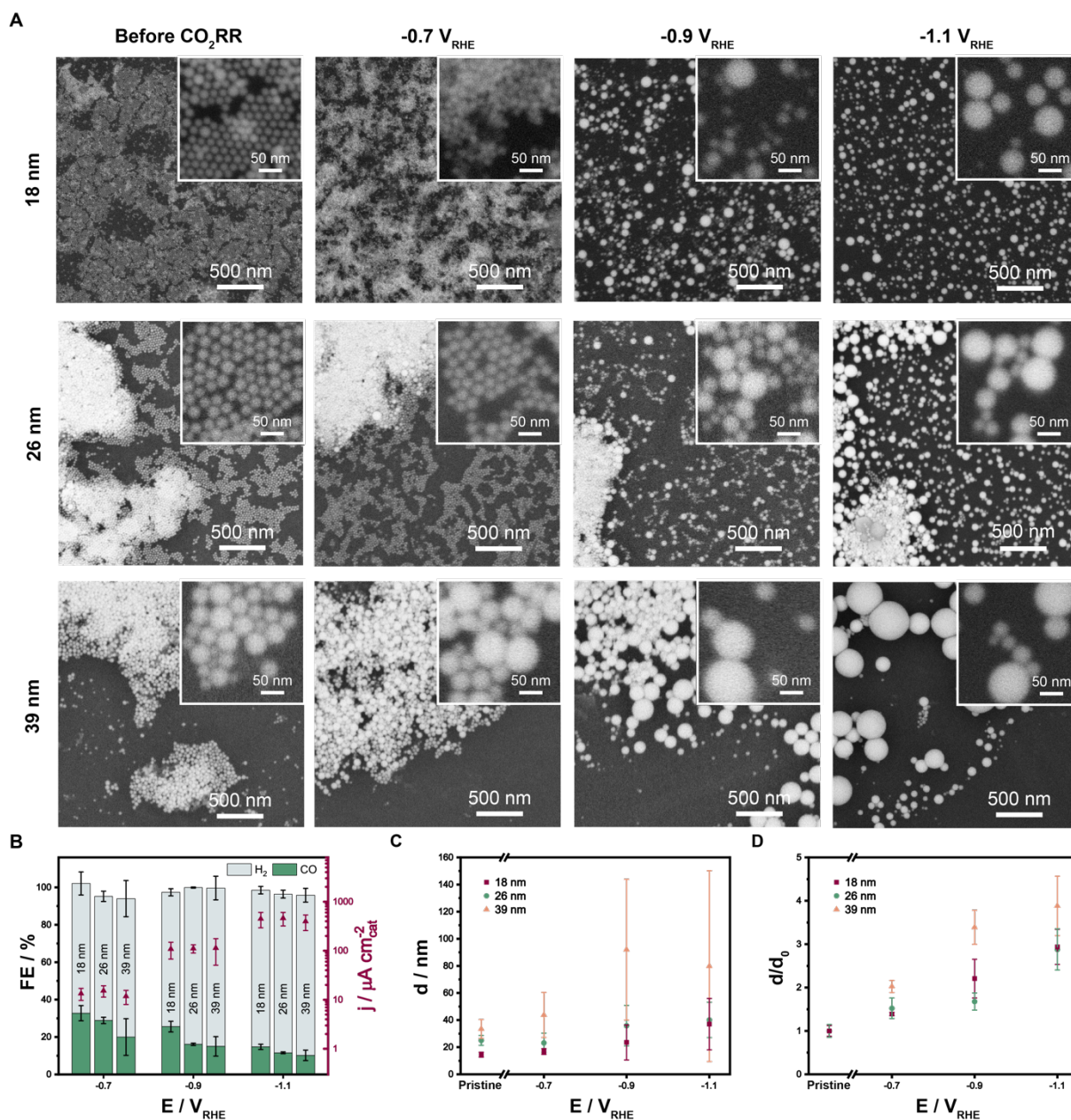


Figure 4.12. Comparison of Ga NPs with different sizes. (A) SEM images of 18 nm, 26 nm and 39 nm Ga NPs electrodes before and after electrolysis at $-0.7 V_{\text{RHE}}$, $-0.9 V_{\text{RHE}}$ and $-1.1 V_{\text{RHE}}$. (B) Average CO and H₂ FE and current density for Ga NPs of 18 nm, 26 nm and 39 nm over 1 h CO₂RR at different potentials. (C,D) Statistical analysis performed on SEM images of 18 nm, 26 nm and 39 nm Ga NPs electrodes after electrolysis at $-0.7 V_{\text{RHE}}$, $-0.9 V_{\text{RHE}}$ $-1.1 V_{\text{RHE}}$. The analysis is based on (C) average particles size and (D) ratio between the average size of coalesced particles vs. initial size of Ga NPs.

4.9 Conclusions

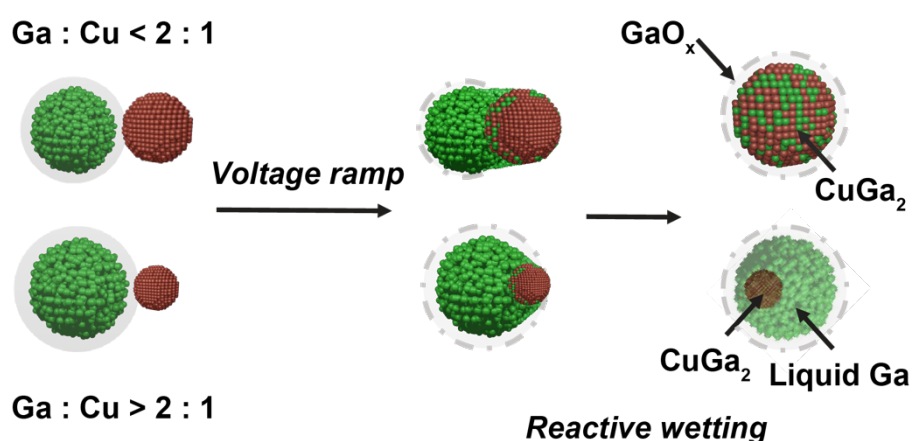
We have demonstrated that Ga NPs can be implemented as liquid metal catalysts for the electrochemical CO₂RR while preserving the nanoparticles morphology. Based on *operando* XAS, we propose an oxide-mediated retarded coalescence mechanism wherein the native oxide skin persists during CO₂RR in a static or dynamic fashion.

This discovery is significant because the same oxide-mediated retarded coalescence mechanism can be conceived for other Ga-based alloys and intermetallics, many of which have been predicted as promising electrocatalysts for different reactions, including CO₂RR.^{21,206} By exploiting colloidal chemistry, which allows the synthesis of well-defined NPs with tunable compositions,^{162,163} we envision a library of LM NPs to emerge as a new class of electrocatalysts which are active, selective and coalescence-resistant.

Chapter 5

Voltage-driven Chemical Reactions Enable the Synthesis of Tunable Liquid Ga – Metal Nanoparticles

The content of this Chapter is based on published work with permission from the journal: *J. Am. Chem. Soc.* 2023: <https://pubs.acs.org/doi/10.1021/jacs.3c09828>. Copyright 2023 American Chemical Society.



Abstract: Nanosized particles of liquid metals are emerging materials which hold promise for applications spanning from microelectronics to catalysis. Yet, the knowledge of their chemical reactivity is largely unknown. Here, we study the reactivity of liquid Ga and Cu nanoparticles under the application of a cathodic voltage. We discover that the applied voltage and the spatial proximity of these two particle precursors dictate the reaction outcome. In particular, we find that a gradual voltage ramp is crucial to reduce the native oxide skin of the gallium and enable reactive wetting between the Ga and the Cu nanoparticles; instead, a voltage step causes dewetting between the two. Having learned this, we obtain CuGa₂ alloys or solid@liquid CuGa₂@Ga core@shell nanoparticles by tuning the stoichiometry of the particle precursors. These products reveal an interesting complementarity of thermal and voltage driven synthesis

to expand the compositional range of bimetallic NPs. Finally, we extend the voltage-driven synthesis to the combination of Ga with other elements (Ag, Sn, Co, W). By rationalizing the impact of the native skin reduction rate, the wetting properties and the chemical reactivity between Ga and other metals on the results of such voltage-driven chemical manipulation, we define the criteria to predict the outcome of this reaction and set the ground for future studies targeting various applications for multielement nanomaterials based on liquid Ga.

Authors: **Valery Okatenko**, Coline Boulanger, Alexander N. Chen, Krishna Kumar, Pascal Schouwink, Anna Loiudice, Raffaella Buonsanti.

Contribution: Performed all electrochemical studies and synthesis, colloidal synthesis of Ga/Cu_{0.1}, Ga/Ag_{0.3}, Ga/Sn_{0.1} NDs, bright-field TEM imaging, STEM-EDXS data processing and interpretation, SAED analysis, and wrote the manuscript with contributions from all authors, and wrote the manuscript with contributions from all authors.

5.1 Introduction

In Chapters 1 and 4, we introduced liquid metals and demonstrated the promise of Ga LM NPs for electrocatalytic and, in broad sense, electrochemical applications.¹⁷¹ To date, very little is known about the chemical reactivity of liquid metal NPs with other metals.

Existing knowledge indicates that a native oxide skin passivates the Ga surface and hinders its reactivity with other metals.^{114,162} In bulk materials, dissolution in basic aqueous solutions and electroreduction of this oxide layer are often utilized to expose the metallic Ga surface and create a metallic contact between Ga and other metals.¹¹⁸ Once the metallic contact is established, bulk Ga reacts with and corrodes most metals.¹⁶⁴ The reaction might remain confined to the interface between Ga and the second metal, induce a complete transformation into a bimetallic compound,²⁴² or cause internalization of the second metal within the liquid Ga²⁴³. The extent of the reaction and the nature of the resulting product determine the property of interest, be it electrical conductivity, mechanical flexibility, surface tension or catalytic selectivity. Unfortunately, rational guidelines on how to balance and exploit the chemical reactivity of liquid Ga NPs with other metallic domains to direct the evolution toward a target outcome and thus, regulate their properties, do not exist yet.

Herein, we contribute to fill this knowledge gap by studying the reactivity of liquid Ga NPs with other metallic NPs. We choose the voltage to control the presence of native Ga oxide and, thus, initiate the reaction of the liquid Ga NPs, because of its finer tunability compared to chemical dissolution. We focus on the reaction of Ga with Cu as one exemplificative case because a few reference studies exist on the corresponding bulk materials, which are of interest for creating electrical contacts and antimicrobial coatings as well as driving the electrochemical CO₂ reduction.^{209,242–249} We use colloiddally synthesized Ga and Cu NPs because their size monodispersity and tunability makes them an ideal platform to investigate changes occurring during the reaction and to interrogate the impact of different factors (e.g. relative domain size, stoichiometry, interfaces) on the reaction outcome. We learn that the rate of the applied cathodic voltage is crucial for the reaction to occur. Comparing a physical mixture of Ga and Cu NPs with Ga/Cu nanodimers (NDs), wherein the two NPs share an intimate interface, we demonstrate the importance of spatial proximity and of the relative domain size of the reacting NPs for the reaction outcome, specifically as to whether CuGa₂ alloys or unique solid@liquid CuGa₂@Ga core@shell NPs form as the reaction product. We also study how the reaction occurs for the bulk materials under similar conditions and provide the mechanism which links reactivity at the nano and bulk scale. Finally, we extend the learning lesson from Ga – Cu to other metals.

5.2 Voltage-driven synthesis of Ga – Cu NPs

We started by investigating the voltage-driven reactivity of a physical mixture of liquid 20 nm Ga and 7 nm Cu NPs (**Figure 5.1A-C**). After depositing the liquid Ga and Cu NPs on glassy carbon plates via drop-casting, we applied a linear voltage scan at 5 mV/s from open circuit potential (ocp) to -0.9 V_{RHE} and held this voltage for 5 minutes as the reaction time. The obtained results indicated that the two NPs reacted with formation of new phase and change in the NPs morphology (**Figure 5.1D-G**). However, further interpretation of the data was hindered by the intrinsic inhomogeneity of the reaction product resulting from the not uniform distribution of the reactive interfaces in the physical mixture of the NPs precursors.

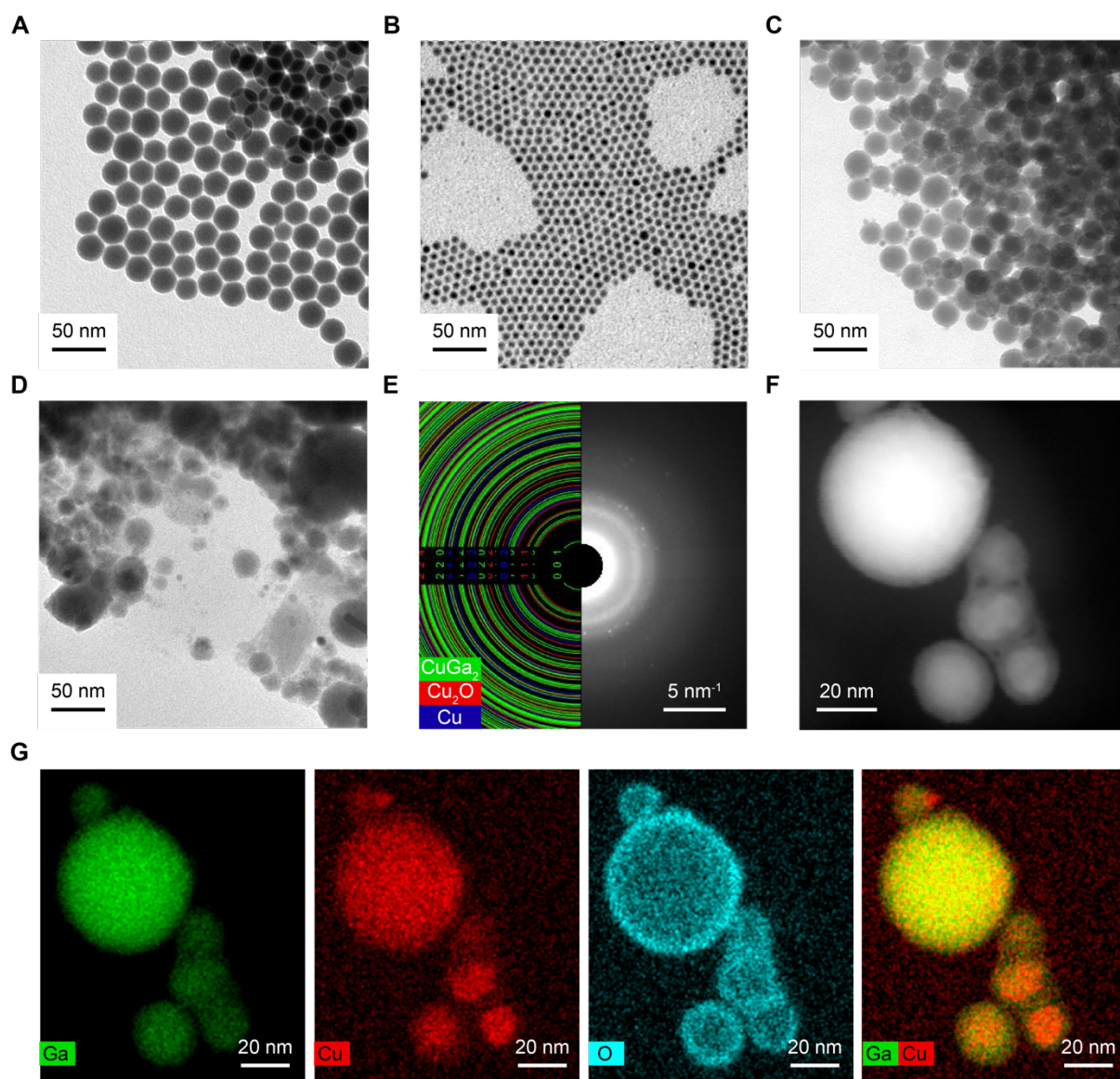


Figure 5.1. Voltage-driven reaction of Ga and Cu NPs physical mixture. (A-C) TEM images of (A) Ga, (B) Cu NPs and (C) their physical mixture of GaCu_{0.1} composition. (D) TEM image, (E) SAED pattern, (F) STEM image and (G) STEM-EDXS elemental maps of Ga (green), Cu (red) and O (cyan) of the NPs obtained via the voltage-driven synthesis from physical mixture of GaCu_{0.1} composition by applying a linear voltammetry scan from ocp to $-0.9 V_{RHE}$ with 5 minutes hold as the reaction time.

To obtain better control on the spatial distribution of the Cu and Ga domains, we synthesized liquid Ga/Cu nanodimers (NDs), following a previously developed synthesis,¹⁶² and reacted them following the same protocol used for the mixture (**Figure 5.2A**). In the NDs, the Ga and Cu NPs share an interface.¹⁶² We prepared two samples with different domain sizes to

investigate the impact of the stoichiometry on the reaction outcome: one with domains of comparable size (~ 15 and 20 nm, Ga/Cu_{0.7} as determined by elemental analysis) and one with a smaller size of the Cu domain relative to Ga (~ 7 and 20 nm, Ga/Cu_{0.1} as determined by elemental analysis). The Cu domain is solid and gives diffraction contrast, while the Ga domain is liquid and amorphous in the TEM images of both samples (**Figure 5.2B,C**).¹⁶²

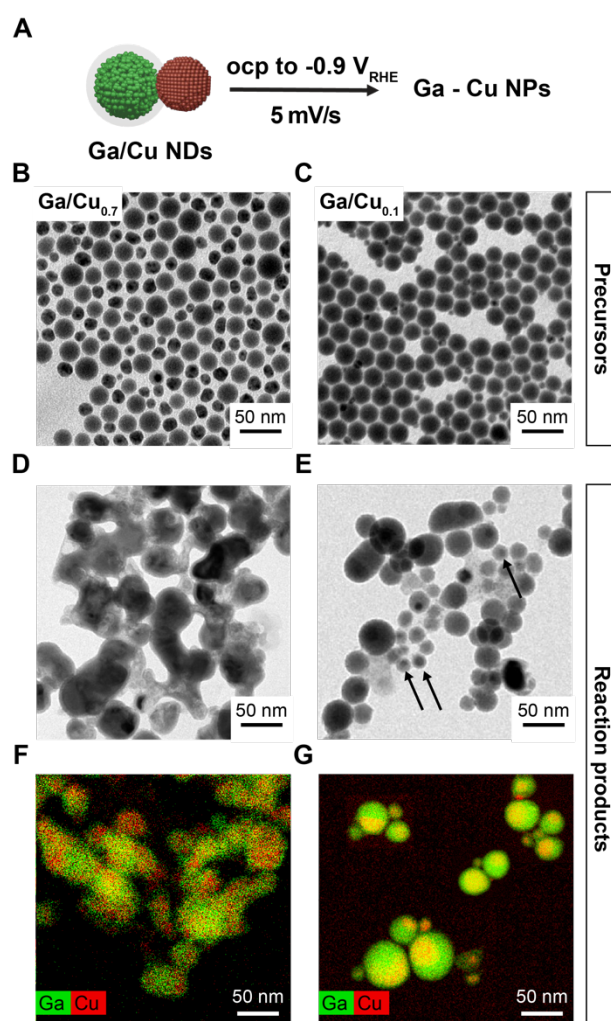


Figure 5.2. Voltage-driven reaction of Ga/Cu NDs. (A) Voltage-driven reaction scheme. (B-E) Bright-field TEM images of (B) Ga/Cu_{0.7} and (C) Ga/Cu_{0.1} NDs with (D,E) the corresponding reaction products NPs. In E, the arrows point at small crystalline domains within the larger amorphous NPs. (F, G) STEM-EDXS elemental maps (Ga – green, Cu – red) of the reaction products obtained from Ga/Cu_{0.7} (F) and Ga/Cu_{0.1} NDs (G). The reaction was performed by applying a linear voltammetry scan at 5mV/s from ocp to $V = -0.9 V_{RHE}$ with 5 minutes hold as the reaction time. These data evidence that both NDs react and their stoichiometry dictates the reaction outcome.

After reaction, TEM evidences that aggregated NPs with a clear diffraction contrast form from the Ga/Cu_{0.7} NDs (**Figure 5.2D**); instead, the Ga/Cu_{0.1} NDs transform into better defined NPs each consisting of a smaller solid domain exhibiting diffraction contrast embedded in a larger amorphous shell (**Figure 5.2E**). The STEM-EDXS elemental map shows a clear overlap between the Ga and Cu signal for the reaction product of the Ga/Cu_{0.7} NDs (**Figure 5.2F**), which hints at the formation of an alloy. The overlap of the Ga and Cu signal is noticeable only in the smaller domains of the reaction product of the Ga/Cu_{0.1} NDs, while the larger shell appears to be mostly constituted by Ga (**Figure 5.2G**). Quantitative analysis of the elemental maps revealed that the Ga/Cu ratio of the NDs is preserved in their final products, which indicates that the reaction goes to completion.

Intrigued by the differences between the reaction products when the NDs of different stoichiometry are used as precursors, we performed additional structural characterization (**Figure 5.3**). Electron (SAED, **Figure 5.3A-C**) and grazing incidence X-Ray diffraction (GIXRD, **Figure 5.3D**) provided information on the crystal structure. Both analyses propose the existence of the same crystalline phase in the reaction products from both Ga/Cu_{0.7} and Ga/Cu_{0.1} NDs. This phase matches well the CuGa₂ intermetallic phase. This observation agrees with reports on bulk liquid Ga – Cu, where reactive wetting results in CuGa₂ formation.^{242–244} The large reflection width in the SAED pattern for the NPs derived from Ga/Cu_{0.1} NDs (**Figure 5.3C**) originates from small crystallite size (<15 nm), small amount of crystalline phase which is only in the core, and peak overlap due to the relatively low symmetry of CuGa₂ phase, which crystallizes in tetragonal *P4/mmm* space group.

In addition, we performed HAADF-STEM imaging and STEM-EDXS line profile and elemental mapping on single NPs (**Figure 5.3E,F**). For the product obtained from Ga/Cu_{0.7} NDs (**Figure 5.3E**), HAADF-STEM evidences that the product NPs are composed of a uniform core with thin (*ca.* 2 nm) shell of lower density. The line profile indicates the homogeneous distribution of the Cu and Ga within the NPs, which, along with the overlap of the Cu and Ga signals in the NPs and their atomic composition (66 at. % Ga, 34 at. % Cu), confirms that these NPs are mostly composed of CuGa₂ intermetallic. A thin layer of oxide, most likely forming from air exposure,^{209,245} surrounds the NPs. We will further refer to these NPs as CuGa₂ NPs.

In contrast, the line profile of the product obtained from Ga/Cu_{0.1} NDs (**Figure 5.3F**) indicates that Cu is mostly concentrated in the *ca.* 10 – 15 nm crystalline core while the Ga is

more uniformly distributed across the entire NPs. The atomic composition of the core is representative of CuGa_2 alloy (66 at. % Ga, 34 at. % Cu). This core is surrounded by a region which is Ga-rich (84 at. % Ga, 16 at. % Cu). Lastly, the NPs are covered with a 2 – 3 nm layer of Ga oxide. As CuGa_2 is the only crystalline Ga-containing phase in the sample, the Ga-rich region between the core and the oxide is amorphous and, most likely, liquid.¹⁷¹ Thus, we will refer to these NPs as solid@liquid CuGa_2 @Ga core@shell.

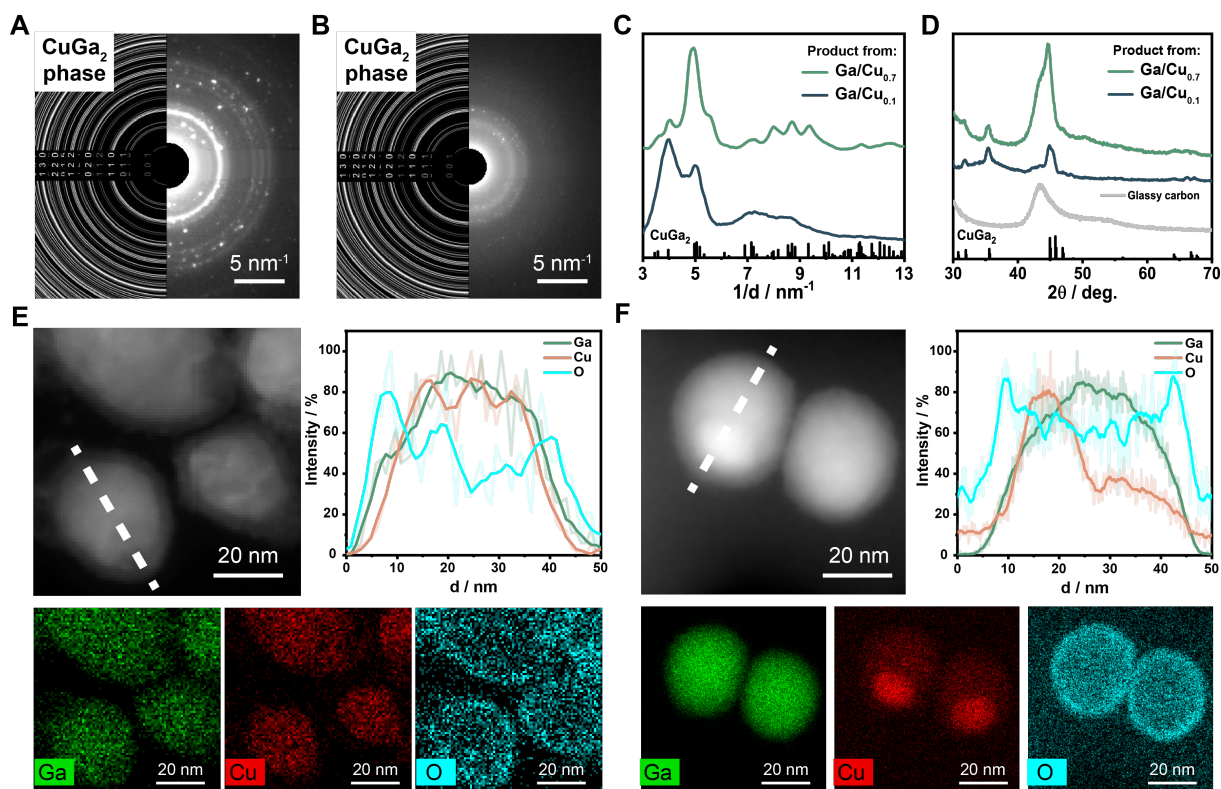


Figure 5.3. Structural characterization of Ga – Cu NPs obtained via the voltage-driven synthesis. (A-C) SAED patterns of the reaction product from (A) $\text{Ga/Cu}_{0.7}$ and (B) $\text{Ga/Cu}_{0.1}$ NDs and (C) their corresponding circular averaged electron diffraction. (D) GIXRD patterns of the reaction products from $\text{Ga/Cu}_{0.7}$ and $\text{Ga/Cu}_{0.1}$ NDs (the broad reflections at *ca.* 43° and 54° in the arise from the amorphous glassy carbon support). (E,F) HAADF-STEM, STEM-EDXS line profiles and elemental maps (Ga – green, Cu – red, O – cyan) of the reaction product from (E) $\text{Ga/Cu}_{0.7}$ and (F) $\text{Ga/Cu}_{0.1}$ NPs. These data indicate that the $\text{Ga/Cu}_{0.7}$ NDs transform into CuGa_2 intermetallic NPs while the $\text{Ga/Cu}_{0.1}$ NDs yield solid@liquid CuGa_2 @Ga core@shell NPs.

5.3 Influence of synthesis parameters on the reaction outcome

We then varied the reaction time and the voltage to understand the impact of these parameters on the formation of Ga – Cu NPs in the voltage-driven synthesis. We used Ga/Cu_{0.7} NDs as the precursor and collected a voltage series, where we changed the voltage from -0.5 V_{RHE} to -1.1 V_{RHE} (**Figure 5.4**). At -0.5 V_{RHE}, no reaction between Cu and Ga occurs and the NDs remain mostly unchanged with separated Cu and Ga domains as seen by HAADF-STEM images and STEM-EDXS elemental maps. The SAED pattern shows no CuGa₂ formation, and the main crystalline phase is Cu₂O.

At -0.7 V_{RHE}, HAADF-STEM indicates substantial change of the NDs into bigger NPs. STEM-EDXS evidences mixing of Cu and Ga, although with inhomogeneity in the sample which still contains some unreacted Ga and Cu domains. SAED pattern indicates the presence of CuGa₂.

The fact that Cu and Ga in the NDs react at a potential more negative than -0.5 V_{RHE} indicates that the oxide removal is crucial for the reaction to occur between the Cu and Ga NPs. In fact, previous studies on Ga NPs under the same conditions indicated that the Ga oxide skin reduces at -0.54 V_{RHE}.¹⁷¹

Sample degradation eventually occurs at -1.1 V_{RHE} which induces Cu fragmentation and coalescence of liquid Ga NPs, consistent with previous studies.^{7,45,46,165,171}

With this information, we conclude that -0.9 V_{RHE} offers a good balance between providing sufficient driving force for alloy formation without leading to undesired reconstruction of the NPs.

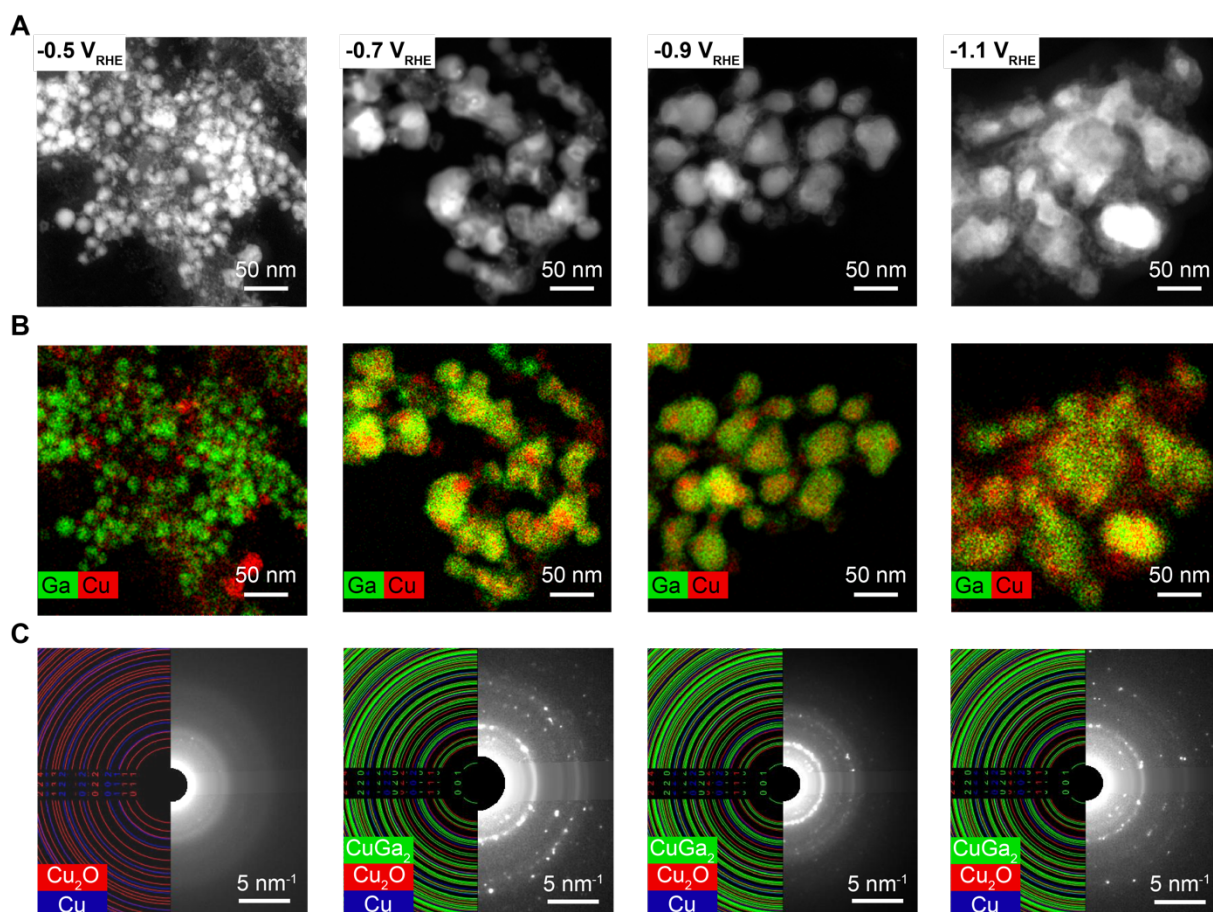


Figure 5.4. Voltage-dependence of the voltage-driven synthesis from Ga/Cu_{0.7} NDs as the precursor. (A) STEM images, (B) STEM-EDXS elemental maps and (C) SAED patterns after voltage scan from ocp to -0.5, -0.7, -0.9 and -1.1 V_{RHE} with 5 min hold as the reaction time. These data indicate that an optimal voltage exists to controllably form the Ga – Cu NPs; this voltage reduces the Ga native skin without driving the reconstruction of the Ga – Cu NPs which form as the reaction product.

In a complementary set of experiments, we fixed the voltage at -0.9 V_{RHE} and varied the reaction time from 1 minute to 60 minutes (**Figure 5.5**). HAADF-STEM image indicates substantial change of the NDs into larger NPs already after 1 minute; however, the STEM-EDXS elemental maps and SAED patterns suggest that the reaction is not complete yet after this time. Indeed, Cu and Ga are mostly separated, as in the NDs used as precursors, and the diffraction signal is relatively weak. During this early reaction time, the reaction is probably still confined at the interface only.

As time passes and the reaction progresses, HAADF-STEM images do not show substantial change, however the STEM-EDXS maps indicate a spatially homogeneous distribution of the Cu and Ga signal while the CuGa₂ diffraction signal in the SAED becomes more intense. The samples at 5 and 30 minutes are quite similar to each other. Instead, segregation between the Cu and Ga occurs after 60 minutes, as indicated by the STEM-EDXS maps, with the SAED pattern suggesting the dominance of crystalline Cu₂O in the sample.

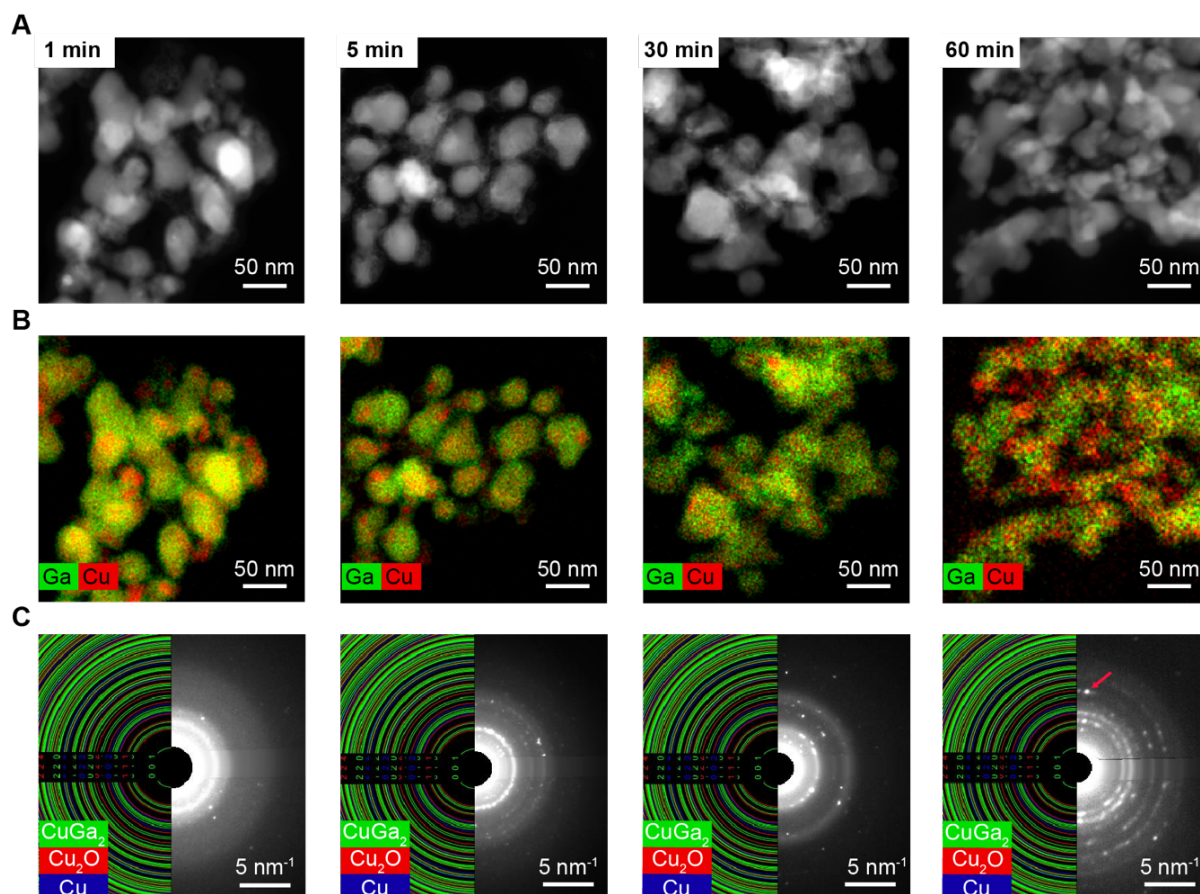


Figure 5.5. Time-dependence of the voltage-driven synthesis from Ga/Cu_{0.7} NDs as the precursor. (A) STEM images, (B) STEM-EDXS elemental maps and (C) SAED patterns after voltage scan from ocp to $-0.9 V_{RHE}$ with 1, 5, 30 and 60 minutes hold as the reaction time. CuGa₂ is the main crystalline phase at 5 and 30 minutes, instead Cu₂O dominates at 60 minutes (the (022) diffraction spot is marked by red arrow for clarity). These data indicate that the reaction reaches completion at 5 minutes while phase segregation takes place for reaction time ≥ 60 minutes.

Lastly, we evaluated the impact of the voltage scan rate on the reaction outcome. Interestingly, the application of a voltage step instead of a voltage scan makes Ga disappear from the substrate, with less Ga being detected at more negative voltage (**Figure 5.6**). CuGa_2 does not form in this scenario.

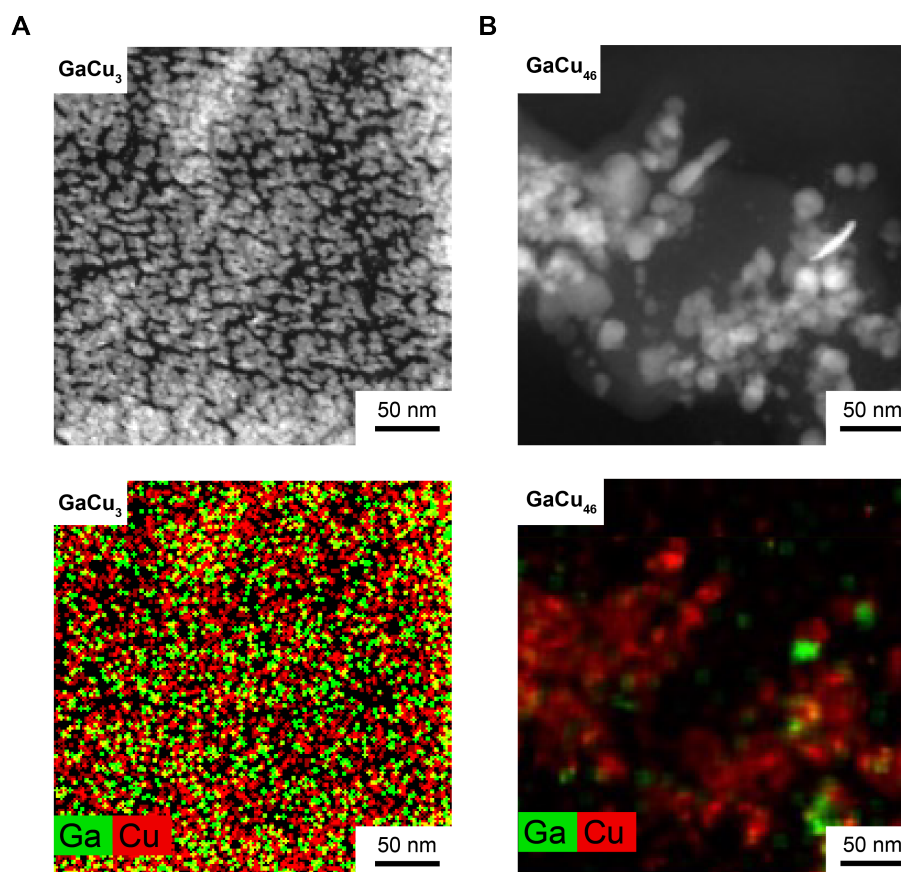


Figure 5.6. Scan rate-dependence of the voltage-driven synthesis from Ga/Cu_{0.7} NDs as the precursor. HAADF-STEM images and STEM-EDXS elemental maps (Ga – green, Cu – red) of Ga/Cu_{0.7} NDs after the application of a voltage step to (A) $-0.9 V_{\text{RHE}}$ and to (B) $-1.4 V_{\text{RHE}}$ then hold for 5 min as the reaction time. The atomic composition in top-left part of the images corresponds to STEM-EDXS quantification results after the reaction and, assuming that Cu content remains the same, corresponds to more than 80 and 90 % Ga loss, respectively

To better understand how the Ga loss takes place, we complemented these tests with studies on bulk liquid Ga – Cu samples, which consisted of a Ga droplet deposited on a Cu foil (**Figures 5.7, 5.8**). Here, we made observations similar to those made on the NDs. The Ga drop remains on Cu surface, eventually wets it and forms CuGa_2 intermetallic at the interface

(**Figure 5.7A**) when the voltage is applied at 5 mV/s.^{242,243} On the contrary, the Ga droplet quickly escapes from the Cu foil surface (**Figure 5.7B**) or from the surface of the inert glassy carbon support (**Figure 5.7C**) upon the application of a voltage step instead of a linear scan. We observed the same behavior for a bulk “dimer” structure which mimics the liquid Ga/Cu NDs, where only a 5 mV/s scan enables Cu and Ga to react and form a CuGa₂ interface (**Figure 5.8**).

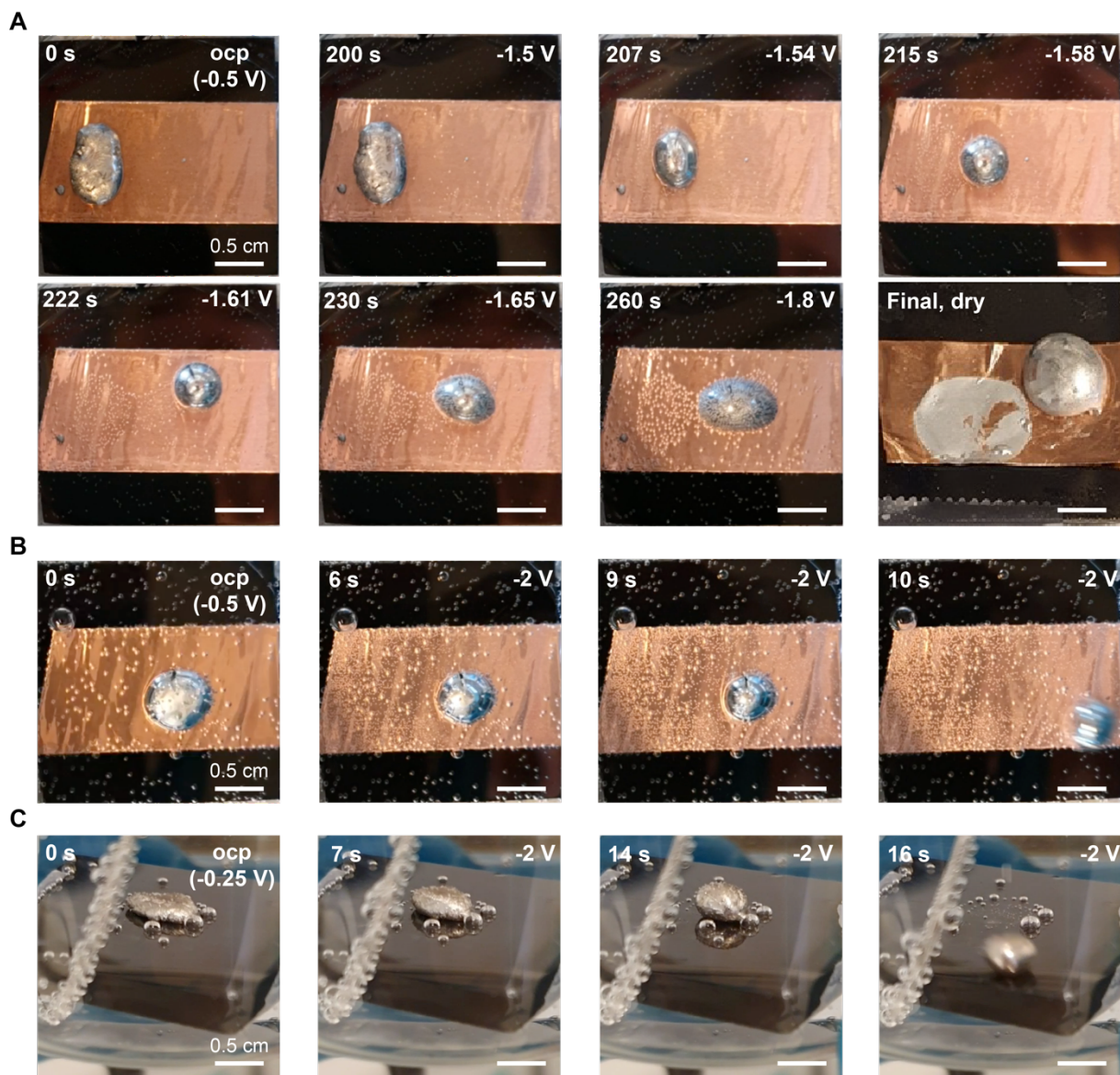


Figure 5.7. Snapshots of voltage-driven reactions between bulk liquid Ga and Cu. Images at selected time points representative of the (bulk liquid Ga – Cu foil and Ga – glassy carbon transformations during (A) linear voltage scan at 5 mV/s and (B, C) application of voltage step. If there is no voltage applied, no interface is formed between Cu and Ga.



Figure 5.8. Snapshots of voltage-driven reactions between bulk liquid Ga and Cu which mimic the dimer configuration. Images at selected time points representative of the bulk liquid Ga – Cu “sphere” mimicking the nanodimer in the bulk during cathodic linear voltage scan at (A) 5 mV/s and (B) 10 mV/s.

5.4 Mechanism of the voltage-driven reaction between Ga and Cu

With the evidence provided by the compositional and structural analyses and the study of the synthesis parameters discussed above, a complete picture of the reaction mechanism shapes up (**Figure 5.9**).

The liquid Ga/Cu ND precursors are described as an oxide-covered Ga domain in contact with a metallic Cu domain. The abrupt application of a cathodic voltage, which is sufficient to reduce the Ga oxide skin ($< -0.54 V_{RHE}$), induces a sudden increase in surface tension of the liquid Ga domain, while Cu domain remains static. Ga does not wet Cu.²⁴² Thus, Ga escapes from Cu. A similar effect was observed by Mayyas et al.²³⁶ Here, the authors showed that In can be expelled from an eutectic GaIn melt in the form of NPs by applying voltage pulses of large magnitude.

The repulsion between Cu and Ga can be overturned by decreasing the reduction rate of the oxide skin to allow sufficient time for the intermetallic to form, which eventually changes the wetting behavior. We achieved such balance by tuning the rate of the applied voltage and found

5 mV/s to be an optimal rate. Once the CuGa_2 interface forms, reactive wetting takes place, and the reaction proceeds further towards the bulk of the NPs. While a similar process may occur in the physical mixture of Cu and liquid Ga NPs (**Figure 5.1**), the NDs provide more uniform mixing of the Cu and Ga domains, which largely improves the uniformity of resulting intermetallic NPs.

As reactive wetting takes place, the stoichiometry of the two reagents Cu and Ga in the ND precursors determines the outcome product. For $\text{Ga}:\text{Cu} < 2:1$ (i.e. $\text{Ga}/\text{Cu}_{0.7}$ NDs), the reaction goes to completion and CuGa_2 forms almost uniquely. Differently, for $\text{Ga}:\text{Cu} > 2:1$ (i.e. $\text{Ga}/\text{Cu}_{0.1}$ NDs), the excess Ga wets the CuGa_2 surface, resulting in a peculiar process described as wetting-assisted internalization of a solid NPs in the liquid Ga NPs, and yielding a solid CuGa_2 core floating inside the liquid metal Ga host NPs, similarly to a phenomenon previously observed in Cu-In microparticles.²⁵⁰ Liquid Ga, in its turn, remains covered by a non-passivating Ga oxide skin, which keeps the NPs separate and hinders their coalescence. This observation provides an interesting correlation with Chapter 4 and suggests that the non-passivating oxide skin is probably of transient nature and is constantly formed and reduced at cathodic voltage (**Figure 4.9B,C**), rather than remaining as a static residual skin (**Figure 4.9A**). Indeed, a static skin would not allow the pure metallic contact of liquid Ga with Cu domain accompanied by the formation of CuGa_2 intermetallic.

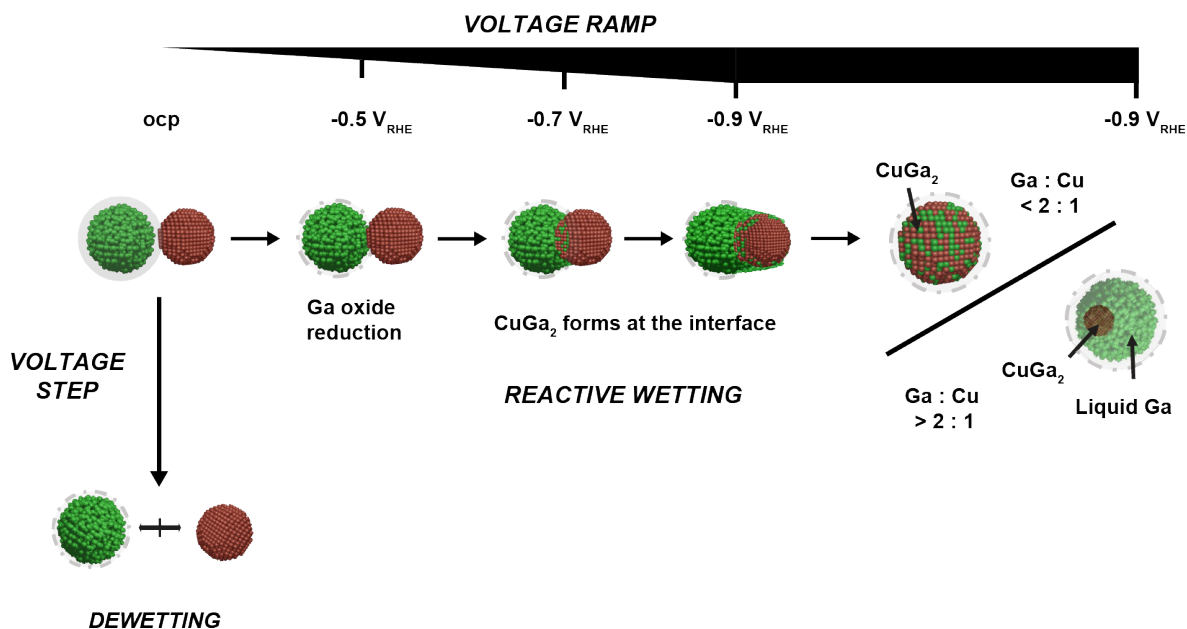


Figure 5.9. Schematic of the voltage-driven reaction of liquid Ga/Cu NDs.

Lastly, we hypothesize that the more Cu-rich phases than CuGa_2 in the Ga-Cu phase diagram (Cu_9Ga_4 and the Cu *fcc*-based solid solution of Ga in Cu) do not form because of the high activation barrier which the transformation from the CuGa_2 structure to these other phases requires. Interestingly, we have approached the opposite limitation in Chapter 3, where we used a seeded-growth amalgamation reaction in solution to form Ga – Cu alloyed NPs. In Chapter 3, starting from a Cu NPs seed and injecting a Ga molecular precursor, we obtained the Cu-rich phases of the Ga – Cu phase diagram (**Figure 3.1**), but any phase more Ga-rich than Cu_9Ga_4 -type phase (such as CuGa_2) was not accessible. With this study, we obtain this missing Ga – Cu intermetallic composition and expand the Ga – Cu NPs library demonstrating the complementarity of synthetic approaches exploiting different driving forces.

5.5 Generality of the voltage-driven liquid Ga reactivity at the nanoscale

Chemical reactivity (*i.e.*, reactivity driven by the formation of stable bimetallic compounds) and wetting are both in place for the Ga – Cu system. To understand if and how the voltage-driven synthesis can be extended to form other Ga-based NPs, we tested the synthesis with other metals. We chose Ag, Co, W and Sn as other elements to react with Ga based on the following reasoning. Ag and Co are both transition metals which form intermetallic compounds with Ga based on bulk phase diagrams. However, Ag is reactively wetted by Ga, while Co may not be, based on its vicinity to Ni for which a previous study exist.²⁴³ W is a transition metal which does not chemically react with Ga in the bulk at ambient conditions.¹⁶⁴ Sn is an example of post-transition metal, for which no intermetallic formation is reported.²⁵¹ To the best of our knowledge, no information on the wettability of W and Sn by Ga has been reported. By evaluating how the reaction between Ga and Ag, Co, W and Sn proceeds, we aimed at create a basis to establish the primary design rules for the formation of Ga-based NPs with other metals among the Periodic Table, where we targeted transition (Ag, Co, W) and post-transition (Sn) metals which normally do (Ag, Co) and do not (W, Sn) react with Ga, potentially with a different wetting behavior between Ag and Co.

With this in mind, we synthesized Ga/M NDs ($M = \text{Ag, Co, Sn}$) and prepared physical mixture of Ga with WO_3 NPs of overall $\text{Ga}(\text{WO}_3)_{0.1}$ composition (**Figure 5.10**). We reacted them under the same optimal conditions found for the Ga – Cu (*i.e.*, 5mV/s ramp from ocp to $-0.9 V_{\text{RHE}}$ and 5 min reaction time at this voltage). **Figure 5.11** summarizes the obtained results.

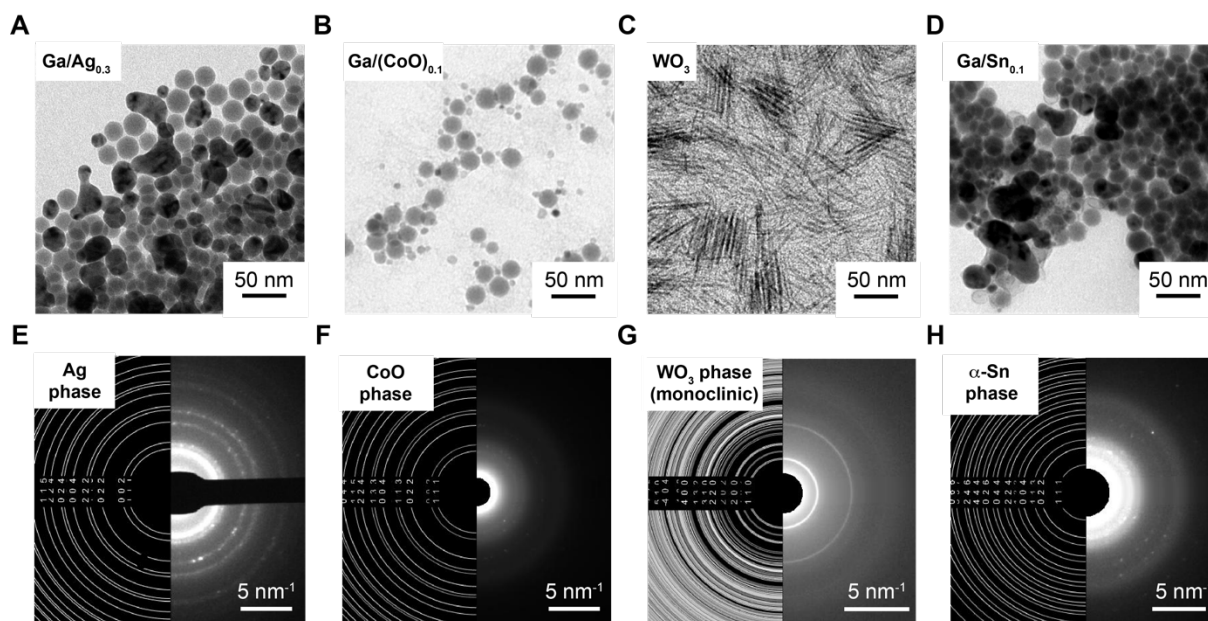


Figure 5.10. Characterization of as-synthesized Ga/M NDs ($M = \text{Ag}, \text{CoO}, \text{Sn}$) and WO_3 NPs. (A-D) TEM images and (E-F) SAED patterns of as-synthesized (A,E) $\text{Ga}/\text{Ag}_{0.3}$, (B, F) $\text{Ga}/(\text{CoO})_{0.1}$ NDs, (C, G) WO_3 NPs and (D, F) $\text{Ga}/\text{Sn}_{0.1}$ NDs. In all cases, we attribute amorphous domains lacking diffraction contrast to Ga, and the crystalline domains to the second metal. We note that the tailored synthesis of NDs of these compositions has not been previously reported and obtaining highly uniform samples requires further optimization of the synthetic procedure. As Ga/W NDs are not synthetically available to date, we have used the physical mixture of liquid Ga NPs and WO_3 NPs in voltage-driven synthesis.

$\text{Ga}/\text{Ag}_{0.3}$ NDs react to form new NPs including smaller NPs with diffraction contrast embedded into larger amorphous NPs (**Figure 5.11A**). STEM-EDXS evidences the presence of Ag and Ga in the smaller NPs and Ga only in the larger domain (**Figure 5.11E**). SAED indicates that the crystalline domains internalized in the Ga are Ag_2Ga (**Figure 5.11I**). Overall, Ag react similarly to Cu, consistently with its wettability by Ga and chemical reactivity.²⁴³

Interestingly, $\text{Ga}/(\text{CoO})_{0.1}$ NDs do not react despite the phase diagram showing that stable intermetallic compounds are formed between Ga and Co. Indeed, both TEM (**Figure 5.11B**) and STEM-EDXS (**Figure 5.11F**) are consistent with the dimer-like configuration of the starting precursor (**Figure 5.10B**), and the SAED (**Figure 5.11J**) indicates only crystalline cobalt oxide. One hypothesis is that the eventual presence of an Co oxide at cathodic voltages hinders its reaction with Ga. However, the Pourbaix diagram makes the existence of CoO

improbable during the reaction, as CoO supposedly reduces to metallic Co at more positive voltages than Ga (0.1 vs. -0.5 V_{RHE} , respectively).¹⁴² Thus, non-wetting of Co with Ga may justify the absence of reaction and internalization of Co into Ga, similar to earlier report suggesting the non-sufficient wetting of Ni with Ga for its internalization in bulk drops.²⁴³

The physical mixture of liquid Ga NPs and WO_3 NPs react to form a new material, based on TEM images, which is different compared to the starting NPs (**Figure 5.11C**, **Figure 5.10C,G**). The W signal in STEM-EDXS spectrum is above the detection limit in the Ga – W NPs after the reaction, yet the intensity is too low to localize it in a particular part of the new NPs (**Figure 5.11G**). The SAED (**Figure 5.11K**) suggests the formation of Ga_5W_2 as minor reaction product, an intermetallic compound which is reported to exist at elevated pressures²⁵². While SAED is not conclusive because of the weak diffraction signal, this result indicates that new reactivities might emerge at the nanoscale.

Lastly, TEM image proposes the presence of a solid particle in Ga (**Figure 5.11D**) as a result of the voltage-driven reaction of Ga/Sn_{0.1} NDs. However, STEM-EDXS elemental mapping shows no reliable Sn signal (**Figure 5.11H**). Yet, SAED suggests that crystalline domains do form (**Figure 5.11L**). While acknowledging the limited information that this diffraction pattern provides for low-symmetry phases, the signal matches δ -Ga, which has been reported to be a stable crystalline phase in the Ga NPs.^{161,171} The Ga and Sn phase diagram does not suggest intermetallic formation.²⁵¹ Thus, we speculatively attribute this result to Ga doping with Sn, facilitating partial Ga solidification.

Altogether, the reactivity studies of Ga/Ag, Ga/(CoO), Ga-(WO_3)_{0.1} and Ga/Sn along with that of the Ga/Cu indicate that wetting and chemical reactivity are good indicators for a successful voltage-driven synthesis of Ga-based NPs. At the same time, new reactivities might still emerge at the nanoscale which deviate from this golden rule and are worth exploring. With the assumption that other metal NPs can be reactively wetted by Ga, we believe our observations indicate the possibility to extend the scope of reactive wetting to synthesize a larger library of bimetallic Ga-based NPs.

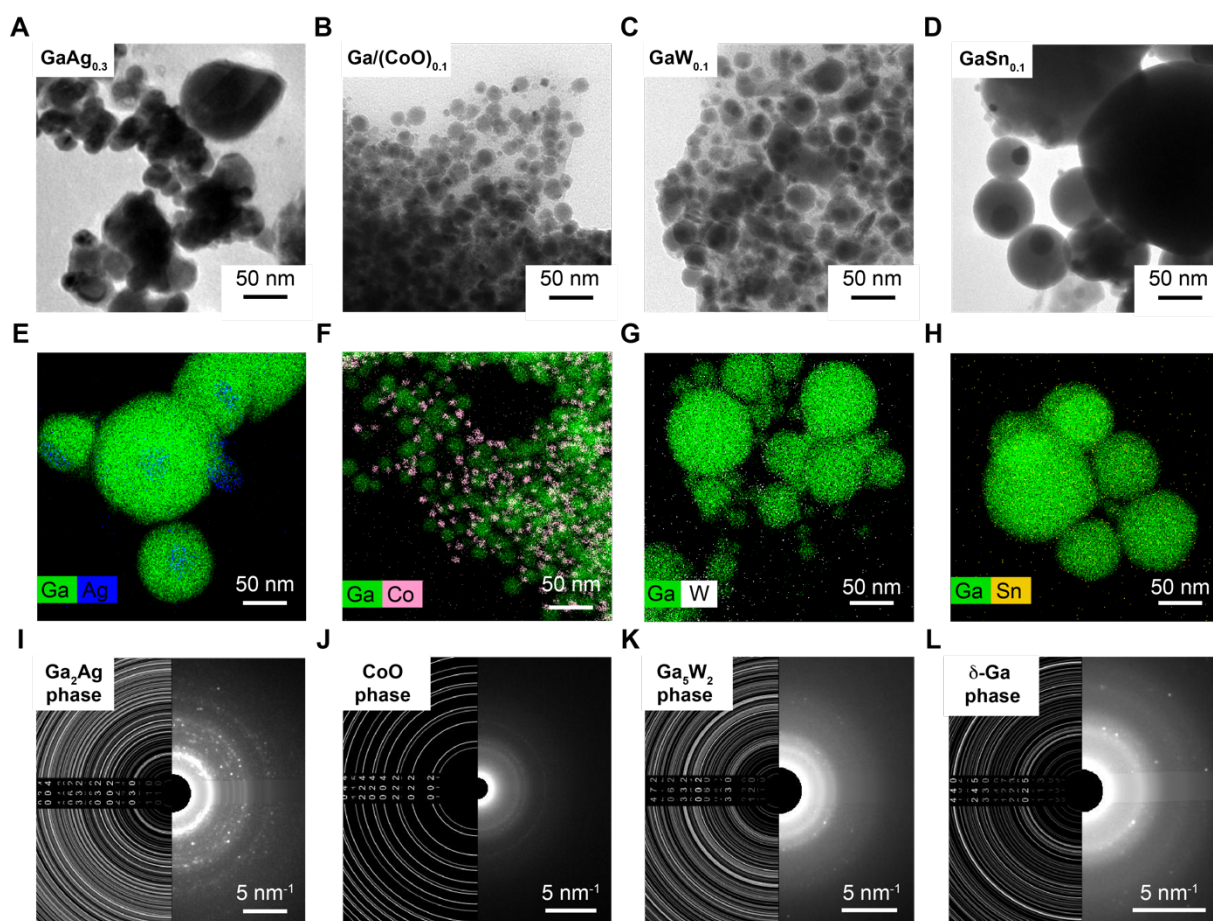


Figure 5.11. Extension of the voltage-driven synthesis to different Ga-M systems. (A – D) TEM images, (E – H) STEM-EDXS elemental maps and (I – K) SAED patterns of the reaction products obtained from (A, E, I) Ga/Ag_{0.3} NDs, (B, F, J) Ga/(CoO)_{0.1} NDs, (C, G, K) physical mixture of Ga and WO₃ NPs and (D, H, L) GaSn_{0.1}. These data indicate that both wettability and chemical reactivity are important in determining the reaction outcome.

5.6 Conclusions

In this study, we explored the chemical reactivity of liquid Ga NPs with other metal NPs driven by an applied voltage. We demonstrated that the rate of such voltage, which controls the reduction rate of the native Ga oxide skin, along with the wetting properties between elements and their chemical reactivities, enables the reactive wetting of liquid Ga NPs and the formation of bimetallic Ga-based NPs.

We discovered that CuGa₂ alloyed NPs and solid@liquid core@shell NPs, where a CuGa₂ nanocrystal floats inside a liquid Ga NPs, can be obtained from liquid Ga/Cu NDs, which we

used as a case study, by tuning the initial stoichiometry of Ga and Cu. While the same approach applies to the physical mixture of Cu and Ga NPs, the NDs ensure more uniform mixing on the NPs precursors. The formation of Ga-rich alloys points at the complementarity of the thermal and voltage driven synthesis to expand the compositional range of bimetallic NPs. The solid@liquid NPs are unique and only a few other examples exist in the literature, although not with the same degree of sample homogeneity obtained herein.^{100,250,253}

Finally, we proved that this approach can be extended to the combination of Ga with other elements (Ag, Co, W, Sn).

By presenting a rational framework which explains the formation of bimetallic NPs via the proposed voltage-driven synthesis, we believe this report sets the ground for future studies targeting various applications for multimetallic Ga-based NPs, including those with a liquid Ga domain.

Chapter 6

Conclusions and outlook

The electrochemical CO₂ reduction (CO₂RR) is a particularly promising approach for CO₂ utilization which enables the simultaneous storage of renewable energy in chemical bonds. Cu-based nanoparticles (NPs), with intrinsically high surface to volume ratio, hold high potential as catalysts of choice to selectively drive this reaction towards desirable products, which include methane, ethylene and ethanol. However, strategies to mitigate the reconstruction of these NPs during CO₂RR are needed to eventually achieve stability of operations.

This thesis proposed two different approaches to obtain more stable CO₂RR catalysts. The first one builds up on the current mechanistic knowledge on the reconstruction of Cu NPs, which is a dissolution/precipitation process driven by intrinsic surface redox processes of copper and by the chemical interaction of copper surface atoms with CO₂RR intermediates, specifically CO. This first strategy consists in alloying Cu with a metal M which is more oxophilic than Cu and provide a Cu-M bond stronger than Cu-Cu. The second approach proposes a shift from solid heterogeneous catalysts to liquid heterogeneous catalysts which are intrinsically dynamic in their nature.

After presenting the relevant context in Chapter 1 and covering the experimental protocols in Chapter 2, Chapter 3 demonstrated the promise of alloying Ga into Cu to enhance the stability of the NPs catalysts in CO₂RR. CuGa NPs with 17 Ga atomic % still preserved 50% of their CO₂RR activity after 20 hours of operation compared to a complete loss of CO₂RR activity in the parent Cu NPs after only 2 hours. A miscellanea of characterization techniques (STEM-EDXS, XPS, *operando* XAS), along with theory, indicated that alloying induces electronic effects which strengthen the chemical bonding of Cu with the lattice and prevents Cu oxidation both at the start-up of operation and during CO₂RR.

Chapters 4 and 5 focused on exploring the possibility of using LM NPs as CO₂ electrocatalysts and, in broader sense, in electrochemical applications.

Chapter 4 proved that LM NPs can be implemented as electrocatalysts in aqueous electrolytes. In particular, the data evidenced that liquid Ga NPs can drive CO₂RR while

remaining well-separated from each other (*i.e.*, not turning into a bulk liquid film). The combination of electrochemical, microscopic, and spectroscopic techniques, including *operando* X-Ray absorption, indicated that the unique properties of the native oxide skin of the Ga NPs account for their resistance to coalescence during operation. Specifically, the oxide stays present in a dynamic fashion while the cathodic potential is applied.

In a complementary manner, Chapter 5 revealed the key role played by the oxide skin in driving the chemical reactivity between Ga and other metals under the application of a cathodic voltage. In fact, the rate of the voltage ramp, which controls the reduction rate of the Ga oxide skin, was found to be crucial to enable reactive wetting of other metals by liquid Ga NPs. This finding is important because it contributes to define the reactivity criteria of liquid metals under conditions relevant for electrochemical applications, which are so far underexplored. Furthermore, the obtained reaction products, which included alloyed NPs and solid@liquid core@shell NPs, unique in their composition and morphology respectively, revealed the potential of this voltage-driven manipulation of chemical reactivity as a synthesis technique on its own.

Looking forward, further development of alloyed Cu-based NPs can be foreseen to diversify the product selectivity. Overall, CuGa NPs were found to be more stable than Cu NPs, however they produced methane, which is not the most desirable CO₂RR product. Other metals which have higher oxophilicity and strong M – Cu bonding energies (*e.g.*, early 3*d* metals: Sc, Ti, and *p*-group metals: Al, In, Bi) are expected to have similar mechanism of hindering Cu reconstruction while driving CO₂RR towards different products of interest and, in general, generating more stable NPs. Thus, they might be worth exploring to understand how to tune their selectivity along with stability.

As for the use of LM NPs as CO₂RR electrocatalysts, the next crucial step is to demonstrate that products different than the CO obtained for Ga NPs can be produced while preserving the liquid nature of the NPs. Here, an ideal system can be envisioned wherein single atoms or clusters of a metal different than Ga are dispersed within the Ga core and pop-up on the surface under reducing conditions, as demonstrated in thermal catalysis, for example. The challenge is now the synthesis and different efforts are needed to increase the library of LM NPs.

Finally, only time will tell if either or both approaches will yield NPs catalyst with unprecedented performance.

References

- (1) Tyndall, J. On the Absorption and Radiation of Heat by Gases and Vapours, and on the Physical Connexion of Radiation, Absorption, and Conduction. *Philos. Trans. R. Soc. London* **1861**, *151*, 1–36. DOI: [10.1098/rstl.1861.0001](https://doi.org/10.1098/rstl.1861.0001).
- (2) Arrhenius, S. On the Influence of Carbonic Acid in the Air upon the Temperature of the Ground. *Philos. Mag. J. Sci. Ser.* **1896**, *5*, 237–276.
- (3) James Rodger Fleming. *Historical Perspectives on Climate Change*; Oxford University Press, Inc.: New York, 1998.
- (4) UNFCCC. *The Paris Agreement*; 2015.
- (5) Shukla, P. R.; Skea, J.; Slade, R.; Khourdajie, A. Al; van Diemen, R.; McCollum, D.; Pathak, M.; Some, S.; Vyas, P.; Fradera, R.; Belkacemi, M.; Hasija, A.; Lisboa, G.; Luz, S.; Malley, J. *Climate Change 2022: Mitigation of Climate Change. Contribution of Working Group III to the Sixth Assessment Report of the Intergovernmental Panel on Climate Change*; Cambridge, New York, 2022. DOI: [10.1017/9781009157926](https://doi.org/10.1017/9781009157926).
- (6) Nitopi, S.; Bertheussen, E.; Scott, S. B.; Liu, X.; Engstfeld, A. K.; Horch, S.; Seger, B.; Stephens, I. E. L.; Chan, K.; Hahn, C.; Nørskov, J. K.; Jaramillo, T. F.; Chorkendorff, I. Progress and Perspectives of Electrochemical CO₂ Reduction on Copper in Aqueous Electrolyte. *Chem. Rev.* **2019**, *119*, 7610–7672. DOI: [10.1021/acs.chemrev.8b00705](https://doi.org/10.1021/acs.chemrev.8b00705).
- (7) Popović, S.; Smiljanić, M.; Jovanović, P.; Vavra, J.; Buonsanti, R.; Hodnik, N. Stability and Degradation Mechanisms of Copper-Based Catalysts for Electrochemical CO₂ Reduction. *Angew. Chem., Int. Ed.* **2020**, *59*, 14736–14746. DOI: [10.1002/anie.202000617](https://doi.org/10.1002/anie.202000617).
- (8) Hori, Y. Electrochemical CO₂ Reduction on Metal Electrodes. In *Modern Aspects of Electrochemistry*; Springer New York, 2008; pp 89–189. DOI: [10.1007/978-0-387-49489-0_3](https://doi.org/10.1007/978-0-387-49489-0_3).
- (9) Gao, D.; Arán-Ais, R. M.; Jeon, H. S.; Roldan Cuenya, B. Rational Catalyst and Electrolyte Design for CO₂ Electroreduction towards Multicarbon Products. *Nat. Catal.* **2019**, *2*, 198–210. DOI: [10.1038/s41929-019-0235-5](https://doi.org/10.1038/s41929-019-0235-5).

- (10) Burdyny, T.; Smith, W. A. CO₂ Reduction on Gas-Diffusion Electrodes and Why Catalytic Performance Must Be Assessed at Commercially-Relevant Conditions. *Energy Environ. Sci.* **2019**, *12*, 1442–1453. DOI: [10.1039/c8ee03134g](https://doi.org/10.1039/c8ee03134g).
- (11) Smith, W. A.; Burdyny, T.; Vermaas, D. A.; Geerlings, H. Pathways to Industrial-Scale Fuel Out of Thin Air from CO₂ Electrolysis. *Joule* **2019**, *3*, 1822–1834. DOI: [10.1016/j.joule.2019.07.009](https://doi.org/10.1016/j.joule.2019.07.009).
- (12) Kuhl, K. P.; Cave, E. R.; Abram, D. N.; Jaramillo, T. F. New Insights into the Electrochemical Reduction of Carbon Dioxide on Metallic Copper Surfaces. *Energy Environ. Sci.* **2012**, *5*, 7050–7059. DOI: [10.1039/c2ee21234j](https://doi.org/10.1039/c2ee21234j).
- (13) De Gregorio, G. L.; Burdyny, T.; Loiudice, A.; Iyengar, P.; Smith, W. A.; Buonsanti, R. Facet-Dependent Selectivity of Cu Catalysts in Electrochemical CO₂ Reduction at Commercially Viable Current Densities. *ACS Catal.* **2020**, *10*, 4854–4862. DOI: [10.1021/acscatal.0c00297](https://doi.org/10.1021/acscatal.0c00297).
- (14) Wang, X.; Wang, Z.; García de Arquer, F. P.; Dinh, C. T.; Ozden, A.; Li, Y. C.; Nam, D. H.; Li, J.; Liu, Y. S.; Wicks, J.; Chen, Z.; Chi, M.; Chen, B.; Wang, Y.; Tam, J.; Howe, J. Y.; Proppe, A.; Todorović, P.; Li, F.; Zhuang, T. T.; Gabardo, C. M.; Kirmani, A. R.; McCallum, C.; Hung, S. F.; Lum, Y.; Luo, M.; Min, Y.; Xu, A.; O'Brien, C. P.; Stephen, B.; Sun, B.; Ip, A. H.; Richter, L. J.; Kelley, S. O.; Sinton, D.; Sargent, E. H. Efficient Electrically Powered CO₂-to-Ethanol via Suppression of Deoxygenation. *Nat. Energy* **2020**, *5*, 478–486. DOI: [10.1038/s41560-020-0607-8](https://doi.org/10.1038/s41560-020-0607-8).
- (15) Xu, A.; Hung, S. F.; Cao, A.; Wang, Z.; Karmodak, N.; Huang, J. E.; Yan, Y.; Sedighian Rasouli, A.; Ozden, A.; Wu, F. Y.; Lin, Z. Y.; Tsai, H. J.; Lee, T. J.; Li, F.; Luo, M.; Wang, Y.; Wang, X.; Abed, J.; Wang, Z.; Nam, D. H.; Li, Y. C.; Ip, A. H.; Sinton, D.; Dong, C.; Sargent, E. H. Copper/Alkaline Earth Metal Oxide Interfaces for Electrochemical CO₂-to-Alcohol Conversion by Selective Hydrogenation. *Nat. Catal.* **2022**, *5*, 1081–1088. DOI: [10.1038/s41929-022-00880-6](https://doi.org/10.1038/s41929-022-00880-6).
- (16) Kim, D.; Yu, S.; Zheng, F.; Roh, I.; Li, Y.; Louisia, S.; Qi, Z.; Somorjai, G. A.; Frei, H.; Wang, L. W.; Yang, P. Selective CO₂ Electrocatalysis at the Pseudocapacitive Nanoparticle/Ordered-Ligand Interlayer. *Nat. Energy* **2020**, *5*, 1032–1042. DOI: [10.1038/s41560-020-00730-4](https://doi.org/10.1038/s41560-020-00730-4).

- (17) Bhargava, S. S.; Proietto, F.; Azmoodeh, D.; Cofell, E. R.; Henckel, D. A.; Verma, S.; Brooks, C. J.; Gewirth, A. A.; Kenis, P. J. A. System Design Rules for Intensifying the Electrochemical Reduction of CO₂ to CO on Ag Nanoparticles. *ChemElectroChem* **2020**, *7*, 2001–2011. DOI: [10.1002/celec.202000089](https://doi.org/10.1002/celec.202000089).
- (18) Li, J.; Zeng, H.; Dong, X.; Ding, Y.; Hu, S.; Zhang, R.; Dai, Y.; Cui, P.; Xiao, Z.; Zhao, D.; Zhou, L.; Zheng, T.; Xiao, J.; Zeng, J.; Xia, C. Selective CO₂ Electrolysis to CO Using Isolated Antimony Alloyed Copper. *Nat. Commun.* **2023**, *14*, 340. DOI: [10.1038/s41467-023-35960-z](https://doi.org/10.1038/s41467-023-35960-z).
- (19) Fan, L.; Xia, C.; Zhu, P.; Lu, Y.; Wang, H. Electrochemical CO₂ Reduction to High-Concentration Pure Formic Acid Solutions in an All-Solid-State Reactor. *Nat. Commun.* **2020**, *11*, 3633. DOI: [10.1038/s41467-020-17403-1](https://doi.org/10.1038/s41467-020-17403-1).
- (20) Chen, X.; Chen, J.; Alghoraibi, N. M.; Henckel, D. A.; Zhang, R.; Nwabara, U. O.; Madsen, K. E.; Kenis, P. J. A.; Zimmerman, S. C.; Gewirth, A. A. Electrochemical CO₂-to-Ethylene Conversion on Polyamine-Incorporated Cu Electrodes. *Nat. Catal.* **2020**, *4*, 20–27. DOI: [10.1038/s41929-020-00547-0](https://doi.org/10.1038/s41929-020-00547-0).
- (21) Zhong, M.; Tran, K.; Min, Y.; Wang, C.; Wang, Z.; Dinh, C. T.; De Luna, P.; Yu, Z.; Rasouli, A. S.; Brodersen, P.; Sun, S.; Voznyy, O.; Tan, C. S.; Askerka, M.; Che, F.; Liu, M.; Seifitokaldani, A.; Pang, Y.; Lo, S. C.; Ip, A.; Ulissi, Z.; Sargent, E. H. Accelerated Discovery of CO₂ Electrocatalysts Using Active Machine Learning. *Nature* **2020**, *581*, 178–183. DOI: [10.1038/s41586-020-2242-8](https://doi.org/10.1038/s41586-020-2242-8).
- (22) Xu, Y.; Li, F.; Xu, A.; Edwards, J. P.; Hung, S.-F. F.; Gabardo, C. M.; O'Brien, C. P.; Liu, S.; Wang, X.; Li, Y.; Wicks, J.; Miao, R. K.; Liu, Y.; Li, J.; Huang, J. E.; Abed, J.; Wang, Y.; Sargent, E. H.; Sinton, D. Low Coordination Number Copper Catalysts for Electrochemical CO₂ Methanation in a Membrane Electrode Assembly. *Nat. Commun.* **2021**, *12*, 2932. DOI: [10.1038/s41467-021-23065-4](https://doi.org/10.1038/s41467-021-23065-4).
- (23) Zhang, X. Y.; Li, W. J.; Wu, X. F.; Liu, Y. W.; Chen, J.; Zhu, M.; Yuan, H. Y.; Dai, S.; Wang, H. F.; Jiang, Z.; Liu, P. F.; Yang, H. G. Selective Methane Electrosynthesis Enabled by a Hydrophobic Carbon Coated Copper Core–Shell Architecture. *Energy Environ. Sci.* **2022**, *15*, 234–243. DOI: [10.1039/d1ee01493e](https://doi.org/10.1039/d1ee01493e).
- (24) Kas, R.; Yang, K.; Bohra, D.; Kortlever, R.; Burdyny, T.; Smith, W. A. Electrochemical CO₂ Reduction on Nanostructured Metal Electrodes: Fact or Defect? *Chem. Sci.* **2020**, *11*, 1738–1749. DOI: [10.1039/c9sc05375a](https://doi.org/10.1039/c9sc05375a).

- (25) Hori, Y.; Kikuchi, K.; Suzuki, S. Production of CO and CH₄ in Electrochemical Reduction of CO₂ at Metal Electrodes in Aqueous Hydrogencarbonate Solution. *Chem. Lett.* **1985**, *14*, 1695–1698. DOI: [10.1246/cl.1985.1695](https://doi.org/10.1246/cl.1985.1695).
- (26) Hori, Y.; Murata, A.; Takahashi, R. Formation of Hydrocarbons in the Electrochemical Reduction of Carbon Dioxide at a Copper Electrode in Aqueous Solution. *J. Chem. Soc. Faraday Trans. 1 Phys. Chem. Condens. Phases* **1989**, *85*, 2309–2326. DOI: [10.1039/f19898502309](https://doi.org/10.1039/f19898502309).
- (27) Huang, J.; Mensi, M.; Oveisi, E.; Mantella, V.; Buonsanti, R. Structural Sensitivities in Bimetallic Catalysts for Electrochemical CO₂ Reduction Revealed by Ag–Cu Nanodimers. *J. Am. Chem. Soc.* **2019**, *141*, 2490–2499. DOI: [10.1021/jacs.8b12381](https://doi.org/10.1021/jacs.8b12381).
- (28) Koper, M. T. M. Electrocatalysis on Bimetallic and Alloy Surfaces. *Surf. Sci.* **2004**, *548*, 1–3. DOI: [10.1016/j.susc.2003.10.045](https://doi.org/10.1016/j.susc.2003.10.045).
- (29) Pedersen, J. K.; Batchelor, T. A. A.; Bagger, A.; Rossmeisl, J. High-Entropy Alloys as Catalysts for the CO₂ and CO Reduction Reactions. *ACS Catal.* **2020**, *10*, 2169–2176. DOI: [10.1021/acscatal.9b04343](https://doi.org/10.1021/acscatal.9b04343).
- (30) Altaf, N.; Liang, S.; Iqbal, R.; Hayat, M.; Reina, T. R.; Wang, Q. Cu-CuO_x/RGO Catalyst Derived from Hybrid LDH/GO with Enhanced C₂H₄ Selectivity by CO₂ Electrochemical Reduction. *J. CO₂ Util.* **2020**, *40*, 101205. DOI: [10.1016/j.jcou.2020.101205](https://doi.org/10.1016/j.jcou.2020.101205).
- (31) Xiao, H.; Goddard, W. A.; Cheng, T.; Liu, Y. Cu Metal Embedded in Oxidized Matrix Catalyst to Promote CO₂ Activation and CO Dimerization for Electrochemical Reduction of CO₂. *Proc. Natl. Acad. Sci. U. S. A.* **2017**, *114*, 6685–6688. DOI: [10.1073/pnas.1702405114](https://doi.org/10.1073/pnas.1702405114).
- (32) García de Arquer, F. P.; Dinh, C. T.; Ozden, A.; Wicks, J.; McCallum, C.; Kirmani, A. R.; Nam, D. H.; Gabardo, C.; Seifitokaldani, A.; Wang, X.; Li, Y. C.; Li, F.; Edwards, J.; Richter, L. J.; Thorpe, S. J.; Sinton, D.; Sargent, E. H. CO₂ Electrolysis to Multicarbon Products at Activities Greater than 1 A cm⁻². *Science* **2020**, *367*, 661–666. DOI: [10.1126/science.aay4217](https://doi.org/10.1126/science.aay4217).
- (33) Li, C. W.; Kanan, M. W. CO₂ Reduction at Low Overpotential on Cu Electrodes Resulting from the Reduction of Thick Cu₂O Films. *J. Am. Chem. Soc.* **2012**, *134*, 7231–7234. DOI: [10.1021/ja3010978](https://doi.org/10.1021/ja3010978).

- (34) Phillips, K. R.; Katayama, Y.; Hwang, J.; Shao-Horn, Y. Sulfide-Derived Copper for Electrochemical Conversion of CO₂ to Formic Acid. *J. Phys. Chem. Lett.* **2018**, *9*, 4407–4412. DOI: [10.1021/acs.jpcclett.8b01601](https://doi.org/10.1021/acs.jpcclett.8b01601).
- (35) Ebaid, M.; Jiang, K.; Zhang, Z.; Drisdell, W. S.; Bell, A. T.; Cooper, J. K. Production of C₂/C₃ Oxygenates from Planar Copper Nitride-Derived Mesoporous Copper via Electrochemical Reduction of CO₂. *Chem. Mater.* **2020**, *32*, 3304–3311. DOI: [10.1021/acs.chemmater.0c00761](https://doi.org/10.1021/acs.chemmater.0c00761).
- (36) Nishimura, Y. F.; Peng, H. J.; Nitopi, S.; Bajdich, M.; Wang, L.; Morales-Guio, C. G.; Abild-Pedersen, F.; Jaramillo, T. F.; Hahn, C. Guiding the Catalytic Properties of Copper for Electrochemical CO₂ Reduction by Metal Atom Decoration. *ACS Appl. Mater. Interfaces* **2021**, *13*, 52044–52054. DOI: [10.1021/acsami.1c09128](https://doi.org/10.1021/acsami.1c09128).
- (37) Cargnello, M. Colloidal Nanocrystals as Building Blocks for Well-Defined Heterogeneous Catalysts. *Chem. Mater.* **2019**, *31*, 576–596. DOI: [10.1021/acs.chemmater.8b04533](https://doi.org/10.1021/acs.chemmater.8b04533).
- (38) Guntern, Y. T.; Okatenko, V.; Pankhurst, J.; Varandili, S. B.; Iyengar, P.; Koolen, C.; Stoian, D.; Vavra, J.; Buonsanti, R. Colloidal Nanocrystals as Electrocatalysts with Tunable Activity and Selectivity. *ACS Catal.* **2021**, *11*, 1248–1295. DOI: [10.1021/acscatal.0c04403](https://doi.org/10.1021/acscatal.0c04403).
- (39) Hori, Y.; Takahashi, I.; Koga, O.; Hoshi, N. Selective Formation of C₂ Compounds from Electrochemical Reduction of CO₂ at a Series of Copper Single Crystal Electrodes. *J. Phys. Chem. B* **2002**, *106*, 15–17. DOI: [10.1021/jp013478d](https://doi.org/10.1021/jp013478d).
- (40) Burdyny, T.; Smith, W. A. CO₂ Reduction on Gas-Diffusion Electrodes and Why Catalytic Performance Must Be Assessed at Commercially-Relevant Conditions. *Energy Environ. Sci.* **2019**, *12*, 1442–1453. DOI: [10.1039/c8ee03134g](https://doi.org/10.1039/c8ee03134g).
- (41) Loiudice, A.; Lobaccaro, P.; Kamali, E. A.; Thao, T.; Huang, B. H.; Ager, J. W.; Buonsanti, R. Tailoring Copper Nanocrystals towards C₂ Products in Electrochemical CO₂ Reduction. *Angew. Chem., Int. Ed.* **2016**, *55*, 5789–5792. DOI: [10.1002/anie.201601582](https://doi.org/10.1002/anie.201601582).
- (42) Mangione, G.; Huang, J.; Buonsanti, R.; Corminboeuf, C. Dual-Facet Mechanism in Copper Nanocubes for Electrochemical CO₂ Reduction into Ethylene. *J. Phys. Chem. Lett.* **2019**, *10*, 4259–4265. DOI: [10.1021/acs.jpcclett.9b01471](https://doi.org/10.1021/acs.jpcclett.9b01471).

- (43) Zaza, L.; Rossi, K.; Buonsanti, R. Well-Defined Copper-Based Nanocatalysts for Selective Electrochemical Reduction of CO₂ to C₂ Products. *ACS Energy Lett.* **2022**, *7*, 1284–1291. DOI: [10.1021/acsenergylett.2c00035](https://doi.org/10.1021/acsenergylett.2c00035).
- (44) Iyengar, P.; Kolb, M. J.; Pankhurst, J. R.; Calle-Vallejo, F.; Buonsanti, R. Elucidating the Facet-Dependent Selectivity for CO₂ Electroreduction to Ethanol of Cu-Ag Tandem Catalysts. *ACS Catal.* **2021**, *11*, 4456–4463. DOI: [10.1021/acscatal.1c00420](https://doi.org/10.1021/acscatal.1c00420).
- (45) Huang, J.; Hörmann, N.; Oveisi, E.; Loiudice, A.; De Gregorio, G. L.; Andreussi, O.; Marzari, N.; Buonsanti, R. Potential-Induced Nanoclustering of Metallic Catalysts during Electrochemical CO₂ Reduction. *Nat. Commun.* **2018**, *9*, 3117. DOI: [10.1038/s41467-018-05544-3](https://doi.org/10.1038/s41467-018-05544-3).
- (46) Möller, T.; Scholten, F.; Thanh, T. N.; Sinev, I.; Timoshenko, J.; Wang, X.; Jovanov, Z.; Gliech, M.; Roldan Cuenya, B.; Varela, A. S.; Strasser, P. Electrocatalytic CO₂ Reduction on CuO_x Nanocubes: Tracking the Evolution of Chemical State, Geometric Structure, and Catalytic Selectivity Using Operando Spectroscopy. *Angew. Chem., Int. Ed.* **2020**, *59*, 17974–17983. DOI: [10.1002/anie.202007136](https://doi.org/10.1002/anie.202007136).
- (47) Kim, D.; Kley, C. S.; Li, Y.; Yang, P. Copper Nanoparticle Ensembles for Selective Electroreduction of CO₂ to C₂–C₃ Products. *Proc. Natl. Acad. Sci. U.S.A.* **2017**, *114*, 10560–10565. DOI: [10.1073/pnas.1711493114](https://doi.org/10.1073/pnas.1711493114).
- (48) Vavra, J.; Shen, T.-H.; Stoian, D.; Tileli, V.; Buonsanti, R. Real-time Monitoring Reveals Dissolution/Redeposition Mechanism in Cu Nanocatalysts during the Initial Stages of the CO₂ Reduction Reaction. *Angew. Chem., Int. Ed.* **2021**, *60*, 1347–1354. DOI: [10.1002/anie.202011137](https://doi.org/10.1002/anie.202011137).
- (49) Amirbeigiab, R.; Tian, J.; Herzog, A.; Qiu, C.; Bergmann, A.; Roldan Cuenya, B.; Magnussen, O. M. Atomic-Scale Surface Restructuring of Copper Electrodes under CO₂ Electroreduction Conditions. *Nat. Catal.* **2023**, *6*, 837–846. DOI: [10.1038/s41929-023-01009-z](https://doi.org/10.1038/s41929-023-01009-z).
- (50) Lopes, P. P. A Framework for the Relationships between Stability and Functional Properties of Electrochemical Energy Materials. *ACS Mater. Au* **2023**, *3*, 8–17. DOI: [10.1021/acsmaterialsau.2c00044](https://doi.org/10.1021/acsmaterialsau.2c00044).

- (51) Vavra, J.; Ramona, G. P. L.; Dattila, F.; Kormányos, A.; Priamushko, T.; Albertini, P.; Loiudice, A.; Cherevko, S.; Lopéz, N.; Buonsanti, R. Cu⁺ Transient Species Mediate Cu Catalyst Reconstruction during CO₂ Electroreduction. *ChemRxiv* **2023**. DOI: [10.26434/chemrxiv-2022-3cr9k-v2](https://doi.org/10.26434/chemrxiv-2022-3cr9k-v2).
- (52) Simon, G. H.; Kley, C. S.; Roldan Cuenya, B. Potential-Dependent Morphology of Copper Catalysts During CO₂ Electroreduction Revealed by In Situ Atomic Force Microscopy. *Angew. Chem., Int. Ed.* **2021**, *60*, 2561–2568. DOI: [10.1002/anie.202010449](https://doi.org/10.1002/anie.202010449).
- (53) Eren, B.; Weatherup, R. S.; Liakakos, N.; Somorjai, G. A.; Salmeron, M. Dissociative Carbon Dioxide Adsorption and Morphological Changes on Cu(100) and Cu(111) at Ambient Pressures. *J. Am. Chem. Soc.* **2016**, *138*, 8207–8211. DOI: [10.1021/jacs.6b04039](https://doi.org/10.1021/jacs.6b04039).
- (54) Eren, B.; Zherebetsky, D.; Patera, L. L.; Wu, C. H.; Bluhm, H.; Africh, C.; Wang, L. W.; Somorjai, G. A.; Salmeron, M. Activation of Cu(111) Surface by Decomposition into Nanoclusters Driven by CO Adsorption. *Science* **2016**, *351*, 475–478. DOI: [10.1126/science.aad8868](https://doi.org/10.1126/science.aad8868).
- (55) Xu, L.; Papanikolaou, K. G.; Lechner, B. A. J.; Je, L.; Somorjai, G. A.; Salmeron, M.; Mavrikakis, M. Formation of Active Sites on Transition Metals through Reaction-Driven Migration of Surface Atoms. *Science* **2023**, *380*, 70–76. DOI: [10.1126/science.add0089](https://doi.org/10.1126/science.add0089).
- (56) Grosse, P.; Gao, D.; Scholten, F.; Sinev, I.; Mistry, H.; Roldan Cuenya, B. Dynamic Changes in the Structure, Chemical State and Catalytic Selectivity of Cu Nanocubes during CO₂ Electroreduction: Size and Support Effects. *Angew. Chem., Int. Ed.* **2018**, *57*, 6192–6197. DOI: [10.1002/anie.201802083](https://doi.org/10.1002/anie.201802083).
- (57) Jung, H.; Lee, S. Y.; Lee, C. W.; Cho, M. K.; Won, D. H.; Kim, C.; Oh, H. S.; Min, B. K.; Hwang, Y. J. Electrochemical Fragmentation of Cu₂O Nanoparticles Enhancing Selective C-C Coupling from CO₂ Reduction Reaction. *J. Am. Chem. Soc.* **2019**, *141*, 4624–4633. DOI: [10.1021/jacs.8b11237](https://doi.org/10.1021/jacs.8b11237).
- (58) Lu, X. K.; Lu, B.; Li, H.; Lim, K.; Seitz, L. C. Stabilization of Undercoordinated Cu Sites in Strontium Copper Oxides for Enhanced Formation of C₂₊ Products in Electrochemical CO₂ Reduction. *ACS Catal.* **2022**, *12*, 6663–6671. DOI: [10.1021/acscatal.2c01019](https://doi.org/10.1021/acscatal.2c01019).

- (59) Liang, Z. Q.; Zhuang, T. T.; Seifitokaldani, A.; Li, J.; Huang, C. W.; Tan, C. S.; Li, Y.; De Luna, P.; Dinh, C. T.; Hu, Y.; Xiao, Q.; Hsieh, P. L.; Wang, Y.; Li, F.; Quintero-Bermudez, R.; Zhou, Y.; Chen, P.; Pang, Y.; Lo, S. C.; Chen, L. J.; Tan, H.; Xu, Z.; Zhao, S.; Sinton, D.; Sargent, E. H. Copper-on-Nitride Enhances the Stable Electrosynthesis of Multi-Carbon Products from CO₂. *Nat. Commun.* **2018**, *9*, 3828. DOI: [10.1038/s41467-018-06311-0](https://doi.org/10.1038/s41467-018-06311-0).
- (60) Zhuang, T. T.; Liang, Z. Q.; Seifitokaldani, A.; Li, Y.; De Luna, P.; Burdyny, T.; Che, F.; Meng, F.; Min, Y.; Quintero-Bermudez, R.; Dinh, C. T.; Pang, Y.; Zhong, M.; Zhang, B.; Li, J.; Chen, P. N.; Zheng, X. L.; Liang, H.; Ge, W. N.; Ye, B. J.; Sinton, D.; Yu, S. H.; Sargent, E. H. Steering Post-C-C Coupling Selectivity Enables High Efficiency Electroreduction of Carbon Dioxide to Multi-Carbon Alcohols. *Nat. Catal.* **2018**, *1*, 421–428. DOI: [10.1038/s41929-018-0084-7](https://doi.org/10.1038/s41929-018-0084-7).
- (61) Zhou, X.; Shan, J.; Chen, L.; Xia, B. Y.; Ling, T.; Duan, J.; Jiao, Y.; Zheng, Y.; Qiao, S. Z. Stabilizing Cu²⁺ Ions by Solid Solutions to Promote CO₂ Electroreduction to Methane. *J. Am. Chem. Soc.* **2022**, *144*, 2079–2084. DOI: [10.1021/jacs.1c12212](https://doi.org/10.1021/jacs.1c12212).
- (62) Lyu, Z.; Zhu, S.; Xie, M.; Zhang, Y.; Chen, Z.; Chen, R.; Tian, M.; Chi, M.; Shao, M.; Xia, Y. Controlling the Surface Oxidation of Cu Nanowires Improves Their Catalytic Selectivity and Stability toward C₂₊ Products in CO₂ Reduction. *Angew. Chem., Int. Ed.* **2021**, *60*, 1909–1915. DOI: [10.1002/anie.202011956](https://doi.org/10.1002/anie.202011956).
- (63) Yoo, J. M.; Shin, H.; Chung, D. Y.; Sung, Y. E. Carbon Shell on Active Nanocatalyst for Stable Electrocatalysis. *Acc. Chem. Res.* **2022**, *55*, 1278–1289. DOI: [10.1021/acs.accounts.1c00727](https://doi.org/10.1021/acs.accounts.1c00727).
- (64) Chung, D. Y.; Jun, S. W.; Yoon, G.; Kwon, S. G.; Shin, D. Y.; Seo, P.; Yoo, J. M.; Shin, H.; Chung, Y.-H.; Kim, H.; Mun, B. S.; Lee, K.-S.; Lee, N.-S.; Yoo, S. J.; Lim, D.-H.; Kang, K.; Sung, Y.-E.; Hyeon, T. Highly Durable and Active PtFe Nanocatalyst for Electrochemical Oxygen Reduction Reaction. *J. Am. Chem. Soc.* **2015**, *137*, 15478–15485. DOI: [10.1021/jacs.5b09653](https://doi.org/10.1021/jacs.5b09653).
- (65) Li, Y.; Cui, F.; Ross, M. B.; Kim, D.; Sun, Y.; Yang, P. Structure-Sensitive CO₂ Electroreduction to Hydrocarbons on Ultrathin 5-Fold Twinned Copper Nanowires. *Nano Lett.* **2017**, *17*, 1312–1317. DOI: [10.1021/acs.nanolett.6b05287](https://doi.org/10.1021/acs.nanolett.6b05287).

- (66) Guntern, Y. T.; Pankhurst, J. R.; Vávra, J.; Mensi, M.; Mantella, V.; Schouwink, P.; Buonsanti, R. Nanocrystal/Metal–Organic Framework Hybrids as Electrocatalytic Platforms for CO₂ Conversion. *Angew. Chem., Int. Ed.* **2019**, *58*, 12632–12639. DOI: [10.1002/anie.201905172](https://doi.org/10.1002/anie.201905172).
- (67) Wang, M.; Nikolaou, V.; Loiudice, A.; Sharp, I. D.; Llobet, A.; Buonsanti, R. Tandem Electrocatalytic CO₂ Reduction with Fe-Porphyrins and Cu Nanocubes Enhances Ethylene Production. *Chem. Sci.* **2022**, *13*, 12673–12680. DOI: [10.1039/d2sc04794b](https://doi.org/10.1039/d2sc04794b).
- (68) Wang, Z.; Yuan, Q.; Shan, J.; Jiang, Z.; Xu, P.; Hu, Y.; Zhou, J.; Wu, L.; Niu, Z.; Sun, J.; Cheng, T.; Goddard, W. A. Highly Selective Electrocatalytic Reduction of CO₂ into Methane on Cu–Bi Nanoalloys. *J. Phys. Chem. Lett.* **2020**, *11*, 7261–7266. DOI: [10.1021/acs.jpcllett.0c01261](https://doi.org/10.1021/acs.jpcllett.0c01261).
- (69) Daeneke, T.; Khoshmanesh, K.; Mahmood, N.; De Castro, I. A.; Esrafilzadeh, D.; Barrow, S. J.; Dickey, M. D.; Kalantar-Zadeh, K. Liquid Metals: Fundamentals and Applications in Chemistry. *Chem. Soc. Rev.* **2018**, *47*, 4073–4111. DOI: [10.1039/c7cs00043j](https://doi.org/10.1039/c7cs00043j).
- (70) Song, H.; Kim, T.; Kang, S.; Jin, H.; Lee, K.; Jae Yoon, H. Ga-Based Liquid Metal Micro/Nanoparticles: Recent Advances and Applications. *Small* **2020**, *16*, 1903391. DOI: [10.1002/sml.201903391](https://doi.org/10.1002/sml.201903391).
- (71) Kalantar-Zadeh, K.; Rahim, M. A.; Tang, J. Low Melting Temperature Liquid Metals and Their Impacts on Physical Chemistry. *Accounts Mater. Res.* **2021**, *2*, 577–580. DOI: [10.1021/accountsmr.1c00143](https://doi.org/10.1021/accountsmr.1c00143).
- (72) Tang, S. Y.; Tabor, C.; Kalantar-Zadeh, K.; Dickey, M. D. Gallium Liquid Metal: The Devil’s Elixir. *Annu. Rev. Mater. Res.* **2021**, *51*, 381–408. DOI: [10.1146/annurev-matsci-080819-125403](https://doi.org/10.1146/annurev-matsci-080819-125403).
- (73) Kalantar-Zadeh, K.; Tang, J.; Daeneke, T.; O’Mullane, A. P.; Stewart, L. A.; Liu, J.; Majidi, C.; Ruoff, R. S.; Weiss, P. S.; Dickey, M. D. Emergence of Liquid Metals in Nanotechnology. *ACS Nano* **2019**, *13*, 7388–7395. DOI: [10.1021/acsnano.9b04843](https://doi.org/10.1021/acsnano.9b04843).
- (74) Zuraiqi, K.; Zavabeti, A.; Allioux, F. M.; Tang, J.; Nguyen, C. K.; Tafazolymotie, P.; Mayyas, M.; Ramarao, A. V.; Spencer, M.; Shah, K.; McConville, C. F.; Kalantar-Zadeh, K.; Chiang, K.; Daeneke, T. Liquid Metals in Catalysis for Energy Applications. *Joule* **2020**, *4*, 2290–2321. DOI: [10.1016/j.joule.2020.10.012](https://doi.org/10.1016/j.joule.2020.10.012).

- (75) Emsley, J. *The Elements*, 3rd ed.; Clarendon Press: Oxford, 1998.
- (76) Barek, J.; Fogg, A. G.; Muck, A.; Zima, J. Polarography and Voltammetry at Mercury Electrodes. *Critical Rev. Anal. Chem.* **2010**, *31*, 291–309. DOI: [10.1080/20014091076776](https://doi.org/10.1080/20014091076776).
- (77) Crook, J.; Mousavi, A. The Chlor-Alkali Process: A Review of History and Pollution. *Environ. Forensics* **2016**, *17*, 211–217. DOI: [10.1080/15275922.2016.1177755](https://doi.org/10.1080/15275922.2016.1177755).
- (78) Lin, Y.; Genzer, J.; Dickey, M. D.; Lin, Y.; Genzer, J.; Dickey, M. D. Attributes, Fabrication, and Applications of Gallium-Based Liquid Metal Particles. *Adv. Sci.* **2020**, *7*, 2000192. DOI: [10.1002/advs.202000192](https://doi.org/10.1002/advs.202000192).
- (79) Markvicka, E. J.; Bartlett, M. D.; Huang, X.; Majidi, C. An Autonomously Electrically Self-Healing Liquid Metal–Elastomer Composite for Robust Soft-Matter Robotics and Electronics. *Nat. Mater.* **2018**, *17*, 618–624. DOI: [10.1038/s41563-018-0084-7](https://doi.org/10.1038/s41563-018-0084-7).
- (80) Li, G.; Wu, X.; Lee, D. W. A Galinstan-Based Inkjet Printing System for Highly Stretchable Electronics with Self-Healing Capability. *Lab Chip* **2016**, *16*, 1366–1373. DOI: [10.1039/c6lc00046k](https://doi.org/10.1039/c6lc00046k).
- (81) Guo, R.; Sun, X.; Yuan, B.; Wang, H.; Liu, J. Magnetic Liquid Metal (Fe-EGaIn) Based Multifunctional Electronics for Remote Self-Healing Materials, Degradable Electronics, and Thermal Transfer Printing. *Adv. Sci.* **2019**, *6*, 1901478. DOI: [10.1002/advs.201901478](https://doi.org/10.1002/advs.201901478).
- (82) Dickey, M. D.; Chiechi, R. C.; Larsen, R. J.; Weiss, E. A.; Weitz, D. A.; Whitesides, G. M. Eutectic Gallium-Indium (EGaIn): A Liquid Metal Alloy for the Formation of Stable Structures in Microchannels at Room Temperature. *Adv. Funct. Mater.* **2008**, *18*, 1097–1104. DOI: [10.1002/adfm.200701216](https://doi.org/10.1002/adfm.200701216).
- (83) Wu, Y.; Huang, L.; Huang, X.; Guo, X.; Liu, D.; Zheng, D.; Zhang, X.; Ren, R.; Qu, D.; Chen, J. A Room-Temperature Liquid Metal-Based Self-Healing Anode for Lithium-Ion Batteries with an Ultra-Long Cycle Life. *Energy Environ. Sci.* **2017**, *10*, 1854–1861. DOI: [10.1039/c7ee01798g](https://doi.org/10.1039/c7ee01798g).
- (84) Liu, G.; Young Kim, J.; Wang, M.; Woo, J.-Y.; Wang, L.; Zou, D.; Kee Lee, J. Soft, Highly Elastic, and Discharge-Current-Controllable Eutectic Gallium–Indium Liquid Metal–Air Battery Operated at Room Temperature. *Adv. Energy Mater.* **2018**, *8*, 1703652. DOI: [10.1002/aenm.201703652](https://doi.org/10.1002/aenm.201703652).

- (85) Lin, Y.; Cooper, C.; Wang, M.; Adams, J. J.; Genzer, J.; Dickey, M. D. Handwritten, Soft Circuit Boards and Antennas Using Liquid Metal Nanoparticles. *Small* **2015**, *11*, 6397–6403. DOI: [10.1002/sml.201502692](https://doi.org/10.1002/sml.201502692).
- (86) Fassler, A.; Majidi, C.; Fassler, A.; Majidi, C. Liquid-Phase Metal Inclusions for a Conductive Polymer Composite. *Adv. Mater.* **2015**, *27*, 1928–1932. DOI: [10.1002/adma.201405256](https://doi.org/10.1002/adma.201405256).
- (87) Tang, J.; Tang, J.; Mayyas, M.; Ghasemian, M. B.; Sun, J.; Rahim, A.; Yang, J.; Han, J.; Lawes, D. J.; Jalili, R.; Daeneke, T.; Saborio, M. G.; Cao, Z.; Echeverria, C. A.; Allioux, F.-M.; Zavabeti, A.; Hamilton, J.; Mitchell, V.; O’Mullane, A. P.; Kaner, R. B.; Esrafilzadeh, D.; Dickey, M. D.; Kalantar-Zadeh, K.. Liquid-Metal-Enabled Mechanical-Energy-Induced CO₂ Conversion. *Adv. Mater.* **2022**, *34*, 2105789. DOI: [10.1002/adma.202105789](https://doi.org/10.1002/adma.202105789).
- (88) Zhang, W.; Naidu, B. S.; Ou, J. Z.; O’Mullane, A. P.; Chrimes, A. F.; Carey, B. J.; Wang, Y.; Tang, S. Y.; Sivan, V.; Mitchell, A.; Bhargava, S. K.; Kalantar-Zadeh, K. Liquid Metal/Metal Oxide Frameworks with Incorporated Ga₂O₃ for Photocatalysis. *ACS Appl. Mater. Interfaces* **2015**, *7*, 1943–1948. DOI: [10.1021/am5077364](https://doi.org/10.1021/am5077364).
- (89) Shen, Q.; Jiang, M.; Wang, R.; Song, K.; Hou Vong, M.; Jung, W.; Krisnadi, F.; Kan, R.; Zheng, F.; Fu, B.; Tao, P.; Song, C.; Weng, G.; Peng, B.; Wang, J.; Shang, W.; Dickey, M. D.; Deng, T. Liquid Metal-Based Soft, Hermetic, and Wireless-Communicable Seals for Stretchable Systems. *Science* **2023**, *379*, 488–493. DOI: [10.1126/science.ade7341](https://doi.org/10.1126/science.ade7341).
- (90) Yang, N.; Gong, F.; Zhou, Y.; Yu, Q.; Cheng, L. Liquid Metals: Preparation, Surface Engineering, and Biomedical Applications. *Coord. Chem. Rev.* **2022**, *471*, 214731. DOI: [10.1016/j.ccr.2022.214731](https://doi.org/10.1016/j.ccr.2022.214731).
- (91) Wang, X.; Yao, W.; Guo, R.; Yang, X.; Tang, J.; Zhang, J.; Gao, W.; Timchenko, V.; Liu, J. Soft and Moldable Mg-Doped Liquid Metal for Conformable Skin Tumor Photothermal Therapy. *Adv. Healthc. Mater.* **2018**, *7*, 1800318. DOI: [10.1002/adhm.201800318](https://doi.org/10.1002/adhm.201800318).
- (92) Lu, Y.; Hu, Q.; Lin, Y.; Pacardo, D. B.; Wang, C.; Sun, W.; Ligler, F. S.; Dickey, M. D.; Gu, Z. Transformable Liquid-Metal Nanomedicine. *Nat. Commun.* **2015**, *6*, 10066. DOI: [10.1038/ncomms10066](https://doi.org/10.1038/ncomms10066).

- (93) Jacob, A. R.; Parekh, P.; Dickey, M. D.; Hsiao, L. C. Interfacial Rheology of Gallium-Based Liquid Metals. *Langmuir* **2019**, *35*, 11774–11783. DOI: [10.1021/acs.langmuir.9b01821](https://doi.org/10.1021/acs.langmuir.9b01821).
- (94) Tang, S.-Y.; Qiao, R.; Yan, S.; Yuan, D.; Zhao, Q.; Yun, G.; Davis, T. P.; Li, W. Microfluidic Mass Production of Stabilized and Stealthy Liquid Metal Nanoparticles. *Small* **2018**, *14*, 1800118. DOI: [10.1002/sml.201800118](https://doi.org/10.1002/sml.201800118).
- (95) Taccardi, N.; Grabau, M.; Debuschewitz, J.; Distaso, M.; Brandl, M.; Hock, R.; Maier, F.; Papp, C.; Erhard, J.; Neiss, C.; Peukert, W.; Görling, A.; Steinrück, H. P.; Wasserscheid, P. Gallium-Rich Pd–Ga Phases as Supported Liquid Metal Catalysts. *Nat. Chem.* **2017**, *9*, 862–867. DOI: [10.1038/nchem.2822](https://doi.org/10.1038/nchem.2822).
- (96) Hou, Y.; Wang, F.; Qin, C.; Wu, S.; Cao, M.; Yang, P.; Huang, L.; Wu, Y. A Self-Healing Electrocatalytic System via Electrohydrodynamics Induced Evolution in Liquid Metal. *Nat. Commun.* **2022**, *13*, 7625. DOI: [10.1038/s41467-022-35416-w](https://doi.org/10.1038/s41467-022-35416-w).
- (97) Rahim, M. A.; Tang, J.; Christofferson, A. J.; Kumar, P. V.; Meftahi, N.; Centurion, F.; Cao, Z.; Tang, J.; Baharfar, M.; Mayyas, M.; Allioux, F. M.; Koshy, P.; Daeneke, T.; McConville, C. F.; Kaner, R. B.; Russo, S. P.; Kalantar-Zadeh, K. Low-Temperature Liquid Platinum Catalyst. *Nat. Chem.* **2022**, *14*, 935–941. DOI: [10.1038/s41557-022-00965-6](https://doi.org/10.1038/s41557-022-00965-6).
- (98) Ye, L.; Syed, N.; Wang, D.; Guo, J.; Yang, J.; Buston, J.; Singh, R.; Alivand, M. S.; Kevin Li, G.; Zavabeti, A. Low-Temperature CO₂ Reduction Using Mg–Ga Liquid Metal Interface. *Adv. Mater. Interfaces* **2023**, *10*, 2201625. DOI: [10.1002/admi.202201625](https://doi.org/10.1002/admi.202201625).
- (99) Crawford, J.; Yin, H.; Du, A.; O’Mullane, A. P. Nitrate-to-Ammonia Conversion at an InSn-Enriched Liquid-Metal Electrode. *Angew. Chem., Int. Ed.* **2022**, *61*, e202201604. DOI: [10.1002/anie.202201604](https://doi.org/10.1002/anie.202201604).
- (100) Parker, C. J.; Krishnamurthi, V.; Zuraiqi, K.; Nguyen, C. K.; Irfan, M.; Jabbar, F.; Yang, D.; Aukarasereenont, M. P.; Mayes, E. L. H.; Murdoch, B. J.; Elbourne, A.; Chiang, K.; Daeneke, T. Synthesis of Planet-Like Liquid Metal Nanodroplets with Promising Properties for Catalysis. *Adv. Funct. Mater.* **2023**, 2304248. DOI: [10.1002/adfm.202304248](https://doi.org/10.1002/adfm.202304248).

- (101) Upham, D. C.; Agarwal, V.; Khechfe, A.; Snodgrass, Z. R.; Gordon, M. J.; Metiu, H.; McFarland, E. W. Catalytic Molten Metals for the Direct Conversion of Methane to Hydrogen and Separable Carbon. *Science* **2017**, *358*, 917–921. DOI: [10.1126/science.aao5023](https://doi.org/10.1126/science.aao5023).
- (102) Raman, N.; Maisel, S.; Grabau, M.; Taccardi, N.; Debuschewitz, J.; Wolf, M.; Wittkämper, H.; Bauer, T.; Wu, M.; Haumann, M.; Papp, C.; Görling, A.; Spiecker, E.; Libuda, J.; Steinrück, H. P.; Wasserscheid, P. Highly Effective Propane Dehydrogenation Using Ga-Rh Supported Catalytically Active Liquid Metal Solutions. *ACS Catal.* **2019**, *9*, 9499–9507. DOI: [10.1021/acscatal.9b02459](https://doi.org/10.1021/acscatal.9b02459).
- (103) Palmer, C.; Upham, D. C.; Smart, S.; Gordon, M. J.; Metiu, H.; McFarland, E. W. Dry Reforming of Methane Catalysed by Molten Metal Alloys. *Nat. Catal.* **2020**, *3*, 83–89. DOI: [10.1038/s41929-019-0416-2](https://doi.org/10.1038/s41929-019-0416-2).
- (104) Esrafilzadeh, D.; Zavabeti, A.; Jalili, R.; Atkin, P.; Choi, J.; Carey, B. J.; Brkljača, R.; O’Mullane, A. P.; Dickey, M. D.; Officer, D. L.; MacFarlane, D. R.; Daeneke, T.; Kalantar-Zadeh, K. Room Temperature CO₂ Reduction to Solid Carbon Species on Liquid Metals Featuring Atomically Thin Ceria Interfaces. *Nat. Commun.* **2019**, *10*, 865. DOI: [10.1038/s41467-019-08824-8](https://doi.org/10.1038/s41467-019-08824-8).
- (105) Liu, H.; Xia, J.; Zhang, N.; Cheng, H.; Bi, W.; Zu, X.; Chu, W.; Wu, H. A.; Wu, C.; Xie, Y. Solid–Liquid Phase Transition Induced Electrocatalytic Switching from Hydrogen Evolution to Highly Selective CO₂ Reduction. *Nat. Catal.* **2021**, *4*, 202–211. DOI: [10.1038/s41929-021-00576-3](https://doi.org/10.1038/s41929-021-00576-3).
- (106) Allieux, F. M.; Merhebi, S.; Tang, J.; Idrus-Saidi, S. A.; Abbasi, R.; Saborio, M. G.; Ghasemian, M. B.; Han, J.; Namivandi-Zangeneh, R.; O’Mullane, A. P.; Koshy, P.; Daiyan, R.; Amal, R.; Boyer, C.; Kalantar-Zadeh, K. Catalytic Metal Foam by Chemical Melting and Sintering of Liquid Metal Nanoparticles. *Adv. Funct. Mater.* **2020**, *30*, 1907879. DOI: [10.1002/adfm.201907879](https://doi.org/10.1002/adfm.201907879).
- (107) Tang, J.; Daiyan, R.; Ghasemian, M. B.; Idrus-Saidi, S. A.; Zavabeti, A.; Daeneke, T.; Yang, J.; Koshy, P.; Cheong, S.; Tilley, R. D.; Kaner, R. B.; Amal, R.; Kalantar-Zadeh, K. Advantages of Eutectic Alloys for Creating Catalysts in the Realm of Nanotechnology-Enabled Metallurgy. *Nat. Commun.* **2019**, *10*, 4645. DOI: [10.1038/s41467-019-12615-6](https://doi.org/10.1038/s41467-019-12615-6).
- (108) Tang, J.; Kumar, P. V.; Scott, J. A.; Tang, J.; Ghasemian, M. B.; Mousavi, M.; Han, J.;

- Esfafilzadeh, D.; Khoshmanesh, K.; Daeneke, T.; O'Mullane, A. P.; Kaner, R. B.; Rahim, M. A.; Kalantar-Zadeh, K. Low Temperature Nano Mechano-Electrocatalytic CH₄ Conversion. *ACS Nano* **2022**. DOI: [10.1021/acsnano.2c02326](https://doi.org/10.1021/acsnano.2c02326).
- (109) Rupprechter, G. Popping up to the Surface. *Nat. Chem.* **2017**, *9*, 833–834. DOI: [10.1038/nchem.2849](https://doi.org/10.1038/nchem.2849).
- (110) Goodman, E. D.; Schwalbe, J. A.; Cargnello, M. Mechanistic Understanding and the Rational Design of Sinter-Resistant Heterogeneous Catalysts. *ACS Catal.* **2017**, *7*, 7156–7173. DOI: [10.1021/acscatal.7b01975](https://doi.org/10.1021/acscatal.7b01975).
- (111) Otor, H. O.; Steiner, J. B.; García-Sancho, C.; Alba-Rubio, A. C. Encapsulation Methods for Control of Catalyst Deactivation: A Review. *ACS Catal.* **2020**, *10*, 7630–7656. DOI: [10.1021/acscatal.0c01569](https://doi.org/10.1021/acscatal.0c01569).
- (112) Yan, C.; Lin, L.; Gao, D.; Wang, G.; Bao, X. Selective CO₂ Electroreduction over an Oxide-Derived Gallium Catalyst. *J. Mater. Chem. A* **2018**, *6*, 19743–19749. DOI: [10.1039/c8ta08613c](https://doi.org/10.1039/c8ta08613c).
- (113) Hori, Y.; Wakebe, H.; Tsukamoto, T.; Koga, O. Electrocatalytic Process of CO Selectivity in Electrochemical Reduction of CO₂ at Metal Electrodes in Aqueous Media. *Electrochim. Acta* **1994**, *39*, 1833–1839. DOI: [10.1016/0013-4686\(94\)85172-7](https://doi.org/10.1016/0013-4686(94)85172-7).
- (114) Martin, A.; Du, C.; Chang, B.; Thuo, M. Complexity and Opportunities in Liquid Metal Surface Oxides. *Chem. Mater.* **2020**, *32*, 9045–9055. DOI: [10.1021/acs.chemmater.0c02047](https://doi.org/10.1021/acs.chemmater.0c02047).
- (115) Zhong, J. Q.; Shaikhutdinov, S.; Roldan Cuenya, B. Structural Evolution of Ga-Cu Model Catalysts for CO₂ Hydrogenation Reactions. *J. Phys. Chem. C* **2021**, *125*, 1361–1367. DOI: [10.1021/acs.jpcc.0c09382](https://doi.org/10.1021/acs.jpcc.0c09382).
- (116) Chiechi, R. C.; Weiss, E. A.; Dickey, M. D.; Whitesides, G. M. Eutectic Gallium-Indium (EGaIn): A Moldable Liquid Metal for Electrical Characterization of Self-Assembled Monolayers. *Angew. Chem., Int. Ed.* **2008**, *47*, 142–144. DOI: [10.1002/anie.200703642](https://doi.org/10.1002/anie.200703642).
- (117) Larsen, R. J.; Dickey, M. D.; Whitesides, G. M.; Weitz, D. A. Viscoelastic Properties of Oxide-Coated Liquid Metals. *J. Rheol.* **2009**, *53*, 1305–1326. DOI: [10.1122/1.3236517](https://doi.org/10.1122/1.3236517).
- (118) Khan, M. R.; Eaker, C. B.; Bowden, E. F.; Dickey, M. D. Giant and Switchable Surface Activity of Liquid Metal via Surface Oxidation. *Proc. Natl. Acad. Sci. U. S. A.* **2014**, *111*, 14047–14051. DOI: [10.1073/pnas.1412227111](https://doi.org/10.1073/pnas.1412227111).

- (119) Ayyad, A. H.; Freyland, W. Wetting Transition in Liquid Ga–Bi Alloys: Light Scattering Study of Surface Energy and Entropy. *Surf. Sci.* **2002**, *506*, 1–11. DOI: [10.1016/s0039-6028\(02\)01439-5](https://doi.org/10.1016/s0039-6028(02)01439-5).
- (120) Han, J.; Tang, J.; Idrus-Saidi, S. A.; Christoe, M. J.; O’Mullane, A. P.; Kalantar-Zadeh, K. Exploring Electrochemical Extrusion of Wires from Liquid Metals. *ACS Appl. Mater. Interfaces* **2020**, *12*, 31010–31020. DOI: [10.1021/acsami.0c07697](https://doi.org/10.1021/acsami.0c07697).
- (121) Popova, T. I.; Simonova, N. A.; Moiseeva, Z. J.; Bardina, N. G. Formation of Passivating Films on Ga in Aqueous Electrolytes I (Образование Пассивирующих Пленок На Галлии в Водных Растворах I). *Elektrokhimiya* **1970**, *6*, 706–708.
- (122) Popova, T. I.; Simonova, N. A.; Moiseeva, Z. J.; Bardina, N. G. Formation of Passivating Films on Ga in Aqueous Electrolytes II (Образование Пассивирующих Пленок На Галлии в Водных Растворах II). *Elektrokhimiya* **1970**, *6*, 1125–1128.
- (123) Popova, T. I.; Timofeeva, L. Z.; Simonova, N. A.; Bardina, N. G. Influence of F⁻ Ions Adsorption on Passive Ga Dissolution (Влияние Адсорбции Ионов Фтора На Кинетику Растворения Пассивного Галлия). *Elektrokhimiya* **1975**, *11*, 1430–1432.
- (124) Korshunov, V. N. Behaviour of Rotating Disk Ga-Anode in Alkaline Environment (Поведение Вращающегося Дискового Ga-Анода в Щелочной Среде). *Elektrokhimiya* **1995**, *31*, 1122–1136.
- (125) Korshunov, V. N.; Safonov, V. A. Behavior of Gallium Anodes in Carbonate Buffer Solutions. *Russ. J. Electrochem.* **2001**, *37*, 1089–1095. DOI: [10.1023/a:1012331416046](https://doi.org/10.1023/a:1012331416046).
- (126) Korshunov, V. N.; Safonov, V. A. Electroreduction of Peroxodisulfate Anions as a Probe Reaction for Studying Passivation of Solid Gallium in Sulfate Media. *Russ. J. Electrochem.* **2002**, *38*, 768–774. DOI: [10.1023/a:1016348700915](https://doi.org/10.1023/a:1016348700915).
- (127) Cabrera, N.; Mott, N. F. Theory of the Oxidation of Metals. *Reports Prog. Phys.* **1949**, *12*, 163–184. DOI: [10.1088/0034-4885/12/1/308](https://doi.org/10.1088/0034-4885/12/1/308).
- (128) Zhdanov, V. P.; Kasemo, B. Cabrera–Mott Kinetics of Oxidation of nm-Sized Metal Particles. *Chem. Phys. Lett.* **2008**, *452*, 285–288. DOI: [10.1016/j.cplett.2008.01.006](https://doi.org/10.1016/j.cplett.2008.01.006).
- (129) Farrell, Z. J.; Tabor, C. Control of Gallium Oxide Growth on Liquid Metal Eutectic Gallium/Indium Nanoparticles via Thiolation. *Langmuir* **2018**, *34*, 234–240. DOI: [10.1021/acs.langmuir.7b03384](https://doi.org/10.1021/acs.langmuir.7b03384).

- (130) Di Cicco, A. Phase Transitions in Confined Gallium Droplets. *Phys. Rev. Lett.* **1998**, *81*, 2942–2945. DOI: [10.1103/physrevlett.81.2942](https://doi.org/10.1103/physrevlett.81.2942).
- (131) He, H.; Fei, G. T.; Cui, P.; Zheng, K.; Liang, L. M.; Li, Y.; De Zhang, L. Relation between Size and Phase Structure of Gallium: Differential Scanning Calorimeter Experiments. *Phys. Rev. B* **2005**, *72*, 073310. DOI: [10.1103/physrevb.72.073310](https://doi.org/10.1103/physrevb.72.073310).
- (132) Martin, A.; Chang, B. S.; Pauls, A. M.; Du, C.; Thuo, M. Stabilization of Undercooled Metals via Passivating Oxide Layers. *Angew. Chem., Int. Ed.* **2021**, *60*, 5928–5935. DOI: [10.1002/anie.202013489](https://doi.org/10.1002/anie.202013489).
- (133) Mingear, J.; Farrell, Z.; Hartl, D.; Tabor, C. Gallium–Indium Nanoparticles as Phase Change Material Additives for Tunable Thermal Fluids. *Nanoscale* **2021**, *13*, 730–738. DOI: [10.1039/d0nr06526a](https://doi.org/10.1039/d0nr06526a).
- (134) Di Cicco, A.; Fusari, S.; Stizza, S. Phase Transitions and Undercooling in Confined Gallium. *Philos. Mag. B* **2009**, *79*, 2113–2120. DOI: [10.1080/13642819908223100](https://doi.org/10.1080/13642819908223100).
- (135) Martin, A.; Chang, B. S.; Martin, Z.; Paramanik, D.; Frankiewicz, C.; Kundu, S.; Tevis, I. D.; Thuo, M. Heat-Free Fabrication of Metallic Interconnects for Flexible/Wearable Devices. *Adv. Funct. Mater.* **2019**, *29*. DOI: [10.1002/adfm.201903687](https://doi.org/10.1002/adfm.201903687).
- (136) Martin, A.; Du, C.; Pauls, A. M.; Ward, T.; Thuo, M. Polydispersity-Driven Printing of Conformal Solid Metal Traces on Non-Adhering Biological Surfaces. *Adv. Mater. Interfaces* **2020**, *7*, 2001294. DOI: [10.1002/admi.202001294](https://doi.org/10.1002/admi.202001294).
- (137) Cheek, Q.; Fahrenkrug, E.; Hlynchuk, S.; Alsem, D. H.; Salmon, N. J.; Maldonado, S. In Situ Transmission Electron Microscopy Measurements of Ge Nanowire Synthesis with Liquid Metal Nanodroplets in Water. *ACS Nano* **2020**, *14*, 2869–2879. DOI: [10.1021/acsnano.9b06468](https://doi.org/10.1021/acsnano.9b06468).
- (138) Zhang, W.; Ou, J. Z.; Tang, S.-Y.; Sivan, V.; Yao, D. D.; Latham, K.; Khoshmanesh, K.; Mitchell, A.; O’Mullane, A. P.; Kalantar-Zadeh, K. Liquid Metal/Metal Oxide Frameworks. *Adv. Funct. Mater.* **2014**, *24*, 3799–3807. DOI: [10.1002/adfm.201304064](https://doi.org/10.1002/adfm.201304064).
- (139) Idrus-Saidi, S. A.; Tang, J.; Ghasemian, M. B.; Yang, J.; Han, J.; Syed, N.; Daeneke, T.; Abbasi, R.; Koshy, P.; O’Mullane, A. P.; Kalantar-Zadeh, K. Liquid Metal Core–Shell Structures Functionalised via Mechanical Agitation: The Example of Field’s Metal. *J. Mater. Chem. A* **2019**, *7*, 17876–17887. DOI: [10.1039/c9ta05200c](https://doi.org/10.1039/c9ta05200c).

- (140) Chung, Y.; Lee, C.-W. Electrochemistry of Gallium. *J. Electrochem. Sci. Technol.* **2013**, *4*, 1–18. DOI: [10.5229/jecst.2013.4.1.1](https://doi.org/10.5229/jecst.2013.4.1.1).
- (141) Ohira, S.; Arai, N. Wet Chemical Etching Behavior of β -Ga₂O₃ Single Crystal. *Phys. status solidi* **2008**, *5*, 3116–3118. DOI: [10.1002/pssc.200779223](https://doi.org/10.1002/pssc.200779223).
- (142) Pourbaix, M. *Atlas of Electrochemical Equilibria in Aqueous Solutions*, 2nd ed.; National Association of Corrosion Engineers: Houston, 1966.
- (143) Bratsch, S. G. Standard Electrode Potentials and Temperature Coefficients in Water at 298.15 K. *J. Phys. Chem. Ref. Data* **1989**, *18*, 1–21. DOI: [10.1063/1.555839](https://doi.org/10.1063/1.555839).
- (144) Selekhnova, N. P.; Lyubimova, N. A.; Leikis, D. I. Anodic Dissolution of Ga in Alkaline Gallate Electrolytes (Анодное Растворения Галлия в Щелочных Галлатных Электролитах). *Elektrokhimiya* **1972**, *8*, 721–723.
- (145) Faizullin, F. F.; Nikitin, E. V.; Gudina, N. N. On the Mechanism of Anodic Ga Films Formation on Liquid Ga (О Механизме Образования Анодных Пленок На Жидком Галлии). *Elektrokhimiya* **1967**, *3*, 120.
- (146) Corbett, J. D.; McMullan, R. K. The Preparation of Acid-Stabilized Subhalides from Molten Metal-Metal Halide Solutions. *J. Am. Chem. Soc.* **1956**, *78*, 2906–2907. DOI: [10.1021/ja01593a071](https://doi.org/10.1021/ja01593a071).
- (147) Corbett, J. D.; McMullan, R. K. The Lower Oxidation States of Gallium. I. The GaI₃-GaI₂-GaI System. *J. Am. Chem. Soc.* **1955**, *77*, 4217–4219. DOI: [10.1021/ja01621a009](https://doi.org/10.1021/ja01621a009).
- (148) Corbett, J. D.; Hershaft, A. The Lower Oxidation States of Gallium. II. The Ga₂Br₄-GaBr System. *J. Am. Chem. Soc.* **1958**, *80*, 1530–1532. DOI: [10.1021/ja01540a003](https://doi.org/10.1021/ja01540a003).
- (149) McMullan, R. K.; Corbett, J. D. The Lower Oxidation States of Gallium. III. The Constitution of Ga₂Cl₄ and Its Analogy with Ga(AlCl₄). *J. Am. Chem. Soc.* **1958**, *80*, 4761–4764. DOI: [10.1021/ja01551a002](https://doi.org/10.1021/ja01551a002).
- (150) Corbett, J. D. Discussion of “Electrodeposition of Gallium on Liquid and Solid Gallium Electrodes in Alkaline Solutions” [J. O’M. Bockris and E. Enyo (Pp. 48–54, Vol. 109, No. 1)]. *J. Electrochem. Soc.* **1962**, *109*, 1214. DOI: [10.1149/1.2425280](https://doi.org/10.1149/1.2425280).
- (151) Faizullin, F. F.; Nikitin, E. N. On Dependencies of Anodic Ga Oxidation in KOH Solution (О Закономерностях Анодного Окисления Галлия в Растворе KOH). *Elektrokhimiya* **1966**, *2*, 112.

- (152) ISO/TC 229 Nanotechnologies, ISO 80004-1:2023, 2023.
- (153) Lin, Y.; Genzer, J.; Li, W.; Qiao, R.; Dickey, M. D.; Tang, S. Y. Sonication-Enabled Rapid Production of Stable Liquid Metal Nanoparticles Grafted with Poly(1-Octadecene-Alt-Maleic Anhydride) in Aqueous Solutions. *Nanoscale* **2018**, *10*, 19871–19878. DOI: [10.1039/c8nr05600e](https://doi.org/10.1039/c8nr05600e).
- (154) Yamaguchi, A.; Mashima, Y.; Iyoda, T. Reversible Size Control of Liquid-Metal Nanoparticles under Ultrasonication. *Angew. Chem., Int. Ed.* **2015**, *54*, 12809–12813. DOI: [10.1002/anie.201506469](https://doi.org/10.1002/anie.201506469).
- (155) Lu, H.; Tang, S. Y.; Dong, Z.; Liu, D.; Zhang, Y.; Zhang, C.; Yun, G.; Zhao, Q.; Kalantar-Zadeh, K.; Qiao, R.; Li, W. Dynamic Temperature Control System for the Optimized Production of Liquid Metal Nanoparticles. *ACS Appl. Nano Mater.* **2020**, *3*, 6905–6914. DOI: [10.1021/acsanm.0c01257](https://doi.org/10.1021/acsanm.0c01257).
- (156) Hohman, J. N.; Kim, M.; Wadsworth, G. A.; Bednar, H. R.; Jiang, J.; Lethai, M. A.; Weiss, P. S. Directing Substrate Morphology via Self-Assembly: Ligand-Mediated Scission of Gallium-Indium Microspheres to the Nanoscale. *Nano Lett.* **2011**, *11*, 5104–5110. DOI: [10.1021/nl202728j](https://doi.org/10.1021/nl202728j).
- (157) Tevis, I. D.; Newcomb, L. B.; Thuo, M. Synthesis of Liquid Core-Shell Particles and Solid Patchy Multicomponent Particles by Shearing Liquids into Complex Particles (SLICE). *Langmuir* **2014**, *30*, 14308–14313. DOI: [10.1021/la5035118](https://doi.org/10.1021/la5035118).
- (158) Yu, F.; Xu, J.; Li, H.; Wang, Z.; Sun, L.; Deng, T.; Tao, P.; Liang, Q. Ga-In Liquid Metal Nanoparticles Prepared by Physical Vapor Deposition. *Prog. Nat. Sci. Mater. Int.* **2018**, *28*, 28–33. DOI: [10.1016/j.pnsc.2017.12.004](https://doi.org/10.1016/j.pnsc.2017.12.004).
- (159) Mantella, V.; Castilla-Amorós, L.; Buonsanti, R. Shaping Non-Noble Metal Nanocrystals via Colloidal Chemistry. *Chem. Sci.* **2020**, *11*, 11394–11403. DOI: [10.1039/d0sc03663c](https://doi.org/10.1039/d0sc03663c).
- (160) Jin, R.; Zeng, C.; Zhou, M.; Chen, Y. Atomically Precise Colloidal Metal Nanoclusters and Nanoparticles: Fundamentals and Opportunities. *Chem. Rev.* **2016**, *116*, 10346–10413. DOI: [10.1021/acs.chemrev.5b00703](https://doi.org/10.1021/acs.chemrev.5b00703).

- (161) Yarema, M.; Wörle, M.; Rossell, M. D.; Erni, R.; Caputo, R.; Protesescu, L.; Kravchyk, K. V.; Dirin, D. N.; Lienau, K.; Von Rohr, F.; Schilling, A.; Nachttegaal, M.; Kovalenko, M. V. Monodisperse Colloidal Gallium Nanoparticles: Synthesis, Low Temperature Crystallization, Surface Plasmon Resonance and Li-Ion Storage. *J. Am. Chem. Soc.* **2014**, *136*, 12422–12430. DOI: [10.1021/ja506712d](https://doi.org/10.1021/ja506712d).
- (162) Castilla-Amoros, L.; Stoian, D.; Pankhurst, J.; Varandili, S.; Buonsanti, R. Exploring the Chemical Reactivity of Gallium Liquid Metal Nanoparticles in Galvanic Replacement. *J. Am. Chem. Soc.* **2020**, *142*, 19283–19290. DOI: [10.1021/jacs.0c09458](https://doi.org/10.1021/jacs.0c09458).
- (163) Clarysse, J.; Moser, A.; Yarema, O.; Wood, V.; Yarema, M. Size- and Composition-Controlled Intermetallic Nanocrystals via Amalgamation Seeded Growth. *Sci. Adv.* **2021**, *7*, eabg1934. DOI: [10.1126/sciadv.abg1934](https://doi.org/10.1126/sciadv.abg1934).
- (164) Lyon, R. N. *Liquid-Metals Handbook*, 1st ed.; Lyon, R. N., Ed.; U.S. Government Printing Office: Washington, D.C., 1954.
- (165) Kim, D.; Kley, C. S.; Li, Y.; Yang, P. Copper Nanoparticle Ensembles for Selective Electroreduction of CO₂ to C₂-C₃ Products. *Proc. Natl. Acad. Sci. U. S. A.* **2017**, *114*, 10560–10565. DOI: [10.1073/pnas.1711493114](https://doi.org/10.1073/pnas.1711493114).
- (166) He, M.; Protesescu, L.; Caputo, R.; Krumeich, F.; Kovalenko, M. V. A General Synthesis Strategy for Monodisperse Metallic and Metalloid Nanoparticles (In, Ga, Bi, Sb, Zn, Cu, Sn, and Their Alloys) via in Situ Formed Metal Long-Chain Amides. *Chem. Mater.* **2015**, *27*, 635–647. DOI: [10.1021/cm5045144](https://doi.org/10.1021/cm5045144).
- (167) Falchevskaya, A. S.; Prilepskii, A. Y.; Tsvetikova, S. A.; Koshel, E. I.; Vinogradov, V. V. Facile Synthesis of a Library of Hollow Metallic Particles through the Galvanic Replacement of Liquid Gallium. *Chem. Mater.* **2021**, *33*, 1571–1580. DOI: [10.1021/acs.chemmater.0c03969](https://doi.org/10.1021/acs.chemmater.0c03969).
- (168) Mattox, T. M.; Bergerud, A.; Agrawal, A.; Milliron, D. J. Influence of Shape on the Surface Plasmon Resonance of Tungsten Bronze Nanocrystals. *Chem. Mater.* **2014**, *26*, 1779–1784. DOI: [10.1021/cm4030638](https://doi.org/10.1021/cm4030638).
- (169) Loiudice, A.; Cooper, J. K.; Hess, L. H.; Mattox, T. M.; Sharp, I. D.; Buonsanti, R. Assembly and Photocarrier Dynamics of Heterostructured Nanocomposite Photoanodes from Multicomponent Colloidal Nanocrystals. *Nano Lett.* **2015**, *15*, 7347–7354. DOI: [10.1021/acs.nanolett.5b03871](https://doi.org/10.1021/acs.nanolett.5b03871).

- (170) Van Beek, W.; Safonova, O. V.; Wiker, G.; Emerich, H. SNBL, a Dedicated Beamline for Combined in Situ X-Ray Diffraction, X-Ray Absorption and Raman Scattering Experiments. *Phase Transitions* **2011**, *84*, 726–732. DOI: [10.1080/01411594.2010.549944](https://doi.org/10.1080/01411594.2010.549944).
- (171) Okatenko, V.; Castilla-Amorós, L.; Stoian, D. C.; Vávra, J.; Loiudice, A.; Buonsanti, R. The Native Oxide Skin of Liquid Metal Ga Nanoparticles Prevents Their Rapid Coalescence during Electrocatalysis. *J. Am. Chem. Soc.* **2022**, *144*, 10053–10063. DOI: [10.1021/jacs.2c03698](https://doi.org/10.1021/jacs.2c03698).
- (172) Varandili, S. B.; Stoian, D.; Vavra, J.; Rossi, K.; Pankhurst, J. R.; Guntern, Y. T.; López, N.; Buonsanti, R. Elucidating the Structure-Dependent Selectivity of CuZn towards Methane and Ethanol in CO₂ Electroreduction Using Tailored Cu/ZnO Precatalysts. *Chem. Sci.* **2021**, *12*, 14484–14493. DOI: [10.1039/d1sc04271h](https://doi.org/10.1039/d1sc04271h).
- (173) Ravel, B.; Newville, M. ATHENA, ARTEMIS, HEPHAESTUS: Data Analysis for X-Ray Absorption Spectroscopy Using IFEFFIT. *J. Synchrotron Radiat.* **2005**, *12*, 537–541. DOI: [10.1107/s0909049505012719](https://doi.org/10.1107/s0909049505012719).
- (174) Figueroa, S. J. A.; Prestipino, C. PrestoPronto: A Code Devoted to Handling Large Data Sets. *J. Phys. Conf. Ser.* **2016**, *712*, 012012. DOI: [10.1088/1742-6596/712/1/012012](https://doi.org/10.1088/1742-6596/712/1/012012).
- (175) Binsted, N. EXCURV98, CCLRC Daresbury Laboratory Computer Program. CCLRC Daresbury Laboratory: Daresbury 1998.
- (176) Batchellor, A. S.; Boettcher, S. W. Pulse-Electrodeposited Ni-Fe (Oxy)Hydroxide Oxygen Evolution Electrocatalysts with High Geometric and Intrinsic Activities at Large Mass Loadings. *ACS Catal.* **2015**, *5*, 6680–6689. DOI: [10.1021/acscatal.5b01551](https://doi.org/10.1021/acscatal.5b01551).
- (177) Doyle, R. L.; Lyons, M. E. G. An Electrochemical Impedance Study of the Oxygen Evolution Reaction at Hydrous Iron Oxide in Base. *Phys. Chem. Chem. Phys.* **2013**, *15*, 5224–5237. DOI: [10.1039/c3cp43464h](https://doi.org/10.1039/c3cp43464h).
- (178) Lyons, M. E. G.; Brandon, M. P. The Significance of Electrochemical Impedance Spectra Recorded during Active Oxygen Evolution for Oxide Covered Ni, Co and Fe Electrodes in Alkaline Solution. *J. Electroanal. Chem.* **2009**, *631*, 62–70. DOI: [10.1016/j.jelechem.2009.03.019](https://doi.org/10.1016/j.jelechem.2009.03.019).

- (179) Moysiadou, A.; Lee, S.; Hsu, C. S.; Chen, H. M.; Hu, X. Mechanism of Oxygen Evolution Catalyzed by Cobalt Oxyhydroxide: Cobalt Superoxide Species as a Key Intermediate and Dioxygen Release as a Rate-Determining Step. *J. Am. Chem. Soc.* **2020**, *142*, 11901–11914. DOI: [10.1021/jacs.0c04867](https://doi.org/10.1021/jacs.0c04867).
- (180) Reske, R.; Mistry, H.; Behafarid, F.; Roldan Cuenya, B.; Strasser, P. Particle Size Effects in the Catalytic Electroreduction of CO₂ on Cu Nanoparticles. *J. Am. Chem. Soc.* **2014**, *136*, 6978–6986. DOI: [10.1021/ja500328k](https://doi.org/10.1021/ja500328k).
- (181) Castilla-Amorós, L.; Chien, T. C. C.; Pankhurst, J. R.; Buonsanti, R. Modulating the Reactivity of Liquid Ga Nanoparticle Inks by Modifying Their Surface Chemistry. *J. Am. Chem. Soc.* **2022**, *144*, 1993–2001. DOI: [10.1021/jacs.1c12880](https://doi.org/10.1021/jacs.1c12880).
- (182) Hutter, J.; Iannuzzi, M.; Schiffmann, F.; VandeVondele, J. Cp2k: Atomistic Simulations of Condensed Matter Systems. *Wiley Interdiscip. Rev. Comput. Mol. Sci.* **2014**, *4*, 15–25. DOI: [10.1002/wcms.1159](https://doi.org/10.1002/wcms.1159).
- (183) VandeVondele, J.; Hutter, J. Gaussian Basis Sets for Accurate Calculations on Molecular Systems in Gas and Condensed Phases. *J. Chem. Phys.* **2007**, *127*, 114105. DOI: [10.1063/1.2770708](https://doi.org/10.1063/1.2770708).
- (184) Krack, M. Pseudopotentials for H to Kr Optimized for Gradient-Corrected Exchange-Correlation Functionals. *Theor. Chem. Acc.* **2005**, *114*, 145–152. DOI: [10.1007/s00214-005-0655-y](https://doi.org/10.1007/s00214-005-0655-y).
- (185) Henkelman, G.; Arnaldsson, A.; Jónsson, H. A Fast and Robust Algorithm for Bader Decomposition of Charge Density. *Comput. Mater. Sci.* **2006**, *36*, 354–360. DOI: [10.1016/j.commatsci.2005.04.010](https://doi.org/10.1016/j.commatsci.2005.04.010).
- (186) Wang, X.; Ou, P.; Wicks, J.; Xie, Y.; Wang, Y.; Li, J.; Tam, J.; Ren, D.; Howe, J. Y.; Wang, Z.; Ozden, A.; Finfrock, Y. Z.; Xu, Y.; Li, Y.; Rasouli, A. S.; Bertens, K.; Ip, A. H.; Graetzel, M.; Sinton, D.; Sargent, E. H. Gold-in-Copper at Low *CO Coverage Enables Efficient Electromethanation of CO₂. *Nat. Commun.* **2021**, *12*, 3387. DOI: [10.1038/s41467-021-23699-4](https://doi.org/10.1038/s41467-021-23699-4).
- (187) Hung, S. F.; Xu, A.; Wang, X.; Li, F.; Hsu, S. H.; Li, Y.; Wicks, J.; Cervantes, E. G.; Rasouli, A. S.; Li, Y. C.; Luo, M.; Nam, D. H.; Wang, N.; Peng, T.; Yan, Y.; Lee, G.; Sargent, E. H. A Metal-Supported Single-Atom Catalytic Site Enables Carbon Dioxide Hydrogenation. *Nat. Commun.* **2022**, *13*, 819. DOI: [10.1038/s41467-022-28456-9](https://doi.org/10.1038/s41467-022-28456-9).

- (188) Huang, Y.; Chen, Y.; Cheng, T.; Wang, L. W.; Goddard, W. A. Identification of the Selective Sites for Electrochemical Reduction of CO to C₂₊ Products on Copper Nanoparticles by Combining Reactive Force Fields, Density Functional Theory, and Machine Learning. *ACS Energy Lett.* **2018**, *3*, 2983–2988. DOI: [10.1021/acsenergylett.8b01933](https://doi.org/10.1021/acsenergylett.8b01933).
- (189) Zhang, J.; Sasaki, K.; Sutter, E.; Adzic, R. R. Stabilization of Platinum Oxygen-Reduction Electrocatalysts Using Gold Clusters. *Science* **2007**, *315*, 220–222. DOI: [10.1126/science.1134569](https://doi.org/10.1126/science.1134569).
- (190) Zhang, J.; Xu, W.; Liu, Y.; Hung, S. F.; Liu, W.; Lam, Z.; Tao, H. B.; Yang, H.; Cai, W.; Xiao, H.; Chen, H.; Liu, B. In Situ Precise Tuning of Bimetallic Electronic Effect for Boosting Oxygen Reduction Catalysis. *Nano Lett.* **2021**, *21*, 7753–7760. DOI: [10.1021/acs.nanolett.1c02705](https://doi.org/10.1021/acs.nanolett.1c02705).
- (191) Jong Yoo, S.; Kim, S. K.; Jeon, T. Y.; Jun Hwang, S.; Lee, J. G.; Lee, S. C.; Lee, K. S.; Cho, Y. H.; Sung, Y. E.; Lim, T. H. Enhanced Stability and Activity of Pt–Y Alloy Catalysts for Electrocatalytic Oxygen Reduction. *Chem. Commun.* **2011**, *47*, 11414–11416. DOI: [10.1039/c1cc12448j](https://doi.org/10.1039/c1cc12448j).
- (192) Lv, F.; Feng, J.; Wang, K.; Dou, Z.; Zhang, W.; Zhou, J.; Yang, C.; Luo, M.; Yang, Y.; Li, Y.; Gao, P.; Guo, S. Iridium-Tungsten Alloy Nanodendrites as pH-Universal Water-Splitting Electrocatalysts. *ACS Cent. Sci.* **2018**, *4*, 1244–1252. DOI: [10.1021/acscentsci.8b00426](https://doi.org/10.1021/acscentsci.8b00426).
- (193) Lončar, A.; Escalera-López, D.; Ruiz-Zepeda, F.; Hrnjić, A.; Šala, M.; Jovanovič, P.; Bele, M.; Cherevko, S.; Hodnik, N. Sacrificial Cu Layer Mediated the Formation of an Active and Stable Supported Iridium Oxygen Evolution Reaction Electrocatalyst. *ACS Catal.* **2021**, *11*, 12510–12519. DOI: [10.1021/acscatal.1c02968](https://doi.org/10.1021/acscatal.1c02968).
- (194) Đukić, T.; Moriau, L. J.; Pavko, L.; Kostelec, M.; Prokop, M.; Ruiz-Zepeda, F.; Šala, M.; Dražić, G.; Gatalo, M.; Hodnik, N. Understanding the Crucial Significance of the Temperature and Potential Window on the Stability of Carbon Supported Pt-Alloy Nanoparticles as Oxygen Reduction Reaction Electrocatalysts. *ACS Catal.* **2022**, *12*, 101–115. DOI: [10.1021/acscatal.1c04205](https://doi.org/10.1021/acscatal.1c04205).

- (195) Cheng, H.; Gui, R.; Yu, H.; Wang, C.; Liu, S.; Liu, H.; Zhou, T.; Zhang, N.; Zheng, X.; Chu, W.; Lin, Y.; Wu, H. A.; Wu, C.; Xie, Y. Subsize Pt-Based Intermetallic Compound Enables Long-Term Cyclic Mass Activity for Fuel-Cell Oxygen Reduction. *Proc. Natl. Acad. Sci. U. S. A.* **2021**, *118*, e2104026118. DOI: [10.1073/pnas.2104026118](https://doi.org/10.1073/pnas.2104026118).
- (196) Chookajorn, T.; Murdoch, H. A.; Schuh, C. A. Design of Stable Nanocrystalline Alloys. *Science* **2012**, *337*, 951–954. DOI: [10.1126/science.1224737](https://doi.org/10.1126/science.1224737).
- (197) Ma, S.; Sadakiyo, M.; Heim, M.; Luo, R.; Haasch, R. T.; Gold, J. I.; Yamauchi, M.; Kenis, P. J. A. Electroreduction of Carbon Dioxide to Hydrocarbons Using Bimetallic Cu-Pd Catalysts with Different Mixing Patterns. *J. Am. Chem. Soc.* **2017**, *139*, 47–50. DOI: [10.1021/jacs.6b10740](https://doi.org/10.1021/jacs.6b10740).
- (198) Castilla-Amorós, L.; Schouwink, P.; Oveisi, E.; Okatenko, V.; Buonsanti, R. Tailoring Morphology and Elemental Distribution of Cu-In Nanocrystals via Galvanic Replacement. *J. Am. Chem. Soc.* **2022**, *144*, 18286–18295. DOI: [10.1021/jacs.2c05792](https://doi.org/10.1021/jacs.2c05792).
- (199) Kim, D.; Resasco, J.; Yu, Y.; Asiri, A. M.; Yang, P. Synergistic Geometric and Electronic Effects for Electrochemical Reduction of Carbon Dioxide Using Gold–Copper Bimetallic Nanoparticles. *Nat. Commun.* **2014**, *5*, 4948. DOI: [10.1038/ncomms5948](https://doi.org/10.1038/ncomms5948).
- (200) Kim, D.; Xie, C.; Becknell, N.; Yu, Y.; Karamad, M.; Chan, K.; Crumlin, E. J.; Nørskov, J. K.; Yang, P. Electrochemical Activation of CO₂ through Atomic Ordering Transformations of AuCu Nanoparticles. *J. Am. Chem. Soc.* **2017**, *139*, 8329–8336. DOI: [10.1021/jacs.7b03516](https://doi.org/10.1021/jacs.7b03516).
- (201) Yin, Z.; Gao, D.; Yao, S.; Zhao, B.; Cai, F.; Lin, L.; Tang, P.; Zhai, P.; Wang, G.; Ma, D.; Bao, X. Highly Selective Palladium-Copper Bimetallic Electrocatalysts for the Electrochemical Reduction of CO₂ to CO. *Nano Energy* **2016**, *27*, 35–43. DOI: [10.1016/j.nanoen.2016.06.035](https://doi.org/10.1016/j.nanoen.2016.06.035).
- (202) Luo, Y. R. *Comprehensive Handbook of Chemical Bond Energies*, 1st Ed.; Luo, Y. R., Ed.; CRC Press: Boca Raton, FL, 2007. DOI: [10.1201/9781420007282](https://doi.org/10.1201/9781420007282).
- (203) Boeyens, J. C. A. The Periodic Electronegativity Table. *Zeitschrift fur Naturforsch. - Sect. B J. Chem. Sci.* **2008**, *63*, 199–209. DOI: [10.1515/znb-2008-0214](https://doi.org/10.1515/znb-2008-0214).
- (204) Priputen, P.; Drienovský, M.; Noga, P.; Kusý, M.; Černičková, I.; Janovec, J. Isothermal Section of Ga-Co-Cu Phase Diagram at 830 °C and Its Peculiarities. *J. Alloys Compd.* **2019**, *785*, 1173–1179. DOI: [10.1016/j.jallcom.2019.01.288](https://doi.org/10.1016/j.jallcom.2019.01.288).

- (205) Jendrzeczyk-Handzlik, D.; Fitzner, K.; Gierlotka, W. On the Cu–Ga System: Electromotive Force Measurement and Thermodynamic Reoptimization. *J. Alloys Compd.* **2015**, *621*, 287–294. DOI: [10.1016/j.jallcom.2014.08.037](https://doi.org/10.1016/j.jallcom.2014.08.037).
- (206) Tran, K.; Ulissi, Z. W. Active Learning across Intermetallics to Guide Discovery of Electrocatalysts for CO₂ Reduction and H₂ Evolution. *Nat. Catal.* **2018**, *1*, 696–703. DOI: [10.1038/s41929-018-0142-1](https://doi.org/10.1038/s41929-018-0142-1).
- (207) Li, J. B.; Ji, L. N.; Liang, J. K.; Zhang, Y.; Luo, J.; Li, C. R.; Rao, G. H. A Thermodynamic Assessment of the Copper–Gallium System. *Calphad* **2008**, *32*, 447–453. DOI: [10.1016/j.calphad.2008.03.006](https://doi.org/10.1016/j.calphad.2008.03.006).
- (208) Stokhuyzen, R.; Brandon, J. K.; Chieh, P. C.; Pearson, W. B. Copper–Gallium, $\Gamma 1\text{Cu}_9\text{Ga}_4$. *Acta Crystallogr. Sect. B* **1974**, *30*, 2910–2911. DOI: [10.1107/s0567740874008478](https://doi.org/10.1107/s0567740874008478).
- (209) Bagchi, D.; Raj, J.; Kumar Singh, A.; Cherevotan, A.; Roy, S.; Manoj, K. S.; Vinod, C. P.; Peter, S. C. Structure-Tailored Surface Oxide on Cu-Ga Intermetallics Enhances CO₂ Reduction Selectivity to Methanol at Ultra-Low Potential. *Adv. Mater.* **2022**, 2109426. DOI: [10.1002/adma.202109426](https://doi.org/10.1002/adma.202109426).
- (210) Jeon, H. S.; Sinev, I.; Scholten, F.; Divins, N. J.; Zegkinoglou, I.; Pielsticker, L.; Roldan Cuenya, B. Operando Evolution of the Structure and Oxidation State of Size-Controlled Zn Nanoparticles during CO₂ Electroreduction. *J. Am. Chem. Soc.* **2018**, *140*, 9383–9386. DOI: [10.1021/jacs.8b05258](https://doi.org/10.1021/jacs.8b05258).
- (211) Ross, M. B.; Dinh, C. T.; Li, Y.; Kim, D.; De Luna, P.; Sargent, E. H.; Yang, P. Tunable Cu Enrichment Enables Designer Syngas Electrosynthesis from CO₂. *J. Am. Chem. Soc.* **2017**, *139*, 9359–9363. DOI: [10.1021/jacs.7b04892](https://doi.org/10.1021/jacs.7b04892).
- (212) Cui, C.; Gan, L.; Heggen, M.; Rudi, S.; Strasser, P. Compositional Segregation in Shaped Pt Alloy Nanoparticles and Their Structural Behaviour during Electrocatalysis. *Nat. Mater.* **2013**, *12*, 765–771. DOI: [10.1038/nmat3668](https://doi.org/10.1038/nmat3668).
- (213) Cademartiri, L.; Thuo, M. M.; Nijhuis, C. A.; Reus, W. F.; Tricard, S.; Barber, J. R.; Sodhi, R. N. S.; Brodersen, P.; Kim, C.; Chiechi, R. C.; Whitesides, G. M. Electrical Resistance of Ag^{TS}-S(CH₂)_{n-1}CH₃//Ga₂O₃/EGaIn Tunneling Junctions. *J. Phys. Chem. C* **2012**, *116*, 10848–10860. DOI: [10.1021/jp212501s](https://doi.org/10.1021/jp212501s).

- (214) Kuhn, M.; Sham, T. K. Charge Redistribution and Electronic Behavior in a Series of Au-Cu Alloys. *Phys. Rev. B* **1994**, *49*, 1647–1661. DOI: [10.1103/physrevb.49.1647](https://doi.org/10.1103/physrevb.49.1647).
- (215) Li, G.; Hu, S.; Xu, Q.; Zhu, J. Interaction between Cu Nanoparticles and CeO₂(111) Film Surfaces. *J. Phys. Chem. C* **2019**, *123*, 23563–23571. DOI: [10.1021/acs.jpcc.9b07146](https://doi.org/10.1021/acs.jpcc.9b07146).
- (216) Huizinga, T.; van 't Blik, H. F. J.; Vis, J. C.; Prins, R. XPS Investigations of Pt and Rh Supported on γ -Al₂O₃ and TiO₂. *Surf. Sci.* **1983**, *135*, 580–596. DOI: [10.1016/0039-6028\(83\)90243-1](https://doi.org/10.1016/0039-6028(83)90243-1).
- (217) Biesinger, M. C. Advanced Analysis of Copper X-Ray Photoelectron Spectra. *Surf. Interface Anal.* **2017**, *49*, 1325–1334. DOI: [10.1002/sia.6239](https://doi.org/10.1002/sia.6239).
- (218) Bourque, J. L.; Biesinger, M. C.; Baines, K. M. Chemical State Determination of Molecular Gallium Compounds Using XPS. *Dalt. Trans.* **2016**, *45*, 7678–7696. DOI: [10.1039/c6dt00771f](https://doi.org/10.1039/c6dt00771f).
- (219) Lee, S. H.; Lin, J. C.; Farmand, M.; Landers, A. T.; Feaster, J. T.; Avilés Acosta, J. E.; Beeman, J. W.; Ye, Y.; Yano, J.; Mehta, A.; Davis, R. C.; Jaramillo, T. F.; Hahn, C.; Drisdell, W. S. Oxidation State and Surface Reconstruction of Cu under CO₂ Reduction Conditions from in Situ X-Ray Characterization. *J. Am. Chem. Soc.* **2021**, *143*, 588–592. DOI: [10.1021/jacs.0c10017](https://doi.org/10.1021/jacs.0c10017).
- (220) Gao, D.; Sinev, I.; Scholten, F.; Arán-Ais, R. M.; Divins, N. J.; Kvashnina, K.; Timoshenko, J.; Roldan Cuenya, B. Selective CO₂ Electroreduction to Ethylene and Multicarbon Alcohols via Electrolyte-Driven Nanostructuring. *Angew. Chem., Int. Ed.* **2019**. DOI: [10.1002/anie.201910155](https://doi.org/10.1002/anie.201910155).
- (221) Yang, P. P.; Zhang, X. L.; Gao, F. Y.; Zheng, Y. R.; Niu, Z. Z.; Yu, X.; Liu, R.; Wu, Z. Z.; Qin, S.; Chi, L. P.; Duan, Y.; Ma, T.; Zheng, X. S.; Zhu, J. F.; Wang, H. J.; Gao, M. R.; Yu, S. H. Protecting Copper Oxidation State via Intermediate Confinement for Selective CO₂ Electroreduction to C₂₊ Fuels. *J. Am. Chem. Soc.* **2020**, *142*, 6400–6408. DOI: [10.1021/jacs.0c01699](https://doi.org/10.1021/jacs.0c01699).
- (222) Chou, T. C.; Chang, C. C.; Yu, H. L.; Yu, W. Y.; Dong, C. L.; Velasco-Vélez, J. J.; Chuang, C. H.; Chen, L. C.; Lee, J. F.; Chen, J. M.; Wu, H. L. Controlling the Oxidation State of the Cu Electrode and Reaction Intermediates for Electrochemical CO₂ Reduction to Ethylene. *J. Am. Chem. Soc.* **2020**, *142*, 2857–2867. DOI: [10.1021/jacs.9b11126](https://doi.org/10.1021/jacs.9b11126).

- (223) Peng, X. D.; Wang, A. W.; Toseland, B. A.; Tijm, P. J. A. Single-Step Syngas-to-Dimethyl Ether Processes for Optimal Productivity, Minimal Emissions, and Natural Gas-Derived Syngas. *Ind. Eng. Chem. Res.* **1999**, *38*, 4381–4388. DOI: [10.1021/ie9901269](https://doi.org/10.1021/ie9901269).
- (224) Ciferno, J. P.; Marano, J. J. *Benchmarking Biomass Gasification Technologies for Fuels, Chemicals and Hydrogen Production*; 2009.
- (225) Manthiram, K.; Surendranath, Y.; Alivisatos, A. P. Dendritic Assembly of Gold Nanoparticles during Fuel-Forming Electrocatalysis. *J. Am. Chem. Soc.* **2014**, *136*, 7237–7240. DOI: [10.1021/ja502628r](https://doi.org/10.1021/ja502628r).
- (226) Chen, X. M.; Fei, G. T.; Zheng, K. The Solid State Phase Transition of Gallium Particles and Its Size Dependence. *J. Phys. Condens. Matter* **2009**, *21*, 245403. DOI: [10.1088/0953-8984/21/24/245403](https://doi.org/10.1088/0953-8984/21/24/245403).
- (227) Di Cicco, A. Phase Transitions in Confined Gallium Droplets. *Phys. Rev. Lett.* **1998**, *81*, 2942–2945. DOI: [10.1103/physrevlett.81.2942](https://doi.org/10.1103/physrevlett.81.2942).
- (228) Zheludev, N. Single Nanoparticle as Photonic Switch and Optical Memory Element. *J. Opt. A Pure Appl. Opt.* **2006**, *8*, S1. DOI: [10.1088/1464-4258/8/4/s01](https://doi.org/10.1088/1464-4258/8/4/s01).
- (229) Ghigna, P.; Spinolo, G.; Parravicini, G. B.; Stella, A.; Migliori, A.; Kofman, R. Metallic versus Covalent Bonding: Ga Nanoparticles as a Case Study. *J. Am. Chem. Soc.* **2007**, *129*, 8026–8033. DOI: [10.1021/ja0706100](https://doi.org/10.1021/ja0706100).
- (230) Breaux, G. A.; Hillman, D. A.; Neal, C. M.; Benirschke, R. C.; Jarrold, M. F. Gallium Cluster “Magic Melters.” *J. Am. Chem. Soc.* **2004**, *126*, 8628–8629. DOI: [10.1021/ja0477423](https://doi.org/10.1021/ja0477423).
- (231) Losurdo, M.; Suvorova, A.; Rubanov, S.; Hingerl, K.; Brown, A. S. Thermally Stable Coexistence of Liquid and Solid Phases in Gallium Nanoparticles. *Nat. Mater.* **2016**, *15*, 995–1002. DOI: [10.1038/nmat4705](https://doi.org/10.1038/nmat4705).
- (232) Borisov, B. F.; Charnaya, E. V.; Hoffmann, W. D.; Michel, D.; Shelyapin, A. V.; Kumzerov, Y. A. Nuclear Magnetic Resonance and Acoustic Investigations of the Melting - Freezing Phase Transition of Gallium in a Porous Glass. *J. Phys. Condens. Matter* **1997**, *9*, 3377–3386. DOI: [10.1088/0953-8984/9/16/010](https://doi.org/10.1088/0953-8984/9/16/010).

- (233) Reier, T.; Oezaslan, M.; Strasser, P. Electrocatalytic Oxygen Evolution Reaction (OER) on Ru, Ir, and Pt Catalysts: A Comparative Study of Nanoparticles and Bulk Materials. *ACS Catal.* **2012**, *2*, 1765–1772. DOI: [10.1021/cs3003098](https://doi.org/10.1021/cs3003098).
- (234) Ma, H.; Gao, P.; Qian, P.; Su, Y. Size-Dependent Electrochemical Properties of Pure Metallic Nanoparticles. *J. Phys. Chem. C* **2020**, *124*, 3403–3409. DOI: [10.1021/acs.jpcc.9b10962](https://doi.org/10.1021/acs.jpcc.9b10962).
- (235) Varadharaj, A.; Prabhakara Rao, G. Cyclic Voltammetric Studies on Gallium Film Electrodes in Alkaline Media. *Proc. Indian Acad. Sci. - Chem. Sci.* **1990**, *102*, 177–187. DOI: [10.1007/bf02860156](https://doi.org/10.1007/bf02860156).
- (236) Mayyas, M.; Kalantar-Zadeh, K.; Mousavi, M.; Ghasemian, M. B.; Abbasi, R.; Li, H.; Christoe, M. J.; Han, J.; Wang, Y.; Zhang, C.; Rahim, M. A.; Tang, J.; Yang, J.; Esrafilzadeh, D.; Jalili, R.; Allieux, F. M.; O'Mullane, A. P. Pulsing Liquid Alloys for Nanomaterials Synthesis. *ACS Nano* **2020**, *14*, 14070–14079. DOI: [10.1021/acsnano.0c06724](https://doi.org/10.1021/acsnano.0c06724).
- (237) Cheek, Q.; Fahrenkrug, E.; Hlynchuk, S.; Alsem, D. H.; Salmon, N. J.; Maldonado, S. In Situ Transmission Electron Microscopy Measurements of Ge Nanowire Synthesis with Liquid Metal Nanodroplets in Water. *ACS Nano* **2020**, *14*, 2869–2879. DOI: [10.1021/acsnano.9b06468](https://doi.org/10.1021/acsnano.9b06468).
- (238) Kalz, K. F.; Kraehnert, R.; Dvoyashkin, M.; Dittmeyer, R.; Gläser, R.; Krewer, U.; Reuter, K.; Grunwaldt, J. D. Future Challenges in Heterogeneous Catalysis: Understanding Catalysts under Dynamic Reaction Conditions. *ChemCatChem* **2017**, *9*, 17–29. DOI: [10.1002/cctc.201600996](https://doi.org/10.1002/cctc.201600996).
- (239) Burke, L. D. An Interfacial Mediator Interpretation of Noble Metal Electrocatalysis. *Platin. Met. Rev.* **1994**, *38*, 166–173.
- (240) Kumar, V. B.; Monte, M.; Mathon, O.; Pascarelli, S.; Porat, Z.; Gedanken, A. The Interaction between Molten Gallium and the Hydrocarbon Medium Induced by Ultrasonic Energy—Can Gallium Carbide Be Formed? *J. Am. Ceram. Soc.* **2017**, *100*, 3305–3315. DOI: [10.1111/jace.14869](https://doi.org/10.1111/jace.14869).
- (241) Dickey, M. D. Emerging Applications of Liquid Metals Featuring Surface Oxides. *ACS Appl. Mater. Interfaces* **2014**, *6*, 18369–18379. DOI: [10.1021/am5043017](https://doi.org/10.1021/am5043017).

- (242) Ma, J. L.; Dong, H. X.; He, Z. Z. Electrochemically Enabled Manipulation of Gallium-Based Liquid Metals within Porous Copper. *Mater. Horizons* **2018**, *5*, 675–682. DOI: [10.1039/c8mh00203g](https://doi.org/10.1039/c8mh00203g).
- (243) Tang, J.; Zhao, X.; Li, J.; Zhou, Y.; Liu, J.; Tang, J.; Liu, J.; Zhao, X.; Zhou, Y.; Li, J. Liquid Metal Phagocytosis: Intermetallic Wetting Induced Particle Internalization. *Adv. Sci.* **2017**, *4*, 1700024. DOI: [10.1002/advs.201700024](https://doi.org/10.1002/advs.201700024).
- (244) Kwon, K. Y.; Cheeseman, S.; Frias-De-Diego, A.; Hong, H.; Yang, J.; Jung, W.; Yin, H.; Murdoch, B. J.; Scholle, F.; Crook, N.; Crisci, E.; Dickey, M. D.; Truong, V. K.; Kim, T. A Liquid Metal Mediated Metallic Coating for Antimicrobial and Antiviral Fabrics. *Adv. Mater.* **2021**, *33*, 2104298. DOI: [10.1002/adma.202104298](https://doi.org/10.1002/adma.202104298).
- (245) Okatenko, V.; Loiudice, A.; Newton, M. A.; Stoian, D. C.; Blokhina, A.; Chen, A. N.; Rossi, K.; Buonsanti, R. Alloying as a Strategy to Boost the Stability of Copper Nanocatalysts during the Electrochemical CO₂ Reduction Reaction. *J. Am. Chem. Soc.* **2023**, *145*, 5370–5383. DOI: [10.1021/jacs.2c13437](https://doi.org/10.1021/jacs.2c13437).
- (246) Dickey, M. D. Stretchable and Soft Electronics Using Liquid Metals. *Adv. Mater.* **2017**, *29*, 1606425. DOI: [10.1002/adma.201606425](https://doi.org/10.1002/adma.201606425).
- (247) Erlenbach, S.; Mondal, K.; Ma, J.; Neumann, T. V.; Ma, S.; Holbery, J. D.; Dickey, M. D. Flexible-to-Stretchable Mechanical and Electrical Interconnects. *ACS Appl. Mater. Interfaces* **2023**, *15*, 6005–6012. DOI: [10.1021/acsami.2c14260](https://doi.org/10.1021/acsami.2c14260).
- (248) Sato, T.; Yamagishi, K.; Hashimoto, M.; Iwase, E. Method to Reduce the Contact Resistivity between Galinstan and a Copper Electrode for Electrical Connection in Flexible Devices. *ACS Appl. Mater. Interfaces* **2021**, *13*, 18247–18254. DOI: [10.1021/acsami.1c00431](https://doi.org/10.1021/acsami.1c00431).
- (249) Zhu, S.; So, J. H.; Mays, R.; Desai, S.; Barnes, W. R.; Pourdeyhimi, B.; Dickey, M. D. Ultrastretchable Fibers with Metallic Conductivity Using a Liquid Metal Alloy Core. *Adv. Funct. Mater.* **2013**, *23*, 2308–2314. DOI: [10.1002/adfm.201202405](https://doi.org/10.1002/adfm.201202405).
- (250) Tang, S. Y.; Mitchell, D. R. G.; Zhao, Q.; Yuan, D.; Yun, G.; Zhang, Y.; Qiao, R.; Lin, Y.; Dickey, M. D.; Li, W. Phase Separation in Liquid Metal Nanoparticles. *Matter* **2019**, *1*, 192–204. DOI: [10.1016/j.matt.2019.03.001](https://doi.org/10.1016/j.matt.2019.03.001).
- (251) Anderson, T. J.; Ansara, I. The Ga-Sn (Gallium-Tin) System. *J. Phase Equilibria* **1992**, *13*, 181–189. DOI: [10.1007/bf02667485](https://doi.org/10.1007/bf02667485).

- (252) Popova, S.; Fomicheva, L. Crystallization of Tungsten-Gallium Alloys at High Pressure. *J. Less Common Met.* **1981**, *77*, 137–140. DOI: [10.1016/0022-5088\(81\)90016-3](https://doi.org/10.1016/0022-5088(81)90016-3).
- (253) O'Mullane, A. Realizing Solid Core/Liquid Shell Nanomaterials at Room Temperature. *Matter* **2019**, *1*, 22–23. DOI: [10.1016/j.matt.2019.06.006](https://doi.org/10.1016/j.matt.2019.06.006).

Curriculum vitae

Valery Okatenko

Date of birth: 05/02/1995

okatenko.vd@gmail.com

EDUCATION

ÉCOLE POLYTECHNIQUE FÉDÉRALE DE LAUSANNE (EPFL), Sion, Switzerland. *Doctoral Assistant (PhD)*, Supervisor: *Professor Raffaella Buonsanti*. Sep. 2019 – Dec. 2023

SKOLKOVO INSTITUTE OF SCIENCE AND TECHNOLOGY (SKOLTECH), Moscow, Russia. *Master's Degree in Materials Science and Engineering*, Supervisor: *Professor Artem Abakumov*. Sep. 2017 – Jul. 2019

LOMONOSOV MOSCOW STATE UNIVERSITY, Moscow, Russia. *Bachelor's Degree in Materials Chemistry, Physics, and Mechanics*, Supervisors: *Doctor Maria Kirsanova, Professor Artem Abakumov*. Sep. 2013 – Jul. 2017

LIST OF PUBLICATIONS

1. V. Okatenko, C. Boulanger, A. N. Chen, K. Kumar, P. Schouwink, A. Loiudice, R. Buonsanti. Voltage-Driven Chemical Reactions Enable the Synthesis of Tunable Liquid Ga–Metal Nanoparticles. *Journal of American Chemical Society* **2023**, DOI: [10.1021/jacs.3c09828](https://doi.org/10.1021/jacs.3c09828).
2. V. Okatenko, A. Loiudice, M. A. Newton, D. C. Stoian, A. Blokhina, A. N. Chen, K. Rossi, R. Buonsanti. Alloying as a Strategy to Boost the Stability of Copper Nanocatalysts during the Electrochemical CO₂ Reduction Reaction. *Journal of American Chemical Society* **2023**, 145, 9, 5370 – 5383.

3. M. Wang, A. Loiudice, V. Okatenko, I. Sharp, R. Buonsanti. The spatial distribution of cobalt phthalocyanine and copper nanocubes controls the selectivity towards C₂ products in tandem electrocatalytic CO₂ reduction. *Chemical Science* **2023**, 14, 5, 1097 – 1104.
4. L. Castilla-Amorós, P. Schouwink, E. Oveisi, V. Okatenko, R. Buonsanti. Tailoring Morphology and Elemental Distribution of Cu-In Nanocrystals via Galvanic Replacement. *Journal of American Chemical Society* **2022**, 144, 40, 18826 – 18295.
5. V. Okatenko, L. Castilla-Amorós, D. C. Stoian, J. Vávra, A. Loiudice, R. Buonsanti. The native oxide skin of liquid metal Ga nanoparticles prevents their rapid coalescence during electrocatalysis. *Journal of American Chemical Society* **2022**, 144, 22, 10053 – 10063.
6. G. Larrazábal, V. Okatenko, I. Chorkendorff, R. Buonsanti, B. Seger. Investigation of ethylene and propylene production from CO₂ reduction over copper nanocubes in MEA-type electrolyzer. *ACS Applied Materials and Interfaces* **2022**, 14, 7779 – 7787.
7. J. R. Pankhurst, P. Iyengar, V. Okatenko, R. Buonsanti. Copper nanocrystal morphology determines the viability of molecular surface functionalization in tuning electrocatalytic behavior in CO₂ reduction. *Inorganic Chemistry* **2021**, 60, 6939 – 6945.
8. Y. T. Guntern, V. Okatenko, J. Pankhurst, S. B. Varandili, P. Iyengar, C. Koolen, D. Stoian, J. Vavra, R. Buonsanti. Colloidal Nanocrystals as Electrocatalysts with Tunable Activity and Selectivity. *ACS Catalysis* **2021**, 11, 1248 – 1295.
9. M. A. Kirsanova, V. D. Okatenko, D. A. Aksyonov, R. P. Forslund, J. T. Mefford, K. J. Stevenson, A. M. Abakumov. Bifunctional OER/ORR catalytic activity in the tetrahedral YBaCo₄O_{7.3} oxide. *Journal of Materials Chemistry A* **2019**, 7, 330 – 341.

Manuscripts in preparation

10. A. N. Chen, V. Okatenko, A. Loiudice, R. Buonsanti. Compositional Control of Colloidal Liquid Ga-Sn Nanoparticles via Galvanic Replacement.
11. E. Plaza-Mayoral, V. Okatenko, K. N. Dalby, H. Falsig, I. Chorkendorff, P. Sebastián-Pascual, M. Escudero-Escribano. Electrodeposited Cu-Ag nanostructures from deep eutectic solvents for CO₂ reduction.

CONFERENCE CONTRIBUTIONS

1. MATSUS Fall 2023 | Torremolinos, Spain. Poster presentation. Best poster award.
2. 1st Swiss Symposium on Materials Chemistry 2023 | Dubendorf, Switzerland. Poster presentation.
3. The 2022 Gordon Research Conference on Renewable Energy: Solar Fuels | Barga, Italy. Poster presentation.
4. Paul Scherrer Institute Electrochemistry Symposium 2018 | Villigen, Switzerland. Poster presentation.
5. 3rd International Conference of Young Scientists 2018 on “Topical Problems of Modern Electrochemistry and Electrochemical Materials Science” | Moscow Region, Russia. Poster presentation.
6. 3rd International Conference of Young Scientists 2018 on “Topical Problems of Modern Electrochemistry and Electrochemical Materials Science” | Moscow Region, Russia. Poster presentation.
7. XXIV International conference of students and young scientists “Lomonosov” 2017 | Moscow, Russia. Oral presentation.
8. XXV Mendeleev Young Scientists Conference 2015 | Tomsk, Russia. Oral presentation.